JACS Au
AN OPEN ACCESS JOURNAL OF THE AMERICAN CHEMICAL SOCIETY

pubs.acs.org/jacsau
Article

A Broadly Generalizable Dye for Colorimetric Aptamer-Based Sensors

Thinh Nguyen, Adara Bacon, Obtin Alkhamis, Matthew Venzke, Ransom Hill, Gabriel Castro, Caleb Byrd, Konstantin V. Bukhryakov, Jun Ohata, Zoe Millbern, Nelson R. Vinueza, and Yi Xiao*

Cite This: https://doi.org/10.1021/jacsau.6c00703
Read Online

ABSTRACT: Aptamer-based dye-displacement assays offer a simple, rapid, and robust approach for detecting analytes via a visible color change. These assays utilize a dye molecule that binds to aptamers in a monomeric or dimeric form; target binding to the aptamer subsequently displaces the dye, which aggregates in solution and undergoes a marked shift in absorbance. However, the generalizability of these assays remains an open question, and it is unclear whether existing dyes are broadly capable of binding to and undergoing target-induced displacement from diverse aptamers of varying sequence and structure. Here, we evaluate the compatibility of a panel of 105 diverse small-molecule-binding DNA aptamers with dye-displacement assays based on two commonly used cyanine dyes: 3,3′-diethylthiatricarbocyanine (Cy7) and 3,3′-di(3-sulfopropyl)-4,5,4′,5′-dibenzo-9-methyl-thiacarbocyanine (MTC). We found that roughly half of the aptamers tested were incompatible with these dyes. Through extensive evaluation of a large dye library, we identified X-732-91B—an asymmetric cyanine dye that displays unprecedented generalizability in dye-displacement assays. This dye worked with 95% of our 105-member panel of aptamer-target pairs, producing a measurable signal within seconds. This discovery could enable 'plug-and-play' development of aptamer-based colorimetric sensors for a wide range of targets in applications including medical diagnostics, environmental monitoring, quality control, and forensics.

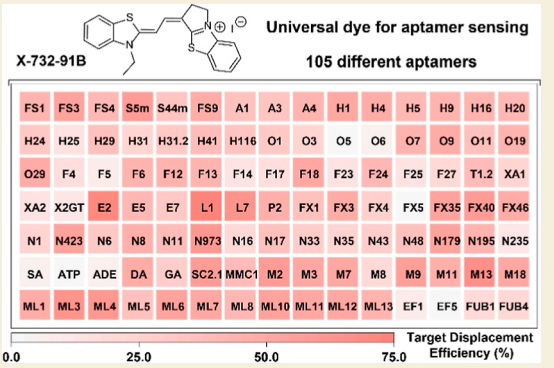

KEYWORDS: *aptamer, 3,3′-diethylthiatricarbocyanine, Cy7, MTC, dye displacement, X-732-91B, cyanine, assay*

INTRODUCTION

Medical diagnostics, health monitoring, quality control, and forensics all require simple, low-cost, and user-friendly methods for the rapid and accurate detection of specific analytes. In this regard, colorimetric sensors represent a suitable approach since they can be easily performed and interpreted without the need for dedicated instruments. Many existing colorimetric methods utilize chemical reagents to identify analytes such as ions (e.g., Pb^{2+}, Hg^{2+}, Cd^{2+}), small organic molecules (e.g., psychoactive drugs), and proteins based on a color change that occurs when the reagent binds or reacts with the analyte.[1−3] However, these tests generally lack specificity, since the employed detection reagents tend to recognize individual functional groups (e.g., aldehydes, aromatic rings, or amines) on targets that are often shared by many nontarget interferents. Alternatively, antibody-based assays offer greater specificity because antibodies typically interact with multiple epitopes on the target rather than just individual moieties. Nevertheless, such approaches are not completely generalizable, because it is impossible to generate antibodies against certain analytes, for instance, ions, toxic substances, and very low molecular weight and nonimmunogenic compounds.[4] Synthetic oligonucleotide bioreceptors known as aptamers[5,6] offer a promising alternative recognition element for colorimetric sensor development due to their excellent affinity and specificity, alongside other merits such as low production cost, tunable binding properties, and high stability.[7,8] Aptamers have one key advantage relative to other receptors in that they can be generated to bind virtually any analyte of interest. This includes metal ions (e.g., Ca^{2+}, Hg^{2+}),[9,10] anions (e.g., F^-),[11] polyatomic ions (e.g., NH_4^+),[12] organic molecules that are of low complexity (e.g., lactate, glucose)[13,14] or nonimmunogenic (e.g., nucleosides, amino acids, fatty acids),[12,13,15] and macromolecules such as proteins[16] and polymers.[17] Aptamer-based dye-displacement assays[18] have proven particularly promising for colorimetric sensing applications due to their ease of use, rapid turn-around time, high sensitivity and specificity, and cost-effectiveness. In these assays, an aptamer is initially bound to an organic dye

Received: May 5, 2026
Revised: June 18, 2026
Accepted: June 19, 2026

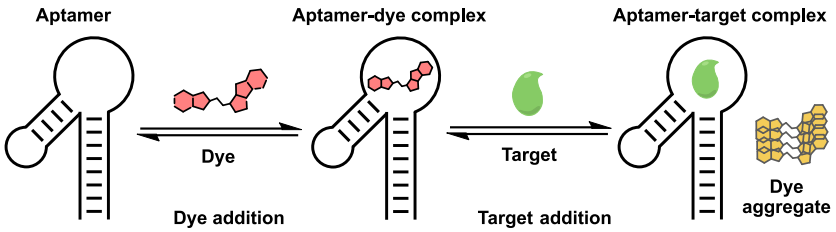

Figure 1. Working principle of aptamer-based dye-displacement assays. An aptamer (left) forms a noncovalent complex with a monomeric or dimeric organic dye molecule (middle), which increases visible absorbance at a particular wavelength. When the target binds to the aptamer, the dye is displaced into solution and subsequently undergoes aggregation (right), resulting in a measurable or even visible shift in the absorbance wavelength.

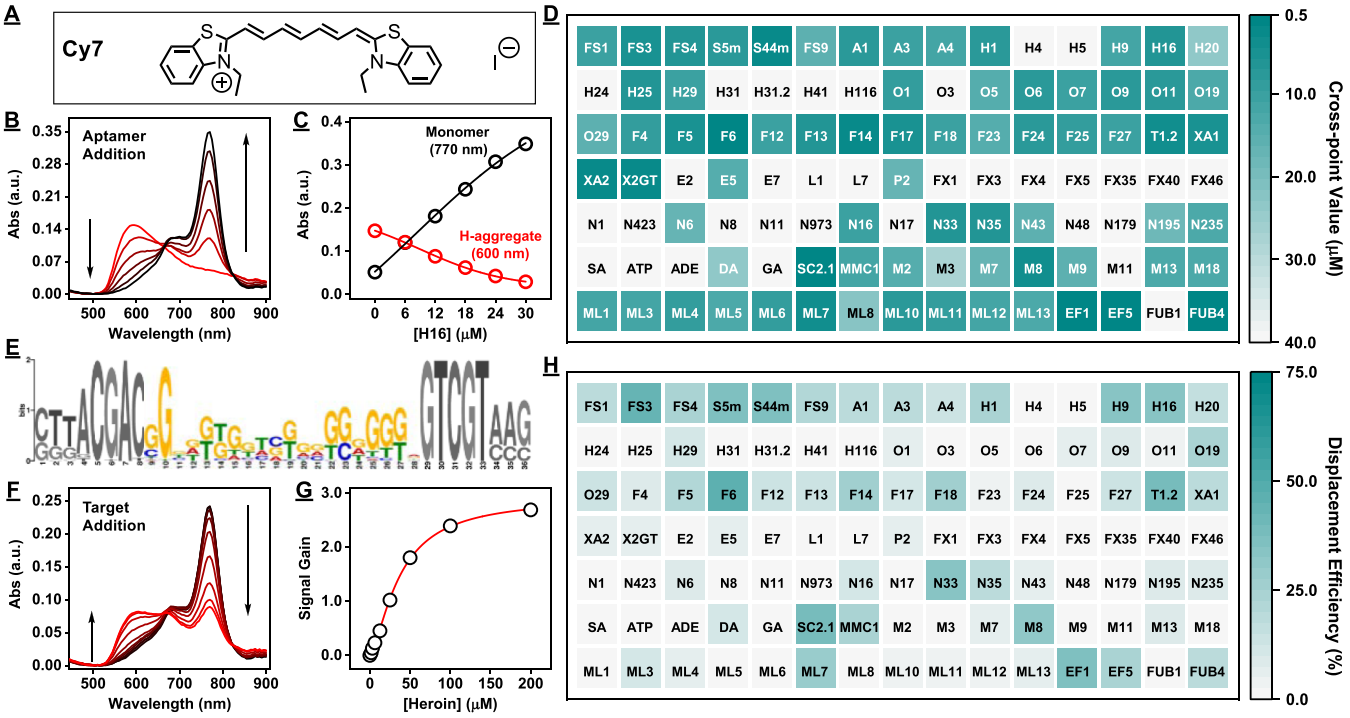

Figure 2. Assessing the generalizability of aptamer-based Cy7-displacement assays. (**A**) Molecular structure of Cy7. (**B**) UV−vis absorption spectrum of Cy7 in the presence of various concentrations of the heroin aptamer H16. (**C**) Plot of Cy7 monomer and H-aggregate peak absorbance versus concentration of aptamer H16. (**D**) A heat map of the relative affinity of 105 DNA aptamers for Cy7, expressed in terms of the "cross-point value": the concentration of aptamer at which the peak absorbance of Cy7 monomers and H-aggregates is equal. (**E**) Sequence logo displaying motifs shared by 53 aptamers that bind to Cy7 with a cross-point value < 12 μM. The 8 base-pair constant region of the aptamers is shaded in gray. (**F**) Absorbance spectra of complexes formed by 4 μM Cy7 and 24 μM H16 challenged with various concentrations of heroin. (**G**) Corresponding calibration curves for the same assay, where signal gain is plotted versus target concentration. (**H**) Heat map depicting each aptamer's displacement efficiency—a metric describing the extent to which target binding can displace Cy7 from a given aptamer at the highest target concentration.

molecule in monomeric or dimeric form (Figure 1). When the aptamer binds to the target, the dye is displaced into solution, and the change in the microenvironment of the displaced dye promotes tautomerization or aggregation. This results in a distinct change in the optical properties of the dye that can be used to detect or quantify the target.

Dye-displacement assays have an advantage over other aptamer-based sensing modalities like strand-displacement or conformation-switching assays in that they do not require any sequence engineering, truncation, or chemical labeling of the aptamer, making assay development straightforward.[19] Since native aptamers typically have higher target affinity than competitor-hybridized or truncated aptamers, the resulting sensors often achieve limits of detection in the nanomolar to micromolar range.[20,21] Moreover, dye-displacement assays are very simple to perform, requiring only sample and reagent mixing, with typical turnaround times of <1 min. Finally, dye-displacement assays are robust and highly resilient to matrix effects, and have been successfully used to detect analytes in biological samples like oral fluid and urine.[21] Despite these advantages, dye-displacement assays face a critical limitation in that they appear to have poor generality among varying aptamers. In this work, we assess the generality of two cyanine dyes commonly employed in aptamer-based displacement assays with a panel of 105 different DNA aptamers that bind to various small molecule targets. We found that these dyes only work with a fraction of aptamers. To address this issue, we identified and synthesized a new cyanine dye with extraordinary generality among the aptamers tested in the panel. Based on these findings, we believe that this new dye can enable plug-and-play development of dye-displacement assays for the colorimetric detection of arbitrary targets.

https://doi.org/10.1021/jacsau.6c00703
JACS Au XXXX, XXX, XXX−XXX

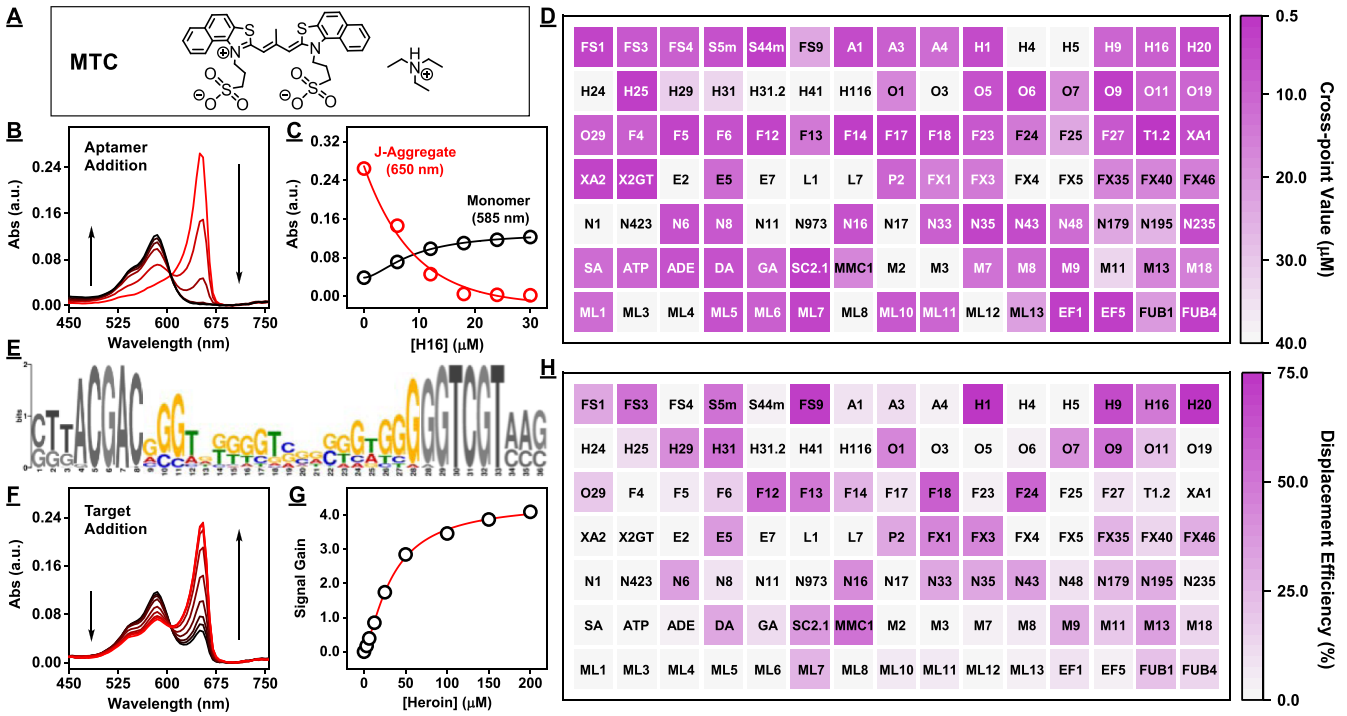

Figure 3. Assessing the generalizability of aptamer-based MTC-displacement assays. (**A**) Molecular structure of MTC. (**B**) UV−vis absorption spectrum of MTC in the presence of various concentrations of heroin-binding aptamer H16. (**C**) Plot of MTC monomer and J-aggregate peak absorbance versus concentration of aptamer H16. (**D**) A heat map presenting the relative affinity (i.e., cross-point value) of a variety of different DNA aptamers for MTC. (**E**) Sequence logo displaying motifs shared by 59 aptamers that bind to MTC with a cross-point value < 12 μM. The 8 base-pair constant region of the aptamers is shaded in gray. (**F**) Absorbance spectra of complexes formed by 2.5 μM MTC and 15 μM H16 challenged with various concentrations of heroin. (**G**) The calibration curve for this same assay, with signal gain plotted versus target concentration. (**H**) Heat map depicting displacement efficiency for each aptamer at the highest target concentration.

RESULTS AND DISCUSSION

Examining the Generality of 3,3′-Diethylthiatricarbocyanine (Cy7) in Aptamer-Based Dye Displacement Assays

Stojanovic et al. first demonstrated the dye-displacement assay with the cocaine-binding aptamer MNS-4.1 and the cyanine dye Cy7 (Figure 2A).[18] In our own studies, we have pursued a systematic approach to develop and optimize dye-displacement assays based on different dye-aptamer combinations, and have observed that Cy7 is compatible with multiple different DNA aptamers, including those containing three-way-junctions and stem-loop features.[19,21,22] To assess the broader applicability of Cy7 in aptamer-based sensors, we performed dye-displacement assays with a panel of 105 different DNA aptamers that bind various small-molecule targets with a wide range of physicochemical properties. The aptamers in this panel range in length from 33−65 nucleotides (nt) and exhibit target-binding affinities in the nanomolar to millimolar range (Supporting Information, Tables S1 and S2, Figures S1 and S2). While all of these aptamers can be generally described as stem-loop structures, it is likely that their tertiary structures are more intricate—with three- and four-way-junctions, G-quadruplexes, triplex-stems, and other noncanonical structures. We began by assessing the optical properties of 4 μM Cy7 in the different binding buffers used for the various aptamers analyzed in this study. We observed that Cy7 primarily exists as H-aggregates with broad absorption between 540−650 nm in aqueous solution (Supporting Information, Figure S3). We next assessed aptamer binding to Cy7 by determining the absorbance spectrum of 4 μM Cy7 in the presence of various concentrations of each of the 105 aptamers (Supporting Information, Figures S4−S24). For most aptamers, we observed that as the concentration of aptamer increased, the absorbance of the aggregate decreased while that of the monomer/dimer (absorbance maxima at ∼770 nm and ∼680 nm, respectively) increased, as seen with the heroin-binding aptamer H16 (Figure 2B,C), indicating aptamer-dye binding. To quantify the degree of aptamer-dye binding, we used a metric termed the "cross-point", which is the concentration of aptamer at which the monomer and H-aggregate have the same peak absorbance value. A small cross-point value indicates strong dye-aptamer binding, and we defined aptamers with cross-points <40 μM as having appreciable binding to Cy7. Only 72 of the 105 aptamers we tested met this criterion (Figure 2D), indicating that Cy7 is not capable of binding to every aptamer. These 72 aptamers exhibited varying affinity for Cy7. For instance, the fentanyl-binding aptamer F6 (Supporting Information, Figure S10D), synthetic cathinone-binding aptamer SC2.1 (Supporting Information, Figure S17A), and AB-FUBINACA-binding aptamers EF1 and EF5 (Supporting Information, Figure S24D,E) all have high apparent affinity for Cy7, as evidenced by a cross-point value < 1 μM and complete dye monomerization/dimerization and depletion of H-aggregates at 4−5 μM aptamer. In contrast, the heroin-binding aptamer H20 (Supporting Information, Figure S6E) and methamphetamine-binding aptamer ML8 (Supporting Information, Figure S23D) had poor dye affinity, with a cross-point value of 22−24 μM and 50% of the dye still present as aggregates in the presence of 20−30 μM aptamer.

https://doi.org/10.1021/jacsau.6c00703
JACS Au XXXX, XXX, XXX−XXX

These results suggest that the binding affinity—and perhaps also binding stoichiometry—of Cy7 to aptamers may be dependent on the sequence or overall structure of the aptamer. To further investigate this, we utilized the sequence alignment program GLAM2[23] to detect motifs common to Cy7-binding sequences. Interestingly, we observed no obvious motif preference among the 53 aptamer sequences capable of binding Cy7 with a cross-point <12 μM (which we defined as "strong Cy7 binders"), with the exception of the shared constant stem sequences (Figure 2E).

We next assessed the extent to which the binding of each aptamer to its respective target triggers displacement of Cy7. To test this, we mixed 4 μM Cy7 with an amount of aptamer sufficient to bind to 80−90% of the dye (based on the data collected above) and then challenged the aptamer-dye complexes with various concentrations of each respective target (Supporting Information, Figures S4−S24). We observed that the binding of the target to the aptamer resulted in a decrease in monomer/dimer absorbance and an increase in H-aggregate absorbance in a target-concentration dependent manner, as seen with the heroin aptamer H16 (Figure 2F,G). We quantified target-induced displacement of Cy7 in terms of 'displacement efficiency'. To calculate this metric, we determined the ratio of the area under the curve (AUC) of dye aggregate absorbance at the highest target concentration used in the assay with (A_T) versus without (A_{TC}) aptamer and then subtracted the ratio of the AUC of dye aggregate absorbance in the absence of target with (A_B) versus without (A_{BC}) aptamer, with the resulting value presented as a percentage. Higher displacement efficiencies indicate greater sensing performance due to higher signal-to-noise ratios. Since the standard deviation in the signals produced by this assay is typically within 5%, we defined any aptamer with a displacement efficiency ≤5% as producing no target-induced dye displacement. Of the 72 tested aptamers, 17 demonstrated ≤5% target-induced dye displacement (H25, O5, O6, O11, F23, F25, M2, M3, M9, M18, ML1, ML5, ML6, ML8, ML10, ML11, ML12), while the other 55 aptamers showed displacement efficiencies ranging from 6−47% (Figure 2H). This indicates that even if an aptamer binds to Cy7, there is no guarantee that the target will be able to effectively displace the dye from the aptamer. There are multiple possible reasons for this. First, it may be that the target and dye do not bind to the same region on the aptamer. Second, target binding may not induce a sufficient conformational change to meaningfully alter the affinity of the dye for the aptamer. Finally, the target-binding affinity of the aptamer may be too weak to effectively displace the dye. In a series of control experiments, we confirmed that the targets employed in the assay do not directly interact with Cy7 or affect the aggregation state of the dye in the absence of aptamer at the concentrations utilized here (Supporting Information, Figure S25). These results further confirm that dye displacement and aggregation are triggered by specific aptamer-target binding.

Examining the Generality of 3,3′-Di-(3-sulfopropyl)-4,5,4′,5′-dibenzo-9-methyl-thiacarbocyanine (MTC) in Aptamer-Based Dye Displacement Assays

Given the apparently limited generalizability of Cy7, we next examined another cyanine dye MTC.[24] This dye contains a 3-carbon polymethine bridge and two naphthylthiazole rings with pendant sulfonic acid groups (Figure 3A). We have previously demonstrated that MTC is compatible with dye-displacement assays using a variety of small-molecule-binding aptamers of differing sequence and affinity, recognizing targets including cocaine, synthetic cathinones, and dopamine.[21] As with Cy7, we began by determining the optical properties of MTC in the various binding buffers used for our 105 aptamers, and observed that the dye primarily forms J-aggregates in aqueous solution with peak absorbance at 650 nm (Supporting Information, Figure S26). We next assessed the binding ability of MTC to the various DNA aptamers. When the dye binds to an aptamer, J-aggregate absorbance decreases and the dye instead exists in monomeric or dimeric forms with absorbance maxima at 585 and 545 nm, respectively (Figure 3B,C). We observed that 81 out of the 105 aptamers could bind 2.5 μM MTC, with complete monomer/dimerization of 2.5 μM dye at aptamer concentrations of ≤40 μM (Figures 3D; Supporting Information, S27−S47), demonstrating that this dye also does not exhibit universal aptamer-binding characteristics. As with Cy7, the MTC-binding aptamers had varying degrees of affinity for MTC. For instance, the THC-binding aptamer T1.2 achieved complete binding to 2.5 μM MTC at a concentration of 4 μM (Supporting Information, Figure S35D), whereas for the fentanyl-binding aptamer E5, approximately 50% of the dye persisted as aggregates in the presence of 12 μM aptamer (Supporting Information, Figure S36D). We could discern no obvious conserved motif among the 59 aptamer sequences that bound MTC strongly (i.e., cross-point <12 μM) (Figure 3E).

We next assessed whether target binding could displace MTC bound to each of the 81 MTC-binding aptamers. We challenged the complexes formed by 2.5 μM MTC with sufficient aptamer to achieve 80−90% dye binding with varying concentrations of target (see Figure 3F,G for data from heroin aptamer H16). Of the 81 aptamers tested, 24 showed no meaningful target response (displacement efficiencies ≤5%), while the other 57 achieved displacement efficiencies ranging between 6−73% (Figure 3H). As with Cy7, target binding could not displace the dye from certain aptamers—most likely due to the same reasons mentioned above. We also confirmed that the various targets had minimal impact on MTC aggregation in the absence of aptamer, with only a 1−5% increase in J-aggregate absorbance even at the highest target concentrations (Supporting Information, Figure S48). Overall, 63% of the 105 aptamers were able to bind both Cy7 and MTC, 6% bound Cy7 but not MTC, 14% bound MTC but not Cy7, and 17% could not bind either dye. We also determined that on average, about half (∼53%) of the aptamers capable of binding Cy7 or MTC demonstrated target-binding induced dye-displacement with ≥6% efficiency.

Identification and Synthesis of X-732-91B, a Broadly Generalizable Dye for Aptamer-Based Dye-Displacement Assays

These data indicate that neither Cy7 nor MTC can be broadly used with aptamers of arbitrary sequence or structure. We therefore investigated whether another dye could be applied universally to aptamer dye-displacement assays. To answer this question, we screened dyes from the Max A. Weaver Dye Library at North Carolina State University—a collection of ∼100,000 organic dye molecules.[25] We selected nearly 200 different organic dye molecules in the azo, cyanine, squaraine, coumarin, xanthine, and anthraquinone families and characterized their absorbance spectra in both aqueous buffer and pure DMSO. We primarily focused on asymmetric cyanine

https://doi.org/10.1021/jacsau.6c00703
JACS Au XXXX, XXX, XXX−XXX

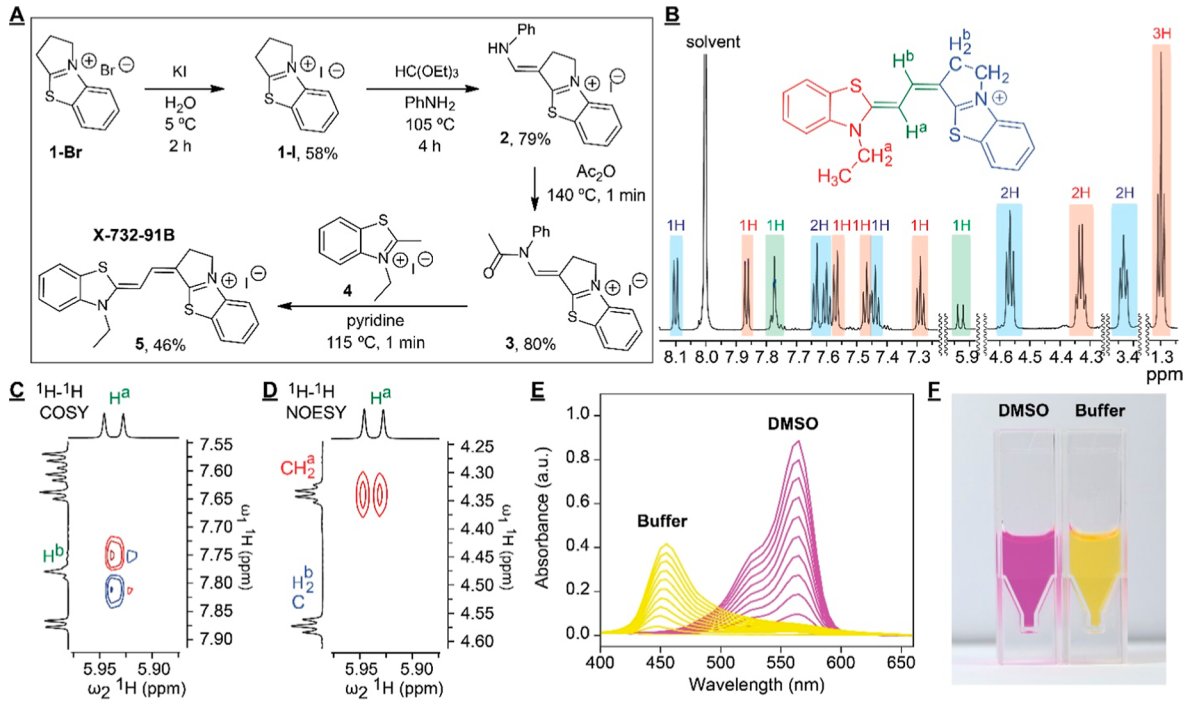

Figure 4. Synthesis and characterization of the asymmetrical cyanine dye X-732-91B. (**A**) Synthesis route of X-732-91B. (**B**) Truncated ^{1}H NMR spectrum of the dye in 95:5 dimethyl sulfoxide (DMSO)-d_6/hexafluoroisopropanol (HFIP)-d_2 confirming overall dye structure. The three parts of the structure and their corresponding spectral peaks are labeled red, green, and blue. (**C, D**) Partial spectra of (**C**) ^{1}H−^{1}H COSY NMR for the adjacent vinyl protons (labeled as H^a and H^b) and (**D**) ^{1}H−^{1}H NOESY NMR for vinyl proton H^a and the methylene protons of the ethyl group of the dye (H^b). Representative peaks/partial spectra are shown; full spectra are available in Supporting Information. (**E**) Absorbance spectra of 0−10 μM X-732-91B in pure DMSO or 1× PBS containing 1 mM $MgCl_2$, 0.01% (v/v) SDS, and 1% (v/v) DMSO. (**F**) Photograph of 4 μM X-732-91B dissolved in pure DMSO or 1× PBS containing 1 mM $MgCl_2$, 0.01% (v/v) SDS, and 1% (v/v) DMSO.

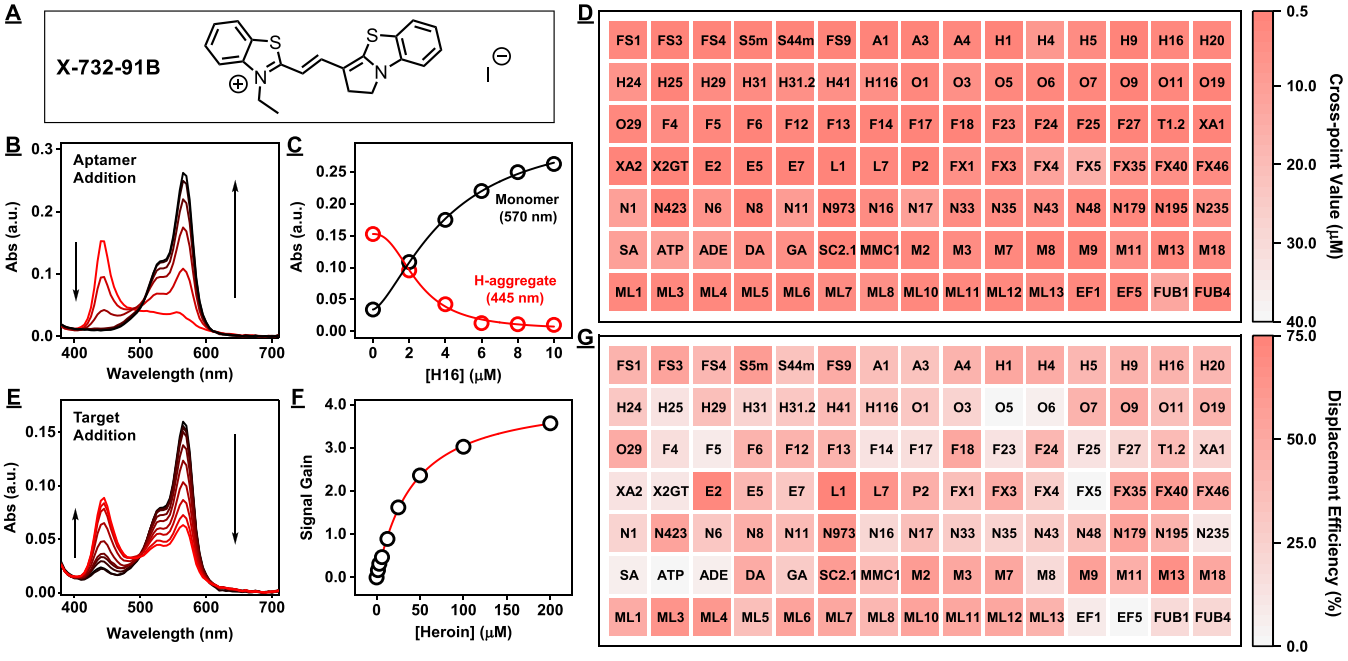

Figure 5. Assessing the generalizability of aptamer-based X-732-91B-displacement assays. (**A**) Molecular structure of X-732-91B. (**B**) UV−vis absorption spectrum of X-732-91B in the presence of various concentrations of heroin aptamer H16. (**C**) Plot of X-732-91B monomer and H-aggregate absorbance versus concentration of aptamer H16. (**D**) Heat map of the relative affinity of 105 DNA aptamers for X-732-91B expressed in terms of cross-point value. (**E**) Absorbance spectra of solutions containing complexes of 4 μM X-732-91B and 5 μM H16 aptamer challenged with various concentrations of heroin. (**F**) The corresponding calibration curve for panel **E**, where signal gain is plotted versus target concentration. (**G**) Heat map depicting displacement efficiency for aptamer-X-732-91B complexes in the presence of each aptamer's corresponding target at the highest concentration employed.

https://doi.org/10.1021/jacsau.6c00703
JACS Au XXXX, XXX, XXX−XXX

dyes, based on the observation that the asymmetric cyanine dyes SYBR Gold and SYBR Green are capable of binding DNA in a relatively sequence-independent manner.[26,27] Through our screening efforts, we identified one promising asymmetric cyanine dye, X-732-91B, that served as an effective signal reporter with several different aptamers in an initial set of dye-displacement assays, including aptamers that were incompatible with Cy7- or MTC-based displacement assays.

We subsequently synthesized this dye in a multistep process that does not require pyrophoric reagents (Figure 4A, see Supporting Information for synthesis details), as described previously.[28] First, we synthesized compound **1-Br** according to a published procedure[29] and performed a salt exchange reaction with potassium iodide to produce compound **1-I** (Supporting Information, Figures S49 and S50). We then installed the first vinyl unit on compound **1-I** through a Mannich-type reaction between the benzothiazolium iodide and $HC(OEt)_3$ in aniline to produce compound **2** (Supporting Information, Figures S51−S54), followed by acylation of the nitrogen in acetic anhydride, yielding compound **3** (Supporting Information, Figures S55 and S56). Finally, we obtained X-732-91B (**5**) (Supporting Information, Figures S57 and S58) through 1,4-addition of *N*-ethylthiazolium (**4**) to intermediate compound **3** and elimination of the acetylaniline moiety.

Upon completion of the synthesis, we confirmed the molecular weight of X-732-91B as 363 Da using high-resolution mass spectrometry (Supporting Information, Figure S59). We characterized the structure of the dye molecule in 95:5 deuterated DMSO/deuterated hexafluoroisopropanol (HFIP) using ^{1}H and ^{13}C nuclear magnetic resonance (NMR) spectroscopy (Supporting Information, Figures S60−S62). The results confirmed the presence of two thiazole/thiazolium units linked through two vinyl moieties (Figure 4B). We also performed $^{1}H-^{1}H$ correlation spectroscopy (COSY), $^{1}H-^{1}H$ nuclear Overhauser effect spectroscopy (NOESY), and $^{1}H-^{13}C$ heteronuclear single quantum correlation (HSQC) NMR, and the resulting spectra revealed the characteristic peaks of the vinyl protons as well as their spin coupling/spatial interactions (Figures 4C,D; Supporting Information, S63−S68). Overall, our NMR analysis of the dye and the intermediates from the synthetic process as well as the Fourier transform infrared (FTIR) spectrum for X-732-91B (Supporting Information, Figure S69) are consistent with previous literature for analogous molecules.[30,31] We then examined the optical properties of newly synthesized X-732-91B dye in both pure DMSO and 1× PBS buffer containing 1 mM $MgCl_2$, 0.01% (v/v) SDS, and 1% (v/v) DMSO (Figure 4E,F). In DMSO, the solution appears pink, with peak absorbance at 570 nm, which corresponds to the dye most likely being in a monomeric state, with a shoulder at 525 nm that presumably arises from a subpopulation of dye molecules in the H-dimer form. In contrast, the buffer solution was yellow, with an absorbance maximum at 445−450 nm, which we attribute to the formation of H-aggregates. We observed similar spectra in other binding buffers, with absorbance maxima blue- or red-shifted by 1−2 nm (Supporting Information, Figure S70).

Assessment of X-732-91B in Dye-Displacement Assays

We next assessed the binding performance of X-732-91B to our panel of 105 aptamers (Figure 5A). We mixed 4 μM dye with varying concentrations of each aptamer, and observed that dye-aptamer binding led to increased monomer/dimer absorbance and decreased aggregate absorbance as a function of aptamer concentration (Figures 5B,C; Supporting Information, S71−S91). All aptamers reached the cross-point values of dye binding at aptamer concentrations ranging from 0.5−15 μM (Figure 5D) a remarkable improvement in generalizability compared to Cy7 and MTC, both of which only bound to 72 aptamers (cross-point values: 0.5−27 μM) and 81 aptamers (cross-point values: 1.6−33 μM) in the 105-aptamer panel, respectively. For instance, certain aptamers for heroin (H5, H24, H31.2, H41, and H116) (Supporting Information, Figures S6−S8, S29−S31), oxycodone (O3) (Supporting Information, Figures S8D and S31D), fentanyl (E2, E7, L1, and L7) (Supporting Information, Figures S13, S14, S36, S37), cocaine (N179, N423, and N973) (Supporting Information, Figures S19, S20, S42, S43), and methamphetamine (ML8) (Supporting Information Figures S23D and S46D) were unable to bind Cy7 or MTC at aptamer concentrations of up to 40 μM. However, these same aptamers all exhibited strong binding to X-732-91B with cross-point values $\leq$6 μM (Supporting Information, Figures S73−75, S80, S81, S86, S87, and S90). Regarding binding strength, out of the 105 aptamers, 64 could completely monomerize/dimerize X-732-91B at $\leq$ 10 μM aptamer, while only 6 and 25 aptamers achieved the same with Cy7 and MTC, respectively. This indicates that X-732-91B generally has relatively high affinity for oligonucleotides.

Finally, we determined the extent to which each aptamer's target could displace X-732-91B from the aptamer. We mixed 4 μM dye with a sufficient concentration of aptamer to monomerize/dimerize 80−90% of the dye and challenged the complex with various concentrations of target (Figures 5E−G; Supporting Information, S71−S91). Among the 105 aptamers tested, only five demonstrated displacement efficiencies below our 5% cutoff (aptamers O5, FX5, ATP, ADE, and EF5), while the other 100 exhibited displacement efficiencies ranging between 6−73%. Impressively, 18 aptamers that failed to bind either Cy7 and MTC even in the presence of 40 μM aptamer bound to X-732-91B, with cross-point values of $< \sim$10 μM and target displacement efficiencies in the range of 25−73%. These results together confirm that X-732-91B offers a much more broadly useful and generally applicable dye for displacement assays than standard dyes like Cy7 and MTC. Lastly, our control experiments demonstrated that all the targets tested in this work had minimal impact (1−5% change) on dye H-aggregation in the absence of aptamer, even at the highest target concentrations (Supporting Information, Figure S92).

We were interested to understand the reason(s) for why the five aptamers O5, FX5, ATP, ADE, and EF5 were not able to function in the dye-displacement assay with X-732-91B. These aptamers have a wide range of target-binding affinities (K_D range from 40 to 15,000 nM), implying that failure of the target to displace the dye is not necessarily related to this parameter. We also could not identify any sequence or structural features that were unique to these aptamers relative to all other aptamers that could bind X-732-91B. The remaining hypotheses for failure include that the target and dye do not bind to the same location on the aptamer, aptamer-target binding does not trigger a sufficiently large conformational change to meaningfully perturb aptamer-dye affinity, or the dye binds to the aptamer with much greater affinity than the target, precluding dye displacement.

https://doi.org/10.1021/jacsau.6c00703
JACS Au XXXX, XXX, XXX−XXX

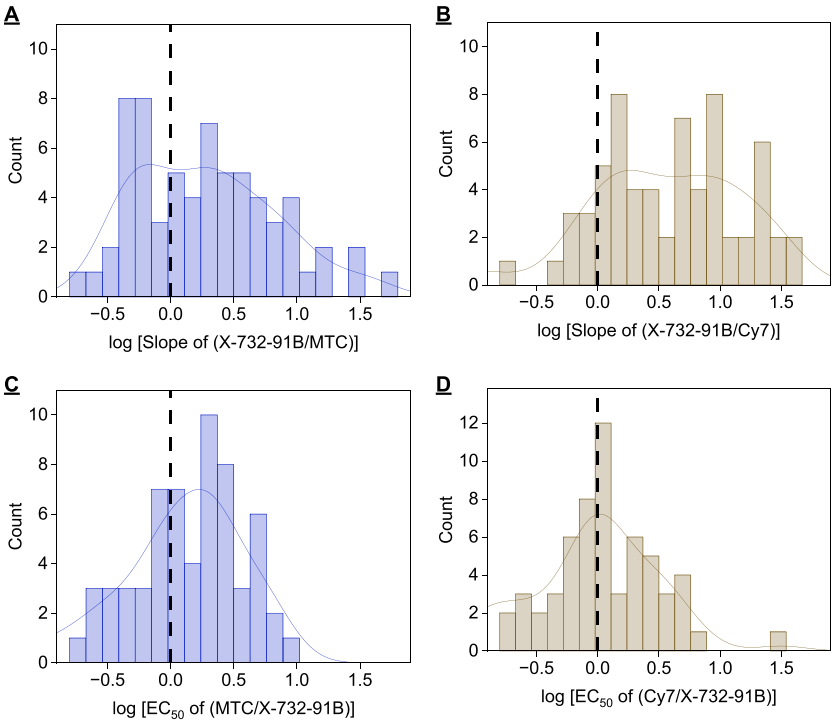

Figure 6. Comparison of the sensitivity of dye-displacement assays based on X-732-91B, MTC, and Cy7. (**A, B**) Histograms showing the logarithm of the ratio of assay calibration curve slope values for X-732-91B versus (**A**) MTC or (**B**) Cy7 for assays conducted with different aptamers. (**C, D**) Histograms showing the logarithm of the ratio of the assay EC_{50} for X-732-91B versus (**C**) MTC or (**D**) Cy7 for assays conducted with different aptamers.

Analysis and Comparison of Dye-Displacement Assay Performance Based on Different Cyanine Dyes

We next performed a comprehensive analysis of the analytical capabilities and performance of all dye-displacement assays conducted in this study. First, we examined the correlation between aptamer length, GC content, and target-binding affinity (K_D) with the capability of the aptamers to bind X-732-91B, Cy7, or MTC. Since all of the 105 tested aptamers were able to bind X-732-91B, there was no apparent correlation between any of the described parameters and binding capability for this dye (Supporting Information, Figure S93A−C). For MTC and Cy7, only a portion of the tested aptamers were able to bind these dyes, but our analysis revealed no correlation between aptamer length, GC content, or target-binding affinity and dye binding (Supporting Information, Figure S93D−I). It remains difficult to understand exactly why X-732-91B can bind to more aptamers than MTC and Cy7 without further experiments, such as structure determination of aptamer-dye complexes by X-ray crystallography. Nevertheless, there are a few hypothetical reasons that could explain this phenomenon. From a thermodynamic perspective, X-732-91B has a shorter conjugated system and a more rigid structure, which reduces the entropy loss upon aptamer binding and hence renders Gibbs free energy more negative (i.e., aptamer-dye binding is a more favorable process). In contrast, the extended and flexible conjugated chain of Cy7 leads to a higher entropic penalty if aptamer-dye binding occurs, rendering Gibbs free energy less negative (i.e., aptamer-dye binding is less favorable). Similarly, given its bulky structure and multiple rotatable bonds, MTC is also expected to experience a considerable entropic penalty and hence weaker affinities for aptamers in general. In terms of size, X-732-91B has a more compact and simpler structural framework compared to Cy7 and MTC. This likely facilitates its accommodation within the binding pockets of aptamers (e.g., minor or major grooves, and intercalation sites between bases), whereas the larger size of Cy7 and especially MTC may hinder efficient binding due to steric hindrance.

To comprehensively assess and compare assay sensitivity, we examined two metrics for all assays: (i) the slope of the linear range of the target calibration curves, and (ii) the EC_{50} of the calibration curves. The former quantifies the sensitivity of the assay at lower target concentrations, while the latter encapsulates assay response at the midpoint of signal saturation. Superficially, EC_{50} and slope have similar patterns to the target response for each particular dye (Supporting Information, Figure S94). Slope and EC_{50} also seem to be correlated, such that aptamers with relatively higher slope values have lower EC_{50} (i.e., high-sensitivity assays) and vice versa. To verify this, we plotted the logarithm of slope against the logarithm of EC_{50} for each aptamer-dye pair and observed an inverse correlation between these two metrics (R^2 for X-732-91B, MTC, and Cy7 was 0.67, 0.55, and 0.60, respectively) (Supporting Information, Figure S95A−C). We also observed a weak negative correlation between the K_D of each aptamer and the assay slope (Supporting Information, Figure S95D−F) and a weak positive correlation between K_D and EC_{50} (Supporting Information, Figure S95G−I). This is logical, as higher target affinity should result in a greater slope and lower EC_{50}. In contrast, we did not find any correlation between dye-displacement efficiency and slope, EC_{50}, or K_D (Supporting Information, Figure S96). This can be explained by the fact that dye-displacement efficiency is influenced by multiple factors, including the location of the binding site of the target and dye on the aptamer, whether target binding

https://doi.org/10.1021/jacsau.6c00703
JACS Au XXXX, XXX, XXX−XXX

induces conformational changes in the aptamer that alter dye affinity, and the target- and dye-binding affinity of the aptamer.

Finally, we compared the slope and EC_{50} values for assays based on different dyes to identify which dye supported more sensitive analytical performance. We first divided the slope values for each X-732-91B-based assay by the slope value for the corresponding MTC- or Cy7-based assay, and then plotted these values logarithmically in a histogram (Figure 6A, B). A log(ratio) value significantly greater than 0 indicates greater sensitivity for the X-732-91B-based assay relative to the MTC- or Cy7-based assay; for the analysis here, we regarded log(ratio) values within −0.02 to 0.1 as being similar in performance. Between X-732-91B and MTC, 58% of aptamers had log(ratio) > 0.1 and 8% had similar performance, while between X-732-91B and Cy7, 80% had log(ratio) > 0.1 and 8% had similar performance. We next performed a similar comparative analysis by dividing the EC_{50} values for each MTC- or Cy7-based assay by the corresponding value for the X-732-91B-based assay and then plotted these values logarithmically in a histogram (Figure 6C, D). Between X-732-91B and MTC, 63% of assays had log(ratio) > 0.1 with 37% being similar, while between X-732-91B and Cy7, 39% of assays had log(ratio) > 0.1 with 25% being similar. These data again support the notion that assays based on X-732-91B are in most cases more sensitive than those based on MTC and Cy7.

CONCLUSIONS

In this work, we explored the general applicability of the dyes Cy7 and MTC in aptamer-based dye-displacement assays and described the identification of X-732-91B, a new asymmetric cyanine dye that can serve as a probe for such assays with extremely broad applicability among a diverse range of aptamers with disparate sequences and structures. We determined that X-732-91B is capable of binding 105 different aptamers with affinity in the low micromolar range, and that target-binding can efficiently displace this dye from 95% of these aptamers. This represents considerably greater generalizability compared to standard dyes like Cy7 and MTC, which were only compatible with roughly half of the aptamer-target pairs evaluated in our study. The identification of this dye should facilitate the development of dye-displacement assays using virtually every aptamer in our tested panel—and most likely many other aptamers as well—which will in turn prove beneficial in applications requiring rapid analyte detection in field settings. The same dye should also offer a useful indicator for assessing the relative binding affinity or specificity of aptamers. In future work, we will pursue structure−activity studies to identify the key structural features that enable a dye such as X-732-91B to bind nucleic acids in a sequence-independent fashion and serve as a general reporter of aptamer-ligand binding. This could guide efforts to tune the optical properties of this and related dyes with modifications to the core scaffold—for example, halogenation or the introduction of electron donating/withdrawing groups—to shift their absorbance maxima and enhance molar absorption coefficients.

EXPERIMENTAL SECTION

Reagents and Materials

Molecular-biology-grade water and 10× phosphate-buffered saline (PBS) were purchased from Corning. Trizma preset crystals (pH 7.4), 1 M magnesium chloride solution, 5 M sodium chloride solution, sodium dodecyl sulfate (SDS), potassium chloride, Triton X−100, 3,3′-diethylthiatricarbocyanine iodide (Cy7), and dimethyl sulfoxide (DMSO), dopamine HCl, serotonin HCl, D-(+)-glucose, flunixin, and adenosine were purchased from Sigma-Aldrich. Fentanyl hydrochloride (HCl), acetyl fentanyl HCl, furanyl fentanyl HCl, oxycodone HCl, heroin HCl, cocaine HCl, remifentanil HCl, Δ9-tetrahydrocannabinol (THC), UR-144, alfentanil HCl, mephedrone HCl, (±)-cis-3-methyl fentanyl HCl, (+)-methamphetamine HCl, and AB-FUBINACA were purchased from Cayman Chemical Company. Adenosine-5′-triphosphate (ATP) disodium salt trihydrate was purchased from MP Biomedical. 3,3′-di(3-sulfopropyl)-4,5,4′,5′-dibenzo-9-methyl-thiacarbocyanine (MTC) triethylammonium salt was synthesized fresh using a previously published protocol.[21,32] A sample of X-732-91B was procured from the Max A. Weaver Dye Library at North Carolina State University. All DNA oligonucleotides were purchased as standard desalted purity from Integrated DNA Technologies and dissolved in molecular-biology-grade water. DNA concentrations were measured using a Nanodrop 2000 spectrophotometer. Transparent 384-well microplates were purchased from Thermo Fisher Scientific.

Buffer Conditions for Dye-Displacement Assays

For all dye-displacement experiments, buffer composition varied depending on the aptamer; refer to Table S2 for details. All buffers included SDS at a final concentration of 0.01% (w/v) to stabilize the dye in aqueous solution and promote dye aggregate formation. DMSO at a final concentration of 1−3% (v/v) was also included in samples to solubilize the dyes. For a typical assay, the dye dissolved in 100% DMSO was mixed with aqueous buffer containing the aptamer, such that the final DMSO concentration was 1%. For hydrophobic targets such as THC, UR-144, and AB-FUBINACA, the final solution contained an additional 1−2% DMSO from the drug since the stock was originally prepared in 100% DMSO.

Measuring the Extent of Aptamer-Dye Binding

Buffer conditions for different aptamers employed in these experiments can be found in Supporting Information, Table S2. 99 μL of aptamer was prepared at various concentrations (0−40 μM) in 1.01× buffer and incubated for 5 min at room temperature. One μL of 100× dye dissolved in DMSO was then added to the aptamer solution and mixed by inverting the tube rapidly or vortexing at low speed. 75 μL of this mixture was loaded into the well of a 384-well transparent plate, and absorbance spectra were recorded from 300−900 nm with a 5 nm step size every 5 min using a Tecan Spark microplate reader.

Target Detection with Dye Displacement Assay

First, the optimal concentration of aptamer, at which 80−90% of the molecules of a given dye were bound in a monomeric/dimeric state, was dissolved in the appropriate buffer (see Supporting Information, Table S2) and incubated at room temperature for 5 min. Dye dissolved in 100% DMSO was then added to the aptamer solution to form aptamer-dye complexes (final concentrations for Cy7, MTC, and X-732-91B were respectively 4.0 μM, 2.5 μM, and 4.0 μM). After mixing by light inversion, 95 μL of aptamer-dye solution was mixed with 5 μL of target at various concentrations in buffer, with the exception of experiments using THC, UR-144, or AB-FUBINACA. In these instances, 98 or 99 μL of aptamer-dye solution in buffer was mixed with 2 or 1 μL of target in DMSO, respectively. 75 μL of sample was then loaded into the wells of a 384-well transparent microplate, and the absorbance spectra were recorded as described above. The area under the curve (AUC) of the absorbance spectra were calculated using Origin Lab software for monomers/dimers at 685−900 nm, 480−600 nm, and 500−600 nm and for aggregates at 500−685 nm, 600−700 nm, and 400−500 nm for Cy7, MTC, and X-732-91B, respectively. Then, the term 'R' was calculated by dividing aggregate AUC by the monomer/dimer AUC. Signal gain was calculated using the following formula: R_T/R_0-1, in which R_T and R_0 represent R calculated in the presence and absence of target, respectively. Displacement efficiency was calculated at the aggregate peak using the following formula: $\%_{Target}-\%_{Blank}$, in which

https://doi.org/10.1021/jacsau.6c00703
JACS Au XXXX, XXX, XXX−XXX

$\%_{Target} = \frac{AUC_{Highest\ Target}}{AUC_{Highest\ Target\ Control}} \times 100$ and $\%_{blank} = \frac{AUC_{Blank\ Target}}{AUC_{Blank\ Control}} \times 100$, where $AUC_{Highest\ Target}$ and $AUC_{Highest\ Target\ Control}$ are the AUC of dye produced at the highest concentration of targetdye with the highest concentration of target with and without aptamer, respectively and $AUC_{Blank\ Target}$ and $AUC_{Blank\ Control}$ are the AUC of dye produced in the absence of target with and without aptamer, respectively, for the aptamer-dye assay at the highest target concentration, $AUC_{Highest\ Target\ Control}$ is the AUC for t. To determine if there was an interaction between the dye and target, we performed control experiments wherein dye dissolved in DMSO was added to solutions containing target at various concentrations in buffer, with absorbance spectra recorded as described above.

■ ASSOCIATED CONTENT

Supporting Information

The Supporting Information is available free of charge at https://pubs.acs.org/doi/10.1021/jacsau.6c00703.

Experimental procedure for X-732-91B synthesis; characterization of X-732-91B via ^{1}H NMR, ^{13}C NMR, $^{1}H-^{1}H$ COSY NMR, $^{1}H-^{1}H$ NOESY NMR, $^{1}H-^{13}C$ HSQC NMR, FT-IR and HPLC-MS; DNA sequences used in this work; reported binding affinity of aptamers and their respective targets; ITC measurements of 16 new aptamers; optical properties of Cy7, MTC or X-732-91B under different experimental conditions; target detection of 105 aptamers based on Cy7, MTC, and X-732-91B; absorbance spectra of 4 μM Cy7, 2.5 μM MTC or 4 μM X-732-91B in the presence of different targets at various concentrations, identifying determinants of aptamer binding to dyes, analyzing the sensitivity of dye-displacement assays using different performance metrics, correlation between different sensitivity parameters for dye-displacement assays, target-binding affinity, and dye-displacement efficiency (PDF)

■ AUTHOR INFORMATION

Corresponding Author

Yi Xiao − *Department of Chemistry, North Carolina State University, Raleigh, North Carolina 27607, United States;* orcid.org/0000-0001-7278-9811; Email: yxiao34@ncsu.edu

Authors

Thinh Nguyen − *Department of Chemistry, North Carolina State University, Raleigh, North Carolina 27607, United States*

Adara Bacon − *Department of Chemistry, North Carolina State University, Raleigh, North Carolina 27607, United States*

Obtin Alkhamis − *Department of Chemistry, North Carolina State University, Raleigh, North Carolina 27607, United States*

Matthew Venzke − *Department of Chemistry, North Carolina State University, Raleigh, North Carolina 27607, United States*

Ransom Hill − *Department of Chemistry, North Carolina State University, Raleigh, North Carolina 27607, United States*

Gabriel Castro − *Department of Chemistry, North Carolina State University, Raleigh, North Carolina 27607, United States*

Caleb Byrd − *Department of Chemistry, North Carolina State University, Raleigh, North Carolina 27607, United States*

Konstantin V. Bukhryakov − *Department of Chemistry and Biochemistry, Florida International University, Miami, Florida 33199, United States;* orcid.org/0000-0002-8425-9671

Jun Ohata − *Department of Chemistry, North Carolina State University, Raleigh, North Carolina 27607, United States;* orcid.org/0000-0002-3614-7472

Zoe Millbern − *Department of Textile Engineering, Wilson College of Textiles, North Carolina State University, Raleigh, North Carolina 27695, United States*

Nelson R. Vinueza − *Department of Chemistry, North Carolina State University, Raleigh, North Carolina 27607, United States; Department of Textile Engineering, Wilson College of Textiles, North Carolina State University, Raleigh, North Carolina 27695, United States;* orcid.org/0000-0002-2608-5431

Complete contact information is available at: https://pubs.acs.org/10.1021/jacsau.6c00703

Notes

The authors declare no competing financial interest.

■ ACKNOWLEDGMENTS

This work was supported in part by the National Institute of Justice, Grant Office of Justice Programs, U.S. Department of Justice Award 2022-GG-04440-RESS and the National Science Foundation [2532545]. We acknowledge Phuong Ly's preliminary information, which is not included in this paper but was used to recollect experimental data with high accuracy for this paper.

■ REFERENCES

(1) Philp, M.; Fu, S. A Review of Chemical 'Spot' Tests: A Presumptive Illicit Drug Identification Technique. *Drug Test. Anal.* **2018**, *10* (1), 95−108.

(2) Chawla, R. *Practical Clinical Biochemistry: Methods and Interpretations*; Jaypee Brothers Medical Publishers, 2014.

(3) Oehme, I.; Wolfbeis, O. S. Optical Sensors for Determination of Heavy Metal Ions. *Microchim. Acta* **1997**, *126* (3), 177−192.

(4) Hughey, J. J.; Colby, J. M. Discovering Cross-Reactivity in Urine Drug Screening Immunoassays through Large-Scale Analysis of Electronic Health Records. *Clin. Chem.* **2019**, *65* (12), 1522−1531.

(5) Ellington, A. D.; Szostak, J. W. In Vitro Selection of RNA Molecules That Bind Specific Ligands. *Nature* **1990**, *346* (6287), 818−822.

(6) Tuerk, C.; Gold, L. Systematic Evolution of Ligands by Exponential Enrichment: RNA Ligands to Bacteriophage T4 DNA Polymerase. *Science* **1990**, *249* (4968), 505−510.

(7) Dunn, M. R.; Jimenez, R. M.; Chaput, J. C. Analysis of Aptamer Discovery and Technology. *Nat. Rev. Chem.* **2017**, *1* (10), 0076.

(8) Zhou, J.; Rossi, J. Aptamers as Targeted Therapeutics: Current Potential and Challenges. *Nat. Rev. Drug Discovery* **2017**, *16* (3), 181−202.

(9) Behnam, V.; McManamen, A. M.; Ballard, H. G.; Aldana, B.; Tamimi, M.; Milosavić, N.; Stojanovic, M. N.; Rubin, M. R.; Sia, S. K. MPatch: A Wearable Hydrogel Microneedle Patch for In Vivo Optical Sensing of Calcium. *Angew. Chem., Int. Ed.* **2025**, *64* (2), No. e202414871.

(10) Qu, H.; Csordas, A. T.; Wang, J.; Oh, S. S.; Eisenstein, M. S.; Soh, H. T. Rapid and Label-Free Strategy to Isolate Aptamers for Metal Ions. *ACS Nano* **2016**, *10* (8), 7558−7565.

https://doi.org/10.1021/jacsau.6c00703
JACS Au XXXX, XXX, XXX−XXX

(11) Ren, A.; Rajashankar, K. R.; Patel, D. J. Fluoride Ion Encapsulation by Mg2+ Ions and Phosphates in a Fluoride Riboswitch. *Nature* **2012**, *486* (7401), 85−89.
(12) Yang, K.; Mitchell, N. M.; Banerjee, S.; Cheng, Z.; Taylor, S.; Kostic, A. M.; Wong, I.; Sajjath, S.; Zhang, Y.; Stevens, J.; Mohan, S.; Landry, D. W.; Worgall, T. S.; Andrews, A. M.; Stojanovic, M. N. A Functional Group-Guided Approach to Aptamers for Small Molecules. *Science* **2023**, *380* (6648), 942−948.
(13) Nakatsuka, N.; Yang, K.-A.; Abendroth, J. M.; Cheung, K. M.; Xu, X.; Yang, H.; Zhao, C.; Zhu, B.; Rim, Y. S.; Yang, Y.; Weiss, P. S.; Stojanović, M. N.; Andrews, A. M. Aptamer−Field-Effect Transistors Overcome Debye Length Limitations for Small-Molecule Sensing. *Science* **2018**, *362* (6412), 319−324.
(14) Huang, P.-J. J.; Liu, J. Simultaneous Detection of L-Lactate and D-Glucose Using DNA Aptamers in Human Blood Serum. *Angew. Chem., Int. Ed.* **2023**, *62* (12), No. e202212879.
(15) Huizenga, D. E.; Szostak, J. W. A DNA Aptamer That Binds Adenosine and ATP. *Biochemistry* **1995**, *34* (2), 656−665.
(16) Bock, L. C.; Griffin, L. C.; Latham, J. A.; Vermaas, E. H.; Toole, J. J. Selection of Single-Stranded DNA Molecules That Bind and Inhibit Human Thrombin. *Nature* **1992**, *355* (6360), 564−566.
(17) Boese, B. J.; Breaker, R. R. In Vitro Selection and Characterization of Cellulose-Binding DNA Aptamers. *Nucleic Acids Res.* **2007**, *35* (19), 6378−6388.
(18) Stojanovic, M. N.; Landry, D. W. Aptamer-Based Colorimetric Probe for Cocaine. *J. Am. Chem. Soc.* **2002**, *124* (33), 9678−9679.
(19) Yu, H.; Yang, W.; Alkhamis, O.; Canoura, J.; Yang, K.-A.; Xiao, Y. In Vitro Isolation of Small-Molecule-Binding Aptamers with Intrinsic Dye-Displacement Functionality. *Nucleic Acids Res.* **2018**, *46* (8), No. e43.
(20) Alkhamis, O.; Canoura, J.; Yu, H.; Liu, Y.; Xiao, Y. Innovative Engineering and Sensing Strategies for Aptamer-Based Small-Molecule Detection. *TrAC, Trends Anal. Chem.* **2019**, *121*, 115699.
(21) Alkhamis, O.; Canoura, J.; Bukhryakov, K. V.; Tarifa, A.; DeCaprio, A. P.; Xiao, Y. DNA Aptamer−Cyanine Complexes as Generic Colorimetric Small-Molecule Sensors. *Angew. Chem., Int. Ed.* **2022**, *61* (3), No. e202112305.
(22) Yang, W.; Yu, H.; Alkhamis, O.; Liu, Y.; Canoura, J.; Fu, F.; Xiao, Y. In Vitro Isolation of Class-Specific Oligonucleotide-Based Small-Molecule Receptors. *Nucleic Acids Res.* **2019**, *47* (12), No. e71.
(23) Frith, M. C.; Saunders, N. F. W.; Kobe, B.; Bailey, T. L. Discovering Sequence Motifs with Arbitrary Insertions and Deletions. *PLoS Comput. Biol.* **2008**, *4* (5), No. e1000071.
(24) Sun, H.; Xiang, J.; Gai, W.; Shang, Q.; Li, Q.; Guan, A.; Yang, Q.; Liu, Y.; Tang, Y.; Xu, G. Visual Detection of Potassium by a Cyanine Dye Supramolecular Aggregate Responsive to G-Quadruplex Motif Transition. *Analyst* **2012**, *137* (24), 5713−5715.
(25) Kuenemann, M. A.; Szymczyk, M.; Chen, Y.; Sultana, N.; Hinks, D.; Freeman, H. S.; Williams, A. J.; Fourches, D.; Vinueza, N. R. Weaver's Historic Accessible Collection of Synthetic Dyes: A CheminformaticsAnalysis. *Chem. Sci.* **2017**, *8* (6), 4334−4339.
(26) Tuma, R. S.; Beaudet, M. P.; Jin, X.; Jones, L. J.; Cheung, C.-Y.; Yue, S.; Singer, V. L. Characterization of SYBR Gold Nucleic Acid Gel Stain: A Dye Optimized for Use with 300-nm Ultraviolet Trans-illuminators. *Anal. Biochem.* **1999**, *268* (2), 278−288.
(27) Kolbeck, P. J.; Vanderlinden, W.; Gemmecker, G.; Gebhardt, C.; Lehmann, M.; Lak, A.; Nicolaus, T.; Cordes, T.; Lipfert, J. Molecular Structure, DNA Binding Mode, Photophysical Properties and Recommendations for Use of SYBR Gold. *Nucleic Acids Res.* **2021**, *49* (9), 5143−5158.
(28) Babichev, F. S.; Shchetsinskaya, E. Mono-, Tri-, and Pentamethinecyanines from 2,3-(Polymethylene)Benzothiazolium Salts. *J. Gen. Chem. USSR* **1964**, *34* (7), 2445.
(29) Tomilov, Y. V.; Platonov, D. N.; Frumkin, A. E.; Lipilin, D. L.; Salikov, R. F. Synthesis of Condensed Heterocycles via Cyclopropylimine Rearrangement of Cyclopropylazoles. *Tetrahedron Lett.* **2010**, *51* (39), 5120−5123.
(30) Kawakami, M.; Koya, K.; Ukai, T.; Tatsuta, N.; Ikegawa, A.; Ogawa, K.; Shishido, T.; Chen, L. B. Synthesis and Evaluation of Novel Rhodacyanine Dyes That Exhibit Antitumor Activity. *J. Med. Chem.* **1997**, *40* (20), 3151−3160.
(31) Katayama, N.; Ozaki, Y.; Yasui, S.; Iriyama, K. Spectroscopic Studies of Thiatri-, Penta-and Heptamethine Cyanine Dyes I. Structure of Thiatri-, Penta-and Heptamethine Cyanine Dyes in Solutions Studied by NMR. *J. Mol. Struct.* **1992**, *274*, 171−181.
(32) Yang, C.; Yang, S.; Song, L.; Yao, Y.; Lin, X.; Cai, K.; Yang, Q.; Tang, Y. A Resettable Supramolecular Platform for Constructing Scalable Encoders. *Chem. Commun.* **2019**, *55* (55), 8005−8008.

https://doi.org/10.1021/jacsau.6c00703
JACS Au XXXX, XXX, XXX−XXX

Supporting Information for

A Broadly Generalizable Dye for Colorimetric Aptamer-Based Sensors

Thinh Nguyen,[1] Adara Bacon,[1] Obtin Alkhamis,[1] Matthew Venzke,[1] Ransom Hill,[1] Gabriel Castro,[1] Caleb Byrd,[1] Konstantin V. Bukhryakov,[2] Jun Ohata,[1] Zoe Millbern,[3] Nelson R. Vinueza[1,3] and Yi Xiao[1*]

1. Department of Chemistry, North Carolina State University, 2620 Yarbrough Drive, Raleigh, NC, USA, 27607. 2. Department of Chemistry and Biochemistry, Florida International University, 11200 SW 8th Street, Miami, FL, 33199. 3. Department of Textile Engineering, Wilson College of Textiles, North Carolina State University, Raleigh, NC, 27695, USA.

*Corresponding author: yxiao34@ncsu.edu

Preparative synthesis of X-732-91B

Compound **1-Br** was prepared according to the published procedure (*Tet. Lett.*, **2010**, 51, 5120–5123). Compound **4** was purchased from TCI (CAS 3119-93-5).

General Scheme

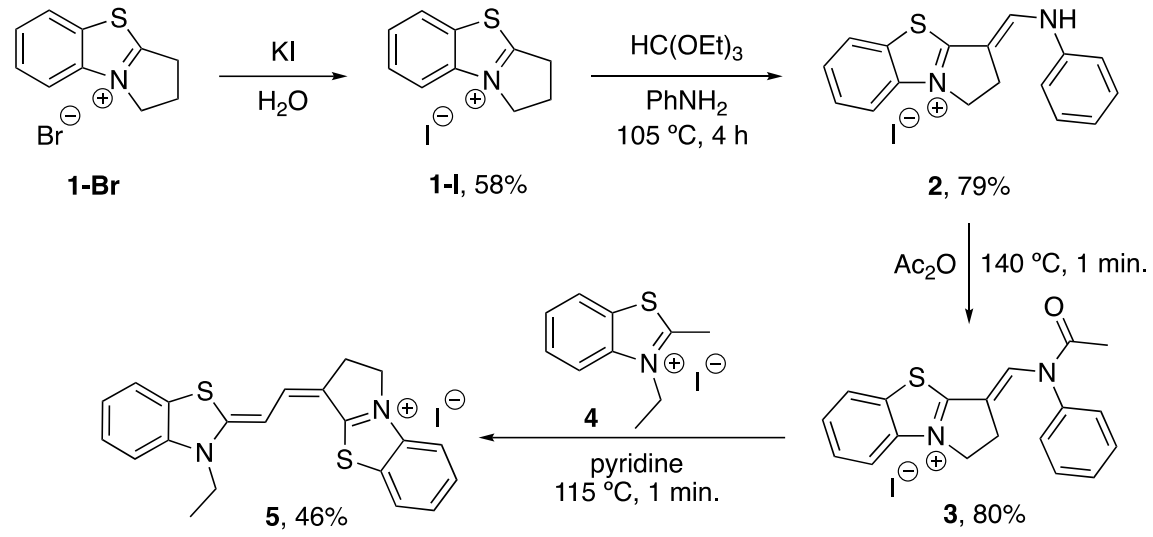

Anion Exchange

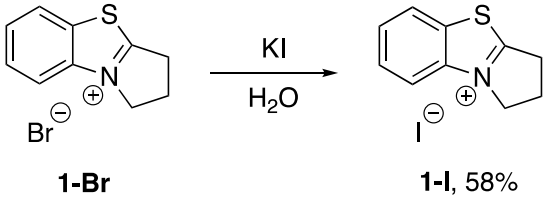

Compound **1-Br** (1.06 g, 4.14 mmol, 1 equiv.) and KI (3.43 g, 20.69 mmol, 5 equiv.) were dissolved in 10 mL of water, and the precipitate formed immediately. The reaction mixture was heated until all precipitate dissolved, and the solution was kept at + 5°C for 2 hours. The product was filtered off and recrystallized in the mixture of *i*-PrOH : water (4:1) to provide a white solid (730 mg, 58%).

^{1}H NMR (400 MHz; DMSO-d$_6$): δ 8.45 (d, *J* = 8.2 Hz, 1H), 8.14 (d, *J* = 8.2 Hz, 1H), 7.85 (t, *J* = 7.6 Hz, 1H), 7.77 (d, *J* = 7.8 Hz, 1H), 4.72 (t, *J* = 7.4 Hz, 2H), 3.72 (t, *J* = 7.5 Hz, 2H), 2.81 (quintet, *J* = 7.5 Hz, 2H). **^{13}C NMR (101 MHz; DMSO-d$_6$)**: δ 181.8, 136.5, 135.3, 129.3, 128.1, 125.7, 117.1, 52.0, 32.5, 25.1. Anal. **Calcd** for $C_{10}H_{10}INS$: C, 39.62%; H, 3.32%; N, 4.62%, **Found**: C, 39.78%; H, 3.26%; N, 4.68.

Synthesis of compound 2

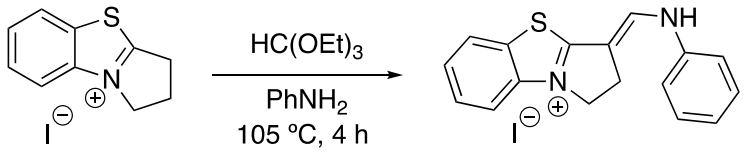

1-I **2**, 79%

Compound **1-I** (643 mg, 2.12 mmol, 1 equiv.) was suspended in aniline (1.00 mL, 1.02 g, 10.97 mmol, 5.17 equiv.). The reaction mixture was stirred at 105 °C under nitrogen until **1-I** dissolved. Triethyl orthoformate (0.35 mL, 314 mg, 2.12 mmol, 1 equiv.) was added, and the resulting mixture was stirred at 105 °C for 4 hours under nitrogen. After that time, the reaction was cooled down, and 20 mL of diethyl ether was added. The precipitate was filtered off and washed with diethyl ether. The product was recrystallized in the mixture of *i*-PrOH : water (10:1) to provide a yellow solid (680 mg, 79%).

^{1}H NMR (400 MHz; DMSO-d$_6$): δ 10.05 (s, 1H), 8.64 (s, 1H), 8.16 (dt, *J* = 8.1, 0.5 Hz, 1H), 7.68 (dd, *J* = 8.1, 0.5 Hz, 1H), 7.61 (ddd, *J* = 8.2, 7.2, 1.0 Hz, 1H), 7.49-7.44 (m, 3H), 7.35 (dd, *J* = 8.5, 7.4 Hz, 2H), 7.07 (t, *J* = 7.3 Hz, 1H), 4.59 (t, *J* = 8.1 Hz, 2H), 3.40 (d, *J* = 7.9 Hz, 2H). **^{13}C NMR (101 MHz; DMSO-d$_6$):** δ 171.8, 140.1, 139.8, 136.6, 131.1, 129.5, 128.5, 125.8, 124.8, 123.9, 116.9, 113.9, 103.6, 48.4, 29.0. Stereochemistry was confirmed by NOESY and HSQC:

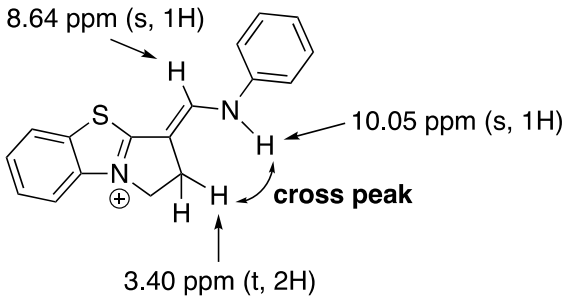

Synthesis of compound 3

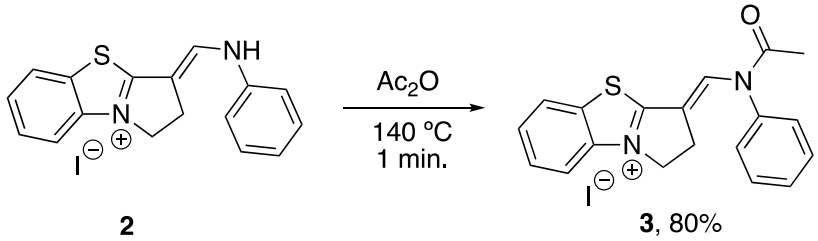

2 **3**, 80%

Compound **2** (570 mg, 1.40 mmol) was suspended in 15 mL of acetic anhydride under nitrogen and heated to reflux until all starting material was dissolved (about 1 minute). The reaction was cooled down. The resulting precipitate was filtered off, washed with ether, and dried to produce a green solid (500 mg, 80%).

^{1}H NMR (400 MHz; DMSO-d$_6$): δ 8.45 (t, *J* = 2.3 Hz, 1H), 8.35 (dt, *J* = 8.2, 0.6 Hz, 1H), 7.91-7.89 (m, 1H), 7.76 (ddd, *J* = 8.3, 7.2, 1.1 Hz, 1H), 7.68 (ddd, *J* = 8.3, 7.2, 1.1 Hz, 1H), 7.64-7.56 (m, 5H), 4.44 (t, *J* = 7.3 Hz, 2H), 2.30 (ddd, *J* = 8.3, 6.2, 2.1 Hz, 2H), 2.06 (s, 3H). **^{13}C NMR (101 MHz; DMSO-d$_6$):** δ 175.7, 170.6, 137.8, 136.6, 134.5, 132.0, 130.04, 129.87, 129.5, 129.2, 127.7, 125.3, 115.7, 112.0, 49.8, 27.9, 23.0.

Synthesis of compound 5

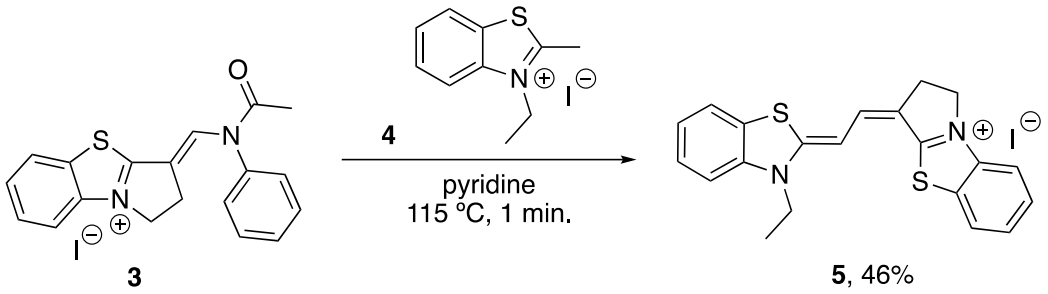

Compounds **3** (200 mg, 0.45 mmol, 1 equiv.) and **4** (136 mg, 0.45 mmol, 1 equiv.) were suspended in 4 mL of pyridine under nitrogen and heated to reflux until all starting materials were dissolved (about 1 minute). The reaction was cooled down. The resulting precipitate was filtered off and washed with ether. The product was recrystallized in the mixture of *i*-PrOH : water (5:2) to provide a purple solid (101 mg, 46%).

^{1}H NMR (400 MHz; DMSO-d$_6$): δ 8.09 (d, *J* = 8.0 Hz, 1H), 7.86 (dd, *J* = 7.8, 0.6 Hz, 1H), 7.75 (d, *J* = 12.7 Hz, 1H), 7.64-7.55 (m, 3H), 7.48-7.41 (m, 2H), 7.30-7.26 (m, 1H), 5.91 (d, *J* = 12.7 Hz, 1H), 4.55 (t, *J* = 8.0 Hz, 2H), 4.31 (q, *J* = 7.1 Hz, 2H), 3.44 (t, *J* = 8.0 Hz, 2H), 1.28 (t, *J* = 7.1 Hz, 3H). **^{13}C NMR (101 MHz; DMSO-d$_6$):** δ 168.1, 161.1, 141.2, 137.6, 137.3, 131.1, 128.7, 127.9, 125.5, 124.89, 124.75, 124.3, 122.9, 113.69, 113.55, 112.5, 93.4, 47.9, 40.8, 30.3, 12.3.

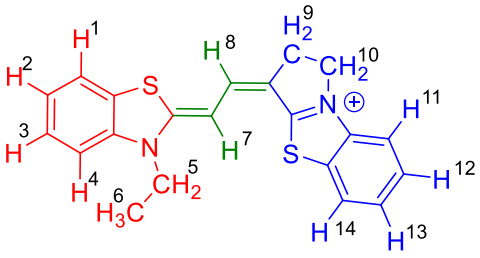

^{1}H NMR (700 MHz; 95:5 DMSO-*d*$_6$/HFIP-*d*$_2$): δ 8.09 (d, *J* = 8.0 Hz, 1H, H14), 7.86 (d, *J* = 7.9 Hz, 1H, H1), 7.78 (m, 1H, H8), 7.64 (d, *J* = 8.0 Hz, 1H, H11), 7.60 (dd, *J* = 7.6, 7.6 Hz, 1H, H12), 7.57 (d, *J* = 8.2 Hz, 1H, H4), 7.47 (dd, *J* = 7.9, 7.9 Hz, 1H, H2), 7.44 (dd, *J* = 7.1, 7.1 Hz, 1H, H13), 7.29 (dd, *J* = 7.6, 7.6 Hz, 1H, H3), 5.92 (d, *J* = 12.7 Hz, 1H, H7), 4.57 (t, *J* = 7.4 Hz, 2H, H10), 4.33 (q, *J* = 7.1 Hz, 2H, H5), 3.44 (t, *J* = 7.4 Hz, 2H, H9), 1.30 (t, *J* = 7.1 Hz, 3H, H6). **^{13}C NMR (175 MHz; 95:5 DMSO-*d*$_6$/HFIP-*d*$_2$):** δ 168.0, 161.1, 141.1, 137.5, 137.2, 131.1, 128.5, 127.7, 125.4, 124.6, 124.2, 122.7, 113.5, 113.4, 112.3, 93.3, 47.8, 40.6, 30.2, 12.1.

Mass spectrometry analysis for X-732-91B. The high-resolution accurate mass spectrometry analysis was performed using a Thermo Scientific Ultimate 3000 system coupled with an Exactive Plus Orbitrap mass spectrometer. The standard dye solution was prepared in methanol at 500 µM, and then this solution was diluted 100-fold, and 2 µL of this diluted solution was injected into the instrument with a flow rate of 0.2 mL/min. The liquid chromatography separation was conducted on a Hypersil Gold C18 column (50 x 2.1 mm, 1.9 µm) using a gradient elution program. Mobile phase A consisted of water with 0.1% formic acid,

and mobile phase B was methanol. The gradient was as follows: 0 min to 0.5 min: 20% B; 0.5 min to 3 min: 90% B; 3 min to 8 min: 90% B; 8.1 min to 10 min: 20% B. The scan range was set to *m/z* 250 – 600 with a resolution of $140{,}000_{FWHM}$ at *m/z* 200. The analysis was conducted in positive ion mode using an automatic gain control target of 1e6. The sheath gas flow rate was 30, the aux gas flow rate was 10, and the sweep gas flow rate was 2. The capillary temperature was maintained at 320°C, while the S-lens RF level was set at 55. Additionally, the aux gas heater temperature was set at 150°C.

Table S1. DNA sequences used in this study.

Sequence ID	Abbreviated name	Sequence (5'-3')
FA-S1-R620	S1	CTTACGACCTAGCAAGGGGGTTTCGGTGGGCAGGTGTGGTCGTAAG
FA-S3-R0	S3	CTTACGACTCGAGGTGTCCTGCTAGGTGGTTCGGTTGAGTCGTAAG
FA-S4-R0	S4	CTTACGACAGGGTGGCAAAGGGTCGGGTGTGGGAAAGCTGTCGTAAG
S5-R0-mut	S5m	CTTACGACGGGAGGTGTTTGCACTAAGTCCGGTTTCCCGTCGTAAG
FA-S9-R0	S9	CTTACGACTGGCGCACAGGTTCGGGTTTCCTACAGAAGTCGTAAG
S44-R6-mut	S44m	CTTACGACGCTGGGTGTGGCCGGGGCAGGCGGGGGAGCGTCGTAAG
A1-S215	A1	CTTACGACCGGCGGTAGTTCTGATGGAAGAGGGGGAAGGTCGTAAG
A3-S286	A3	CTTACGACGGCGGTAGGTCTGAGTATATCGAGGGGGAAGTCGTAAG
A4-S0	A4	CTTACGACGGCGGTAGTTCTGAGGAAAACGAGGGGGAAGTCGTAAG
HM1	H1	GGGACGACGGGATTCGGATCGTGGAACAGTGCCTCGTCGTCGTCCC
HM4	H4	GGGACGACTAGCCCGGCGTTGTTCGAGTGCAGCGAGTAGTCGTCCC
HM5	H5	GGGACGACTAGCCGTGGCGTTGTCCGAACCAGTGAGTAGTCGTCCC
HM9	H9	GGGACGACGGGAAGGTTGGCAGCGCATCGTCGGGTCACGTCGTCCC
HM16	H16	GGGACGACCGTTGGCGAGTGTGTCCGGGGACTACAGGGGTCGTCCC
HM20	H20	GGGACGACATGCGTCGAAAAGACCCCTGAGGGCAGCTGGTCGTCCC
HM24	H24	GGGACGACAAGTACCAAGGGTAGCTCTGCGTTGTTCGAGGTCGTCCC
HM25	H25	GGGACGACGGGGCTGTGGGAGGGGGTTCATGGGTCCCGGTCGTCCC
HM29	H29	GGGACGACTAGCGCATGCGTTGTTCGAGGATACGAGTAGTCGTCCC
HM31	H31	GGGACGACGCGTACCATGGGTAGTTGCACGTCGTCCAAGTCGTCCC
HM31.2	H31.2	GGGACGACTAGCTGGTGCGTTGTCCGAAGTCATGAGTAGTCGTCCC
HM41	H41	GGGACGACTAGCCCTAGCGTTGTTCGAGTCCATGAGTAGTCGTCCC
HM116	H116	GGGACGACTAGCCGTGGCGTTGTTCGAGTGCAGCGAGTAGTCGTCCC
OM1	O1	GGGACGACAAGTCAGGCCTGTCTCAGCGAGTTCGACATGTCGTCCC
OM3	O3	GGGACGACTGGCGCCGGATTCCCTAAGGTACACGGACTGTCGTCCC
OM5	O5	GGGACGACCCGTAGGGGTACACGCTCTATAGGGGCTGGGTCGTCCC
OM6	O6	GGGACGACCCGTAGGGGTACACGCTCTATGGGGGCTGGGTCGTCCC
OM7	O7	GGGACGACATCGTAGGGGCACACGCTTAACGGGCTGATGTCGTCCC
OM9	O9	GGGACGACTACGTAGCCCTGTCTCAGCGAGTTCGCGGAGTCGTCCC
OM11	O11	GGGACGACGGCTTGCATTGAGCAGAAGGGGTACACGCTGTCGTCCC
OM19	O19	GGGACGACCGCGTAGGGGAACACGCTTGCAGGGCTGAGGTCGTCCC
OM29	O29	GGGACGACTGAGTAGGCCTGTCTCAGCGAGTTCACTATGTCGTCCC
F4	F4	CTTACGACACTGGCAGGAGGGTCGGGTGTGGGAACGTGGTCGTAAG
F5	F5	CTTACGACCAGGCCTACGGAAGCAGCGTCAGCGGGGGGGTCGTAAG
F6	F6	CTTACGACTAGTGGAGTAGGGTCGGGTAGTGGGCCTCAGTCGTAAG
F12	F12	CTTACGACATCTGCGTGTGGCCGGTGTGAGGGAGGGATGTCGTAAG
F13	F13	CTTACGACCATGGGTGTTTGCACTAAGTCCGGTTCTTGGTCGTAAG
F14	F14	CTTACGACCGGTGTGCTCGGGGAAGGGGGCCCTAGGTGGTCGTAAG
F17	F17	CTTACGACCGGTGGGGAGGCCGGAGTTGGGAACGGGGGGTCGTAAG
F18	F18	CTTACGACCGGGATCCTTTGGGACAACCTGGTGGGCATGTCGTAAG
F23	F23	CTTACGACCAGGCTACGTGGGGGAGGGTGGGAAGACGGGTCGTAAG
F24	F24	CTTACGACACAGGGTGTGTTGTGCTCAGTGGTGTATGTGTCGTAAG
F25	F25	CTTACGACAGGGGTACCCGCGTATAACGTGGCGTTCGTGTCGTAAG
F27	F27	CTTACGACGAGCGCGTGTGGCCGGCGTGAGGGAGGTGAGTCGTAAG
THC1.2	T1.2	CTTACGACCCAGGGGGGTGGACAGGCGGGGGTTAGGGGGGTCGTAAG
XA1	XA1	CTTACGACTGTGGTCGGGTGGTGGGCCTCTAGAGGGGTGTCGTAAG
XA2	XA2	CTTACGACTGCGGGCATTTGTGGGGGGCGTCGGTGGGCGTCGTAAG
XA2-GT	X2GT	CTTACGATTGCGGGCATTTGTGGGGGGCGTCGGTGGGCGTCGTAAG
E2	E2	GGGACGACAAAATGGCAGCATTGGTGACGGAGTTGCTTGTCGTCCC
E5	E5	GGGACGACGTAATGGGAGCATTGGTCACGCAGGTGCACGTCGTCCC
E7	E7	GGGACGACAGAATGGCAGCATTGGTGAGTTATTTGCCTGTCGTCCC
L1	L1	GGGACGACAAAAATGGAAGCATTGGTTGTTGGTGCTTTGTCGTCCC
L7	L7	GGGACGACAAAAATGGAAGCATTGGTTGTCGGTGCTTTGTCGTCCC
P2	P2	GGGACGACTAATGGGAGCATTGGTCCACGCAGTGTGCAGTCGTCCC
FX1	FX1	GGGACGACGGCCCCTTTTAAGGAGGTAGAGGTGTTCGCTGTCGTCCC
FX3	FX3	GGGACGACGGCCCCTTTTAGGAGGTAGAGGTGTTCGCTGTCGTCCC
FX4	FX4	GGGACGACGGTACCCGGCGACCTTTAGATGGAGGTGATGTCGTCCC

Sequence ID	Abbreviated name	Sequence (5'-3')
FX5	FX5	GGGACGACGGTACCCGGCGATCTTTAGTTGGAGGTAGGGTCGTCCC
FX35	FX35	GGGACGACGGCCCCTTTAAGGAGGTAGAGGTGTTCGCTGTCGTCCC
FX40	FX40	GGGACGACGGCCCCCGGAGAGGAGGTAGAGGTGTTCGCTGTCGTCCC
FX46	FX46	GGGACGACGGCCCCTTTCAAGGAGGTAGAGGTGTTCGCTGTCGTCCC
ATP Apt	ATP	CGCACCTGGGGGAGTATTGCGGAGGAAGGTGCG
G10T-A23G	ADE	CGCACCTGGTGGAGTATTGCGGGGGAAGGTGCG
Serotonin Apt	SA	CGACTGGTAGGCAGATAGGGGAAGCTGATTCGATGCGTGGGTCG
Dopamine Apt	DA	CGACGCCAGTTTGAAGGTTCGTTCGCAGGTGTGGAGTGACGTCG
Glucose Apt	GA	ACGACCGTGTGTGTTGCTCTGTAACAGTGTCCATTGTCGT
MMC1	MMC1	CTTACGACCAGGGTTGGTTTCATCGGTGGTGTAATATGGTCGTAAG
SCA2.1	SC2.1	CTTACGACCTTAAGTGGGGTTCGGGTGGAGTTTATGGGGTCGTAAG
NC195	N195	CTTACGACAGGTTCTGAGGAATCAACGTCGGTGTAGTTGTCGTAAG
NC423	N423	CTTACGACTTGTTCTGAGGGTCAACGGTGGTGTAGTTAGTCGTAAG
NC973	N973	CTTACGACGGGTTCAGAGGGTCAACGGTGGTGTTGTCGTCGTAAG
NC1	N1	CTTACGACCTGTTCTGAGGGTCAACCTTTGGTGTAGTGGTCGTAAG
NC6	N6	CTTACGACAAAGGCTCGGGCTCCCATGATGGATTCGTTGTCGTAAG
NC8	N8	CTTACGACGCGGACGTTGTGGGGCGTGGCAGTCGGTGGGTCGTAAG
NC11	N11	CTTACGACCTGCTCTGAGGGTCAACGGTGGTGTAGTCGGTCGTAAG
NC16	N16	CTTACGACTAGGTGTGGGTCGGCTGCTTTCGCAGGGTAGTCGTAAG
NC17	N17	CTTACGACTTTGGTTTCCTCGATTCGCATGGGTGGTAAGTCGTAAG
NC33	N33	CTTACGACATGGGATGTAAGTTAGTGGGTCGGATCCGGGTCGTAAG
NC35	N35	CTTACGACTAGGTGTGGGTCGGCTCCGGATGGAGGGTAGTCGTAAG
NC43	N43	CTTACGACTAGGTGTGGGTCGGCTCAATTCGGAGGGTAGTCGTAAG
NC48	N48	CTTACGACGCGGACGTTGTGGGGCGTGGCAGTCGGTGAGTCGTAAG
NC179	N179	CTTACGACTAGTTCTGAGGAATCAACGTCGGTGTAGTTGTCGTAAG
NC235	N235	CTTACGACGGTGGGGGGTTGGTAGGGGAGGAGCGCATCGTCGTAAG
METH2	M2	GGGACGACGGGACGGTAAGTGGTAGGTCGTTGGAATTTCTACTGTATCGTCGTCCC
METH3	M3	GGGACGACCGTCCGAGTTTTAGGAGTGGTTGCATTGCGCTGGGAAGAGGTCGTCCC
METH7	M7	GGGACGACGGCACGAGGTTATTCGTTGGTTGCACTGCGCTGGGAGGTAGTCGTCCC
METH8	M8	GGGACGACGGGGCTCTTACCCTGGAGGGTAGAAGGGGAGGTGTGGTCAGTCGTCCC
METH9	M9	GGGACGACGGCACGTGGTTATTCGTTGGTTGCACTGCGCTGGGAGGCAGTCGTCCC
METH11	M11	GGGACGACCGGCTGTCTGGATGCATTGCGCCGGGAACTCGGACGGATGGTCGTCCC
METH13	M13	GGGACGACGGCACGAGGTTATTCGTTGGTTGCACTGCGCTGGGAGGAAGTCGTCCC
METH18	M18	GGGACGACGGCACGAGGTTATTCGTTGGTTGCACTGCGCTGGGAGGCAGTCGTCCC
METH_LI_1	ML1	TTCAAATCTGAGCAGCCTAGTTACTGACGGGTTTATAGTACTCGCATTGAGTCTAGATTTGAA
METH_LI_3	ML3	TTCAAATCTTATGTACGTTCTATCGCATGGATGGGATTTTGGGTTACCTAGTCTAGATTTGAA
METH_LI_4	ML4	TTCAAATCTTGGTACGTTCTGCCTTTTCTTATTTTGCTTTGGGTTACCTAGTCTAGATTTGAA
METH_LI_5	ML5	TTCAAATCTATGGTGCAGTGCGCAGGGACGGAGGTAAAACATGAGTTTTAGTCTAGATTTGAA
METH_LI_6	ML6	TTCAAATCTGAGCAGCCTAGTTACTGACGGGTTTATAGTACTCGCATCGAGTCTAGATTTGAA
METH_LI_7	ML7	TTCAAATCTGGTGCCCTTTCGCAGTCGGTTGGTAATGAGATCACTTTAGAGTCTAGATTTGAA
METH_LI_8	ML8	TTCAAATCTCCACGCTGGACTGGATGCAATGCGCCGGGATATCGTCTAAAGTCTAGATTTGAA
METH_LI_10	ML10	TTCAAATCTGAGCAGCCTAGTTACTGACGGGTTTATAGTACTCACATTGAGTCTAGATTTGAA
METH_LI_11	ML11	TTCAAATCTGAGCAGCCTAGTTACTGACGGGTTTATAGTACTCGTATTGAGTCTAGATTTGAA
METH_LI_12	ML12	TTCAAATCTGCGGCGACTAATTCTTAGTGGTGGTTGCAATGCGCTGGGATGAGTCTAGATTTGAA
METH_LI_13	ML13	TTCAAATCTGAGCAGCCTAGTTACTGACGGGTTTATAGTACTCGCACTGAGTCTAGATTTGAA
EF1	EF1	TTCAAATCTAGCGCAGGTAGGGGTGTAGGTGTGGGGGTAAGTCTAGATTTGAA
EF5	EF5	TTCAAATCTCGCGCAGGTAGGGGTGTAGGTGTGGGGGTAAGTCTAGATTTGAA
FUB1	FUB1	GGGACGACGGAAGGGTGTGCTGCGGTTTGGCTTCTGGCGTCGTCCC
FUB4	FUB4	GGGACGACGGGGGGCTTTAGGGTGTAGGAGTGGGGTGAGTCGTCCC

Table S2. Aptamer ID, determined or reported K_D in each respective buffer and target used in this study.

Sequence ID	Abbreviated name	K_D	Target	Experimental buffer	Reference
FA-S1-R620	S1	1.2 μM[a]	(±)-cis-3-methyl-Fentanyl	10 mM Tris (pH 7.4), 20 mM NaCl, 0.5 mM $MgCl_2$, 0.01% SDS (w/v)	This Work
FA-S3-R0	S3	340 nM[a]			
FA-S4-R0	S4	160 nM[a]			
S5-R0-mut	S5m	73 nM[a]			
FA-S9-R0	S9	1.1 μM[a]			
S44-R6-mut	S44M	2.3 μM[a]	Remifentanil		
A1-S215	A1	2.9 μM[a]	Alfentanil		
A3-S286	A3	4.9 μM[a]			
A4-S0	A4	4.7 μM[a]			
HM1	H1	850 nM	Heroin	10 mM Tris (pH 7.4), 20 mM NaCl, 0.5 mM $MgCl_2$, 0.01% SDS (w/v)	*JACS Au* **2024**, *4*, 1059-1072
HM4	H4	2.4 μM			
HM5	H5	2.6 μM			
HM9	H9	2.4 μM			
HM16	H16	1.6 μM			
HM20	H20	1.1 μM			
HM24	H24	2.2 μM			
HM25	H25	6.5 μM			
HM29	H29	2.7 μM			
HM31	H31	5.6 μM			
HM31.2	H31.2	3.3 μM			
HM41	H41	3.3 μM			
HM116	H116	2.1 μM			
OM1	O1	450 nM	Oxycodone	10 mM Tris (pH 7.4), 20 mM NaCl, 0.5 mM $MgCl_2$, 0.01% SDS (w/v)	
OM3	O3	3.1 μM			
OM5	O5	410 nM			
OM6	O6	500 nM			
OM7	O7	1.4 μM			
OM9	O9	1.2 μM			
OM11	O11	790 nM			
OM19	O19	2.4 μM			
OM29	O29	510 nM			
F4	F4	920 nM	Fentanyl	10 mM Tris (pH 7.4), 20 mM NaCl, 0.5 mM $MgCl_2$, 0.01% SDS (w/v)	*Nucleic Acids Res.* **2022**, *51*, e19
F5	F5	320 nM			
F6	F6	42 nM			
F12	F12	60 nM[b]			
F13	F13	250 nM[b]			
F14	F14	68 nM[b]			
F17	F17	98 nM[b]			
F18	F18	29 nM[b]			
F23	F23	51 nM[c]			
F24	F24	63 nM[c]			
F25	F25	170 nM[c]			
F27	F27	21 nM[b]			
THC1.2	T1.2	61 nM	THC	10 mM Tris (pH 7.4), 20 mM NaCl, 0.5 mM $MgCl_2$, 2% DMSO, 0.01% SDS (w/v)	*Anal. Chem.* **2021**, *93*, 3172-3180
XA1	XA1	130 nM	UR-144	10 mM Tris (pH 7.4), 20 mM NaCl, 0.5 mM $MgCl_2$, 2% DMSO, 0.01% SDS (w/v)	
XA2	XA2	170 nM			
XA2-GT	X2GT	Not tested			
E2	E2	140 nM	Fentanyl	1× PBS (pH 7.4), 1 mM $MgCl_2$, 0.01% SDS (w/v)	*Anal. Chem.* **2023**, *95*, 18258-18267
E5	E5	340 nM[a]			
E7	E7	320 nM[a]			
L1	L1	430 nM			
L7	L7	1.1 μM[a]			
P2	P2	270 nM			

Sequence ID	Abbreviated name	K_D	Target	Experimental buffer	Reference
FX1	FX1	280 nM	Flunixin	1× PBS (pH 7.4), 1 mM $MgCl_2$, 0.01% SDS (w/v)	*J. Am. Chem. Soc.* **2022**, *145*, 194-206
FX3	FX3	340 nM			
FX4	FX4	570 nM			
FX5	FX5	420 nM			
FX35	FX35	510 nM			
FX40	FX40	250 nM			
FX46	FX46	340 nM			
ATP Apt	ATP	10 μM[a]	ATP	10 mM Tris (pH 7.4), 20 mM NaCl, 1.5 mM $MgCl_2$, 0.01% SDS (w/v)	*Biochemistry* **1995**, *34*, 656-665
G10T-A23G	ADE	15 μM[a]	Adenosine	10mM Tris (pH 7.4), 20 mM NaCl, 1.5 mM $MgCl_2$, 0.01% SDS (w/v)	*J. Am. Chem. Soc.* **2021**, *143*, 805-816
Serotonin Apt	SA	22 nM[a]	Serotonin	10 mM Tris (pH 7.4), 140 mM NaCl, 4mM KCl, 2 mM $MgCl_2$, 0.01% SDS (w/v)	*Science* **2018**, *362*, 319-324
Dopamine Apt	DA	890 nM[a]	Dopamine	10mM Tris (pH 7.4), 20 mM NaCl, 4mM KCl, 2 mM $MgCl_2$, 0.01% SDS (w/v)	
Glucose Apt	GA	10 mM	Glucose		
MMC1	MMC1	15 μM	Mephedrone	10 mM Tris (pH 7.4), 20 mM NaCl, 0.5 mM $MgCl_2$, 0.01% SDS (w/v)	*Nucleic Acids Res.* **2020**, *48*, e120
SCA2.1	SC2.1	47 nM	MDPV	10 mM Tris (pH 7.4), 20 mM NaCl, 0.5 mM $MgCl_2$, 0.01% SDS (w/v)	*Nucleic Acids Res.* **2019**, *47*, e71
NC195	N195	22 nM	Cocaine	20 mM Tris (pH 7.4), 140 mM NaCl, 4 mM KCl, 2 mM $MgCl_2$, 0.01% SDS (w/v)	*J. Am. Chem. Soc.* **2024**, *146*, 3230-3240
NC423	N423	22 nM			
NC973	N973	49 nM			
NC1	N1	220 nM			*Science Advances* **2024**, *10*, eadl3426
NC6	N6	280 nM			
NC8	N8	370 nM			
NC11	N11	190 nM			
NC16	N16	350 nM			
NC17	N17	240 nM			
NC33	N33	330 nM			
NC35	N35	510 nM			
NC43	N43	460 nM			
NC48	N48	53 nM			
NC179	N179	33 nM			
NC235	N235	1.1 μM			
METH2	M2	3.6 μM	(+) - Methamphetamine	1× PBS (pH 7.4), 1 mM $MgCl_2$, 0.01% SDS (w/v)	*ACS Central Science* **2024**, *10*, 2213-2238
METH3	M3	4.9 μM			
METH7	M7	6.0 μM			
METH8	M8	8.5 μM			
METH9	M9	6.1 μM			
METH11	M11	8.9 μM			
METH13	M13	3.3 μM			
METH18	M18	7.0 μM			
METH_LI_1	ML1	3.3 μM		0.5× PBS (pH 7.4), 2 mM $MgCl_2$, 0.01% SDS (w/v)	
METH_LI_3	ML3	1.5 μM			
METH_LI_4	ML4	2.5 μM			
METH_LI_5	ML5	1.6 μM			
METH_LI_6	ML6	2.1 μM			
METH_LI_7	ML7	1.3 μM			
METH_LI_8	ML8	8.0 μM			
METH_LI_10	ML10	1.9 μM			
METH_LI_11	ML11	2.5 μM			
METH_LI_12	ML12	5.7 μM			
METH_LI_13	ML13	7.0 μM			
EF1	EF1	24 nM	AB-FUBINACA	0.5× PBS (pH7.4), 2 mM $MgCl_2$, 3% DMSO, 0.01% SDS (w/v)	*J. Am. Chem. Soc.* **2024**, *146*, 21296-21307
EF5	EF5	40 nM			
FUB1	FUB1	230 nM		10 mM Tris (pH 7.4), 137 mM NaCl, 2.7 mM KCl, 1 mM $MgCl_2$, 2% DMSO, 0.01% SDS (w/v)	*Anal. Chem.* **2024**, *96*, 11488-11497
FUB4	FUB4	140 nM			

[a]Affinity reported in this work, [b]K_D for acetyl fentanyl, [c]K_D for furanyl fentanyl.

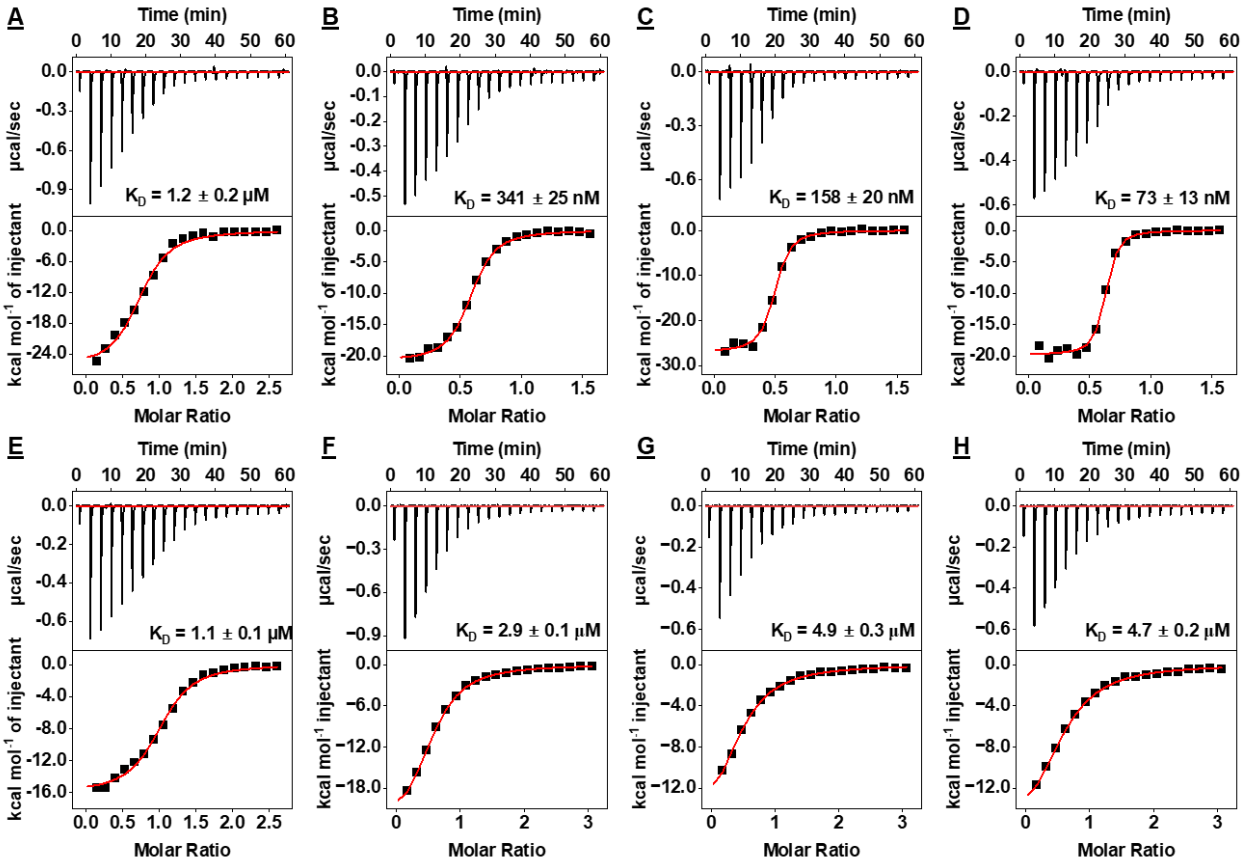

Figure S1. ITC measurement of target binding affinity of new aptamers identified for this work. Top panels display the heat generated from each titration of (±)-cis-3-methylfentanyl into (**A**) S1, (**B**) S3, (**C**) S4, (**D**) S5m, (**E**) S9, or from each titration of alfentanil into (**F**) A1, (**G**) A3, and (**H**) A4. Bottom panels show the integrated heat of each titration after correcting for the heat of dilution of the titrant.

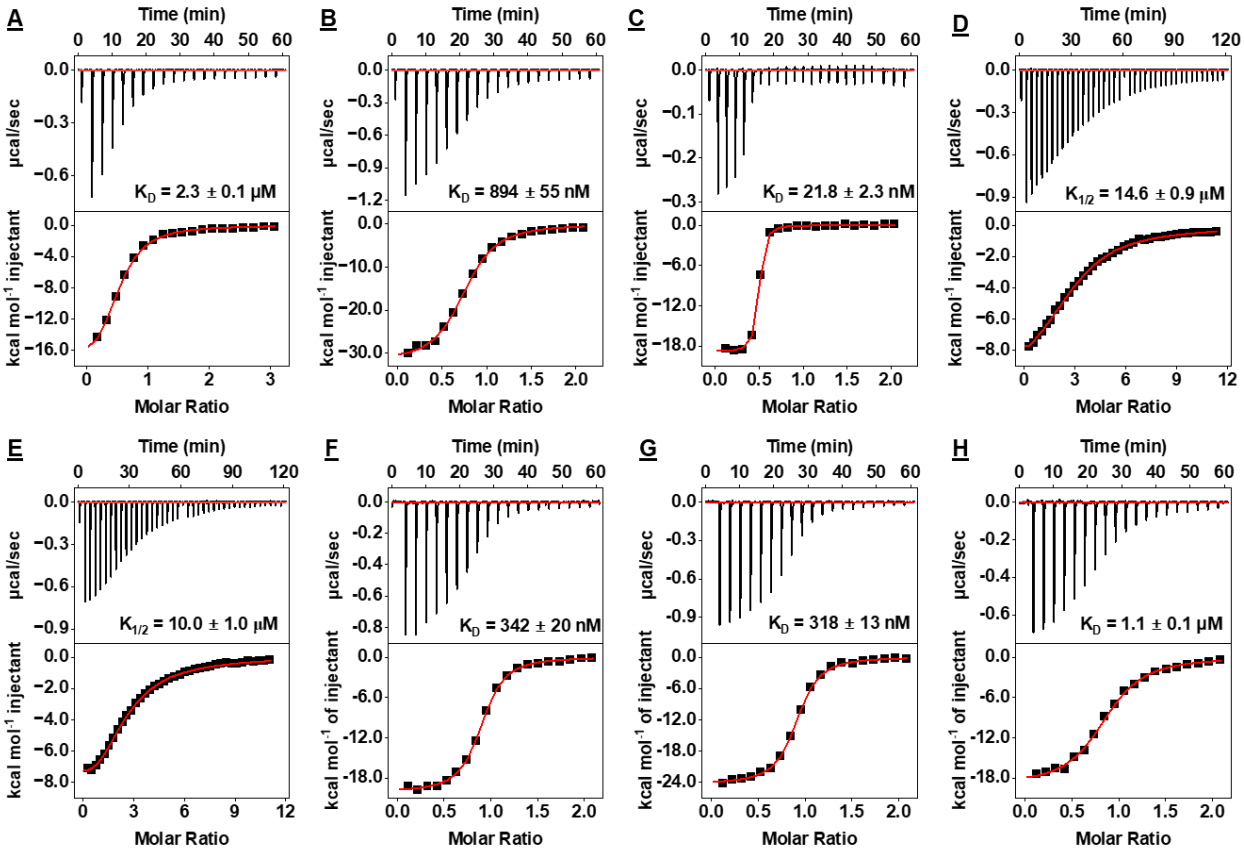

Figure S2. ITC measurement of target binding affinity of new aptamers identified for this work or previously published aptamers in the experimental buffer conditions employed in this work. Top panels display the heat generated from titration of (**A**) remifentanil into S44m, (**B**) dopamine into DA, (**C**) serotonin into SA, (**D**) adenosine into G10T-A23G, (**E**) ATP into ATP Apt, and each titration of fentanyl into (**F**) E5, (**G**) E7, and (**H**) L7. Bottom panels show the integrated heat of each titration after correcting for the heat of dilution of the titrant.

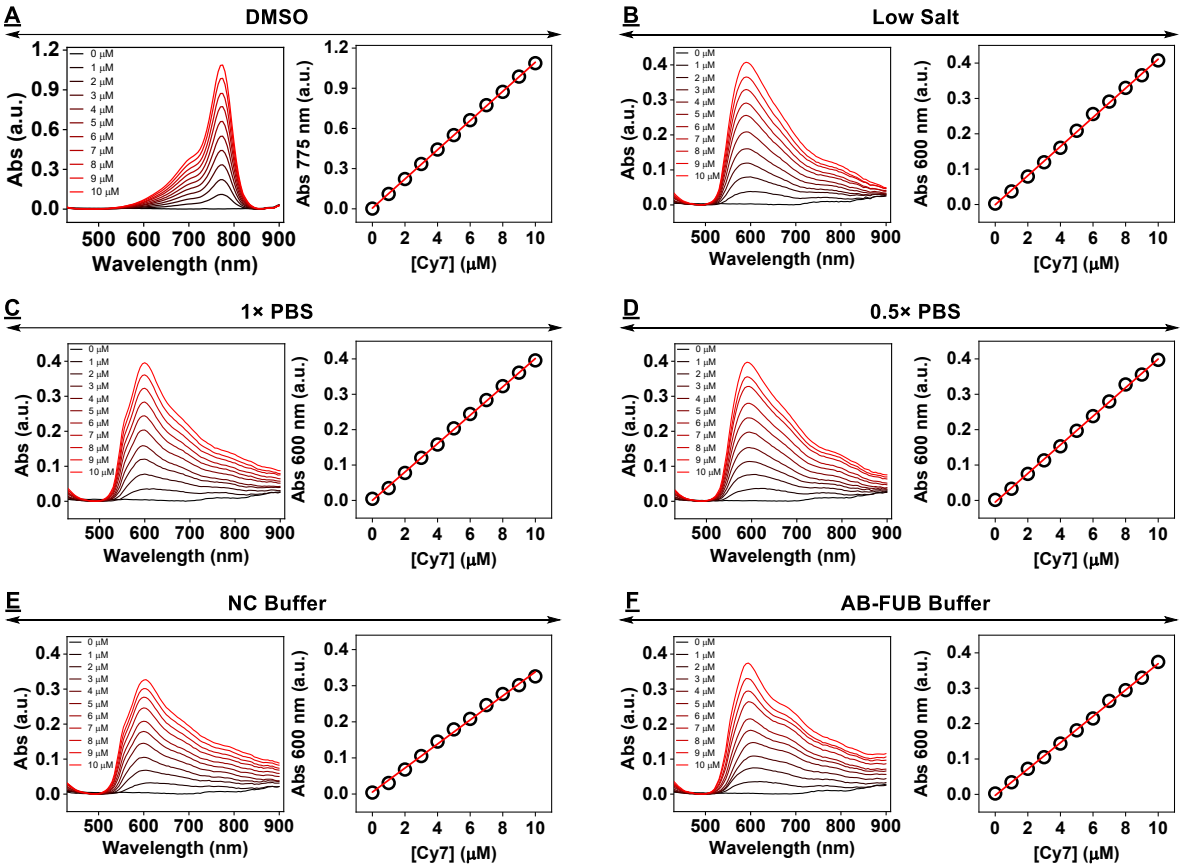

Figure S3. Optical properties of Cy7 under different experimental conditions. Absorbance spectra and calibration curve of Cy7 in (**A**) 100% DMSO, (**B**) low salt buffer (10 mM Tris (pH 7.4), 20 mM NaCl, 0.5 mM $MgCl_2$), (**C**) 1× PBS (1× PBS (pH 7.4), 1 mM $MgCl_2$), (**D**) 0.5× PBS (0.5× PBS (pH 7.4), 2 mM $MgCl_2$), (**E**) NC buffer (20 mM Tris (pH 7.4), 140 mM NaCl, 4 mM KCl, 2 mM $MgCl_2$) and (**F**) AB-FUB buffer (10 mM Tris (pH 7.4), 137 mM NaCl, 2.7 mM KCl, 1 mM $MgCl_2$). All buffer formulations included 1% (v/v) DMSO for (**A-E**) or 3% (v/v) DMSO for (**F**) and 0.01% (v/v) SDS.

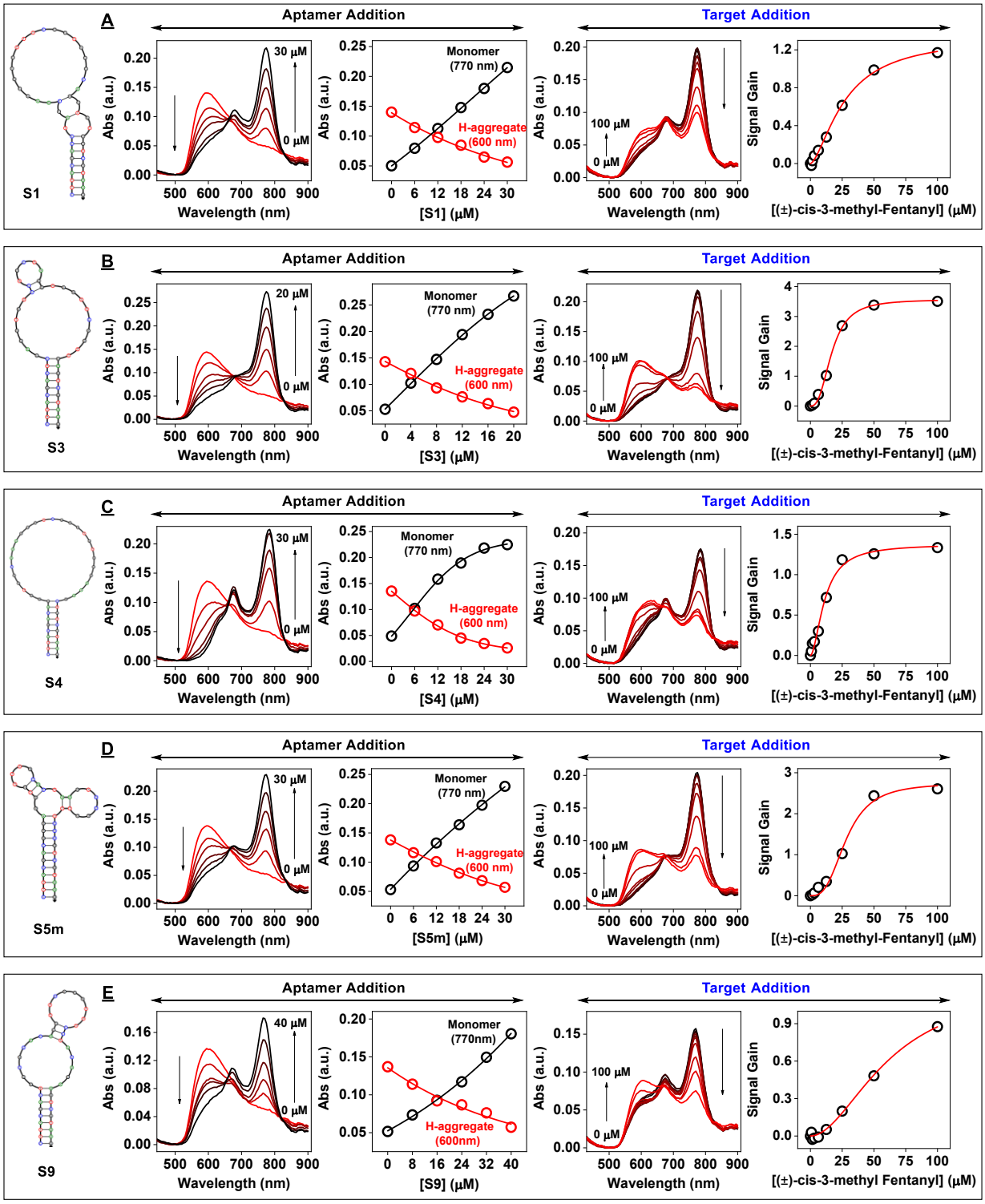

Figure S4. Target detection based on aptamer-based Cy7 displacement assay. For each panel, from left to right are: Secondary structure of the aptamer predicted by NUPACK; 'aptamer addition', which presents the absorbance spectra of 4 µM Cy7 with various concentrations of aptamer and a plot of Cy7 H-aggregate and monomer peak absorbance (respectively at 600 nm and 770 nm) plotted against aptamer concentration; and 'target addition', which presents the absorption spectra of solutions containing aptamer-Cy7 complex challenged with various concentrations of target as well as plot depicting the calibration curve for target detection. (**A**) S1, (**B**) S3, (**C**) S4, (**D**) S5m and (**E**) S9.

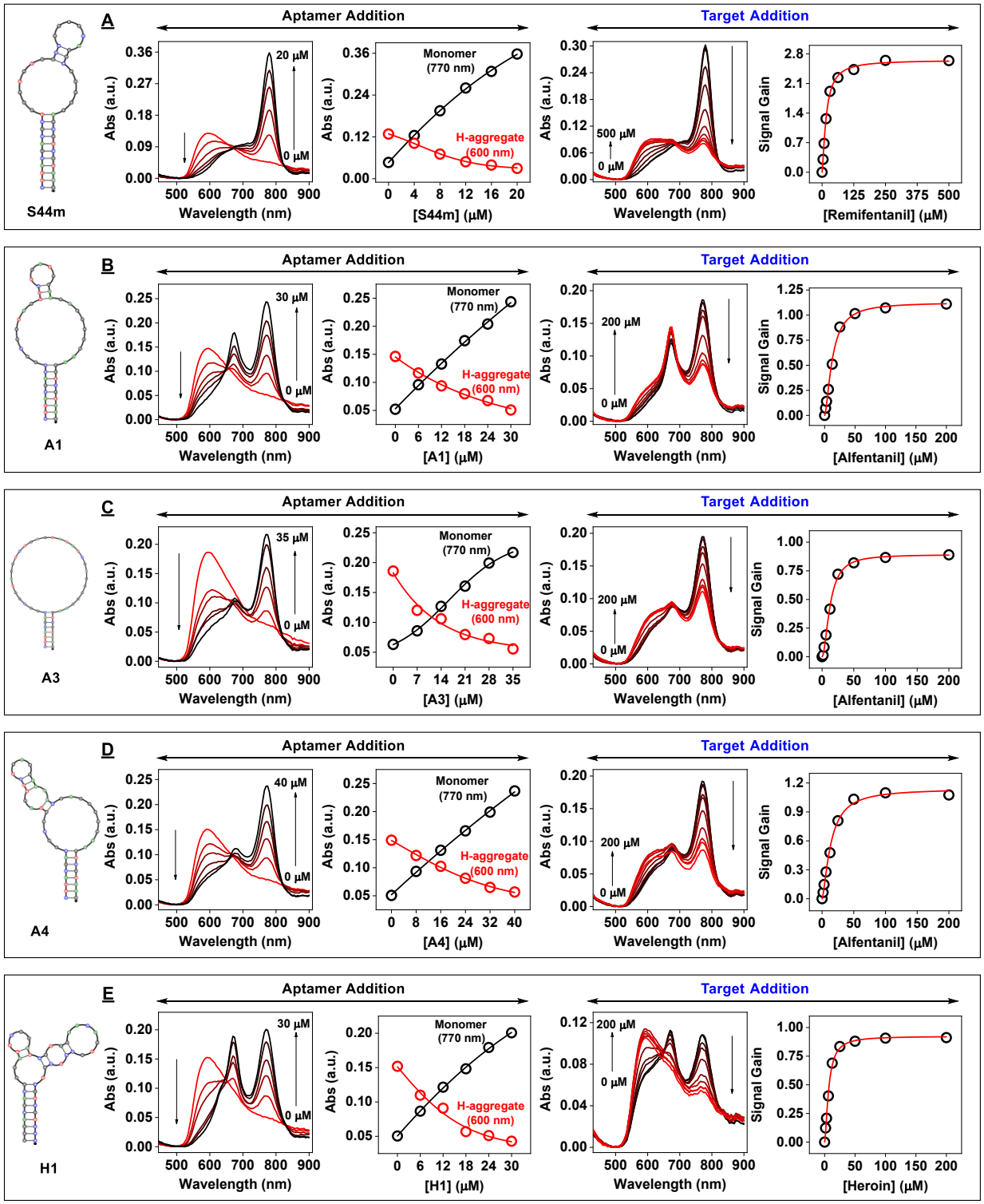

Figure S5. Target detection based on aptamer-based Cy7 displacement assay. For each panel, from left to right are: Secondary structure of the aptamer predicted by NUPACK; 'aptamer addition', which presents the absorbance spectra of 4 μM Cy7 with various concentrations of aptamer and a plot of Cy7 H-aggregate and monomer peak absorbance (respectively at 600 nm and 770 nm) plotted against aptamer concentration; and 'target addition', which presents the absorption spectra of solutions containing aptamer-Cy7 complex challenged with various concentrations of target as well as plot depicting the calibration curve for target detection. (**A**) S44m, (**B**) A1, (**C**) A3, (**D**) A4 and (**E**) H1.

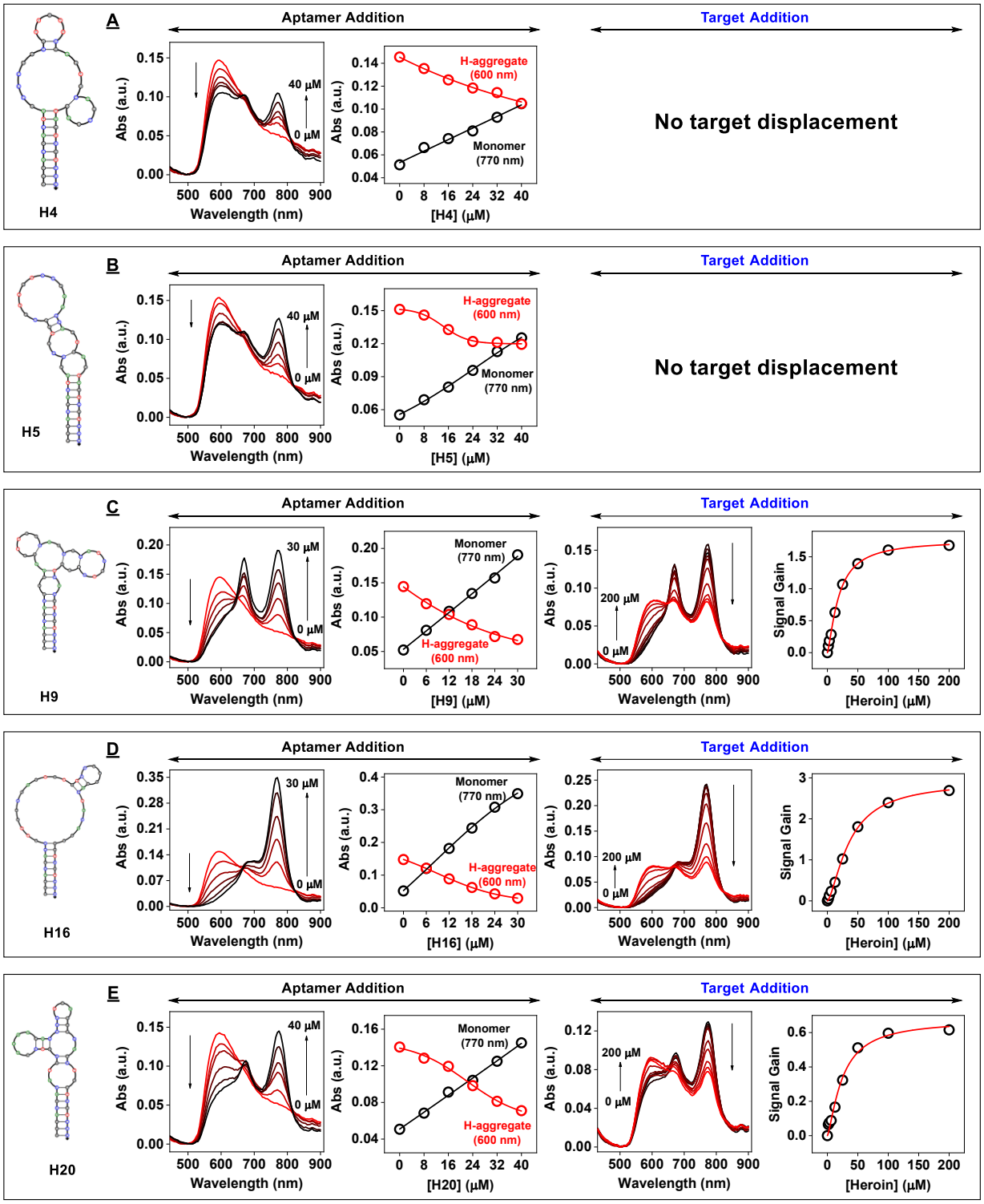

Figure S6. Target detection based on aptamer-based Cy7 displacement assay. For each panel, from left to right are: Secondary structure of the aptamer predicted by NUPACK; 'aptamer addition', which presents the absorbance spectra of 4 μM Cy7 with various concentrations of aptamer and a plot of Cy7 H-aggregate and monomer peak absorbance (respectively at 600 nm and 770 nm) plotted against aptamer concentration; and 'target addition', which presents the absorption spectra of solutions containing aptamer-Cy7 complex challenged with various concentrations of target as well as plot depicting the calibration curve for target detection. (**A**) H4, (**B**) H5, (**C**) H9, (**D**) H16 and (**E**) H20.

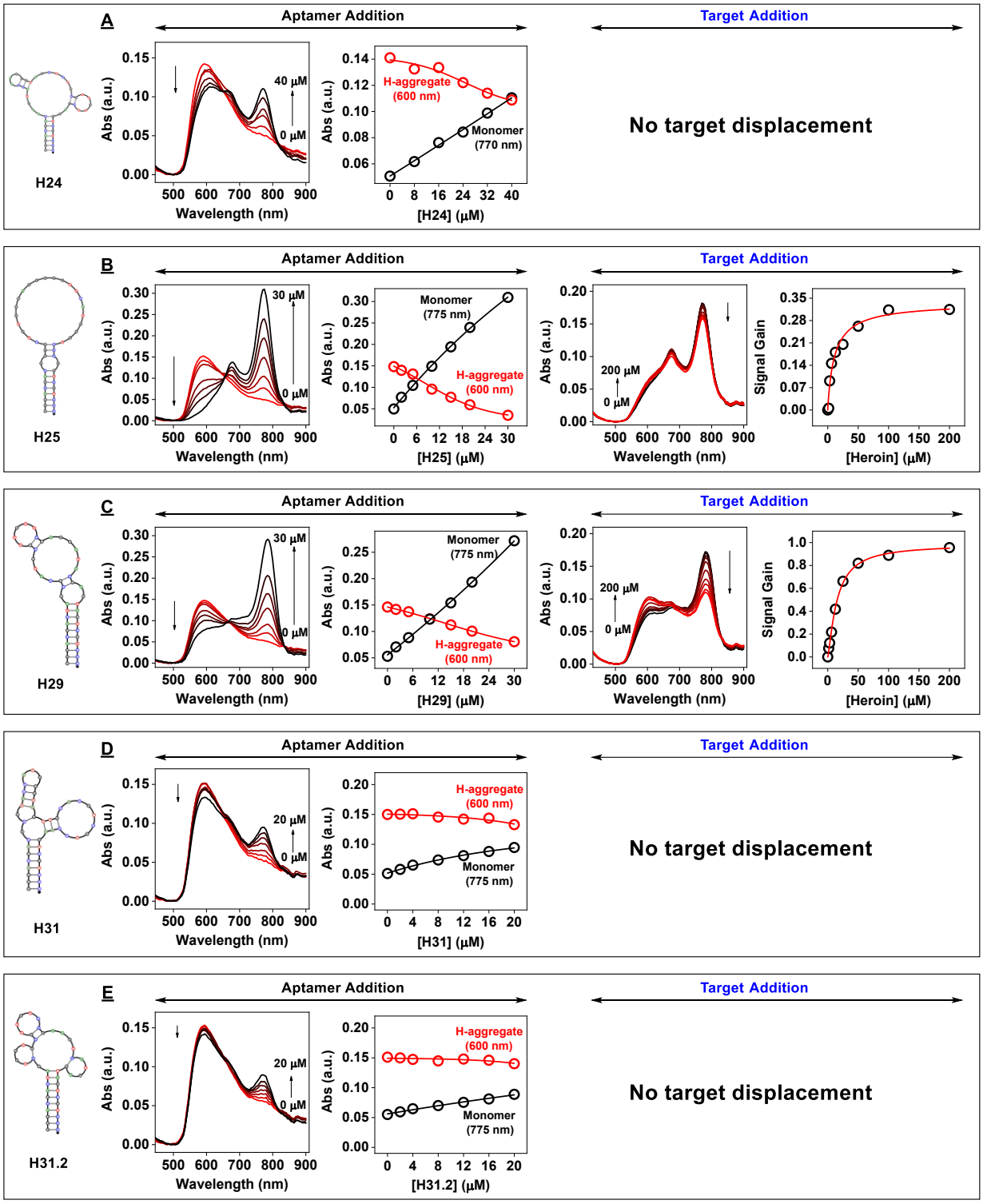

Figure S7. Target detection based on aptamer-based Cy7 displacement assay. For each panel, from left to right are: Secondary structure of the aptamer predicted by NUPACK; 'aptamer addition', which presents the absorbance spectra of 4 μM Cy7 with various concentrations of aptamer and a plot of Cy7 H-aggregate and monomer peak absorbance (respectively at 600 nm and 770-775 nm) plotted against aptamer concentration; and 'target addition', which presents the absorption spectra of solutions containing aptamer-Cy7 complex challenged with various concentrations of target as well as plot depicting the calibration curve for target detection. (**A**) H24, (**B**) H25, (**C**) H29, (**D**) H31 and (**E**) H31.2.

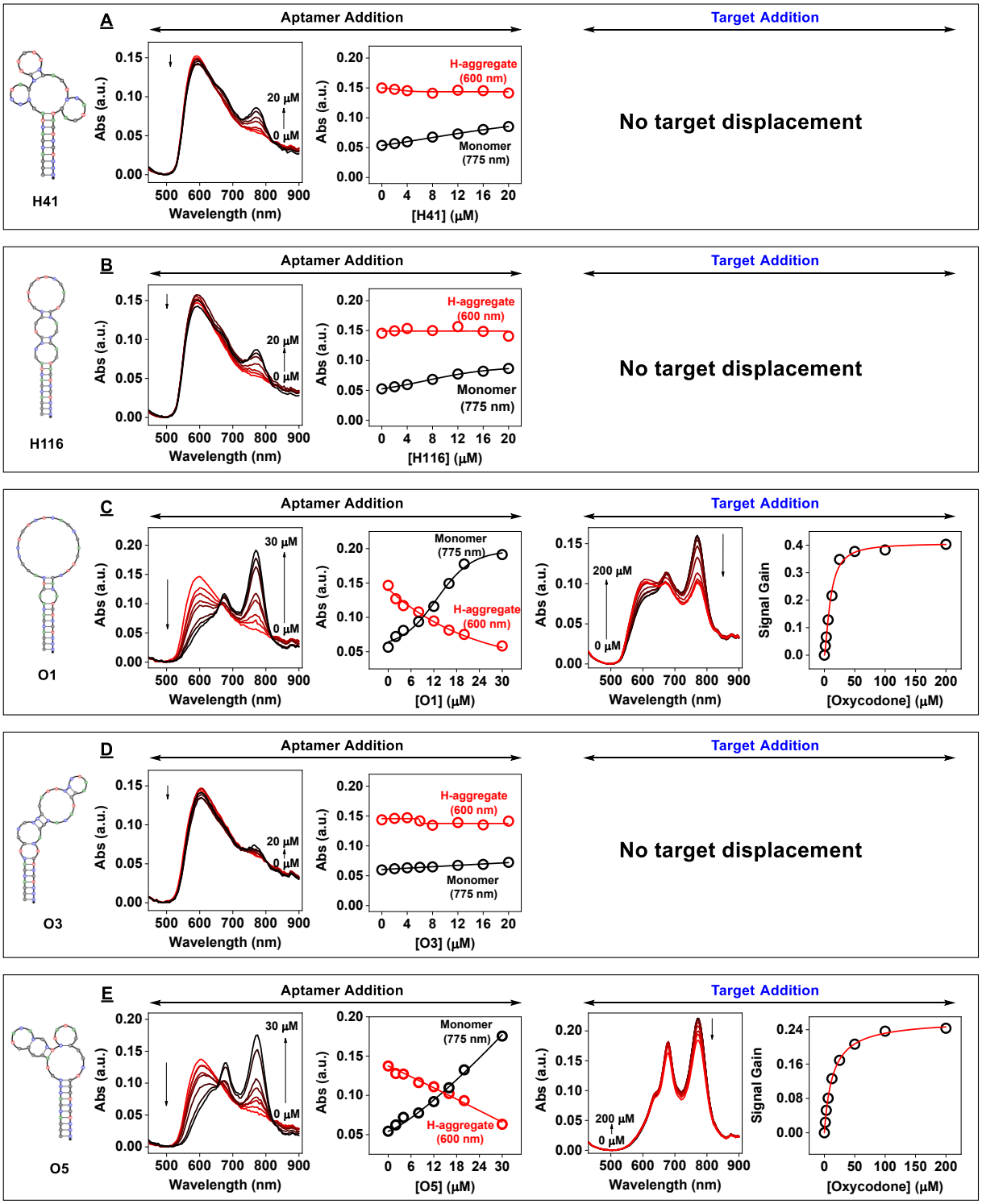

Figure S8. Target detection based on aptamer-based Cy7 displacement assay. For each panel, from left to right are: Secondary structure of the aptamer predicted by NUPACK; 'aptamer addition', which presents the absorbance spectra of 4 μM Cy7 with various concentrations of aptamer and a plot of Cy7 H-aggregate and monomer peak absorbance (respectively at 600 nm and 775 nm) plotted against aptamer concentration; and 'target addition', which presents the absorption spectra of solutions containing aptamer-Cy7 complex challenged with various concentrations of target as well as plot depicting the calibration curve for target detection. (**A**) H41, (**B**) H116, (**C**) O1, (**D**) O3 and (**E**) O5.

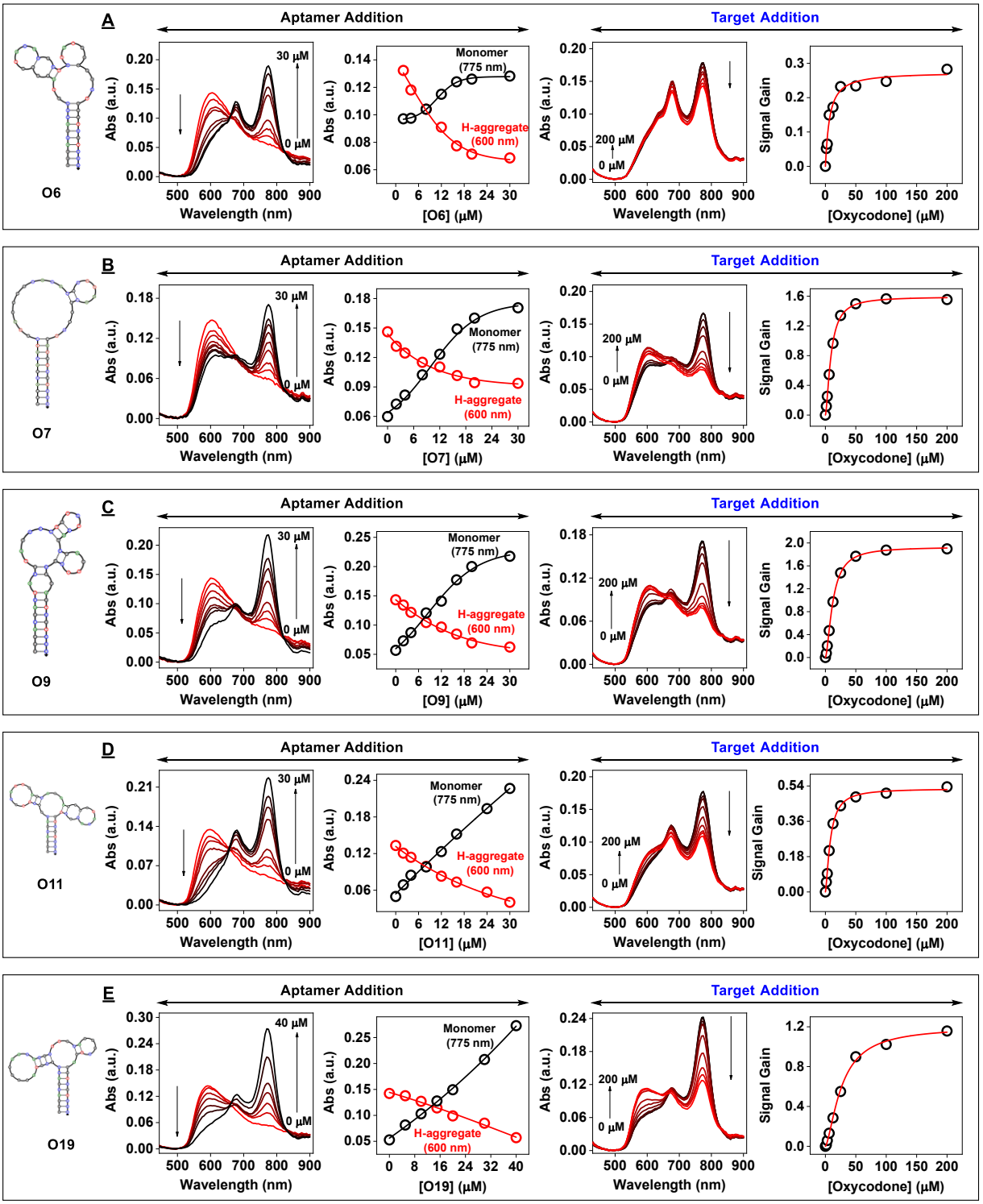

Figure S9. Target detection based on aptamer-based Cy7 displacement assay. For each panel, from left to right are: Secondary structure of the aptamer predicted by NUPACK; 'aptamer addition', which presents the absorbance spectra of 4 μM Cy7 with various concentrations of aptamer and a plot of Cy7 H-aggregate and monomer peak absorbance (respectively at 600 nm and 775 nm) plotted against aptamer concentration; and 'target addition', which presents the absorption spectra of solutions containing aptamer-Cy7 complex challenged with various concentrations of target as well as plot depicting the calibration curve for target detection. (**A**) O6, (**B**) O7, (**C**) O9, (**D**) O11 and (**E**) O19.

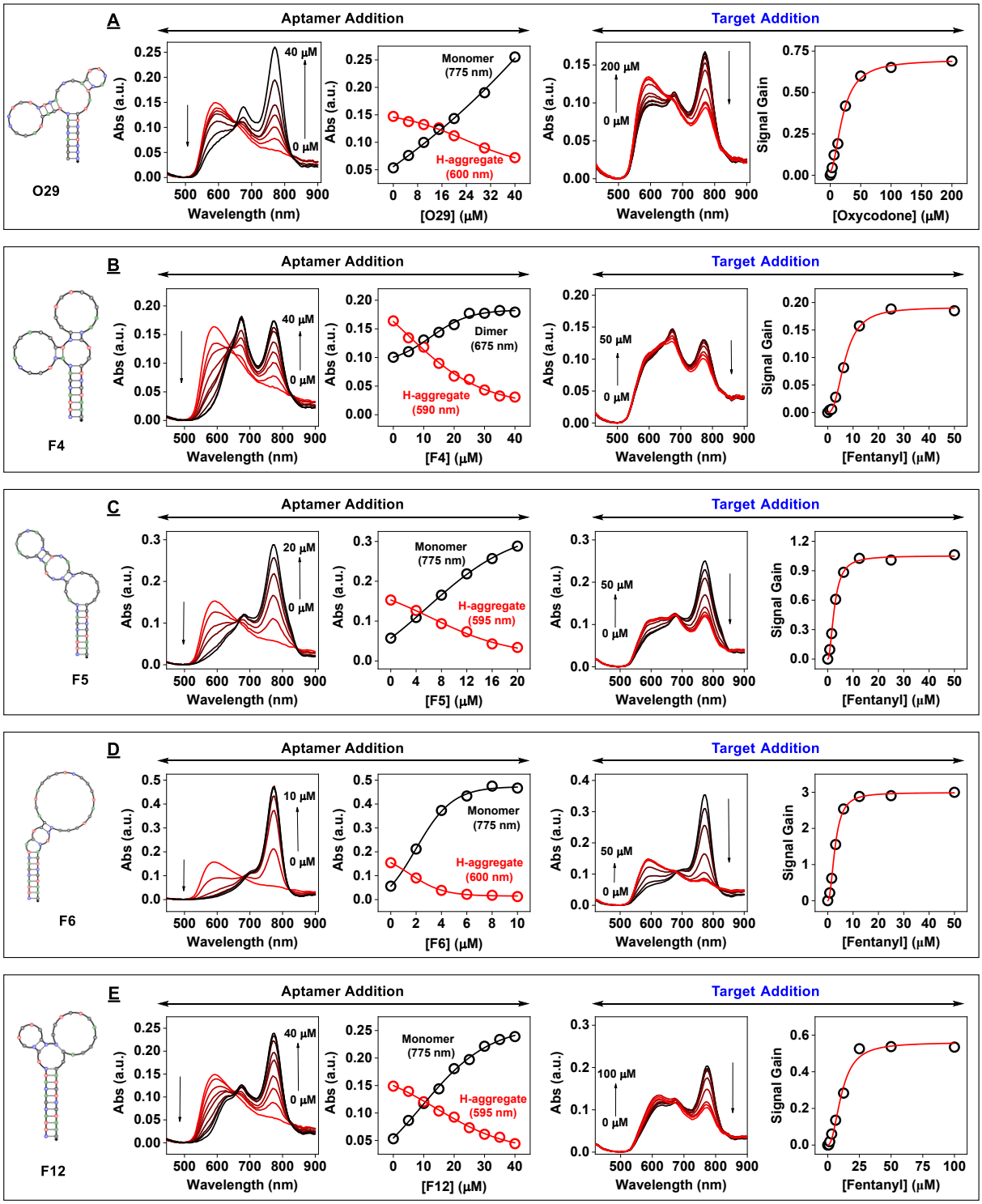

Figure S10. Target detection based on aptamer-based Cy7 displacement assay. For each panel, from left to right are: Secondary structure of the aptamer predicted by NUPACK; 'aptamer addition', which presents the absorbance spectra of 4 μM Cy7 with various concentrations of aptamer and a plot of Cy7 H-aggregate and monomer or dimer peak absorbance (respectively at ~595 nm, 770 nm, and 675 nm) against aptamer concentration; and 'target addition', which presents the absorption spectra of solutions containing aptamer-Cy7 complex challenged with various concentrations of target as well as plot depicting the target calibration curve. (**A**) O29, (**B**) F4, (**C**) F5, (**D**) F6 and (**E**) F12.

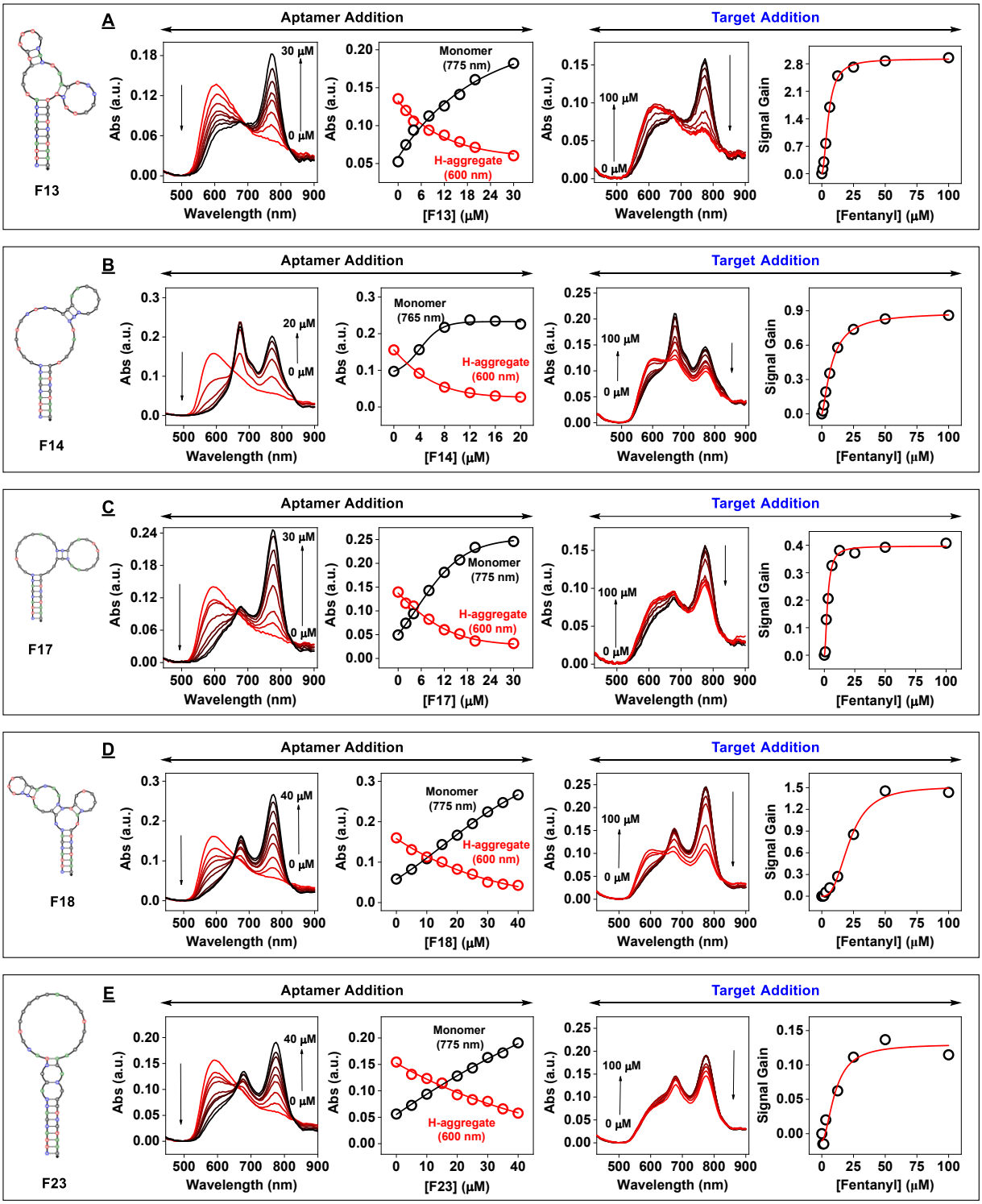

Figure S11. Target detection based on aptamer-based Cy7 displacement assay. For each panel, from left to right are: Secondary structure of the aptamer predicted by NUPACK; 'aptamer addition', which presents the absorbance spectra of 4 μM Cy7 with various concentrations of aptamer and a plot of Cy7 H-aggregate and monomer peak absorbance (respectively at 600 nm and 765-775 nm) plotted against aptamer concentration; and 'target addition', which presents the absorption spectra of solutions containing aptamer-Cy7 complex challenged with various concentrations of target as well as plot depicting the calibration curve for target detection. (**A**) F13, (**B**) F14, (**C**) F17, (**D**) F18 and (**E**) F23.

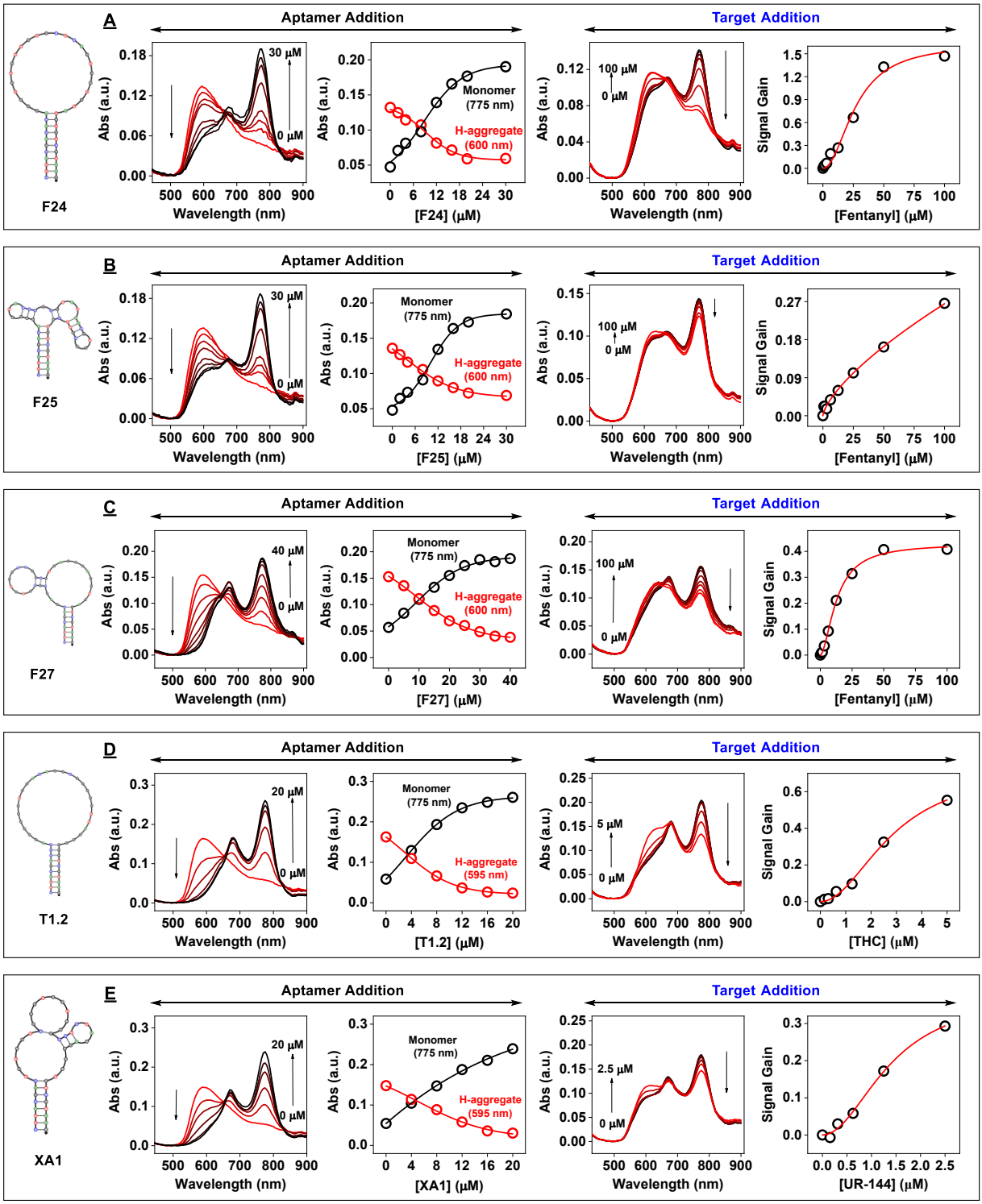

Figure S12. Target detection based on aptamer-based Cy7 displacement assay. For each panel, from left to right are: Secondary structure of the aptamer predicted by NUPACK; 'aptamer addition', which presents the absorbance spectra of 4 μM Cy7 with various concentrations of aptamer and a plot of Cy7 H-aggregate and monomer peak absorbance (respectively at 595-600 nm and 775 nm) against aptamer concentration; and 'target addition', which presents the absorption spectra of solutions containing aptamer-Cy7 complex challenged with various concentrations of target as well as plot depicting the calibration curve for target detection. (**A**) F24, (**B**) F25, (**C**) F27, (**D**) T1.2 and (**E**) XA1.

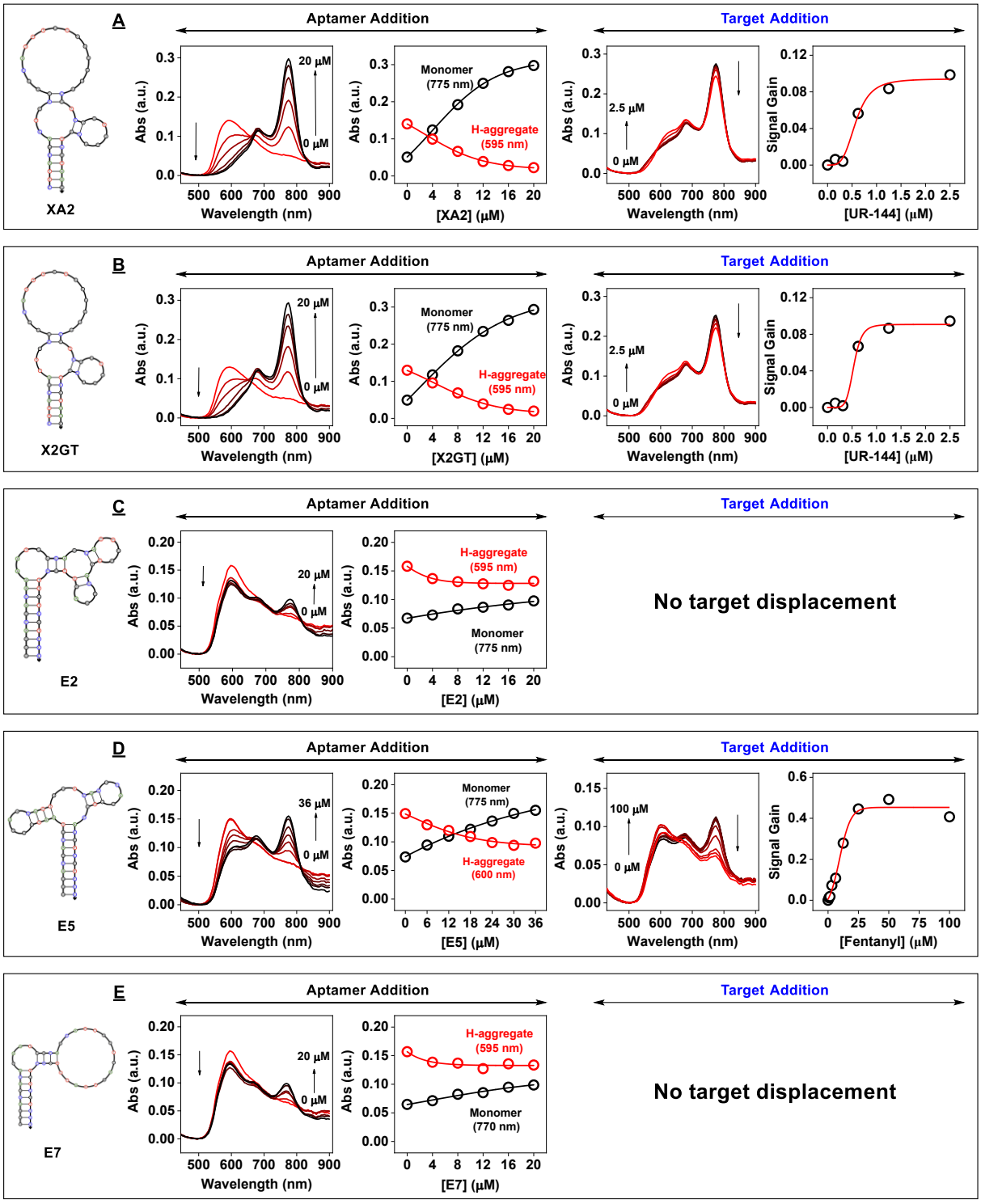

Figure S13. Target detection based on aptamer-based Cy7 displacement assay. For each panel, from left to right are: Secondary structure of the aptamer predicted by NUPACK; 'aptamer addition', which presents the absorbance spectra of 4 μM Cy7 with various concentrations of aptamer and a plot of Cy7 H-aggregate and monomer peak absorbance (respectively at 595-600 nm and 770-775 nm) against aptamer concentration; and 'target addition', which presents the absorption spectra of solutions containing aptamer-Cy7 complex challenged with various concentrations of target as well as plot depicting the calibration curve for target detection. (**A**) XA2, (**B**) X2GT, (**C**) E2, (**D**) E5 and (**E**) E7.

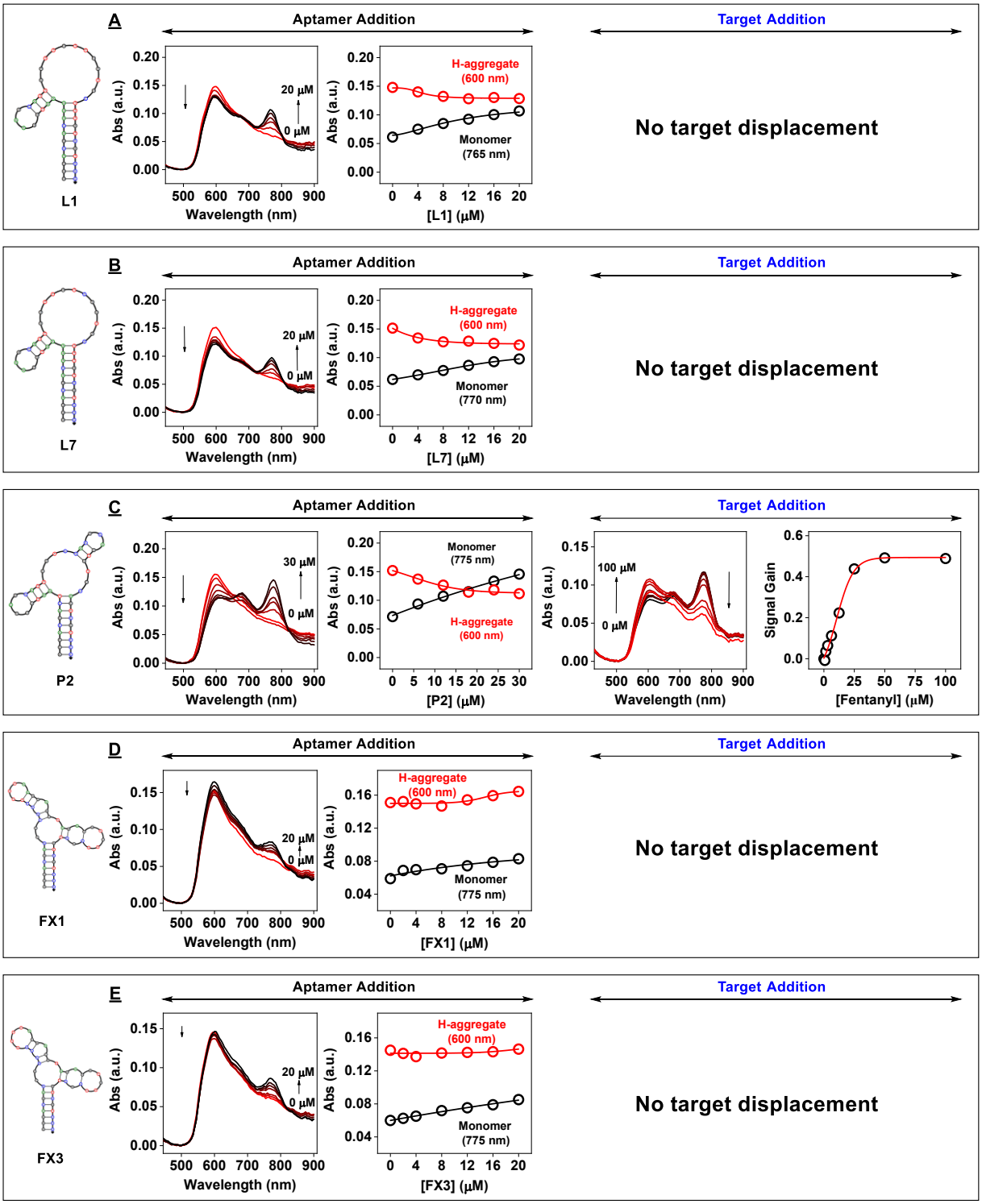

Figure S14. Target detection based on aptamer-based Cy7 displacement assay. For each panel, from left to right are: Secondary structure of the aptamer predicted by NUPACK; 'aptamer addition', which presents the absorbance spectra of 4 μM Cy7 with various concentrations of aptamer and a plot of Cy7 H-aggregate and monomer peak absorbance (respectively at 600 nm and 765-775 nm) against aptamer concentration; and 'target addition', which presents the absorption spectra of solutions containing aptamer-Cy7 complex challenged with various concentrations of target as well as plot depicting the calibration curve for target detection. (**A**) L1, (**B**) L7, (**C**) P2, (**D**) FX1 and (**E**) FX3.

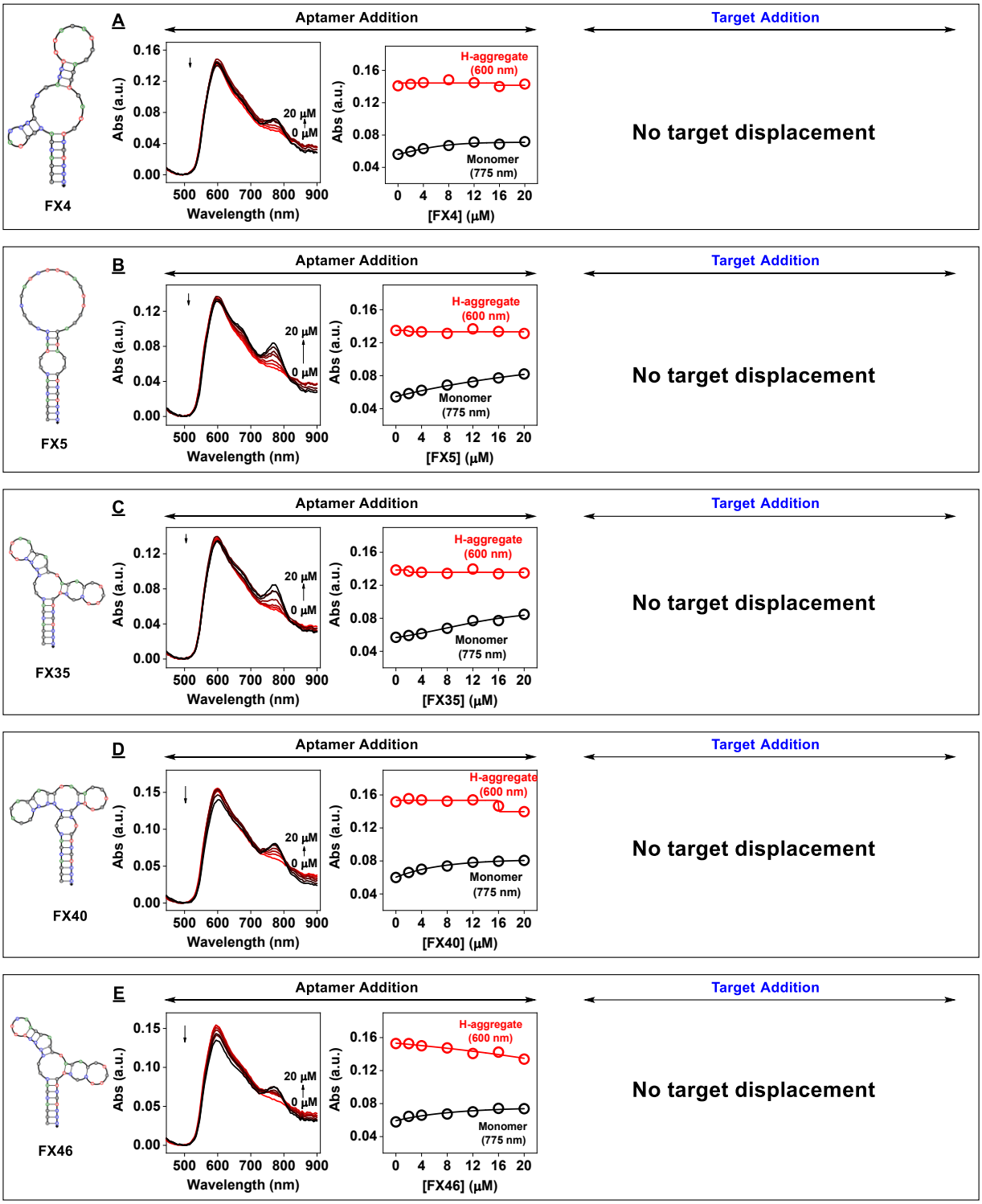

Figure S15. Target detection based on aptamer-based Cy7 displacement assay. For each panel, from left to right are: Secondary structure of the aptamer predicted by NUPACK; 'aptamer addition', which presents the absorbance spectra of 4 μM Cy7 with various concentrations of aptamer and a plot of Cy7 H-aggregate and monomer peak absorbance (respectively at 600 nm and 775 nm) against aptamer concentration; and 'target addition', which presents the absorption spectra of solutions containing aptamer-Cy7 complex challenged with various concentrations of target as well as plot depicting the calibration curve for target detection. (**A**) FX4, (**B**) FX5, (**C**) FX35, (**D**) FX40 and (**E**) FX46.

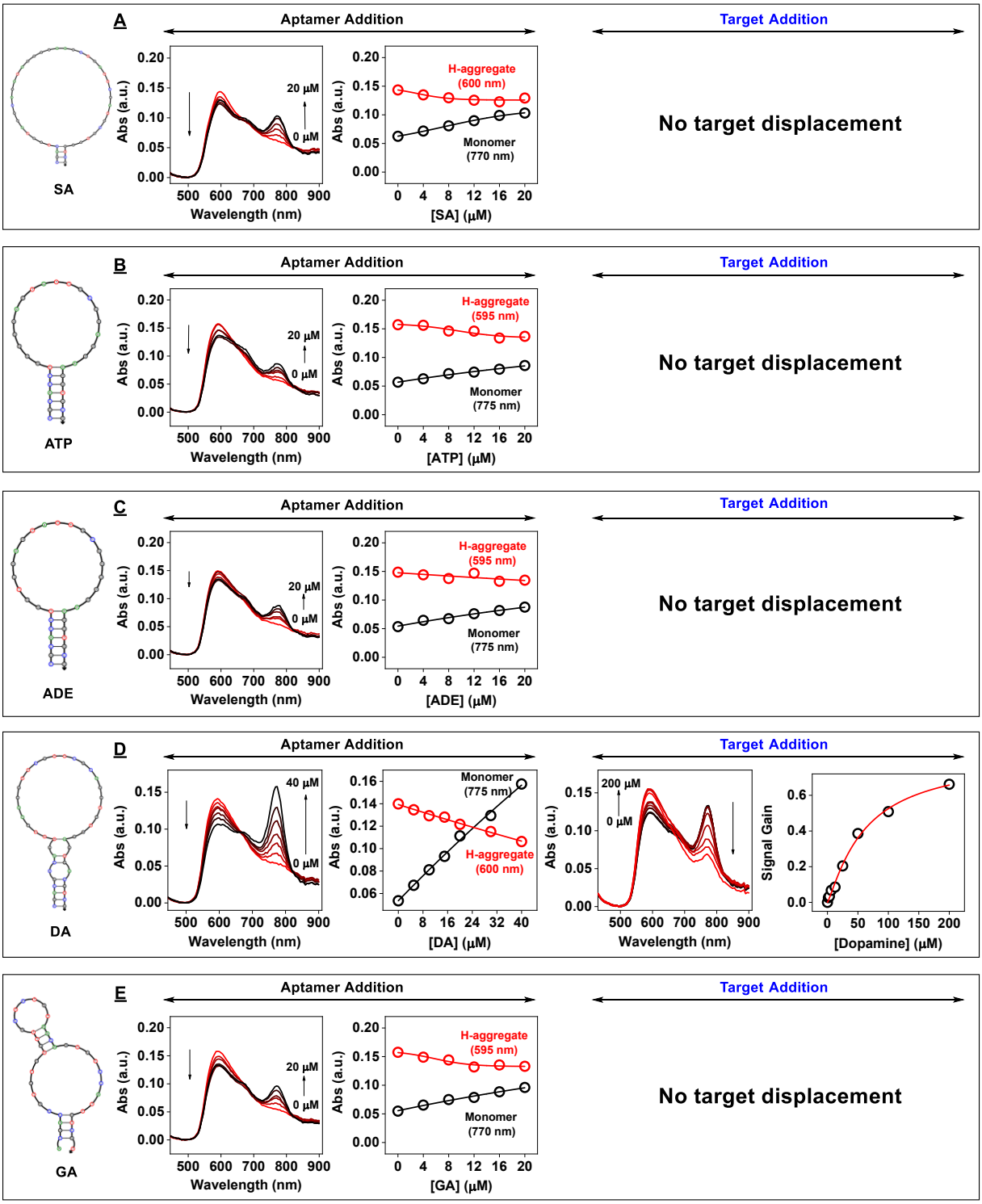

Figure S16. Target detection based on aptamer-based Cy7 displacement assay. For each panel, from left to right are: Secondary structure of the aptamer predicted by NUPACK; 'aptamer addition', which presents the absorbance spectra of 4 μM Cy7 with various concentrations of aptamer and a plot of Cy7 H-aggregate and monomer peak absorbance (respectively at 595-600 nm and 770-775 nm) against aptamer concentration; and 'target addition', which presents the absorption spectra of solutions containing aptamer-Cy7 complex challenged with various concentrations of target as well as plot depicting the calibration curve for target detection. (**A**) SA, (**B**) ATP, (**C**) ADE, (**D**) DA and (**E**) GA.

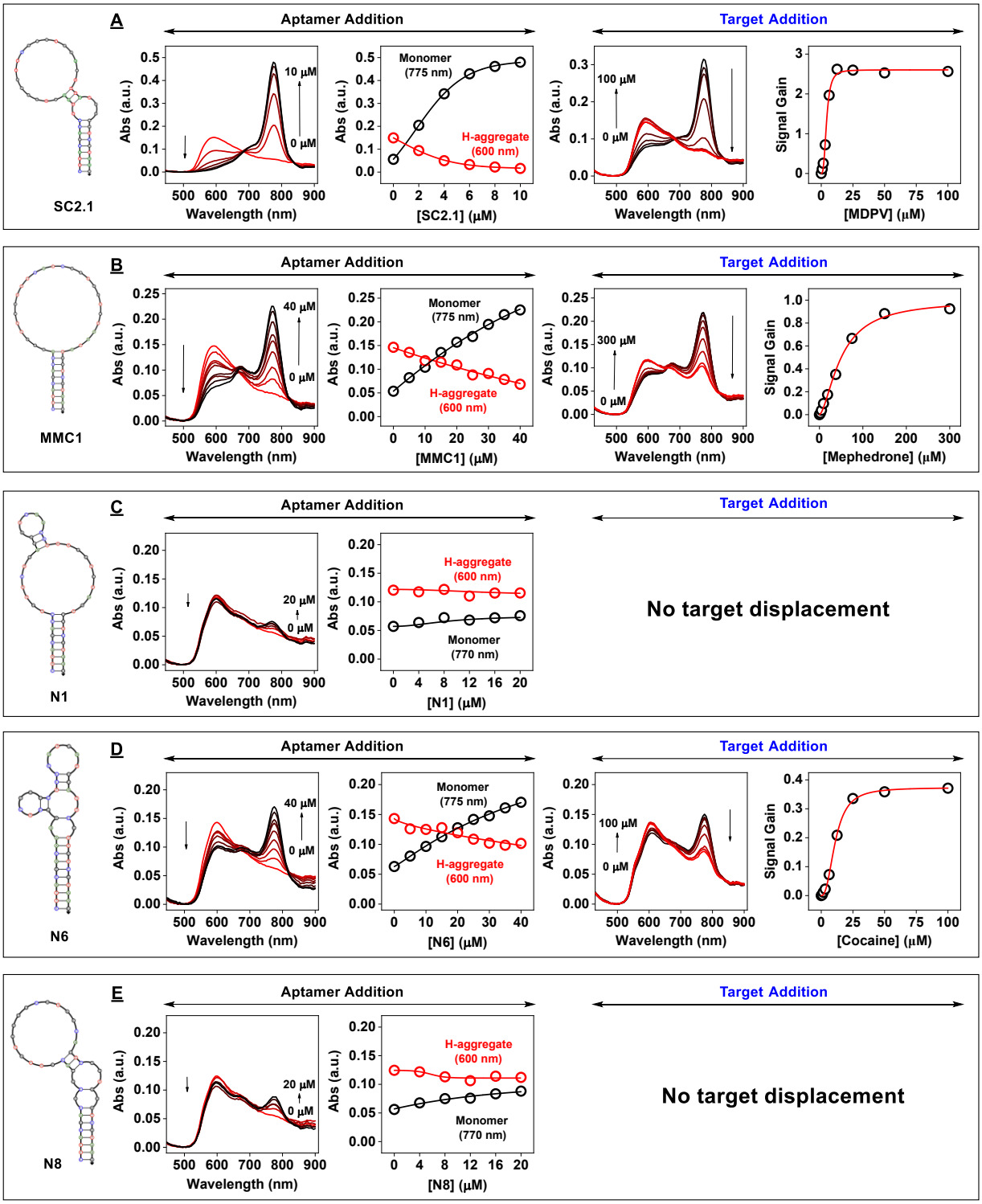

Figure S17. Target detection based on aptamer-based Cy7 displacement assay. For each panel, from left to right are: Secondary structure of the aptamer predicted by NUPACK; 'aptamer addition', which presents the absorbance spectra of 4 μM Cy7 with various concentrations of aptamer and a plot of Cy7 H-aggregate and monomer peak absorbance (respectively at 600 nm and 770-775 nm) against aptamer concentration; and 'target addition', which presents the absorption spectra of solutions containing aptamer-Cy7 complex challenged with various concentrations of target as well as plot depicting the calibration curve for target detection. (**A**) SC2.1, (**B**) MMC1, (**C**) N1, (**D**) N6 and (**E**) N8.

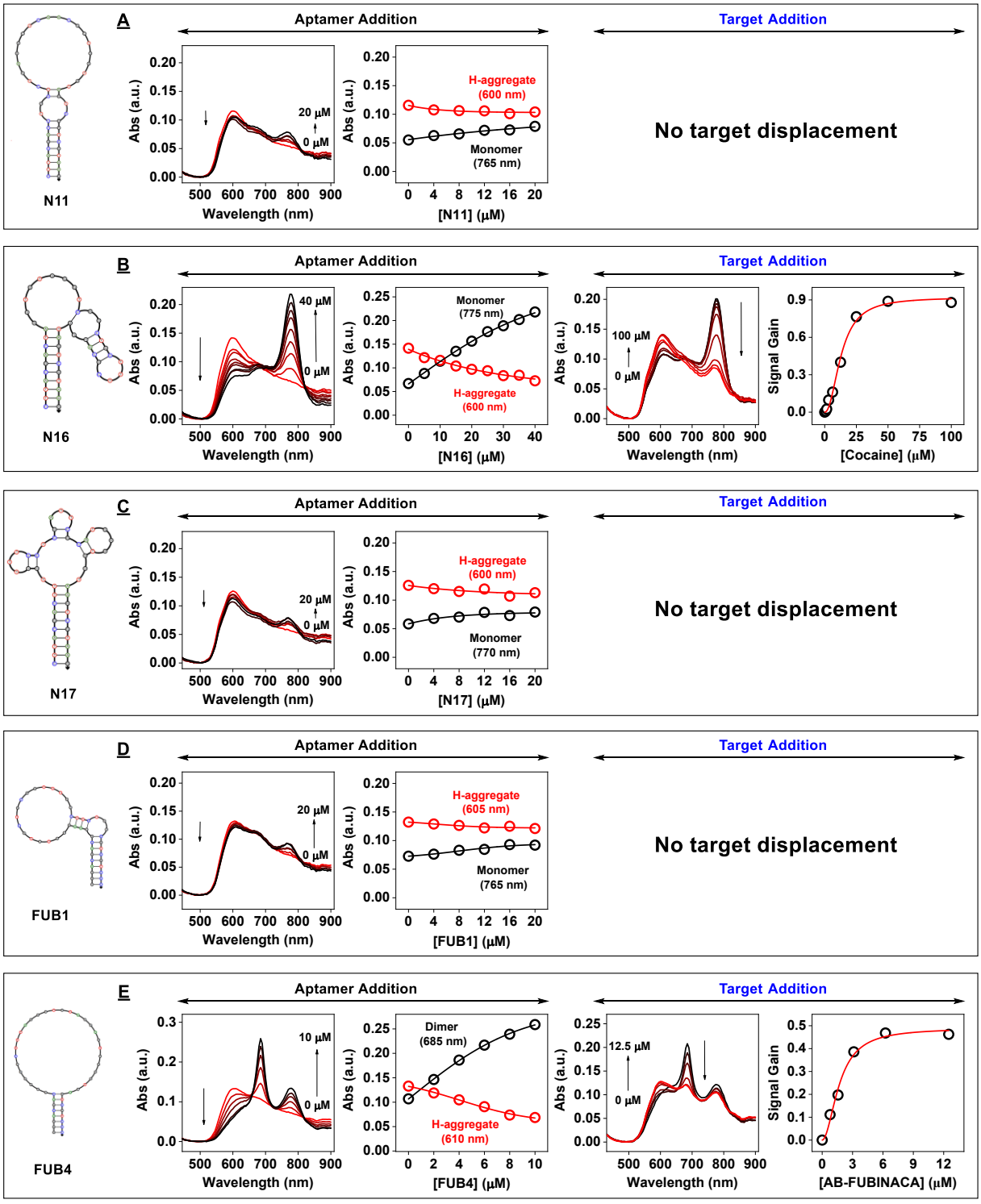

Figure S18. Target detection based on aptamer-based Cy7 displacement assay. For each panel, from left to right are: Secondary structure of the aptamer predicted by NUPACK; 'aptamer addition', which presents the absorbance spectra of 4 μM Cy7 with various concentrations of aptamer and a plot of Cy7 H-aggregate and monomer or dimer peak absorbance (respectively at ~605 nm, 770 nm, and 685 nm) against aptamer concentration; and 'target addition', which presents the absorption spectra of solutions containing aptamer-Cy7 complex challenged with various concentrations of target as well as plot depicting the target calibration curve. (**A**) N11, (**B**) N16, (**C**) N17, (**D**) FUB1 and (**E**) FUB4.

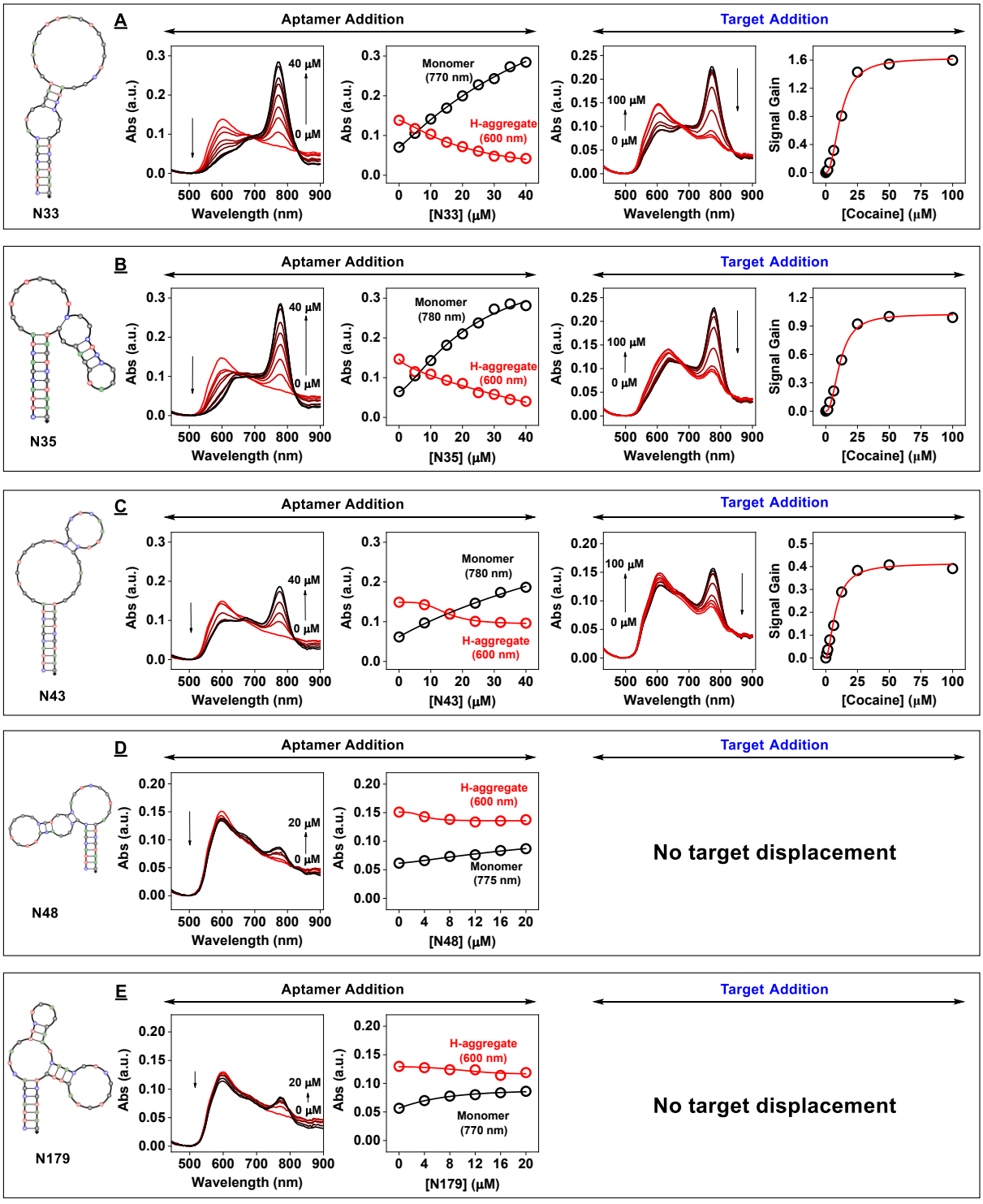

Figure S19. Target detection based on aptamer-based Cy7 displacement assay. For each panel, from left to right are: Secondary structure of the aptamer predicted by NUPACK; 'aptamer addition', which presents the absorbance spectra of 4 μM Cy7 with various concentrations of aptamer and a plot of Cy7 H-aggregate and monomer peak absorbance (respectively at 600 nm and 770-780 nm) against aptamer concentration; and 'target addition', which presents the absorption spectra of solutions containing aptamer-Cy7 complex challenged with various concentrations of target as well as plot depicting the calibration curve for target detection. (**A**) N33, (**B**) N35, (**C**) N43, (**D**) N48 and (**E**) N179.

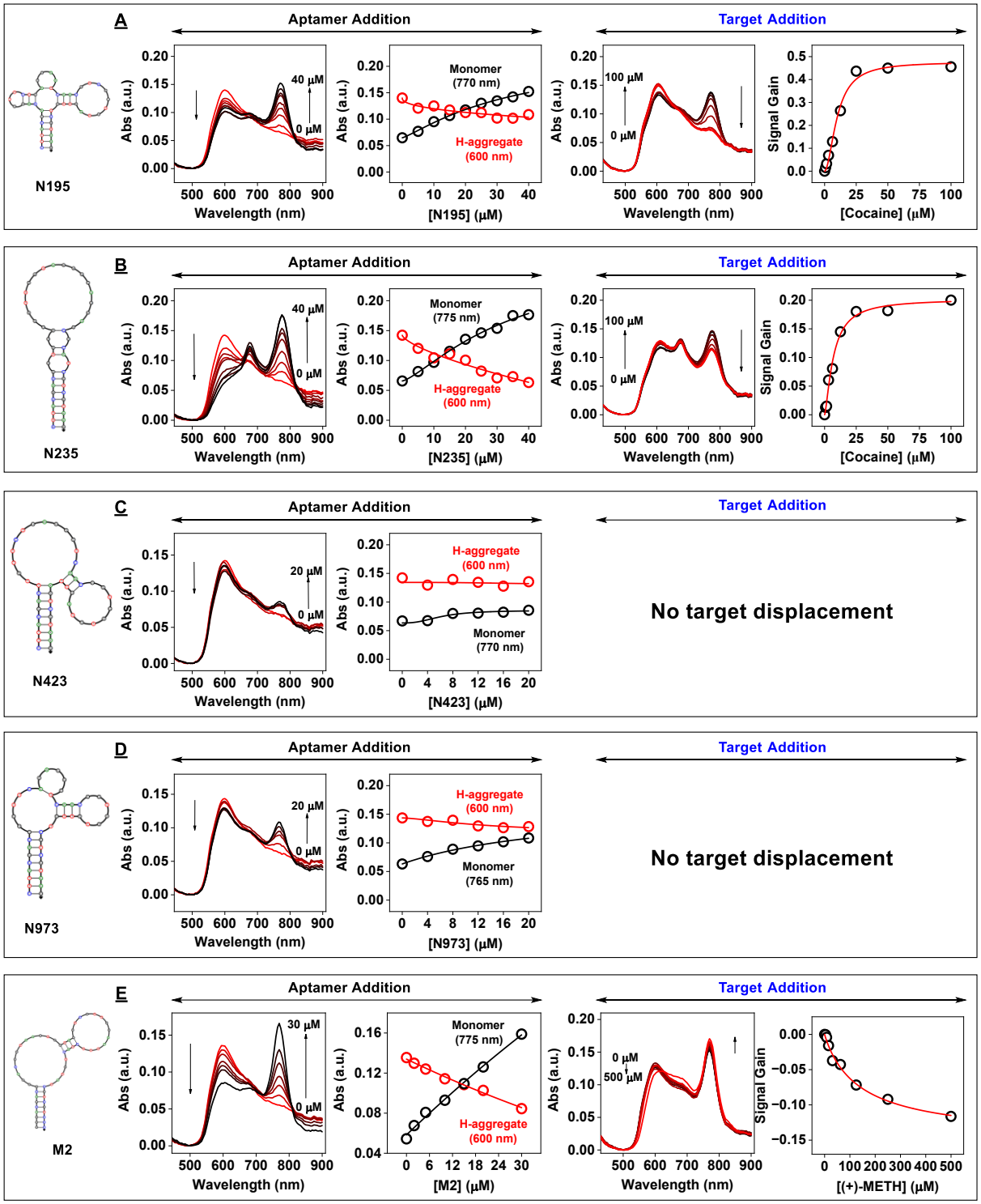

Figure S20. Target detection based on aptamer-based Cy7 displacement assay. For each panel, from left to right are: Secondary structure of the aptamer predicted by NUPACK; 'aptamer addition', which presents the absorbance spectra of 4 μM Cy7 with various concentrations of aptamer and a plot of Cy7 H-aggregate and monomer peak absorbance (respectively at 600 nm and 770 nm) against aptamer concentration; and 'target addition', which presents the absorption spectra of solutions containing aptamer-Cy7 complex challenged with various concentrations of target as well as plot depicting the target calibration curve. (**A**) N195, (**B**) N235, (**C**) N423, (**D**) N973 and (**E**) M2.

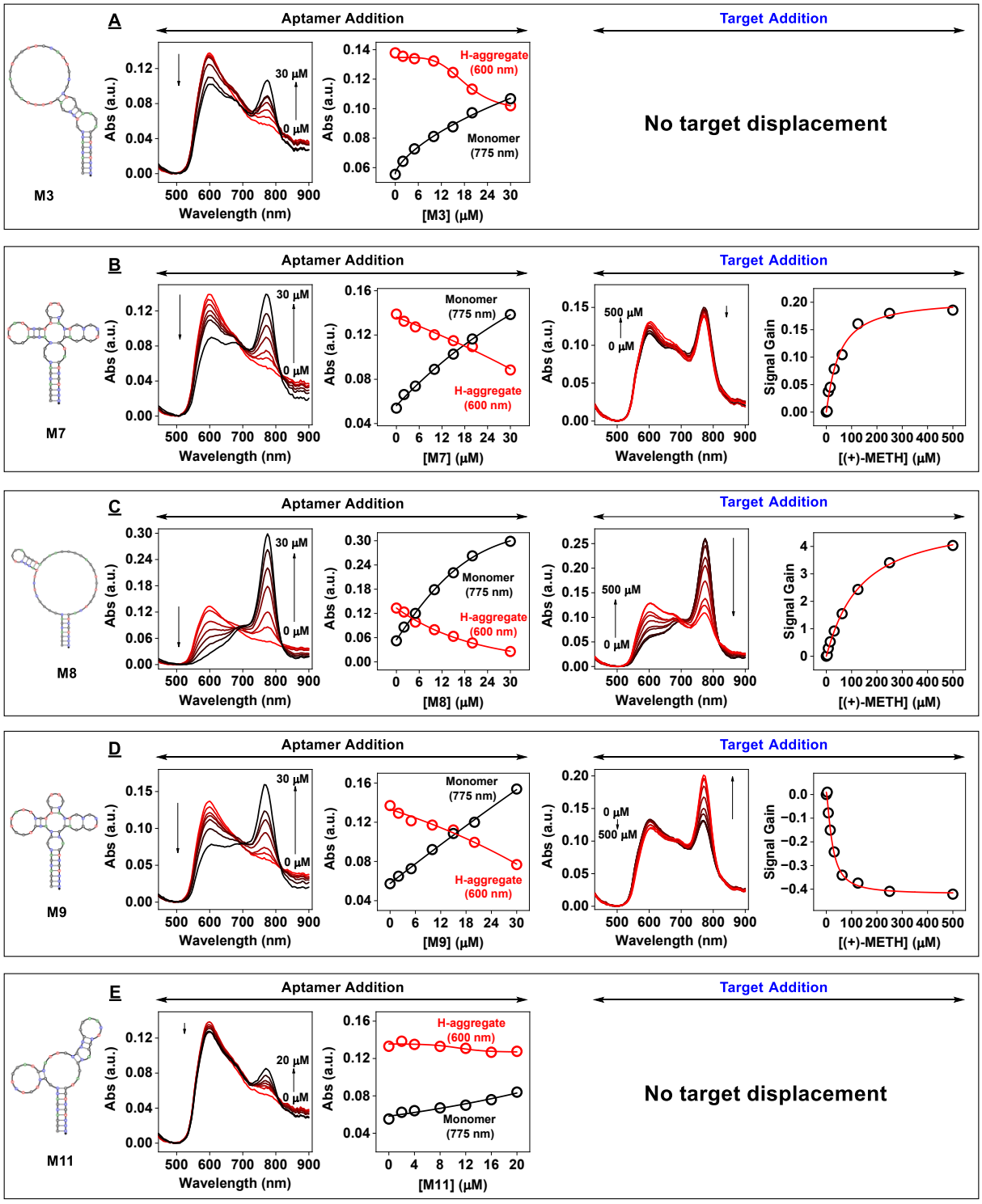

Figure S21. Target detection based on aptamer-based Cy7 displacement assay. For each panel, from left to right are: Secondary structure of the aptamer predicted by NUPACK; 'aptamer addition', which presents the absorbance spectra of 4 μM Cy7 with various concentrations of aptamer and a plot of Cy7 H-aggregate and monomer peak absorbance (respectively at 600 nm and 775 nm) against aptamer concentration; and 'target addition', which presents the absorption spectra of solutions containing aptamer-Cy7 complex challenged with various concentrations of target as well as plot depicting the calibration curve for target detection. (**A**) M3, (**B**) M7, (**C**) M8, (**D**) M9 and (**E**) M11.

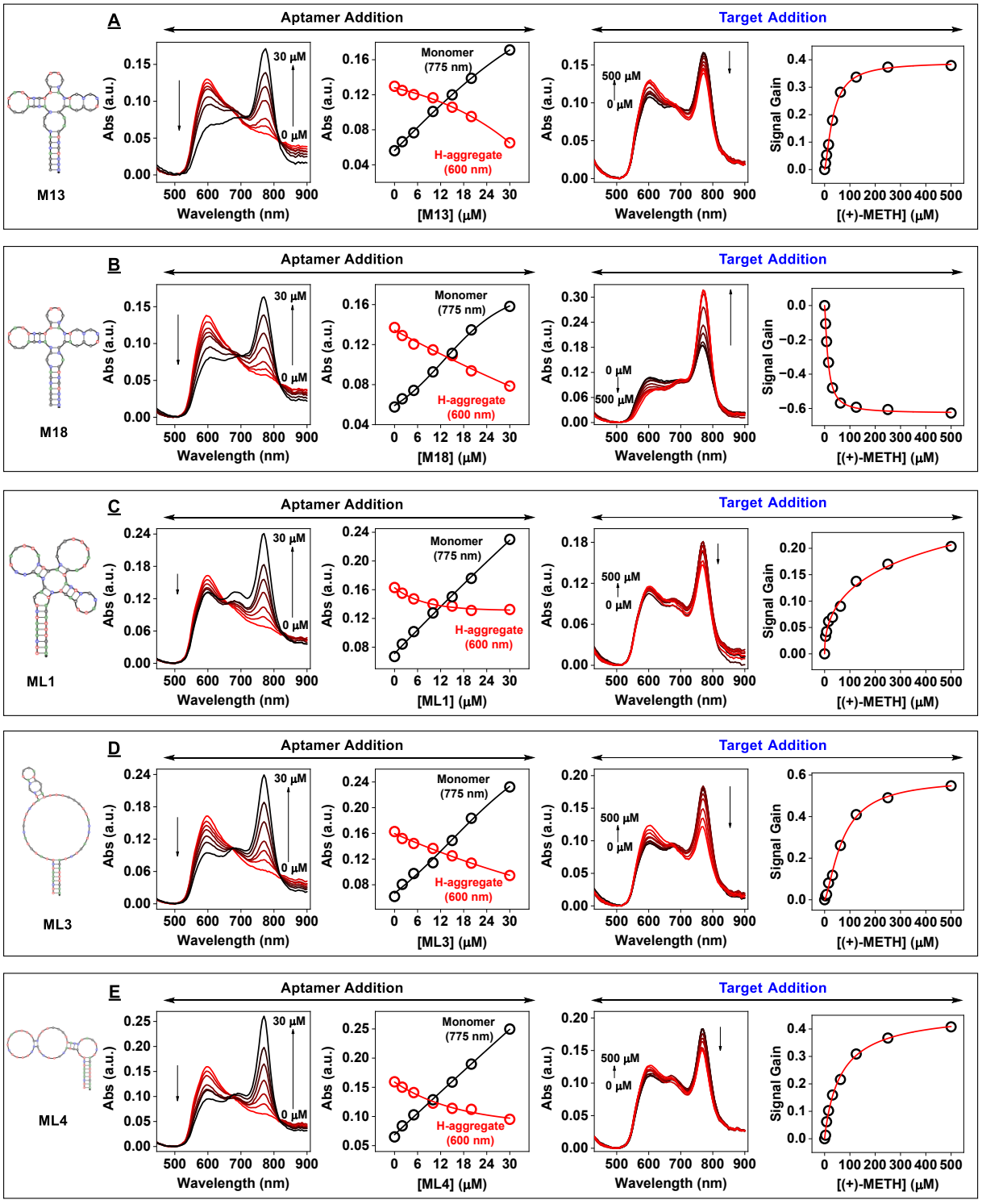

Figure S22. Target detection based on aptamer-based Cy7 displacement assay. For each panel, from left to right are: Secondary structure of the aptamer predicted by NUPACK; 'aptamer addition', which presents the absorbance spectra of 4 μM Cy7 with various concentrations of aptamer and a plot of Cy7 H-aggregate and monomer peak absorbance (respectively at 600 nm and 775 nm) against aptamer concentration; and 'target addition', which presents the absorption spectra of solutions containing aptamer-Cy7 complex challenged with various concentrations of target as well as plot depicting the calibration curve for target detection. (**A**) M13, (**B**) M18, (**C**) ML1, (**D**) ML3 and (**E**) ML4.

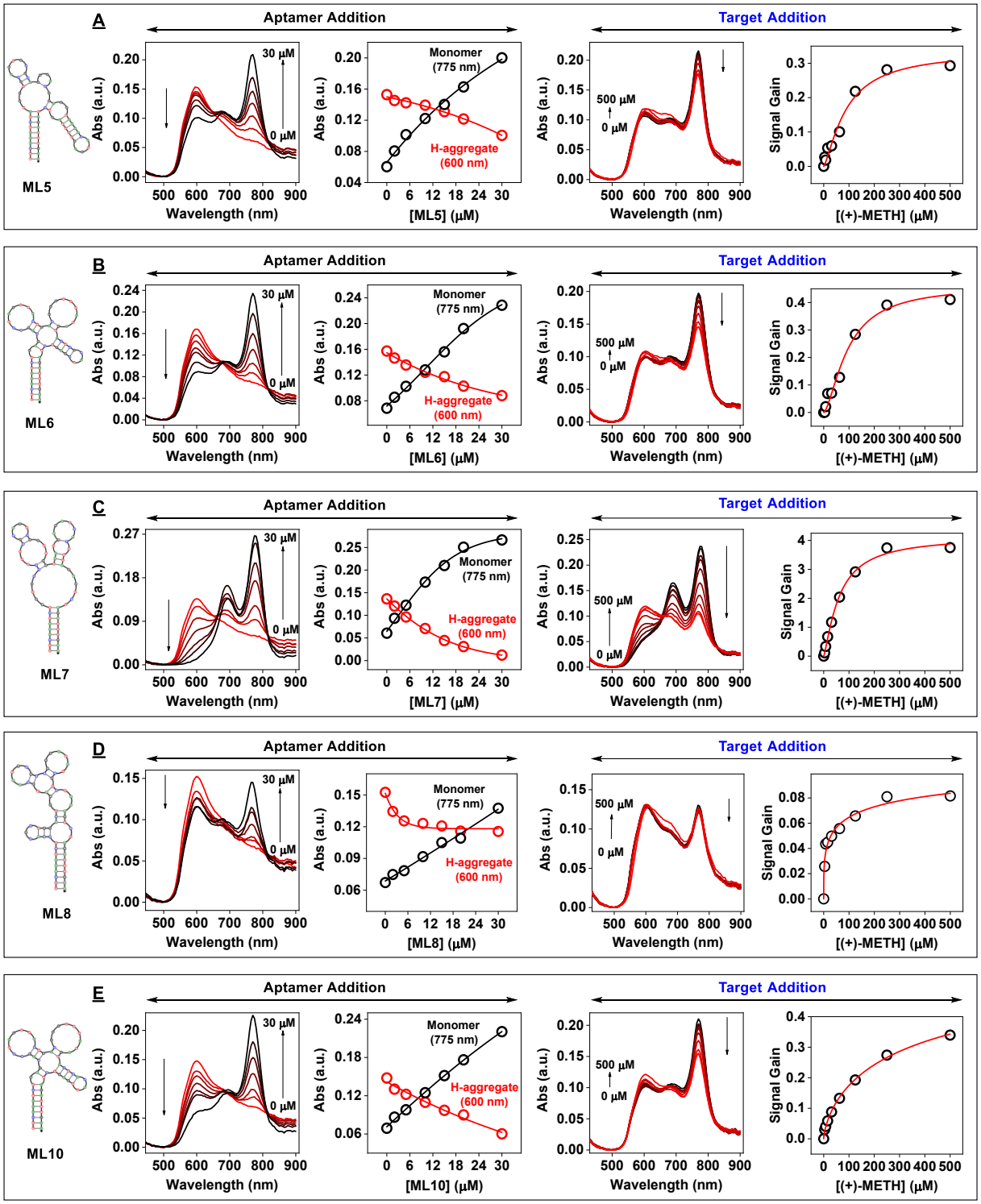

Figure S23. Target detection based on aptamer-based Cy7 displacement assay. For each panel, from left to right are: Secondary structure of the aptamer predicted by NUPACK; 'aptamer addition', which presents the absorbance spectra of 4 μM Cy7 with various concentrations of aptamer and a plot of Cy7 H-aggregate and monomer peak absorbance (respectively at 600 nm and 775 nm) against aptamer concentration; and 'target addition', which presents the absorption spectra of solutions containing aptamer-Cy7 complex challenged with various concentrations of target as well as plot depicting the calibration curve for target detection. (**A**) ML5, (**B**) ML6, (**C**) ML7, (**D**) ML8 and (**E**) ML10.

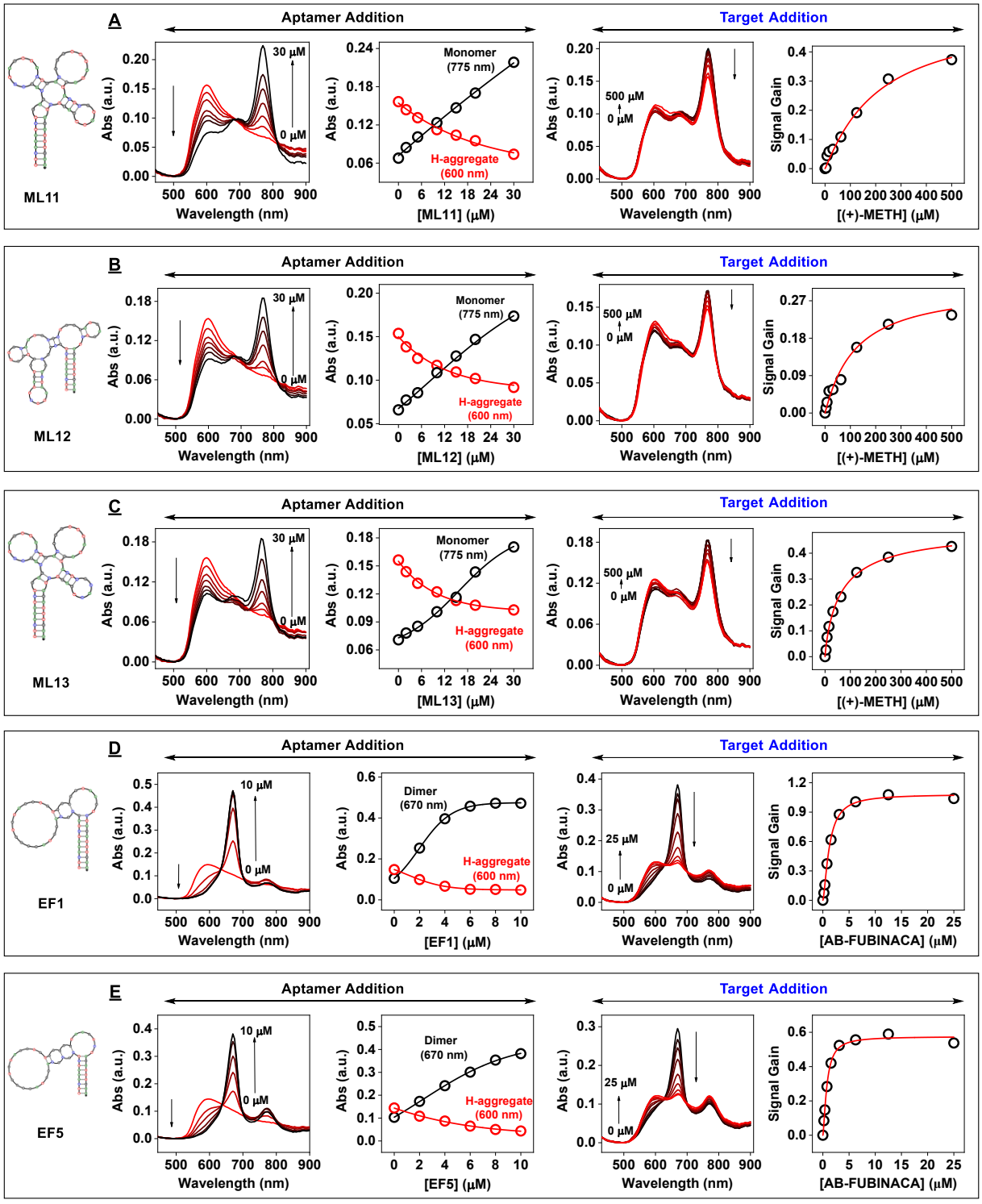

Figure S24. Target detection based on aptamer-based Cy7 displacement assay. For each panel, from left to right are: Secondary structure of the aptamer predicted by NUPACK; 'aptamer addition', which presents the absorbance spectra of 4 μM Cy7 with various concentrations of aptamer and a plot of Cy7 H-aggregate and monomer or dimer peak absorbance (respectively at 600 nm, 775 nm, and 670 nm) against aptamer concentration; and 'target addition', which presents the absorption spectra of solutions containing aptamer-Cy7 complex challenged with various concentrations of target as well as plot depicting the target calibration curve. (**A**) ML11, (**B**) ML12, (**C**) ML13, (**D**) EF1 and (**E**) EF5.

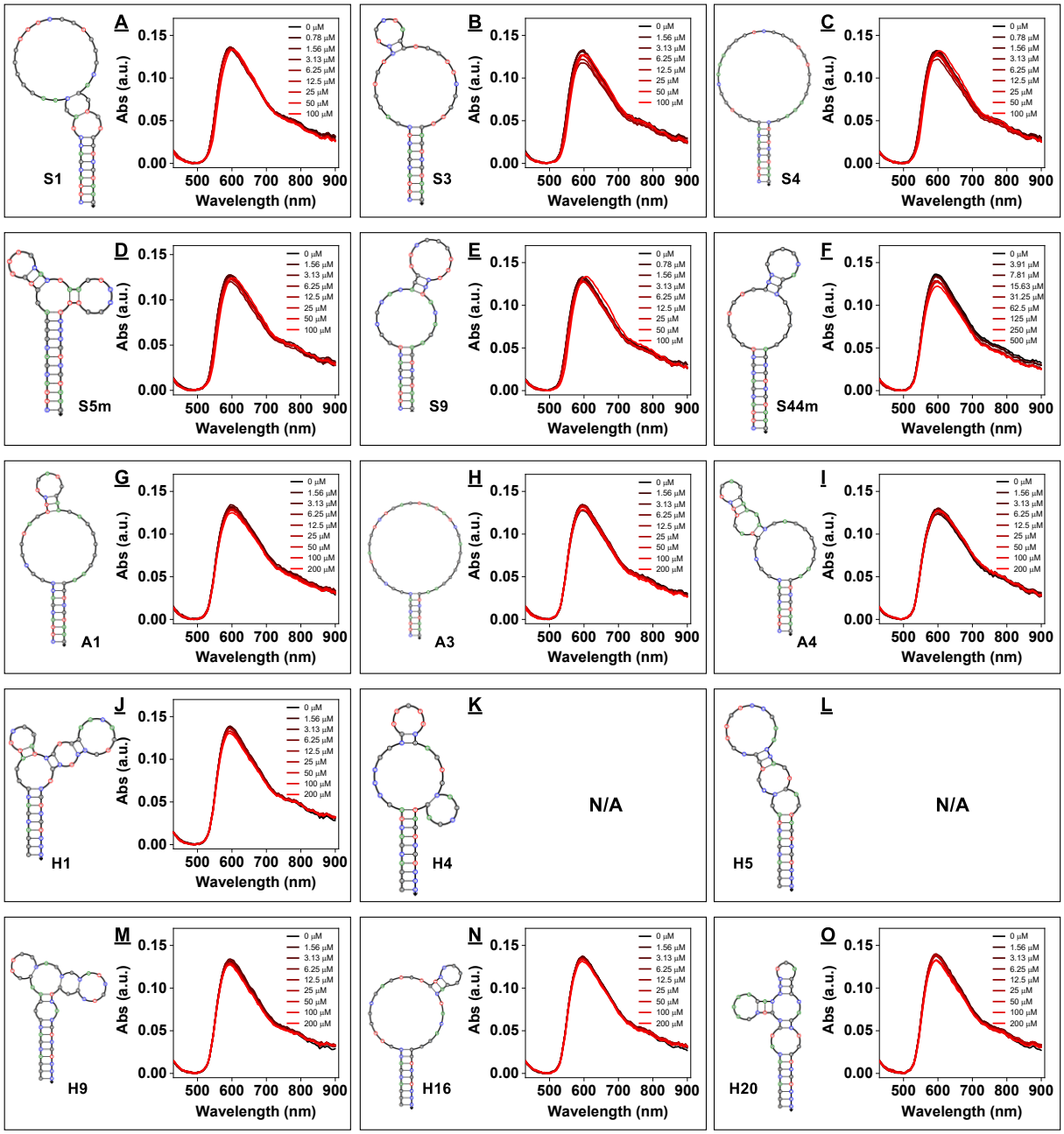

Figure S25. Absorbance spectra of 4 μM Cy7 in the presence of different targets at various concentrations. (**A-E**) (±)-cis-3-methyl-fentanyl, (**F**) remifentanil, (**G-I**) alfentanil and (**J-O**) heroin. N/A indicated that no target control experiments were performed for that aptamer since no target-induced dye-displacement was observed. Black-to-red color gradient represents increasing concentrations of target.

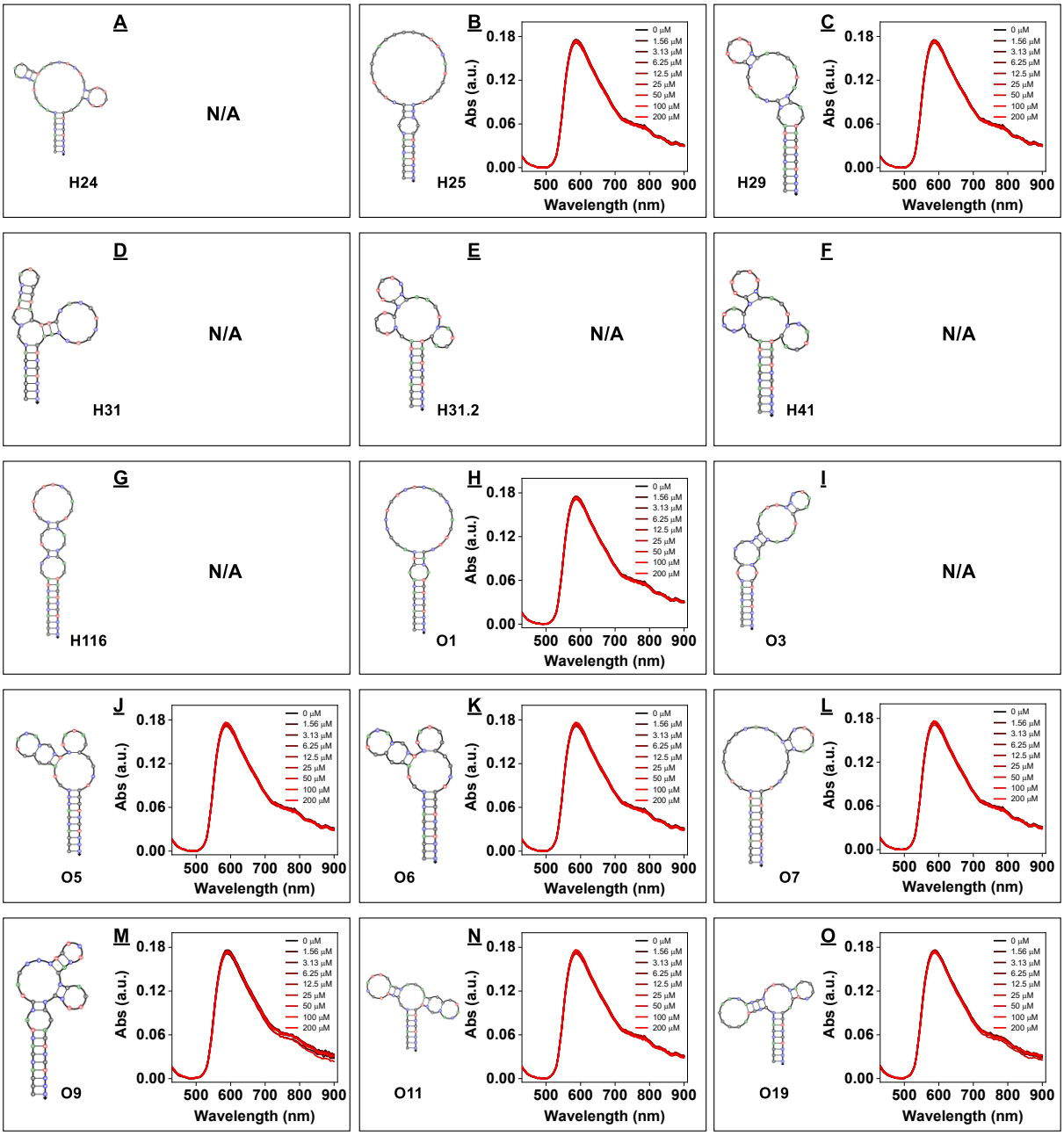

Figure S25 (continued). Absorbance spectra of 4 μM Cy7 in the presence of different targets at various concentrations. (**A-G**) heroin and (**H-O**) oxycodone. N/A indicated that no target control experiments were performed for that aptamer since no target-induced dye-displacement was observed. Black-to-red color gradient represents increasing concentrations of target.

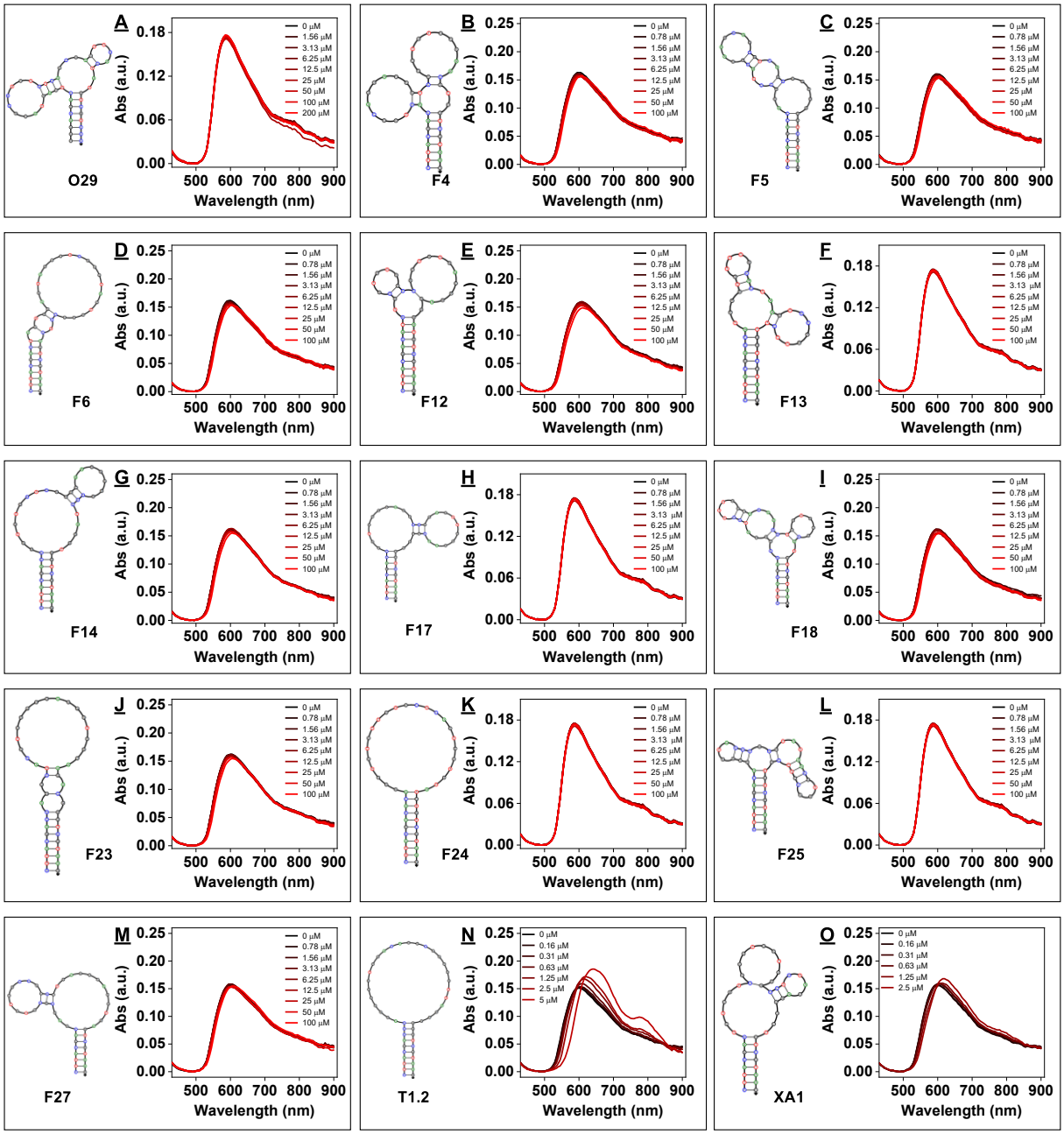

Figure S25 (continued). Absorbance spectra of 4 μM Cy7 in the presence of different targets at various concentrations. (**A**) oxycodone, (**B-M**) fentanyl, (**N**) THC and (**O**) UR-144. Black-to-red color gradient represents increasing concentrations of target.

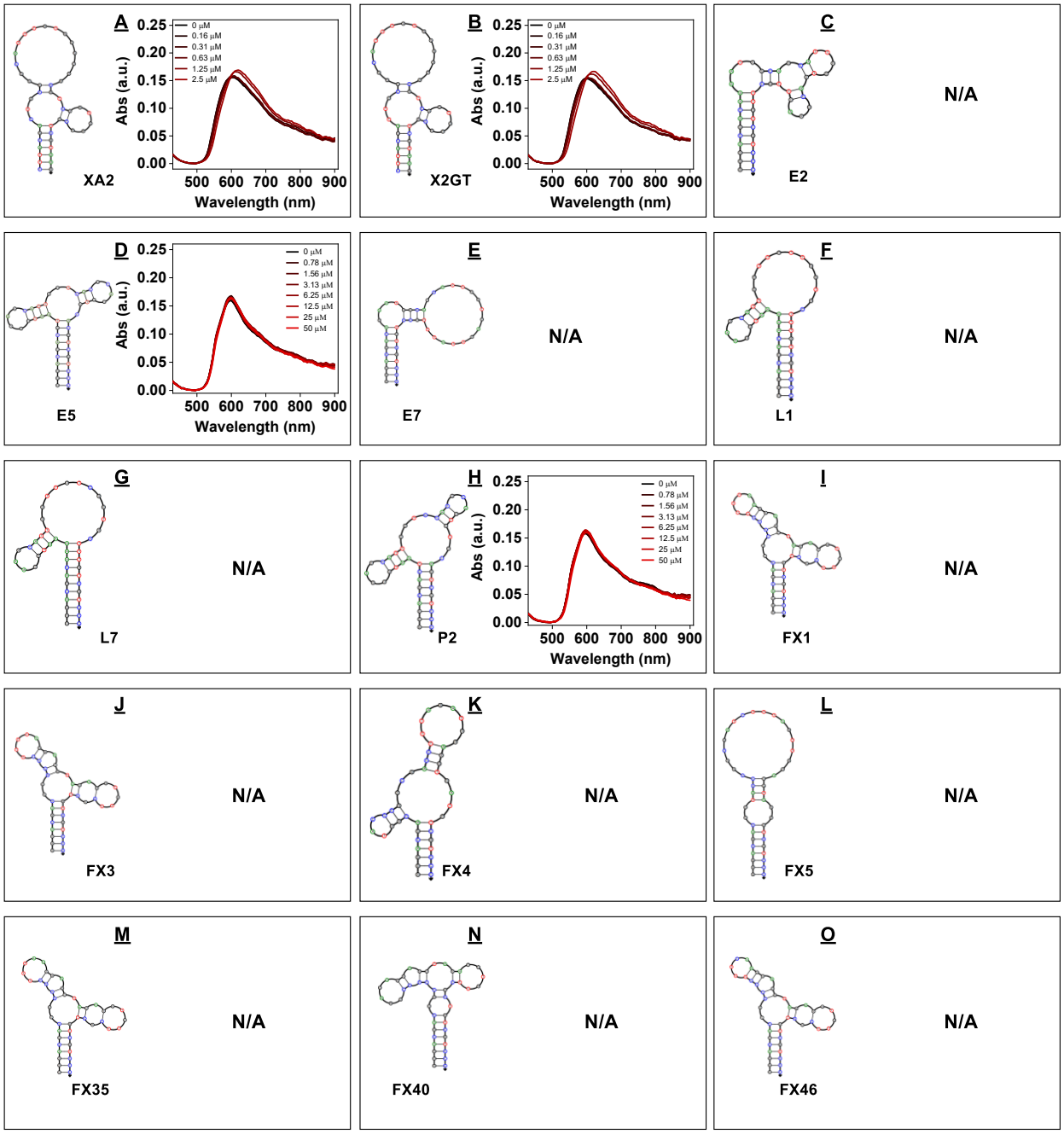

Figure S25 (continued). Absorbance spectra of 4 μM Cy7 in the presence of different targets at various concentrations. (**A-B**) UR-144, (**C-H**) fentanyl, (**I-O**) flunixin. N/A indicated that no target control experiments were performed for that aptamer since no target-induced dye-displacement was observed. Black-to-red color gradient represents increasing concentrations of target.

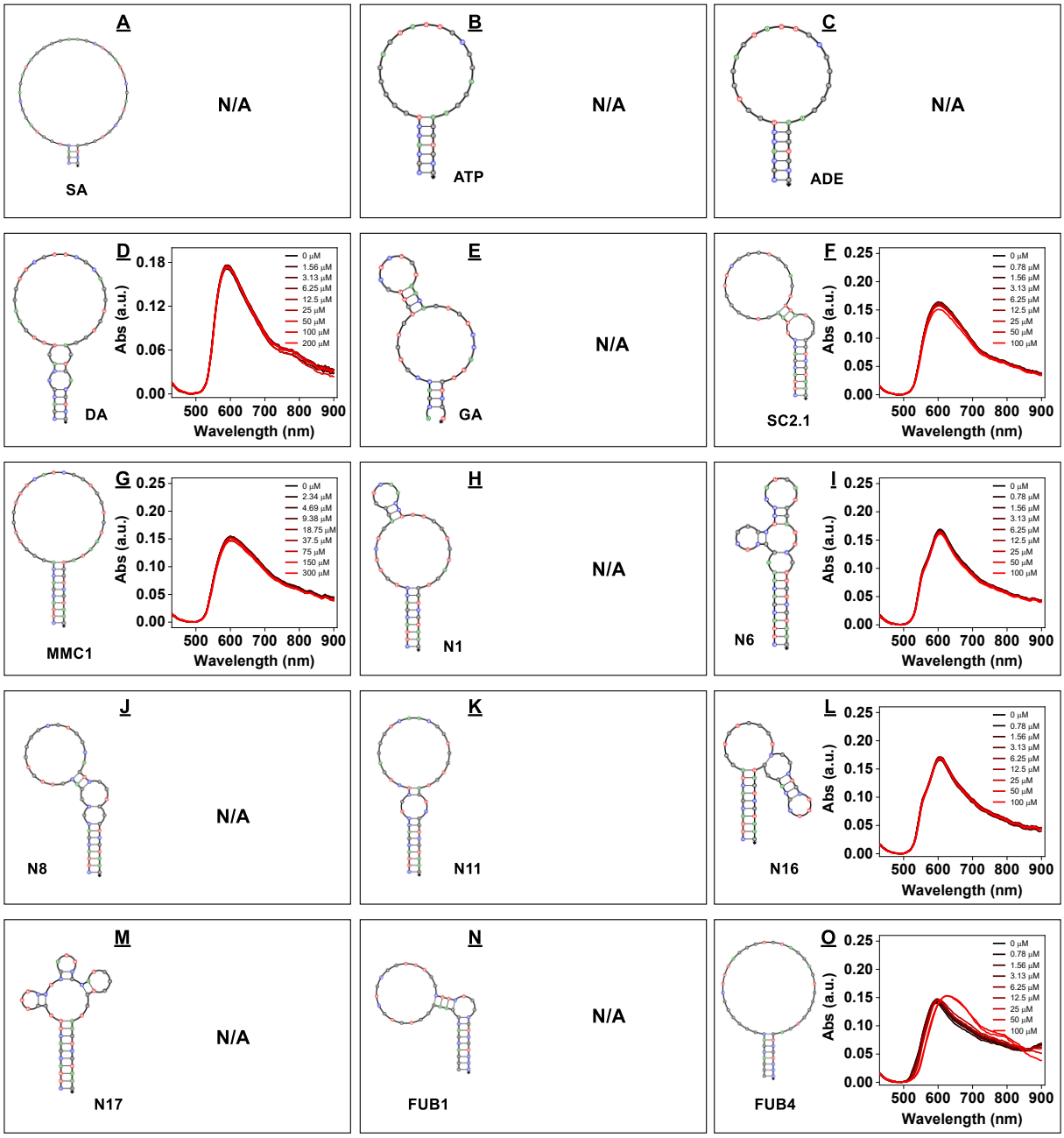

Figure S25 (continued). Absorbance spectra of 4 μM Cy7 in the presence of different targets at various concentrations. (**A**) serotonin, (**B**) ATP, (**C**) adenosine, (**D**) dopamine, (**E**) glucose, (**F**) MDPV, (**G**) mephedrone, (**H-M**) cocaine and (**N-O**) AB-FUBINACA. N/A indicated that no target control experiments were performed for that aptamer since no target-induced dye-displacement was observed. Black-to-red color gradient represents increasing concentrations of target.

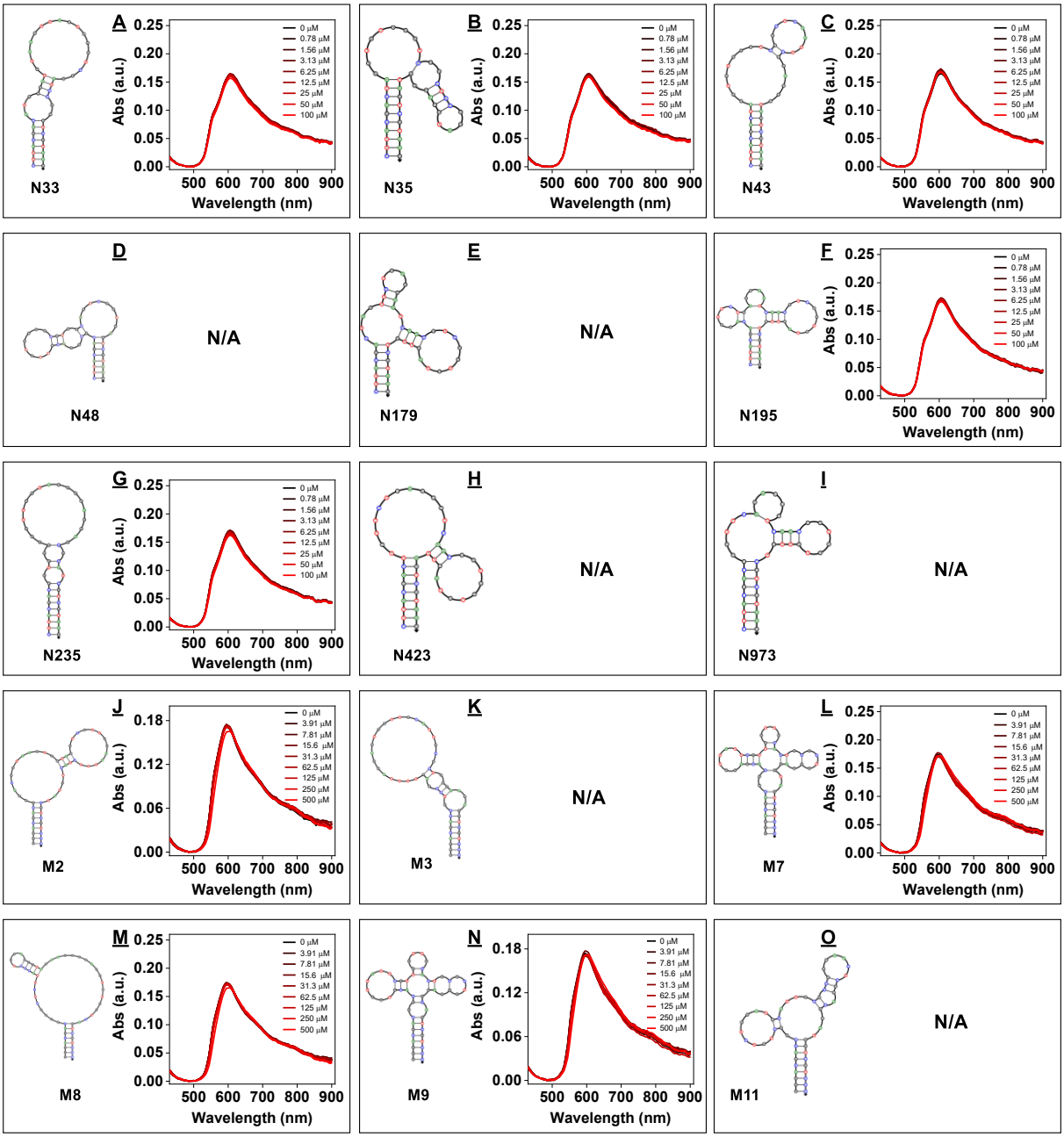

Figure S25 (continued). Absorbance spectra of 4 μM Cy7 in the presence of different targets at various concentrations. (**A-I**) cocaine and (**J-O**) (+)-methamphetamine. N/A indicated that no target control experiments were performed for that aptamer since no target-induced dye-displacement was observed. Black-to-red color gradient represents increasing concentrations of target.

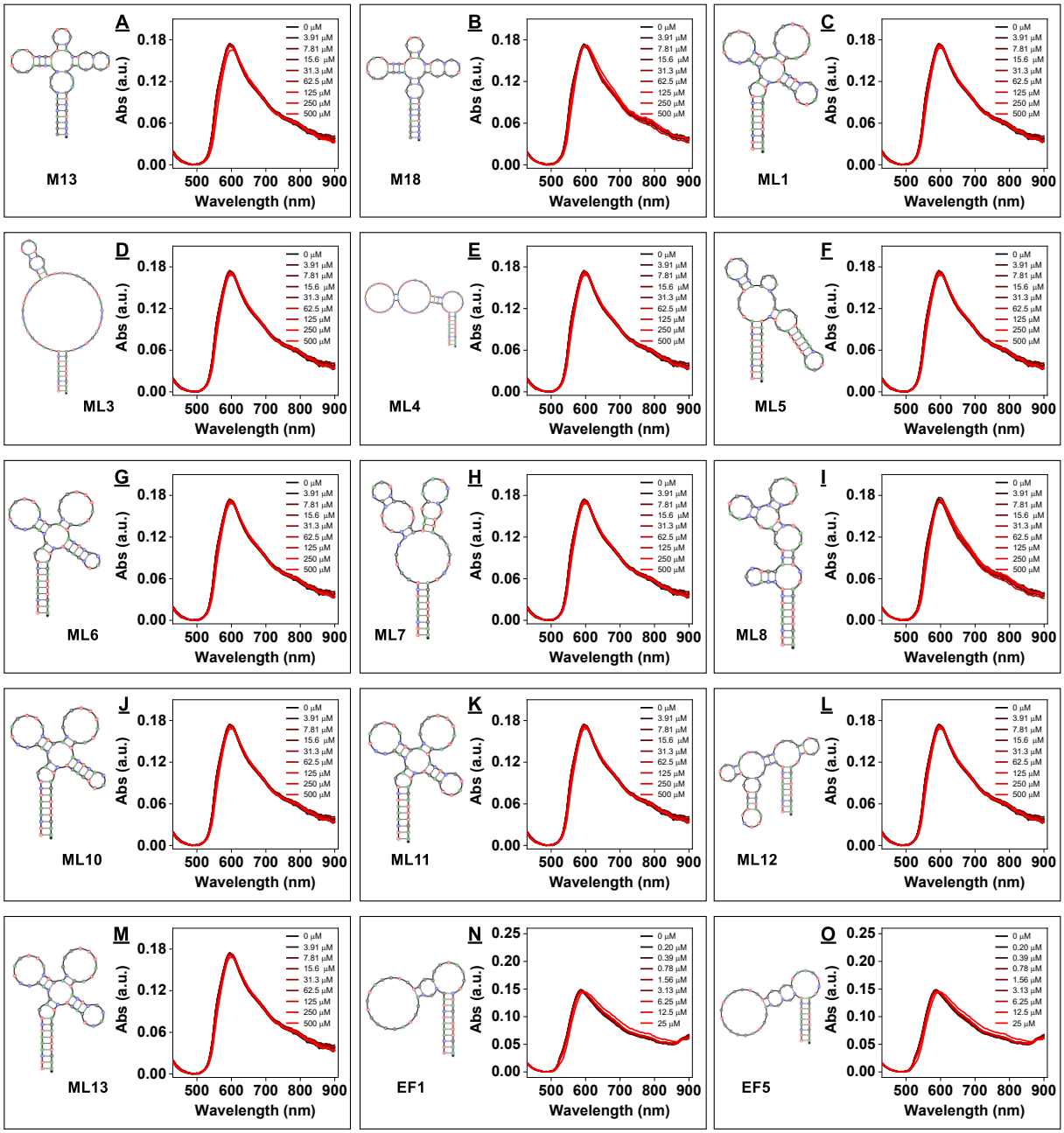

Figure S25 (continued). Absorbance spectra of 4 μM Cy7 in the presence of different targets at various concentrations. (**A-M**) (+)-methamphetamine and (**N-O**) AB-FUBINACA. N/A indicated that no target control experiments were performed for that aptamer since no target-induced dye-displacement was observed. Black-to-red color gradient represents increasing concentrations of target.

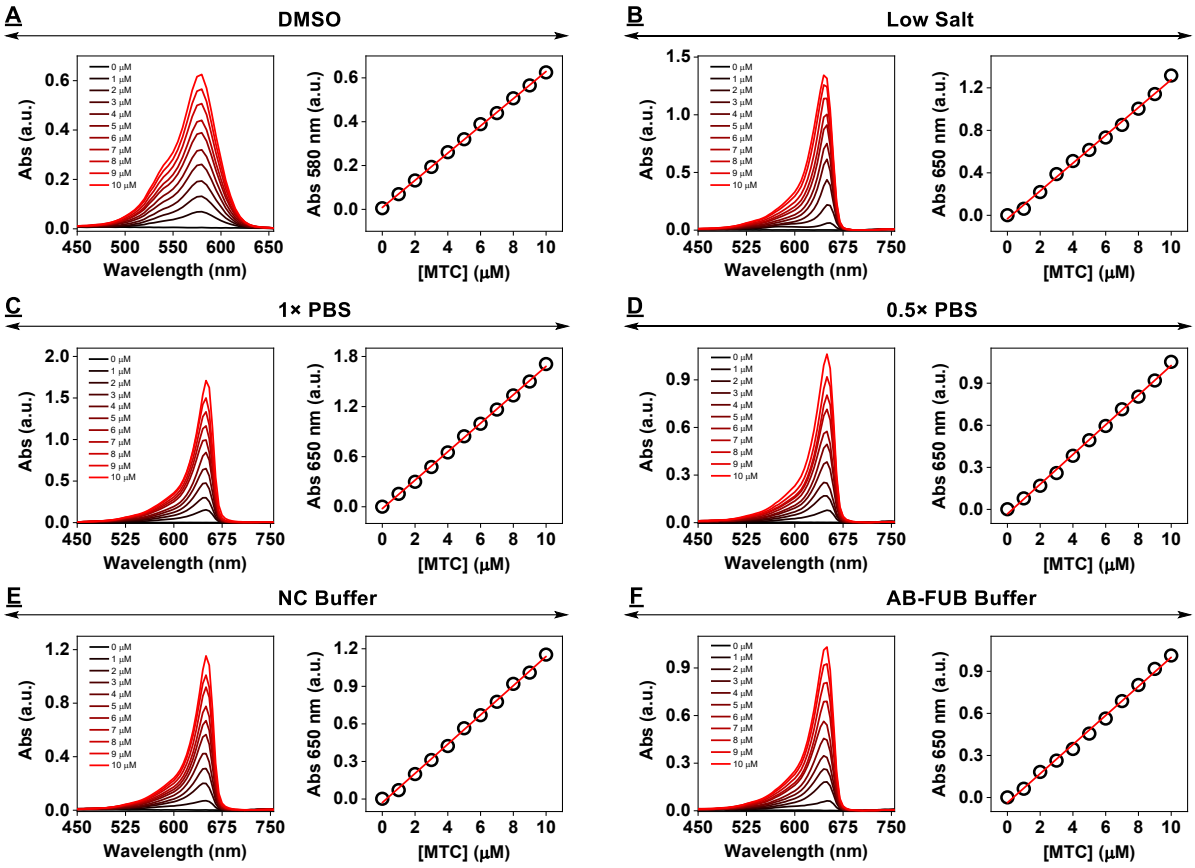

Figure S26. Optical properties of MTC under different experimental conditions. Absorbance spectra and calibration curve of MTC in (**A**) 100% DMSO, (**B**) low salt buffer (10 mM Tris (pH 7.4), 20 mM NaCl, 0.5 mM $MgCl_2$), (**C**) 1×PBS (1 × PBS (pH 7.4), 1 mM $MgCl_2$), (**D**) 0.5 ×PBS (0.5 × PBS (pH 7.4), 2 mM $MgCl_2$,), (**E**) NC buffer (20 mM Tris (pH 7.4), 140 mM NaCl, 4 mM KCl, 2 mM $MgCl_2$) and (**F**) AB-FUB buffer (10 mM Tris (pH 7.4), 137 mM NaCl, 2.7 mM KCl, 1 mM $MgCl_2$). All buffer formulations included 1% (v/v) DMSO for (A-E) or 3% (v/v) DMSO for (F) and 0.01% (v/v) SDS.

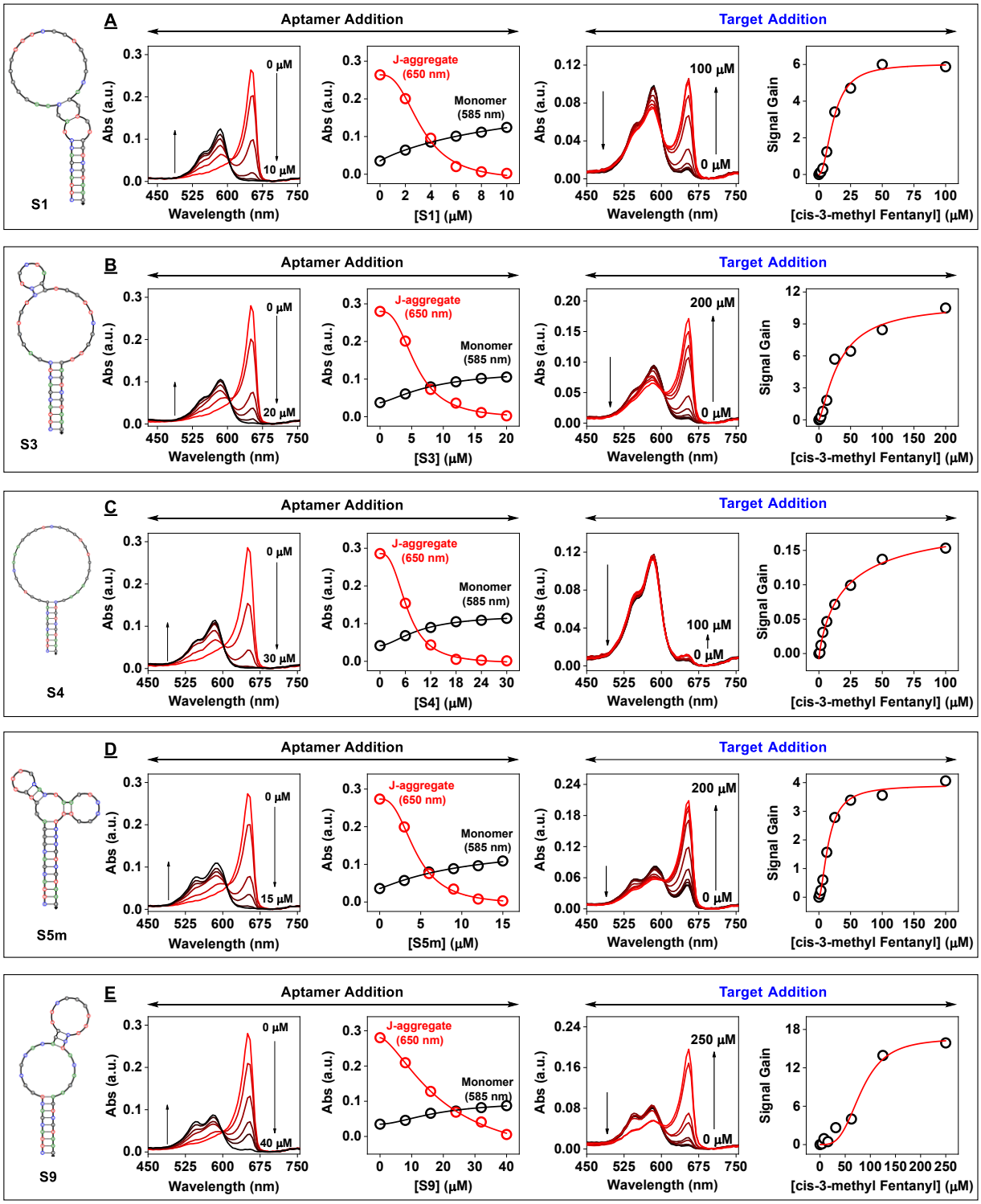

Figure S27. Target detection based on aptamer-based MTC displacement assay. For each panel, from left to right are: Secondary structure of the aptamer predicted by NUPACK; 'aptamer addition', which presents the absorbance spectra of 2.5 μM MTC with various concentrations of aptamer and a plot of MTC monomer and J-aggregate peak absorbance (respectively at 585 nm and 650 nm) against aptamer concentration; and 'target addition', which presents the absorption spectra of solutions containing aptamer-MTC complex challenged with various concentrations of target as well as plot depicting the calibration curve for target detection. (**A**) S1, (**B**) S3, (**C**) S4, (**D**) S5m and (**E**) S9.

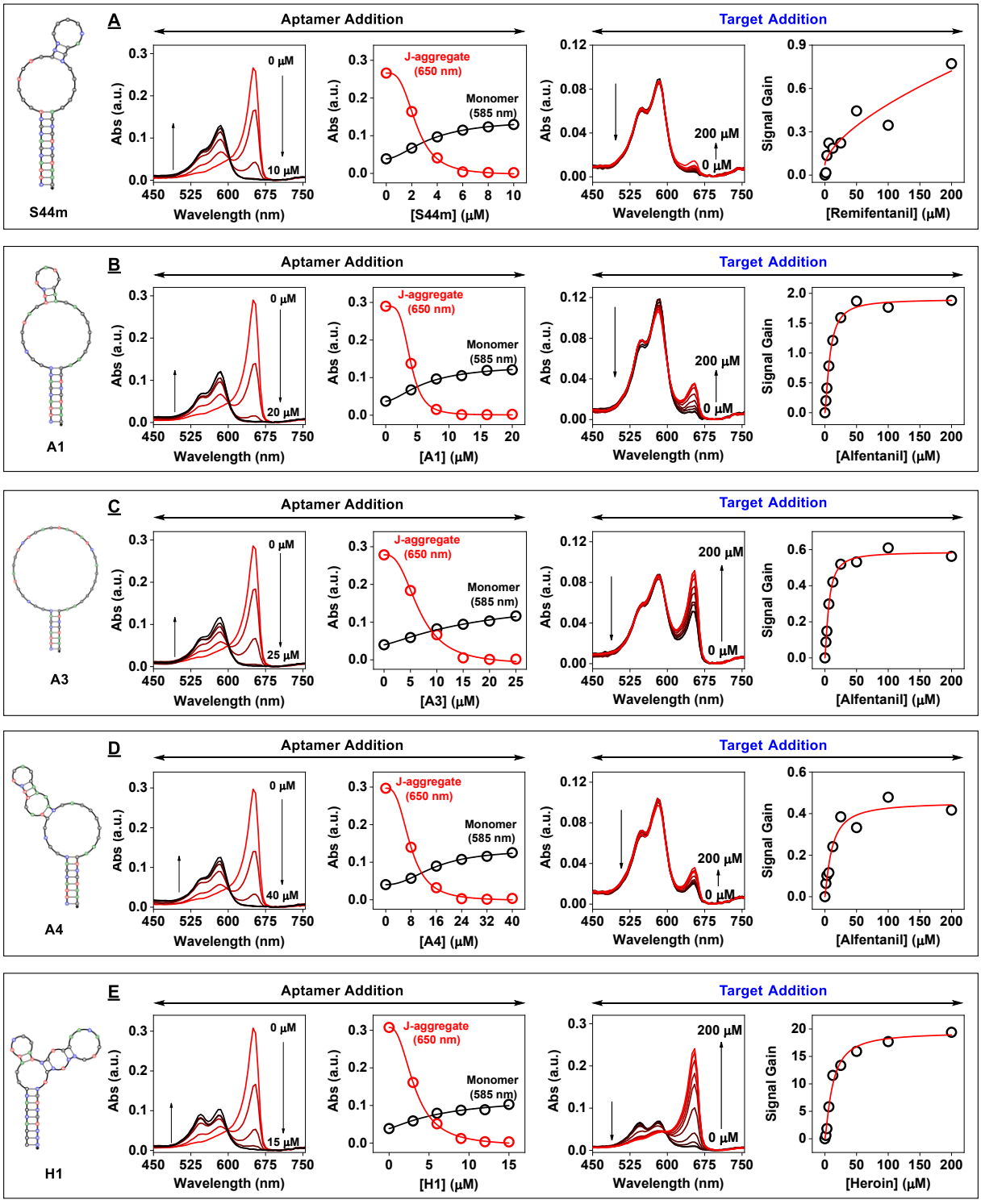

Figure S28. Target detection based on aptamer-based MTC displacement assay. For each panel, from left to right are: Secondary structure of the aptamer predicted by NUPACK; 'aptamer addition', which presents the absorbance spectra of 2.5 μM MTC with various concentrations of aptamer and a plot of MTC monomer and J-aggregate peak absorbance (respectively at 585 nm and 650 nm) against aptamer concentration; and 'target addition', which presents the absorption spectra of solutions containing aptamer-MTC complex challenged with various concentrations of target as well as plot depicting the calibration curve for target detection. (**A**) S44m, (**B**) A1, (**C**) A3, (**D**) A4 and (**E**) H1.

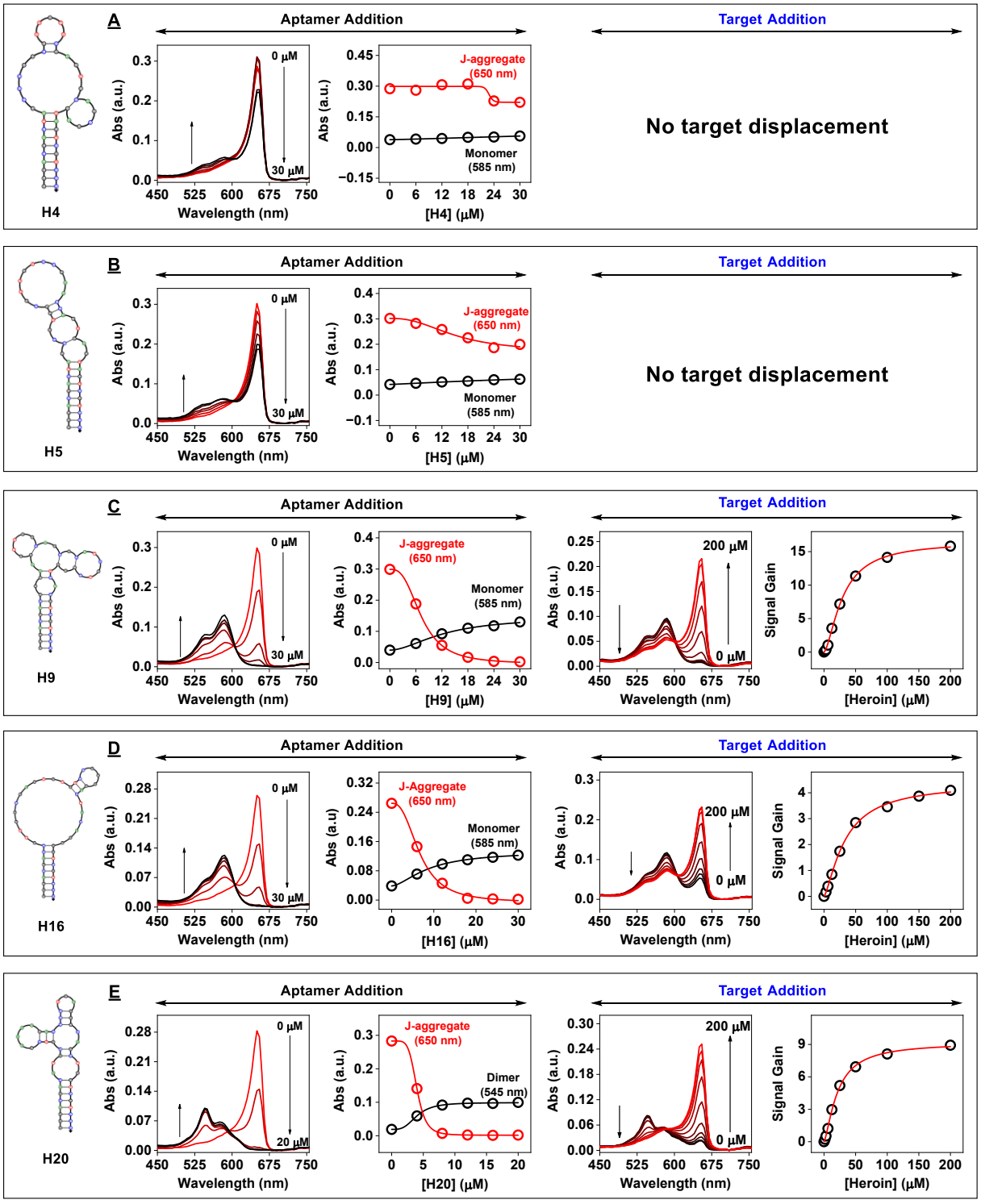

Figure S29. Target detection based on aptamer-based MTC displacement assay. For each panel, from left to right are: Secondary structure of the aptamer predicted by NUPACK; 'aptamer addition', which presents the absorbance spectra of 2.5 μM MTC with various concentrations of aptamer and a plot of MTC monomer or dimer and J-aggregate peak absorbance (respectively at 585 nm, 545 nm, and 650 nm) against aptamer concentration; and 'target addition', which presents the absorption spectra of solutions containing aptamer-MTC complex challenged with various concentrations of target as well as plot depicting the target calibration curve. (**A**) H4, (**B**) H5, (**C**) H9, (**D**) H16 and (**E**) H20.

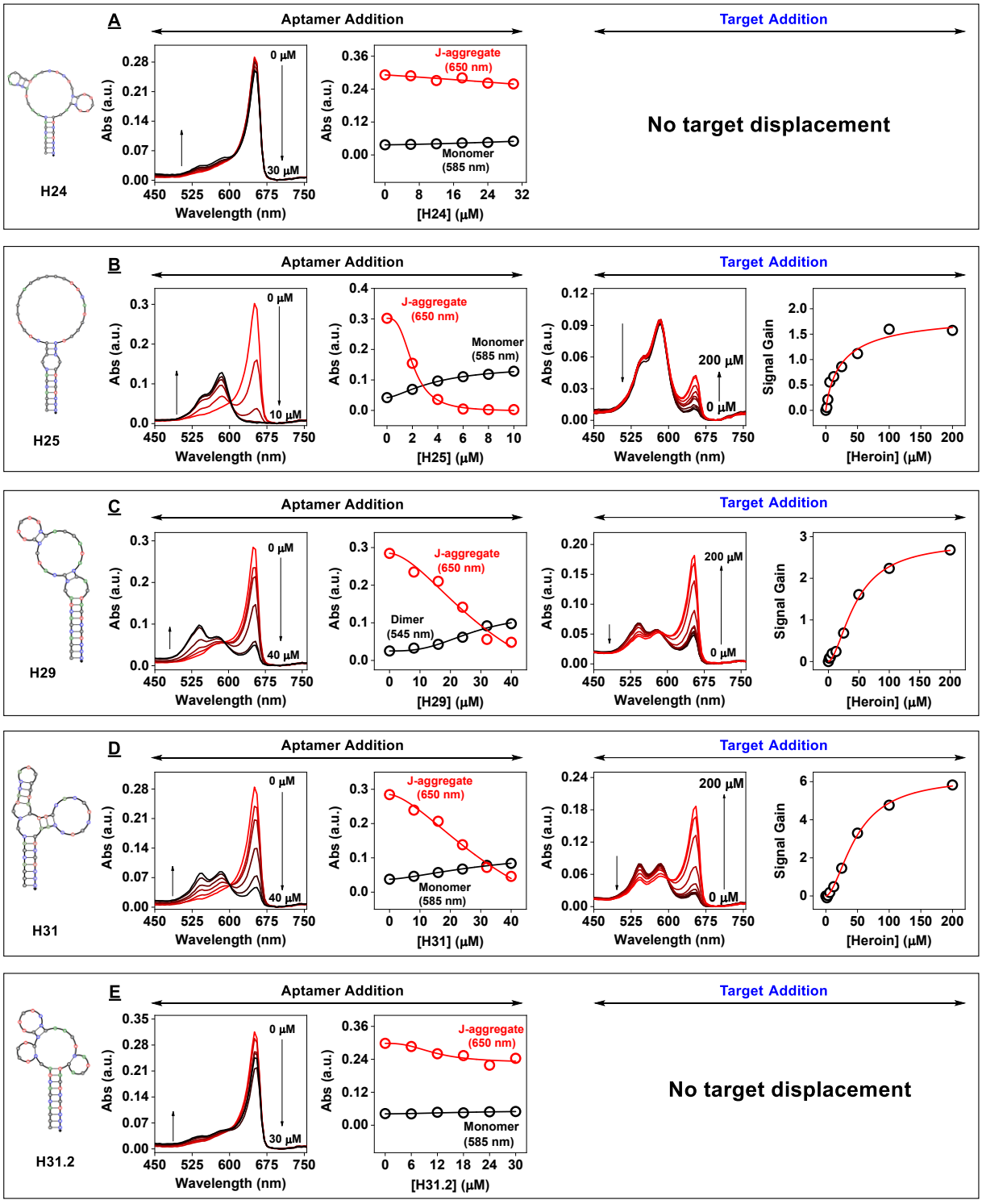

Figure S30. Target detection based on aptamer-based MTC displacement assay. For each panel, from left to right are: Secondary structure of the aptamer predicted by NUPACK; 'aptamer addition', which presents the absorbance spectra of 2.5 μM MTC with various concentrations of aptamer and a plot of MTC monomer, dimer and J-aggregate peak absorbance (respectively at 585 nm, 545 nm and 650 nm) against aptamer concentration; and 'target addition', which presents the absorption spectra of solutions containing aptamer-MTC complex challenged with various concentrations of target as well as plot depicting the target calibration curve. (**A**) H24, (**B**) H25, (**C**) H29, (**D**) H31 and (**E**) H31.2.

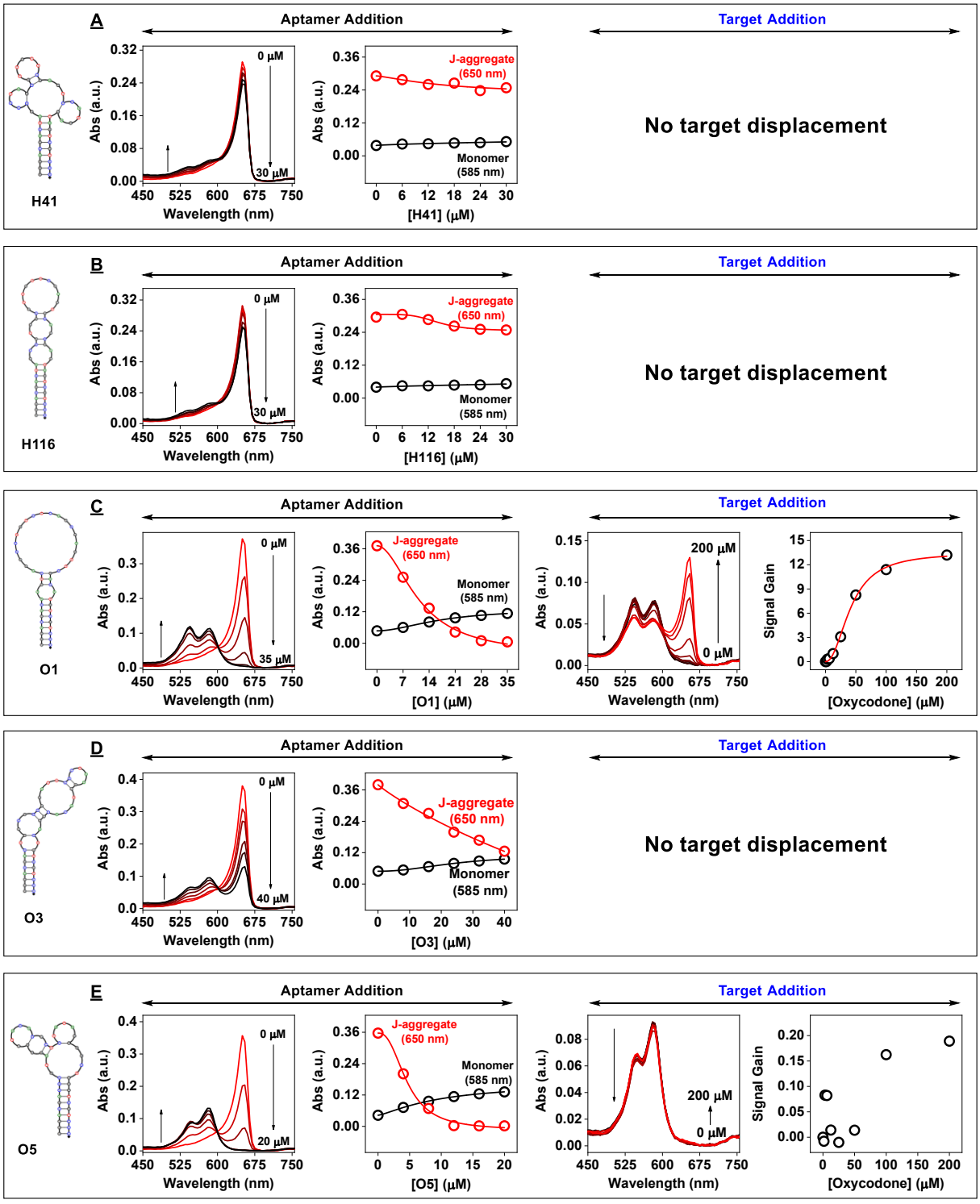

Figure S31. Target detection based on aptamer-based MTC displacement assay. For each panel, from left to right are: Secondary structure of the aptamer predicted by NUPACK; 'aptamer addition', which presents the absorbance spectra of 2.5 μM MTC with various concentrations of aptamer and a plot of MTC monomer and J-aggregate peak absorbance (respectively at 585 nm and 650 nm) against aptamer concentration; and 'target addition', which presents the absorption spectra of solutions containing aptamer-MTC complex challenged with various concentrations of target as well as plot depicting the calibration curve for target detection. (**A**) H41, (**B**) H116, (**C**) O1, (**D**) O3 and (**E**) O5.

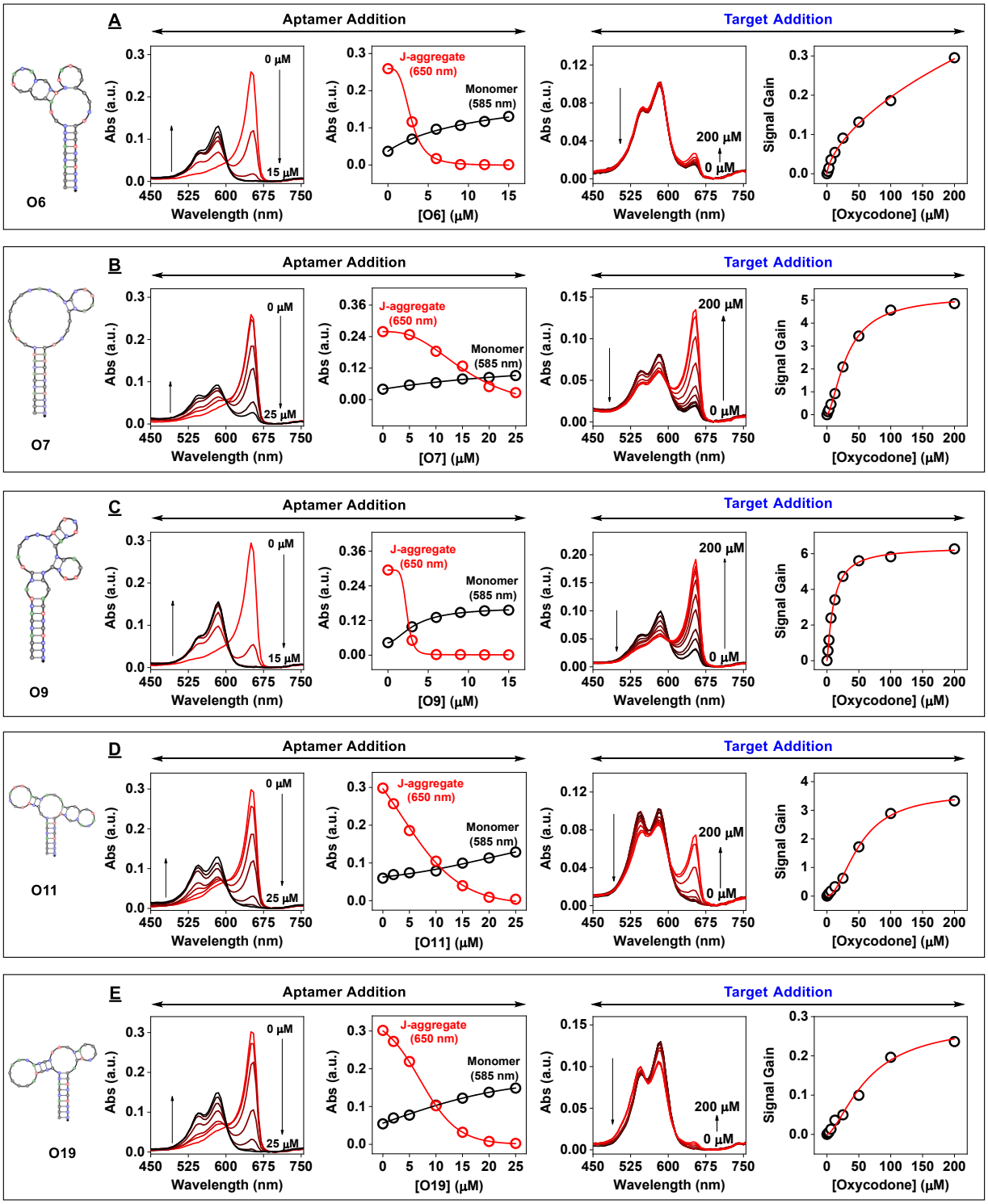

Figure S32. Target detection based on aptamer-based MTC displacement assay. For each panel, from left to right are: Secondary structure of the aptamer predicted by NUPACK; 'aptamer addition', which presents the absorbance spectra of 2.5 µM MTC with various concentrations of aptamer and a plot of MTC monomer and J-aggregate peak absorbance (respectively at 585 nm and 650 nm) against aptamer concentration; and 'target addition', which presents the absorption spectra of solutions containing aptamer-MTC complex challenged with various concentrations of target as well as plot depicting the calibration curve for target detection. (**A**) O6, (**B**) O7, (**C**) O9, (**D**) O11 and (**E**) O19.

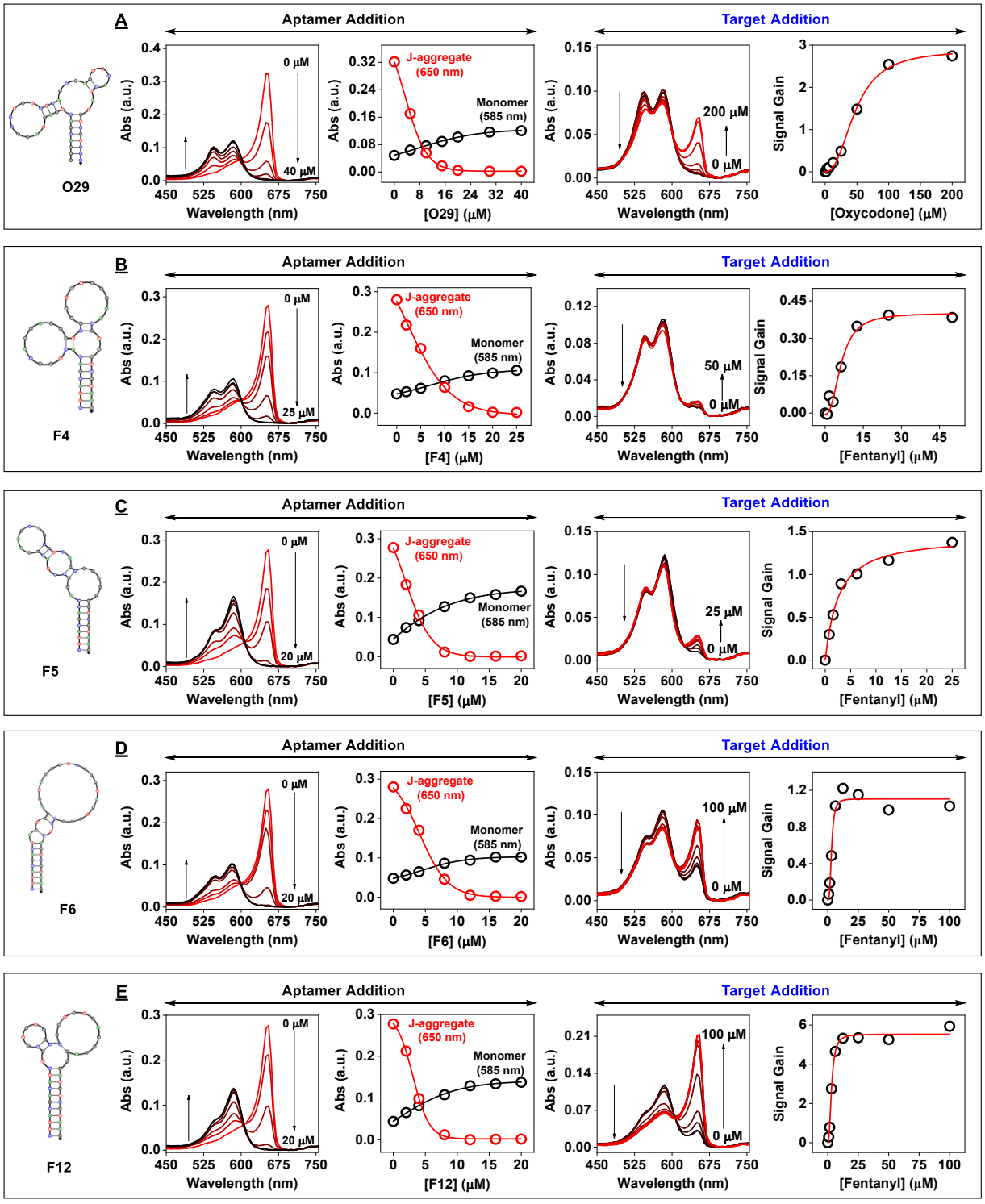

Figure S33. Target detection based on aptamer-based MTC displacement assay. For each panel, from left to right are: Secondary structure of the aptamer predicted by NUPACK; 'aptamer addition', which presents the absorbance spectra of 2.5 μM MTC with various concentrations of aptamer and a plot of MTC monomer and J-aggregate peak absorbance (respectively at 585 nm and 650 nm) against aptamer concentration; and 'target addition', which presents the absorption spectra of solutions containing aptamer-MTC complex challenged with various concentrations of target as well as plot depicting the calibration curve for target detection. (**A**) O29, (**B**) F4, (**C**) F5, (**D**) F6 and (**E**) F12.

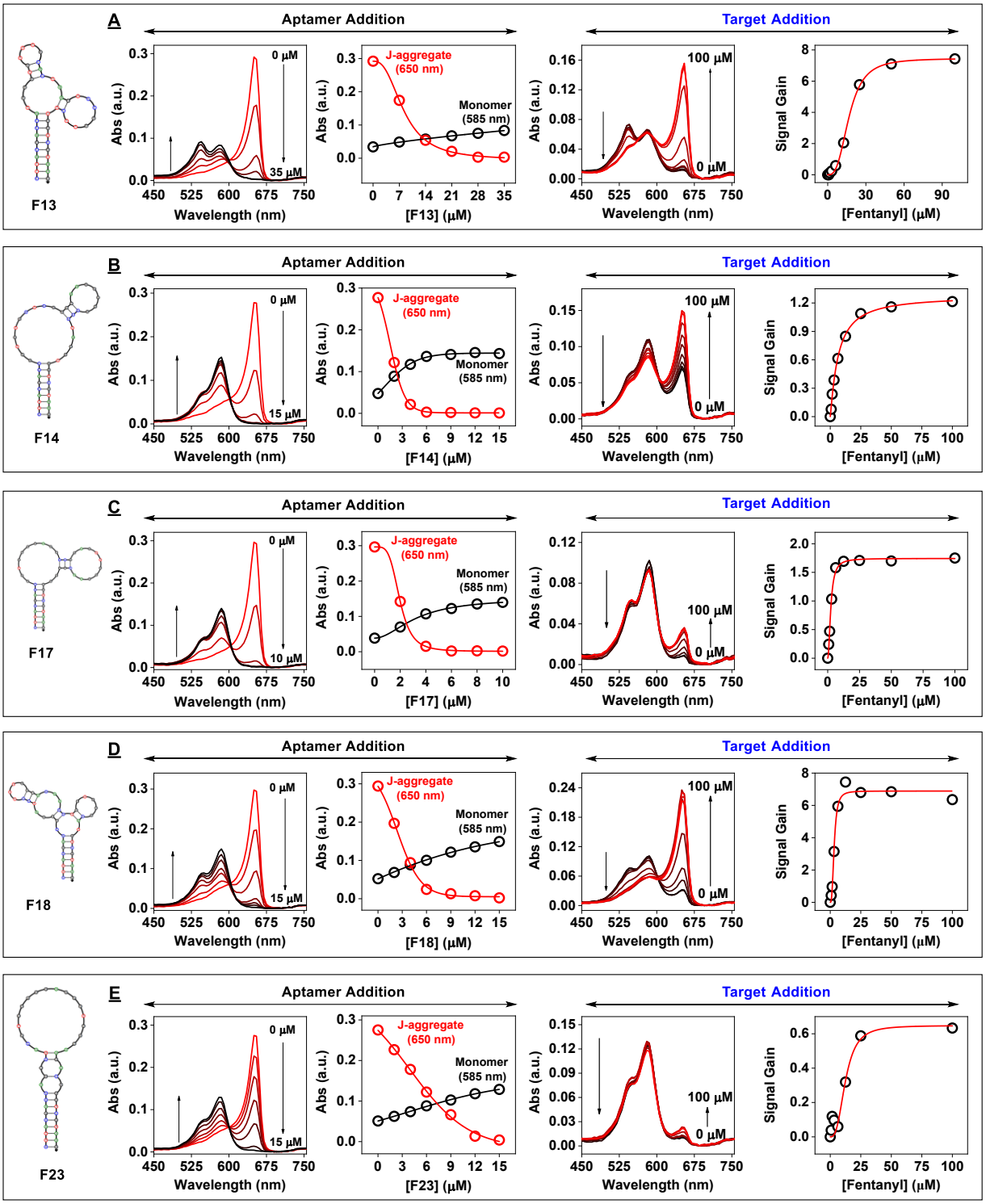

Figure S34. Target detection based on aptamer-based MTC displacement assay. For each panel, from left to right are: Secondary structure of the aptamer predicted by NUPACK; 'aptamer addition', which presents the absorbance spectra of 2.5 µM MTC with various concentrations of aptamer and a plot of MTC monomer and J-aggregate peak absorbance (respectively at 585 nm and 650 nm) against aptamer concentration; and 'target addition', which presents the absorption spectra of solutions containing aptamer-MTC complex challenged with various concentrations of target as well as plot depicting the calibration curve for target detection. (**A**) F13, (**B**) F14, (**C**) F17, (**D**) F18 and (**E**) F23.

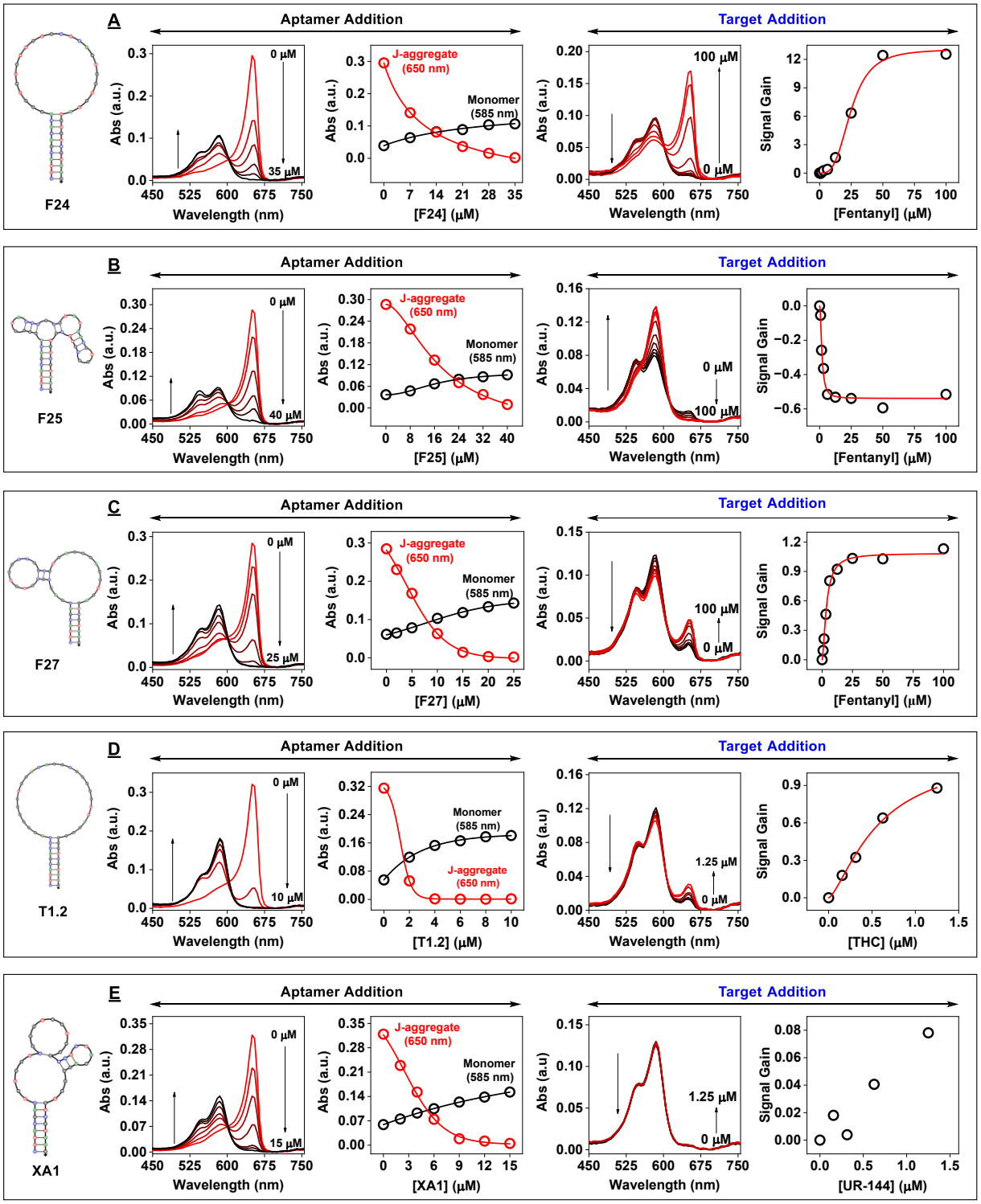

Figure S35. Target detection based on aptamer-based MTC displacement assay. For each panel, from left to right are: Secondary structure of the aptamer predicted by NUPACK; 'aptamer addition', which presents the absorbance spectra of 2.5 µM MTC with various concentrations of aptamer and a plot of MTC monomer and J-aggregate peak absorbance (respectively at 585 nm and 650 nm) against aptamer concentration; and 'target addition', which presents the absorption spectra of solutions containing aptamer-MTC complex challenged with various concentrations of target as well as plot depicting the calibration curve for target detection. (**A**) F24, (**B**) F25, (**C**) F27, (**D**) T1.2 and (**E**) XA1.

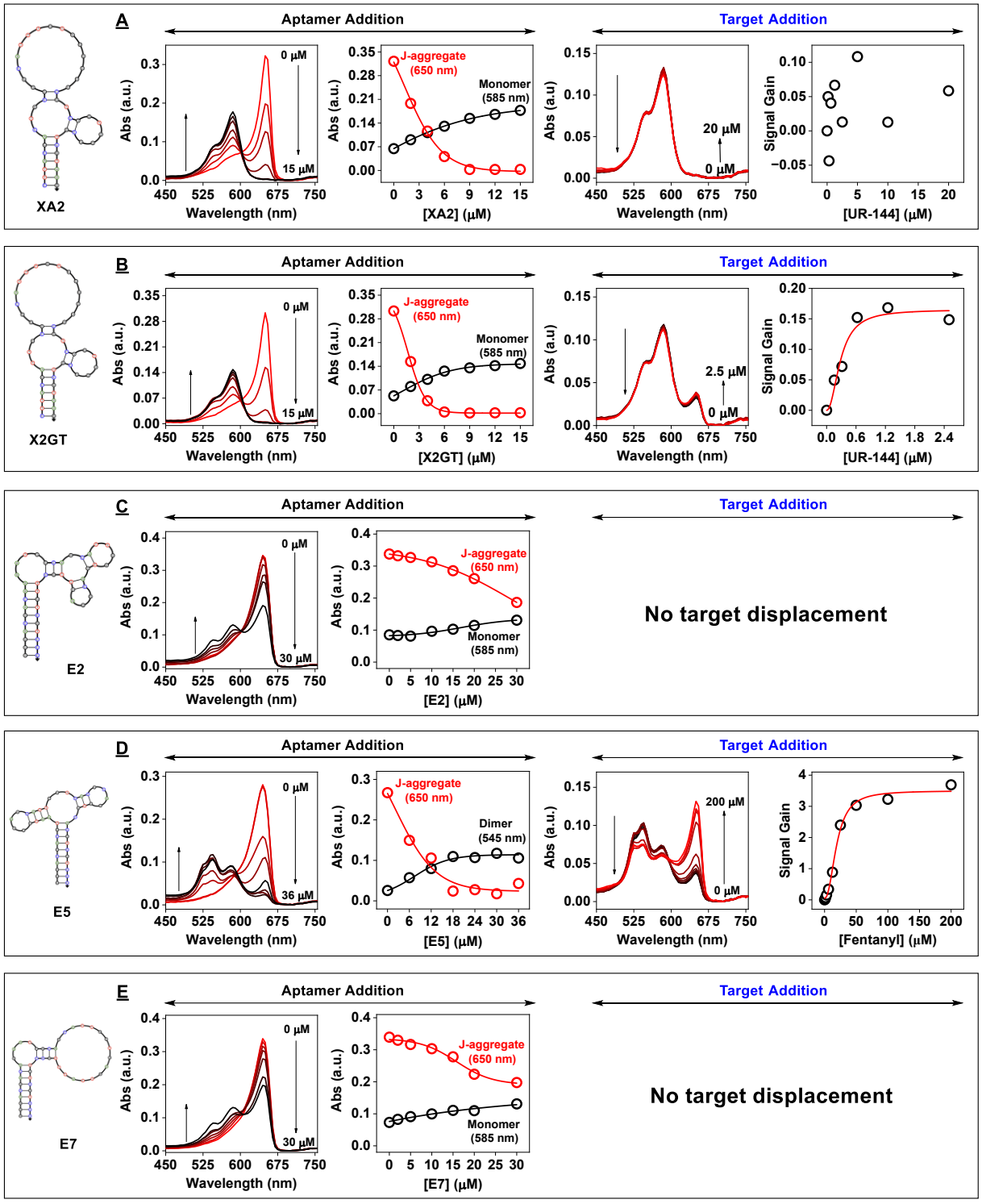

Figure S36. Target detection based on aptamer-based MTC displacement assay. For each panel, from left to right are: Secondary structure of the aptamer predicted by NUPACK; 'aptamer addition', which presents the absorbance spectra of 2.5 μM MTC with various concentrations of aptamer and a plot of MTC monomer or dimer and J-aggregate peak absorbance (respectively at 585 nm, 545 nm, and 650 nm) against aptamer concentration; and 'target addition', which presents the absorption spectra of solutions containing aptamer-MTC complex challenged with various concentrations of target as well as plot depicting the target calibration curve. (**A**) XA2, (**B**) X2GT, (**C**) E2, (**D**) E5 and (**E**) E7.

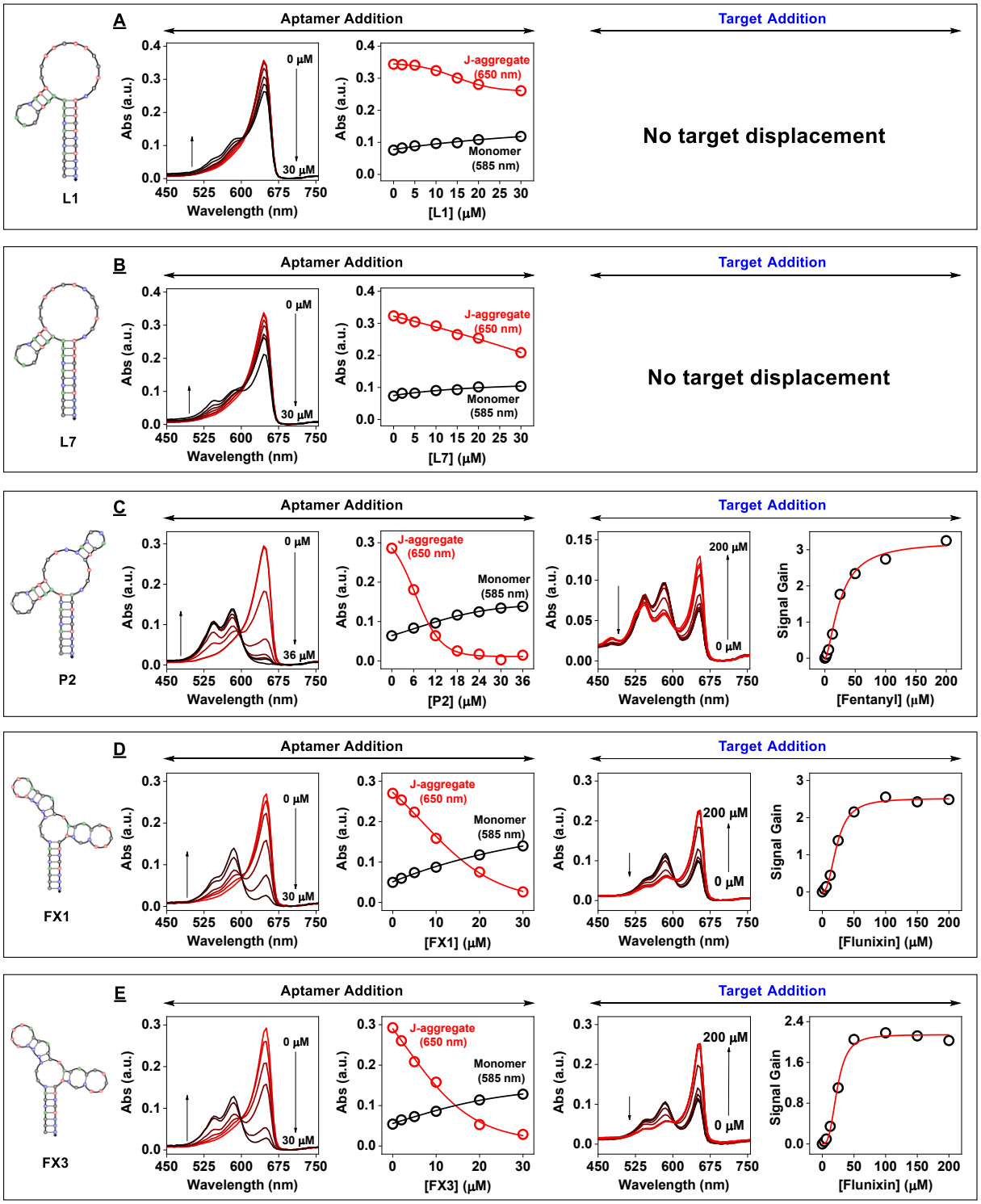

Figure S37. Target detection based on aptamer-based MTC displacement assay. For each panel, from left to right are: Secondary structure of the aptamer predicted by NUPACK; 'aptamer addition', which presents the absorbance spectra of 2.5 μM MTC with various concentrations of aptamer and a plot of MTC monomer and J-aggregate peak absorbance (respectively at 585 nm and 650 nm) against aptamer concentration; and 'target addition', which presents the absorption spectra of solutions containing aptamer-MTC complex challenged with various concentrations of target as well as plot depicting the calibration curve for target detection. (**A**) L1, (**B**) L7, (**C**) P2, (**D**) FX1 and (**E**) FX3.

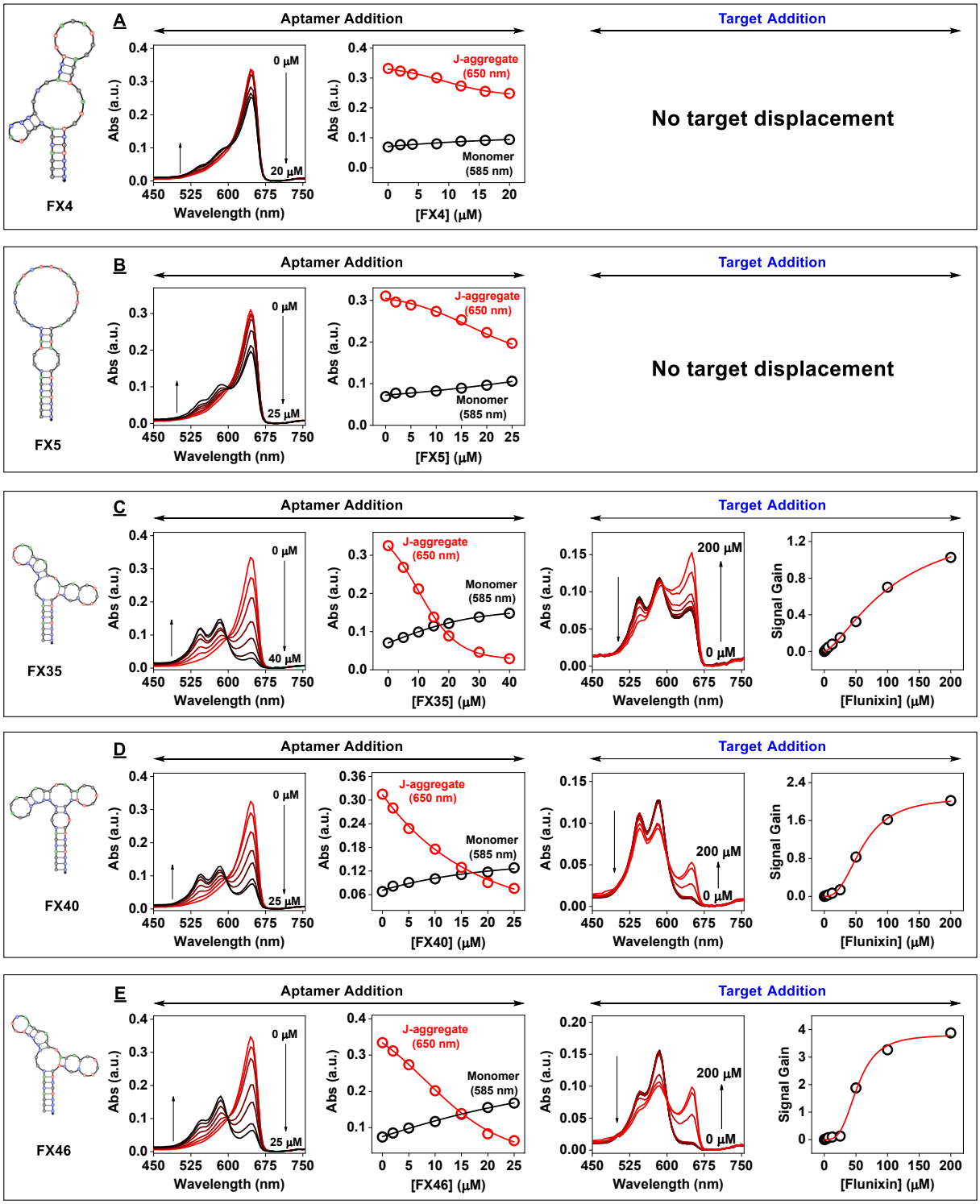

Figure S38. Target detection based on aptamer-based MTC displacement assay. For each panel, from left to right are: Secondary structure of the aptamer predicted by NUPACK; 'aptamer addition', which presents the absorbance spectra of 2.5 µM MTC with various concentrations of aptamer and a plot of MTC monomer and J-aggregate peak absorbance (respectively at 585 nm and 650 nm) against aptamer concentration; and 'target addition', which presents the absorption spectra of solutions containing aptamer-MTC complex challenged with various concentrations of target as well as plot depicting the calibration curve for target detection. (**A**) FX4, (**B**) FX5, (**C**) FX35, (**D**) FX40 and (**E**) FX46.

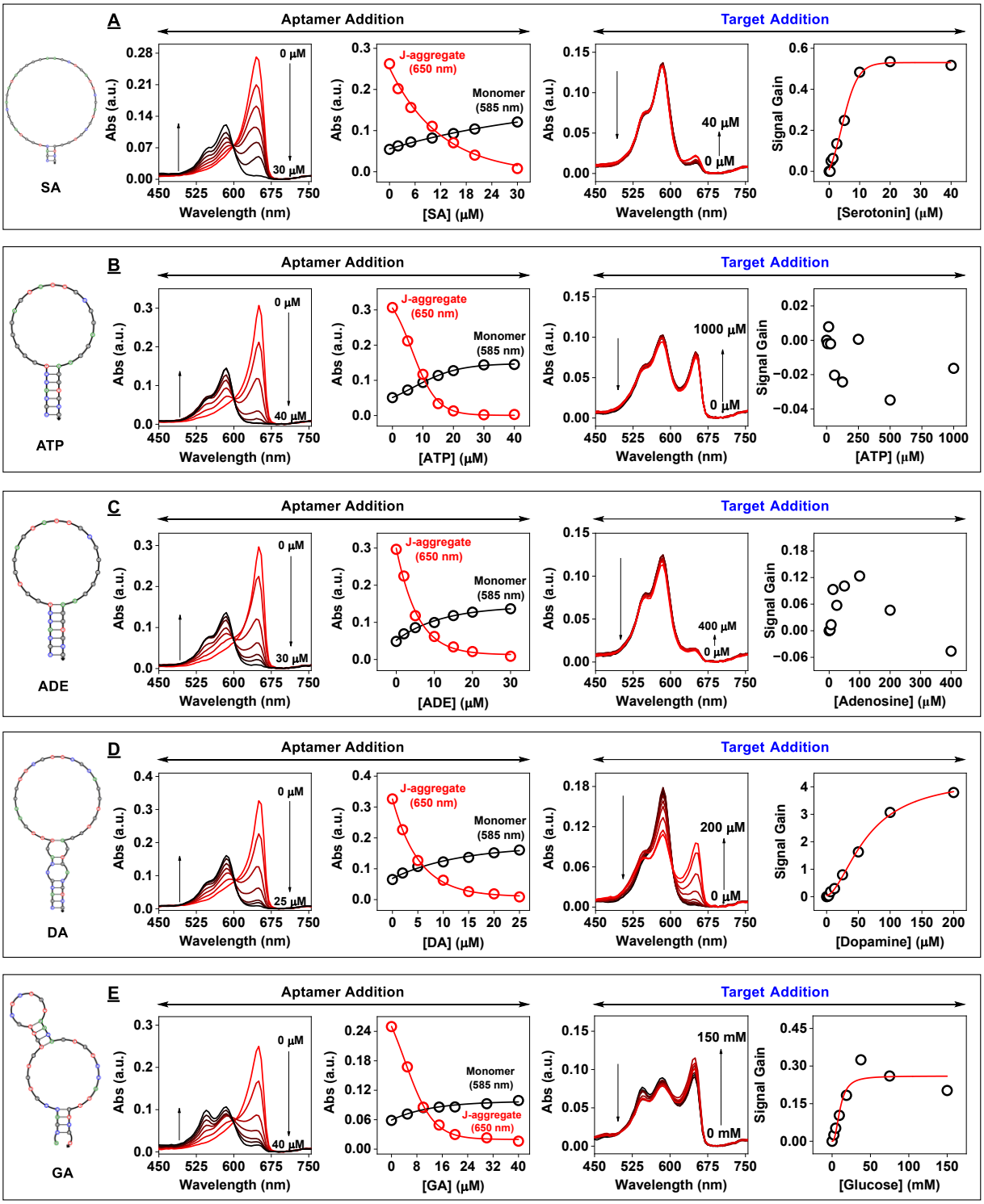

Figure S39. Target detection based on aptamer-based MTC displacement assay. For each panel, from left to right are: Secondary structure of the aptamer predicted by NUPACK; 'aptamer addition', which presents the absorbance spectra of 2.5 μM MTC with various concentrations of aptamer and a plot of MTC monomer and J-aggregate peak absorbance (respectively at 585 nm and 650 nm) against aptamer concentration; and 'target addition', which presents the absorption spectra of solutions containing aptamer-MTC complex challenged with various concentrations of target as well as plot depicting the calibration curve for target detection. (**A**) SA, (**B**) ATP, (**C**) ADE, (**D**) DA and (**E**) GA.

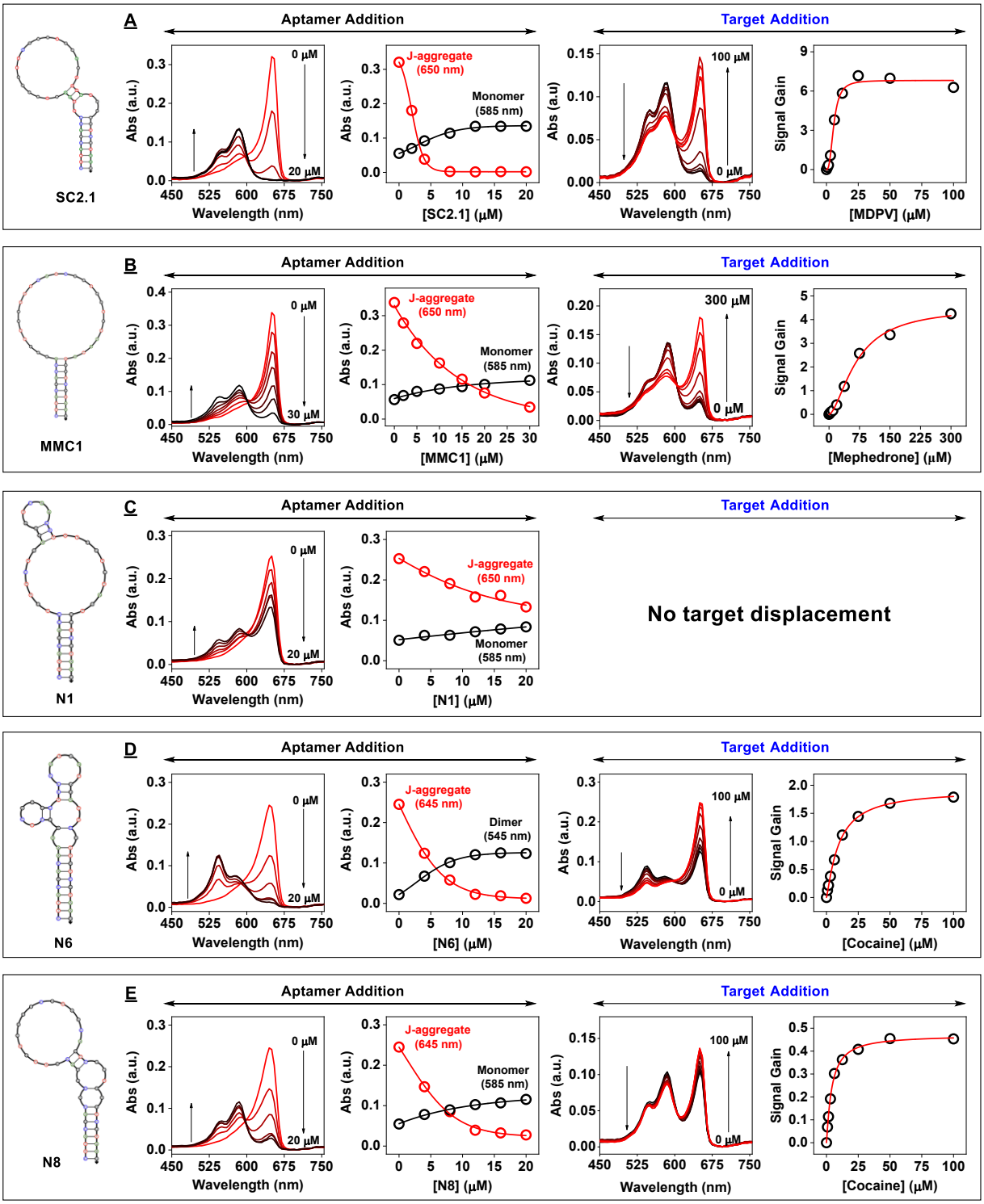

Figure S40. Target detection based on aptamer-based MTC displacement assay. For each panel, from left to right are: Secondary structure of the aptamer predicted by NUPACK; 'aptamer addition', which presents the absorbance spectra of 2.5 μM MTC with various concentrations of aptamer and a plot of MTC monomer or dimer and J-aggregate peak absorbance (respectively at 585 nm, 545 nm, and ~650 nm) against aptamer concentration; and 'target addition', which presents the absorption spectra of solutions containing aptamer-MTC complex challenged with various concentrations of target as well as plot depicting the target calibration curve. (**A**) SC2.1, (**B**) MMC1, (**C**) N1, (**D**) N6 and (**E**) N8.

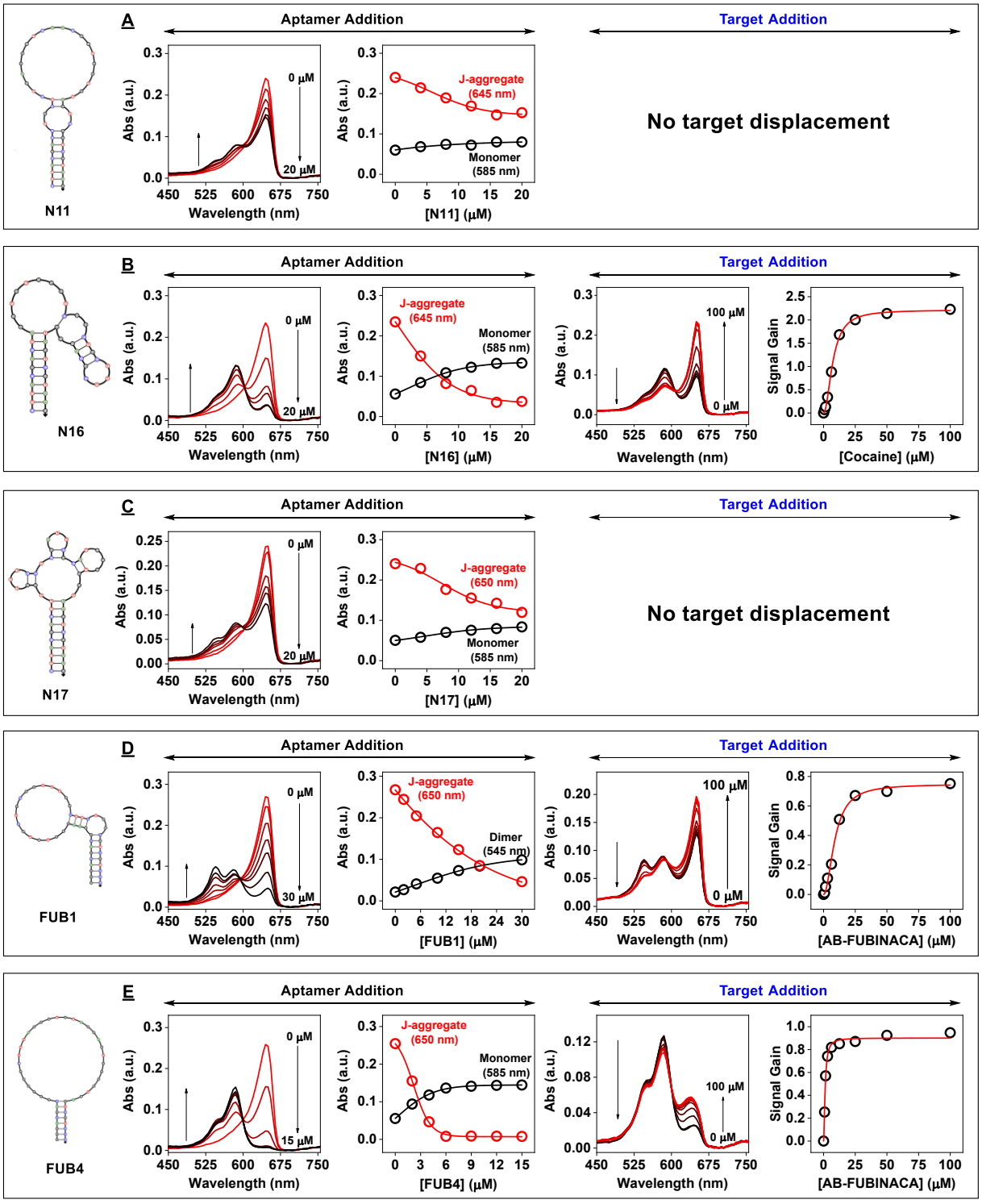

Figure S41. Target detection based on aptamer-based MTC displacement assay. For each panel, from left to right are: Secondary structure of the aptamer predicted by NUPACK; 'aptamer addition', which presents the absorbance spectra of 2.5 μM MTC with various concentrations of aptamer and a plot of MTC monomer or dimer and J-aggregate peak absorbance (respectively at 585 nm, 545 nm, and ~650 nm) against aptamer concentration; and 'target addition', which presents the absorption spectra of solutions containing aptamer-MTC complex challenged with various concentrations of target as well as plot depicting the target calibration curve. (**A**) N11, (**B**) N16, (**C**) N17, (**D**) FUB1 and (**E**) FUB4.

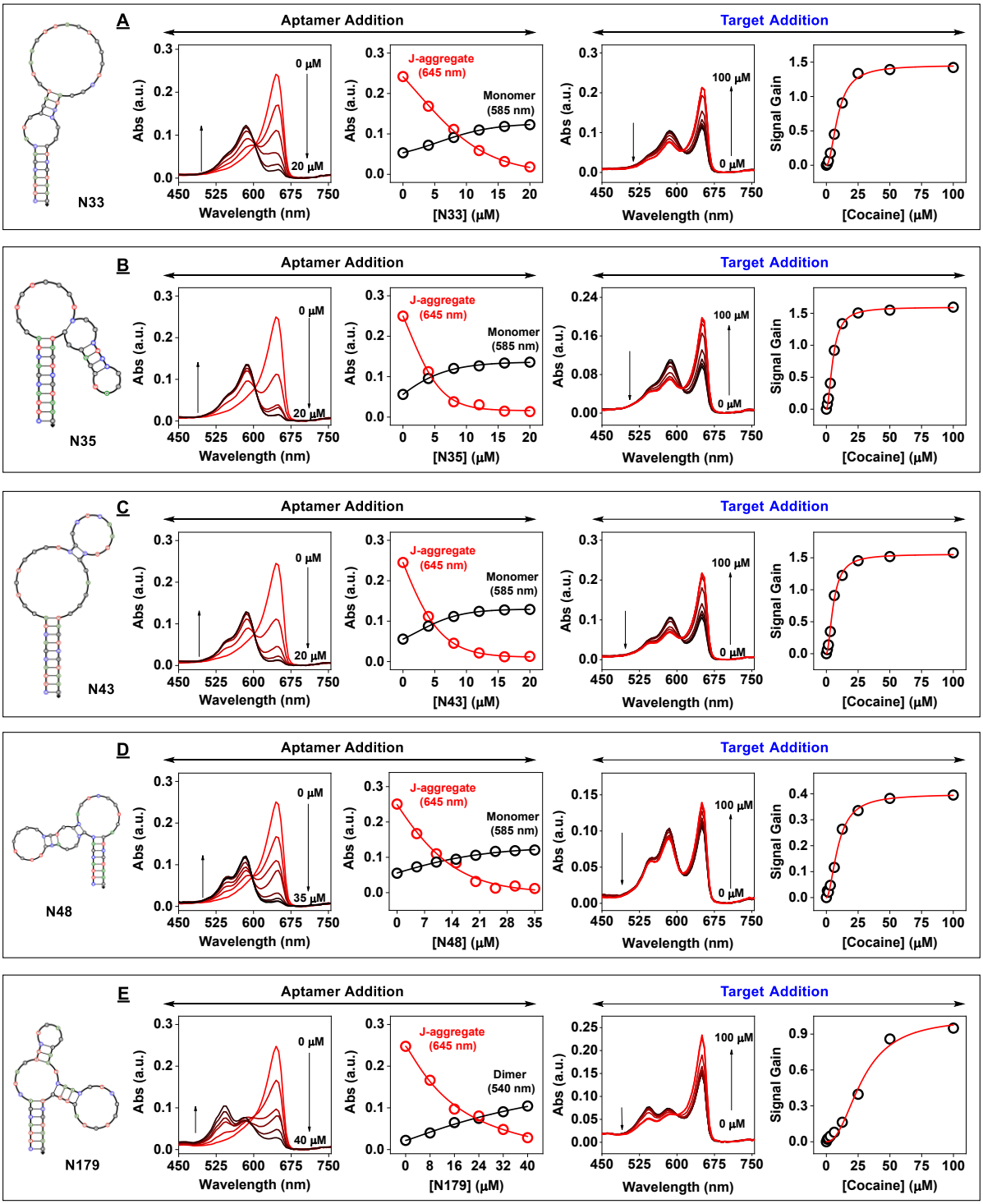

Figure S42. Target detection based on aptamer-based MTC displacement assay. For each panel, from left to right are: Secondary structure of the aptamer predicted by NUPACK; 'aptamer addition', which presents the absorbance spectra of 2.5 μM MTC with various concentrations of aptamer and a plot of MTC monomer or dimer and J-aggregate peak absorbance (respectively at 585 nm, 540 nm, and 645 nm) against aptamer concentration; and 'target addition', which presents the absorption spectra of solutions containing aptamer-MTC complex challenged with various concentrations of target as well as plot depicting the calibration curve for target detection. (**A**) N33, (**B**) N35, (**C**) N43, (**D**) N48 and (**E**) N179.

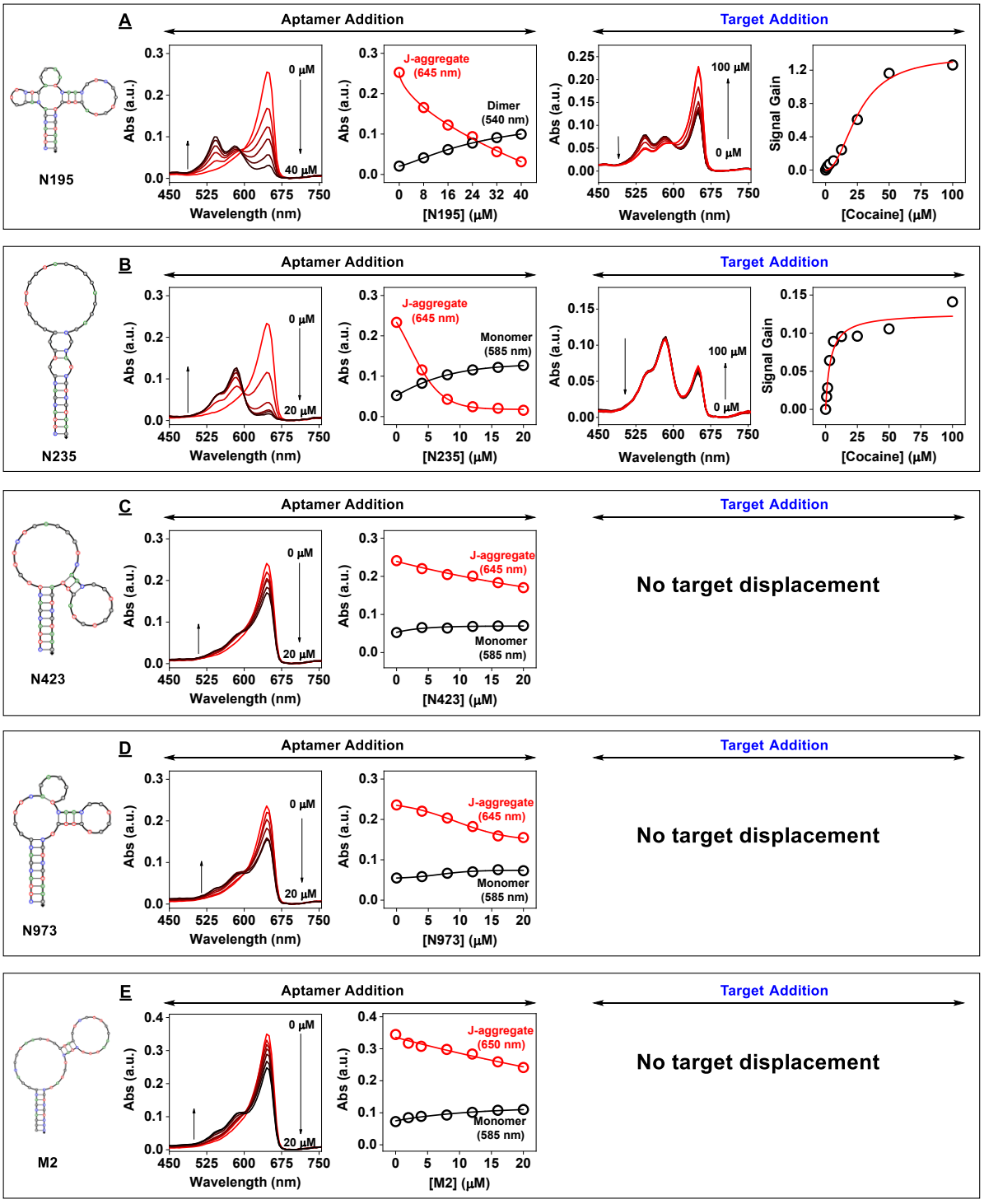

Figure S43. Target detection based on aptamer-based MTC displacement assay. For each panel, from left to right are: Secondary structure of the aptamer predicted by NUPACK; 'aptamer addition', which presents the absorbance spectra of 2.5 μM MTC with various concentrations of aptamer and a plot of MTC monomer or dimer and J-aggregate peak absorbance (respectively at 585 nm, 540 nm, and 645-650 nm) against aptamer concentration; and 'target addition', which presents the absorption spectra of solutions containing aptamer-MTC complex challenged with various concentrations of target as well as plot depicting the target calibration curve. (**A**) N195, (**B**) N235, (**C**) N423, (**D**) N973 and (**E**) M2.

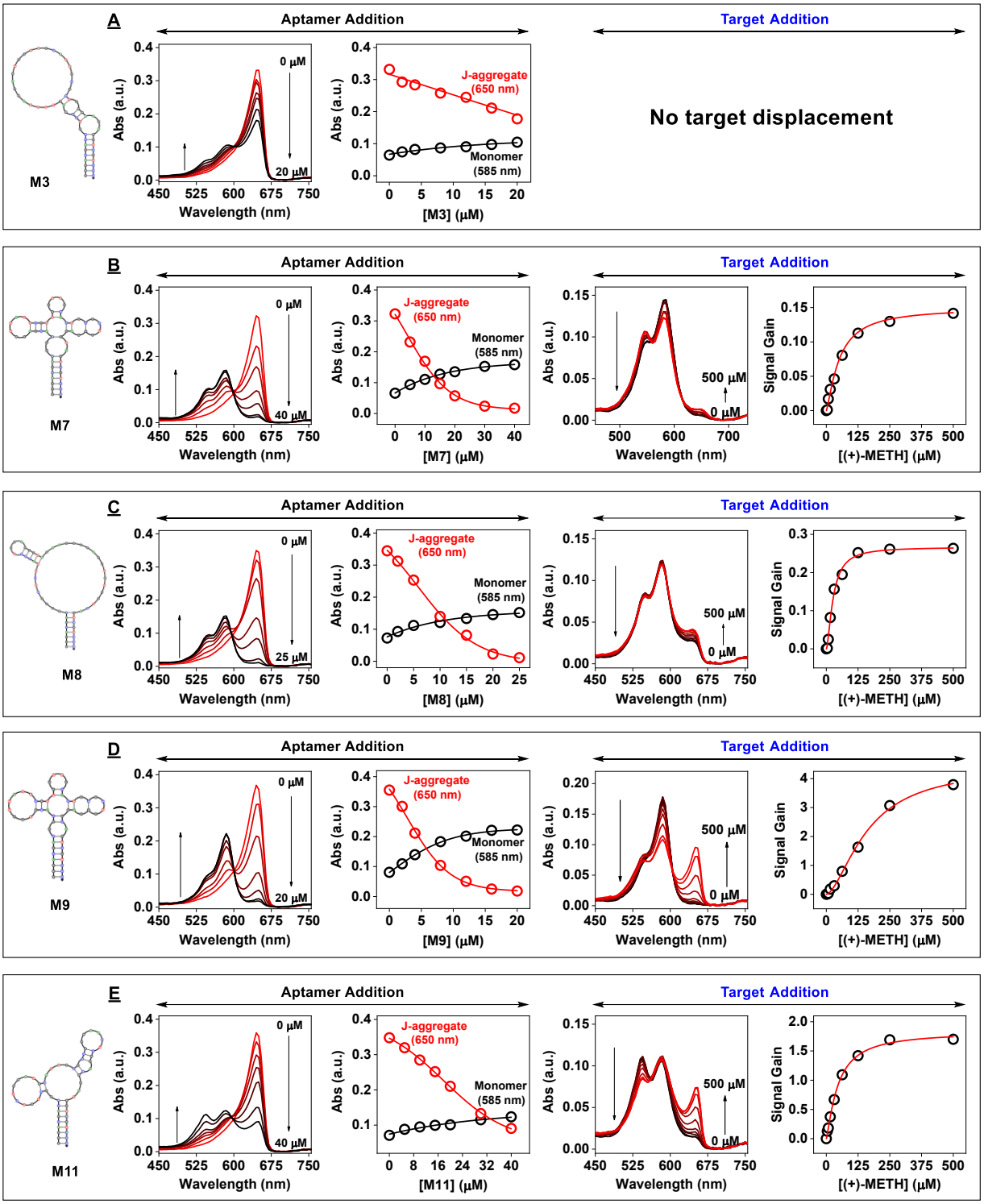

Figure S44. Target detection based on aptamer-based MTC displacement assay. For each panel, from left to right are: Secondary structure of the aptamer predicted by NUPACK; 'aptamer addition', which presents the absorbance spectra of 2.5 μM MTC with various concentrations of aptamer and a plot of MTC monomer and J-aggregate peak absorbance (respectively at 585 nm and 650 nm) against aptamer concentration; and 'target addition', which presents the absorption spectra of solutions containing aptamer-MTC complex challenged with various concentrations of target as well as plot depicting the calibration curve for target detection. (**A**) M3, (**B**) M7, (**C**) M8, (**D**) M9 and (**E**) M11.

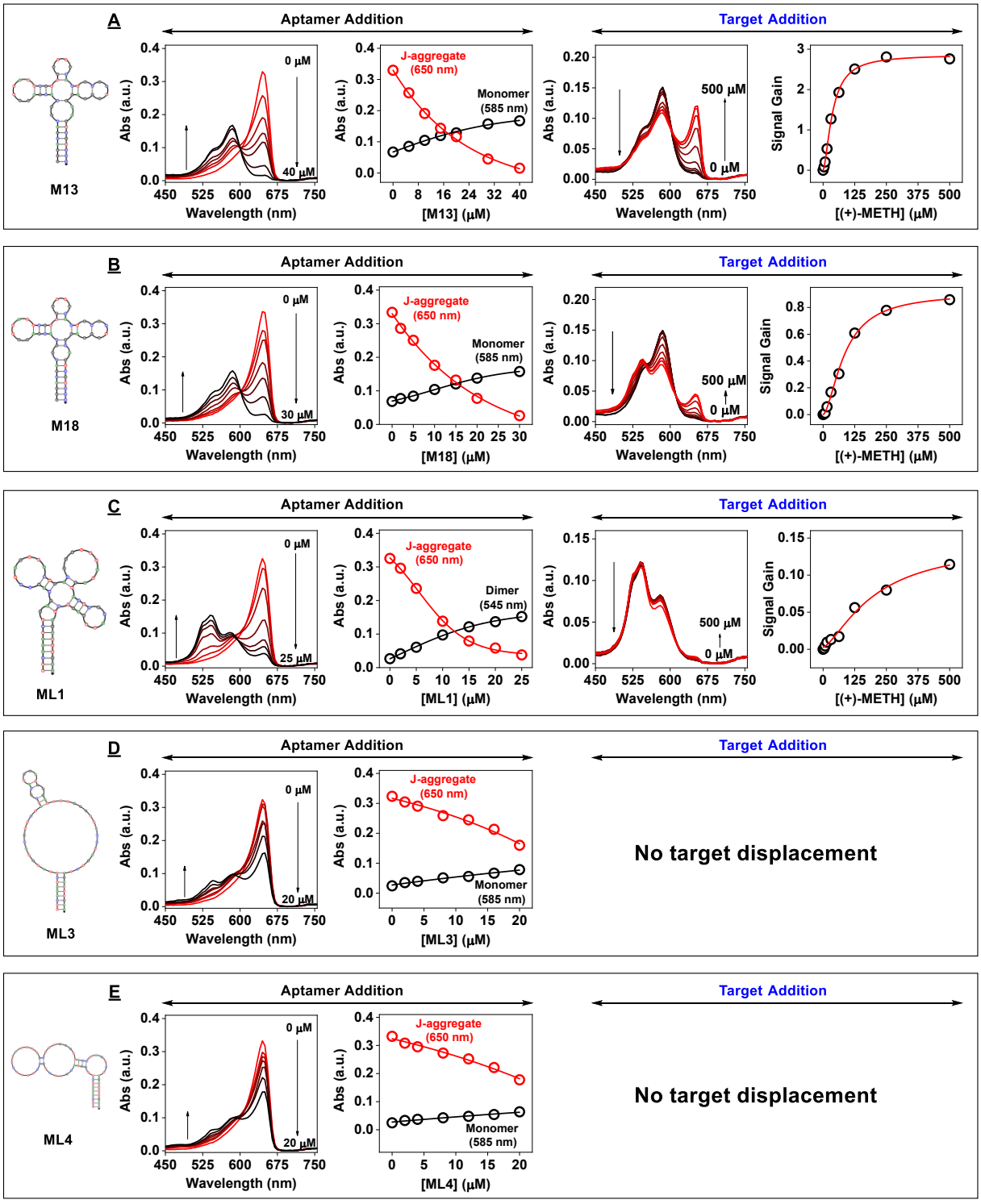

Figure S45. Target detection based on aptamer-based MTC displacement assay. For each panel, from left to right are: Secondary structure of the aptamer predicted by NUPACK; 'aptamer addition', which presents the absorbance spectra of 2.5 μM MTC with various concentrations of aptamer and a plot of MTC monomer or dimer and J-aggregate peak absorbance (respectively at 585 nm, 545 nm, and 650 nm) against aptamer concentration; and 'target addition', which presents the absorption spectra of solutions containing aptamer-MTC complex challenged with various concentrations of target as well as plot depicting the target calibration curve. (**A**) M13, (**B**) M18, (**C**) ML1, (**D**) ML3 and (**E**) ML4.

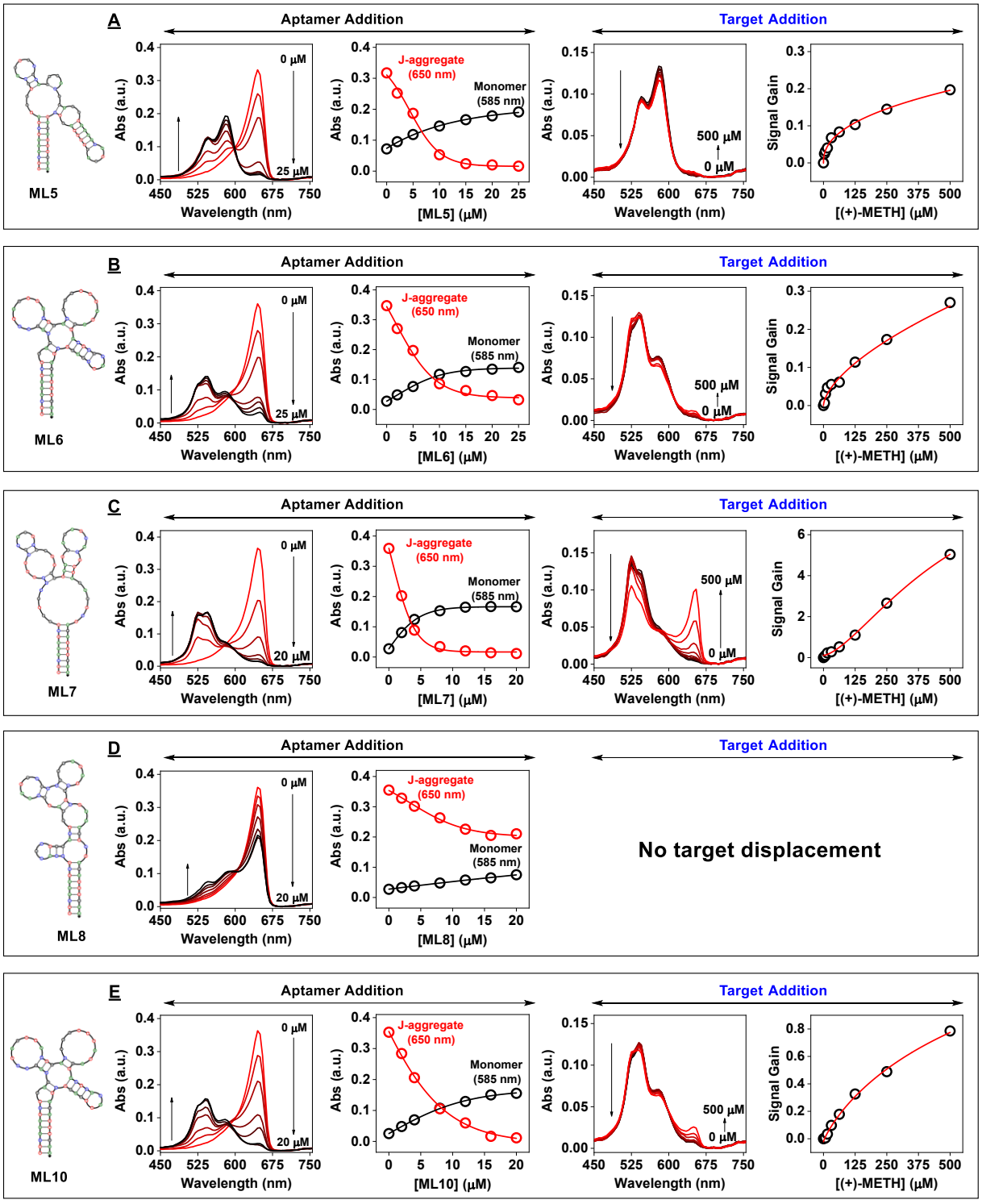

Figure S46. Target detection based on aptamer-based MTC displacement assay. For each panel, from left to right are: Secondary structure of the aptamer predicted by NUPACK; 'aptamer addition', which presents the absorbance spectra of 2.5 μM MTC with various concentrations of aptamer and a plot of MTC monomer and J-aggregate peak absorbance (respectively at 585 nm and 650 nm) against aptamer concentration; and 'target addition', which presents the absorption spectra of solutions containing aptamer-MTC complex challenged with various concentrations of target as well as plot depicting the calibration curve for target detection. (**A**) ML5, (**B**) ML6, (**C**) ML7, (**D**) ML8 and (**E**) ML10.

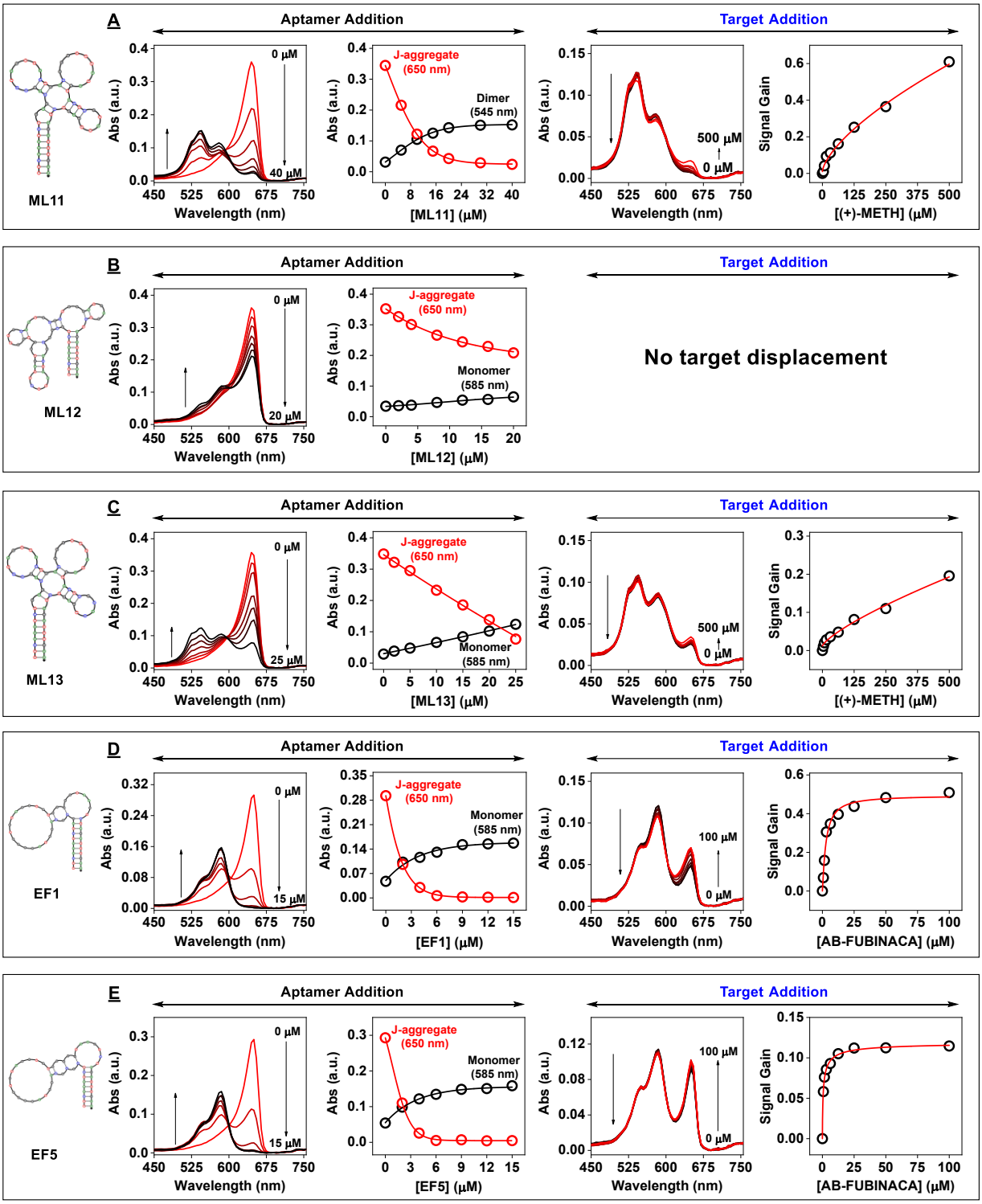

Figure S47. Target detection based on aptamer-based MTC displacement assay. For each panel, from left to right are: Secondary structure of the aptamer predicted by NUPACK; 'aptamer addition', which presents the absorbance spectra of 2.5 μM MTC with various concentrations of aptamer and a plot of MTC monomer or dimer and J-aggregate peak absorbance (respectively at 585 nm, 545 nm, and 650 nm) against aptamer concentration; and 'target addition', which presents the absorption spectra of solutions containing aptamer-MTC complex challenged with various concentrations of target as well as plot depicting the target calibration curve. (**A**) ML11, (**B**) ML12, (**C**) ML13, (**D**) EF1 and (**E**) EF5.

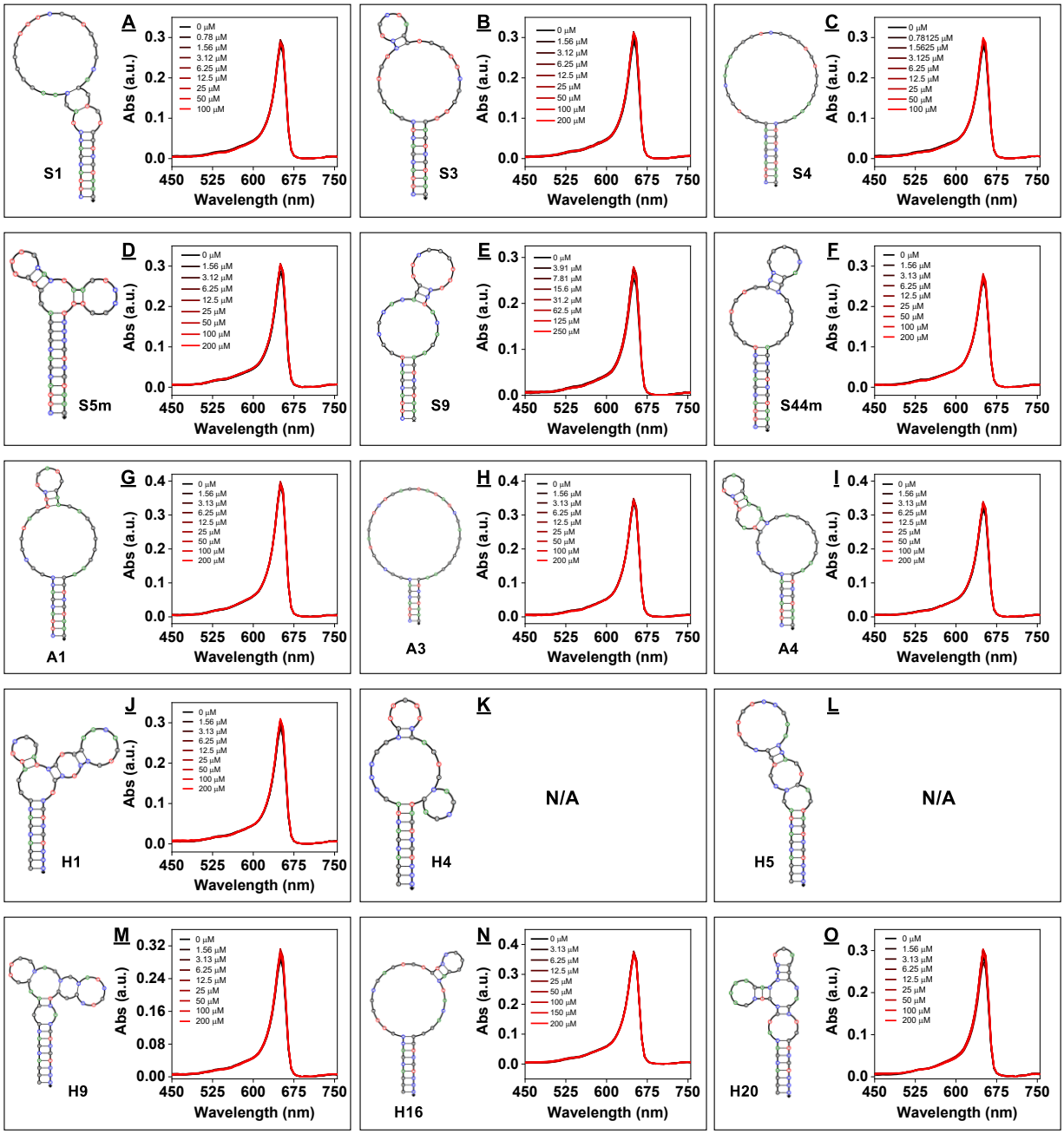

Figure S48. Absorbance spectra of 2.5 μM MTC in the presence of different targets at various concentrations. (**A-E**) (±)-cis-3-methyl-fentanyl, (**F**) remifentanil, (**G-I**) alfentanil and (**J-O**) heroin. N/A indicated that no target control experiments were performed for that aptamer since no target-induced dye-displacement was observed. Black-to-red color gradient represents increasing concentrations of target.

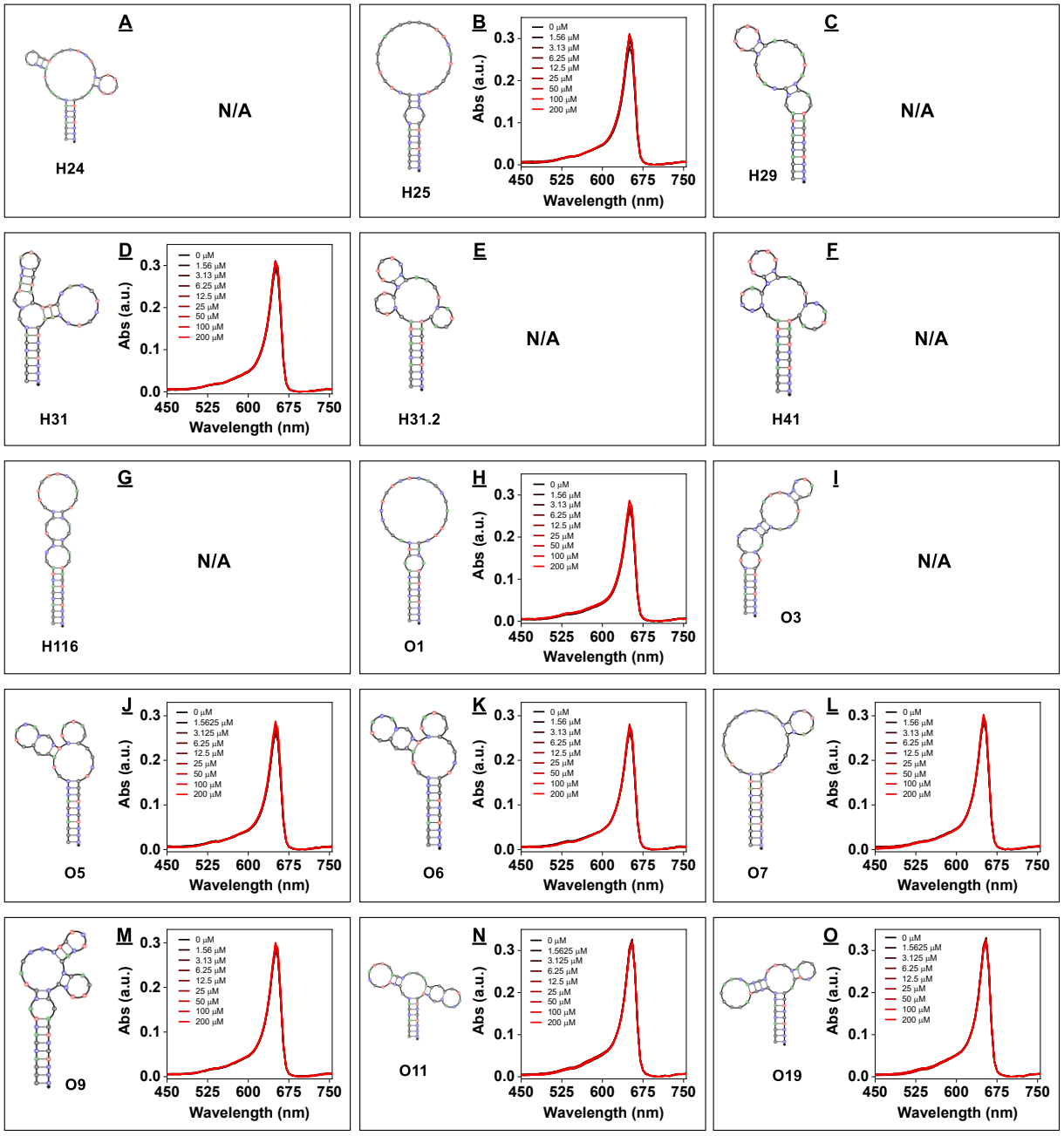

Figure S48 (continued). Absorbance spectra of 2.5 μM MTC in the presence of different targets at various concentrations. (**A-G**) heroin and (**H-O**) oxycodone. N/A indicated that no target control experiments were performed for that aptamer since no target-induced dye-displacement was observed. Black-to-red color gradient represents increasing concentrations of target.

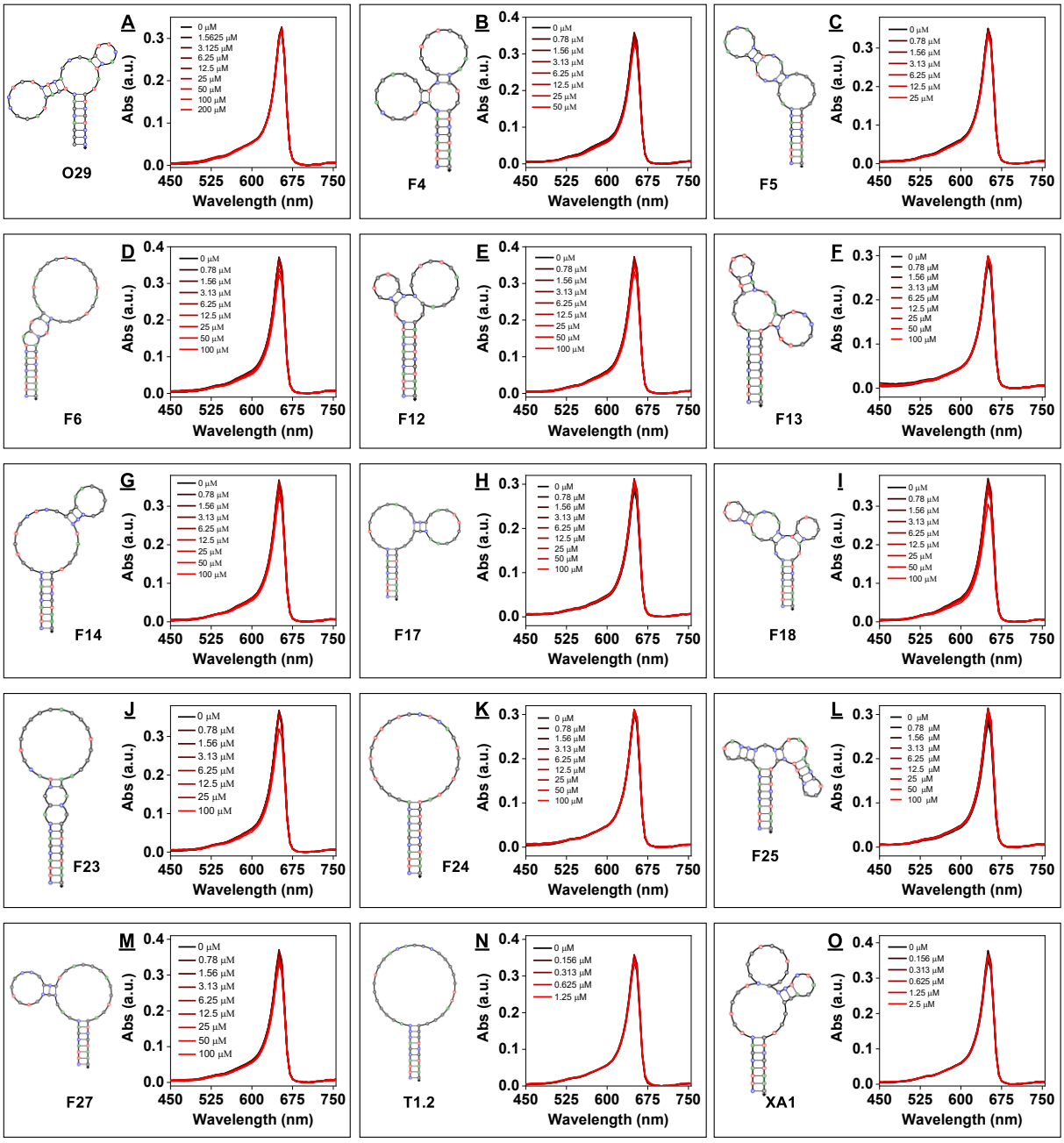

Figure S48 (continued). Absorbance spectra of 2.5 μM MTC in the presence of different targets at various concentrations. (**A**) oxycodone, (**B-M**) fentanyl, (**N**) THC and (**O**) UR-144. Black-to-red color gradient represents increasing concentrations of target.

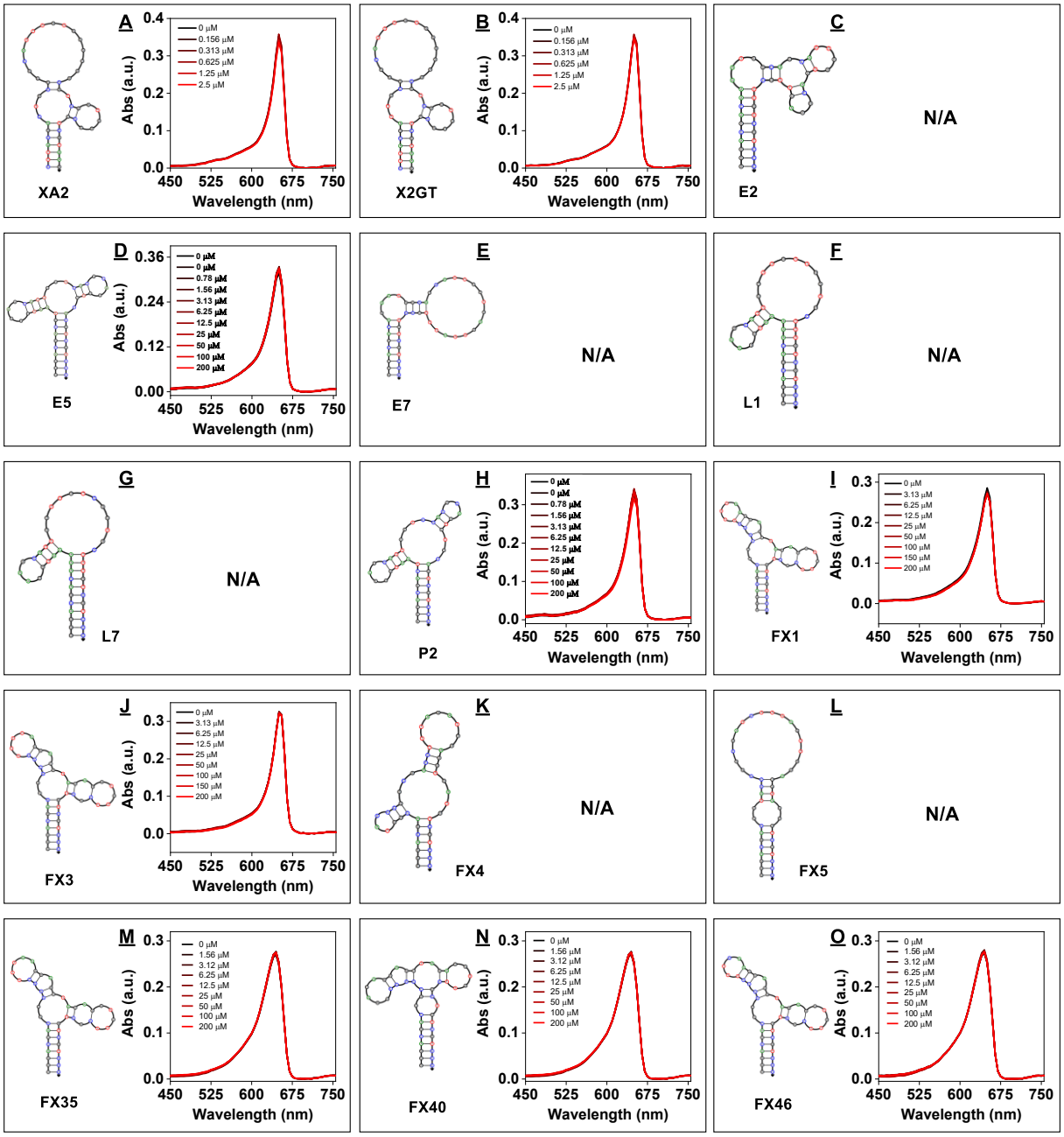

Figure S48 (continued). Absorbance spectra of 2.5 μM MTC in the presence of different targets at various concentrations. (**A-B**) UR-144, (**C-H**) fentanyl, (**I-O**) flunixin. N/A indicated that no target control experiments were performed for that aptamer since no target-induced dye-displacement was observed. Black-to-red color gradient represents increasing concentrations of target.

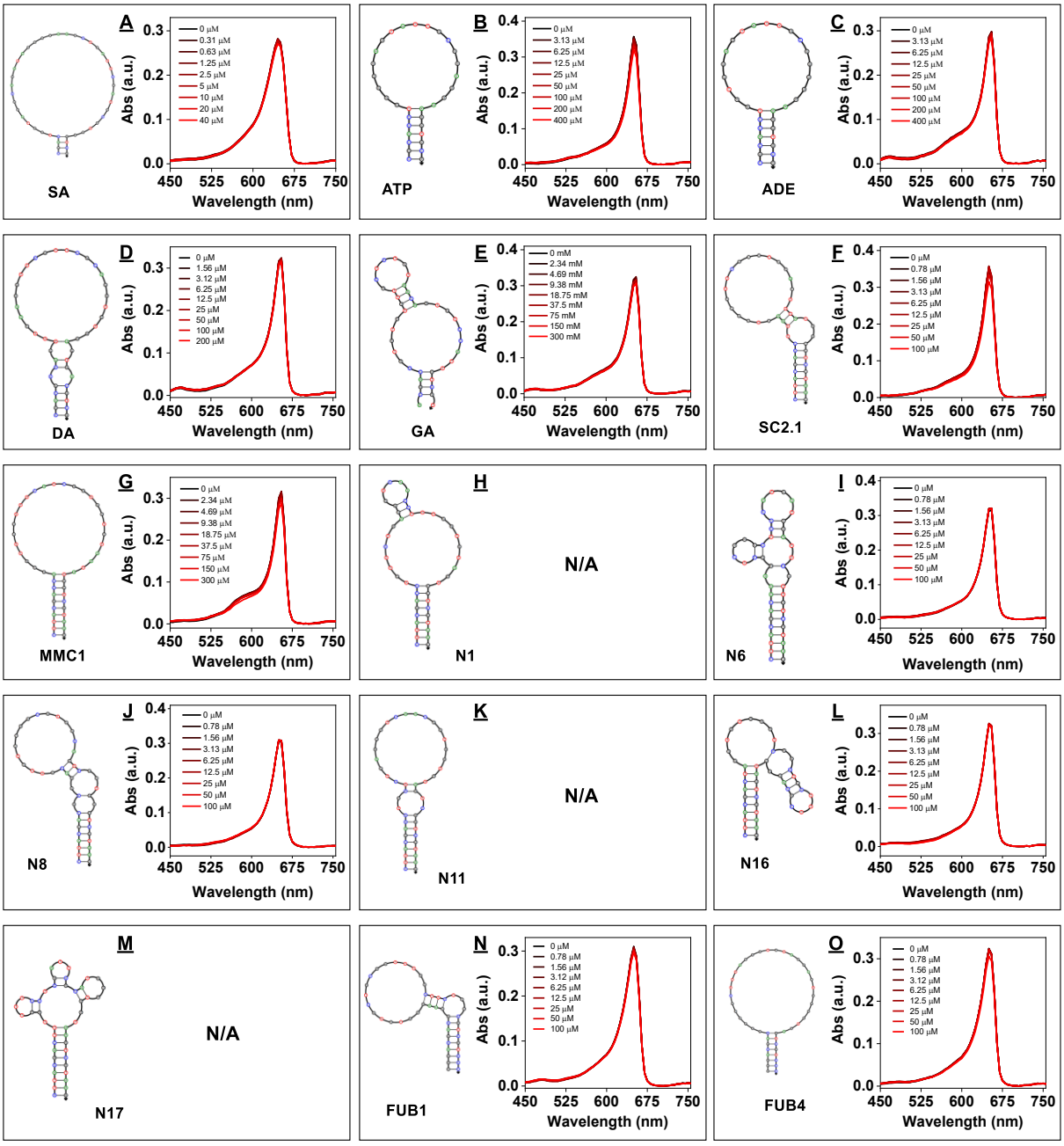

Figure S48 (continued). Absorbance spectra of 2.5 μM MTC in the presence of different targets at various concentrations. (**A**) serotonin, (**B**) ATP, (**C**) adenosine, (**D**) dopamine, (**E**) glucose, (**F**) MDPV, (**G**) mephedrone, (**H-M**) cocaine and (**N-O**) AB-FUBINACA. N/A indicated that no target control experiments were performed for that aptamer since no target-induced dye-displacement was observed. Black-to-red color gradient represents increasing concentrations of target.

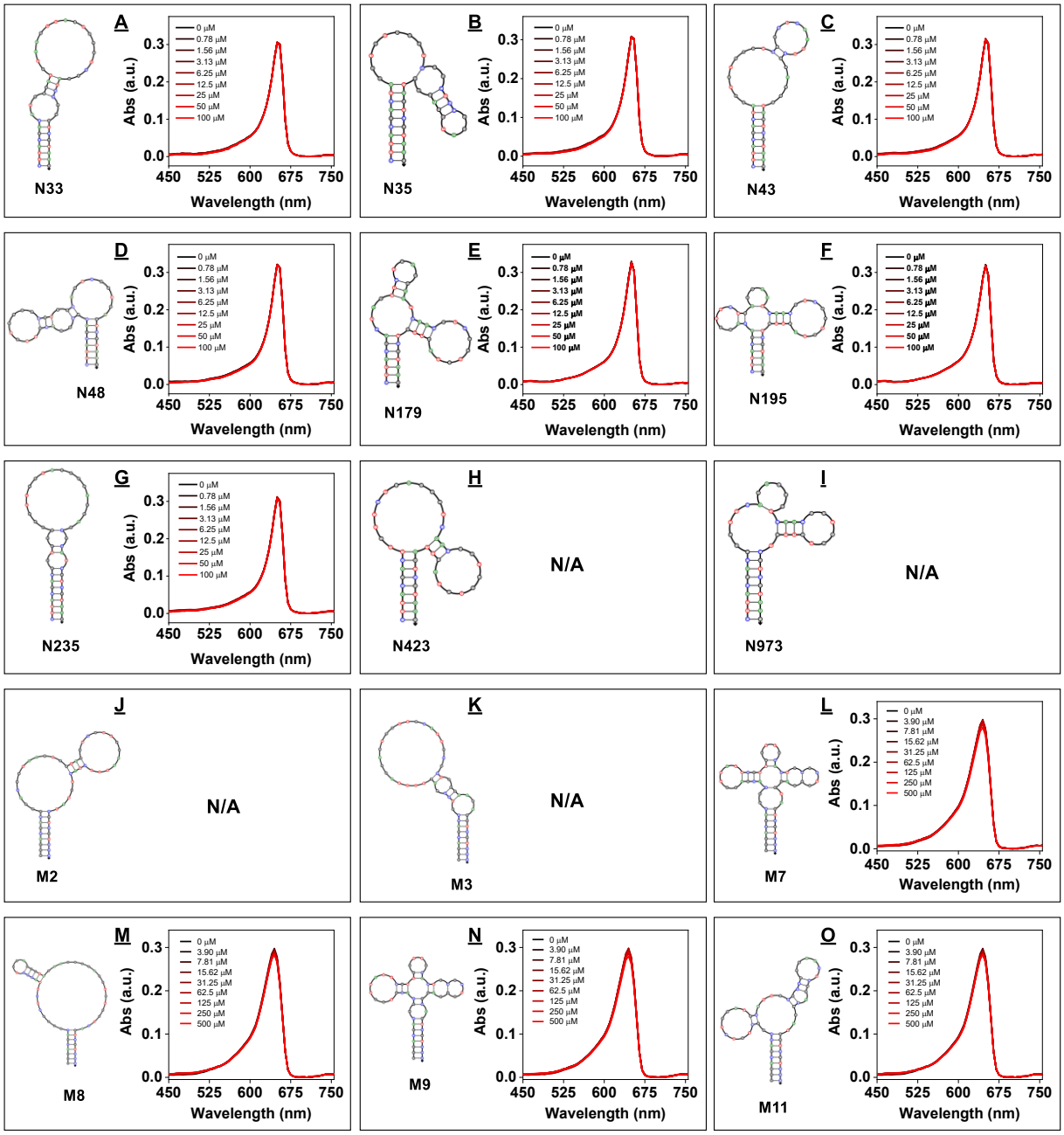

Figure S48 (continued). Absorbance spectra of 2.5 μM MTC in the presence of different targets at various concentrations. (**A-I**) cocaine and (**J-O**) (+)-methamphetamine. N/A indicated that no target control experiments were performed for that aptamer since no target-induced dye-displacement was observed. Black-to-red color gradient represents increasing concentrations of target.

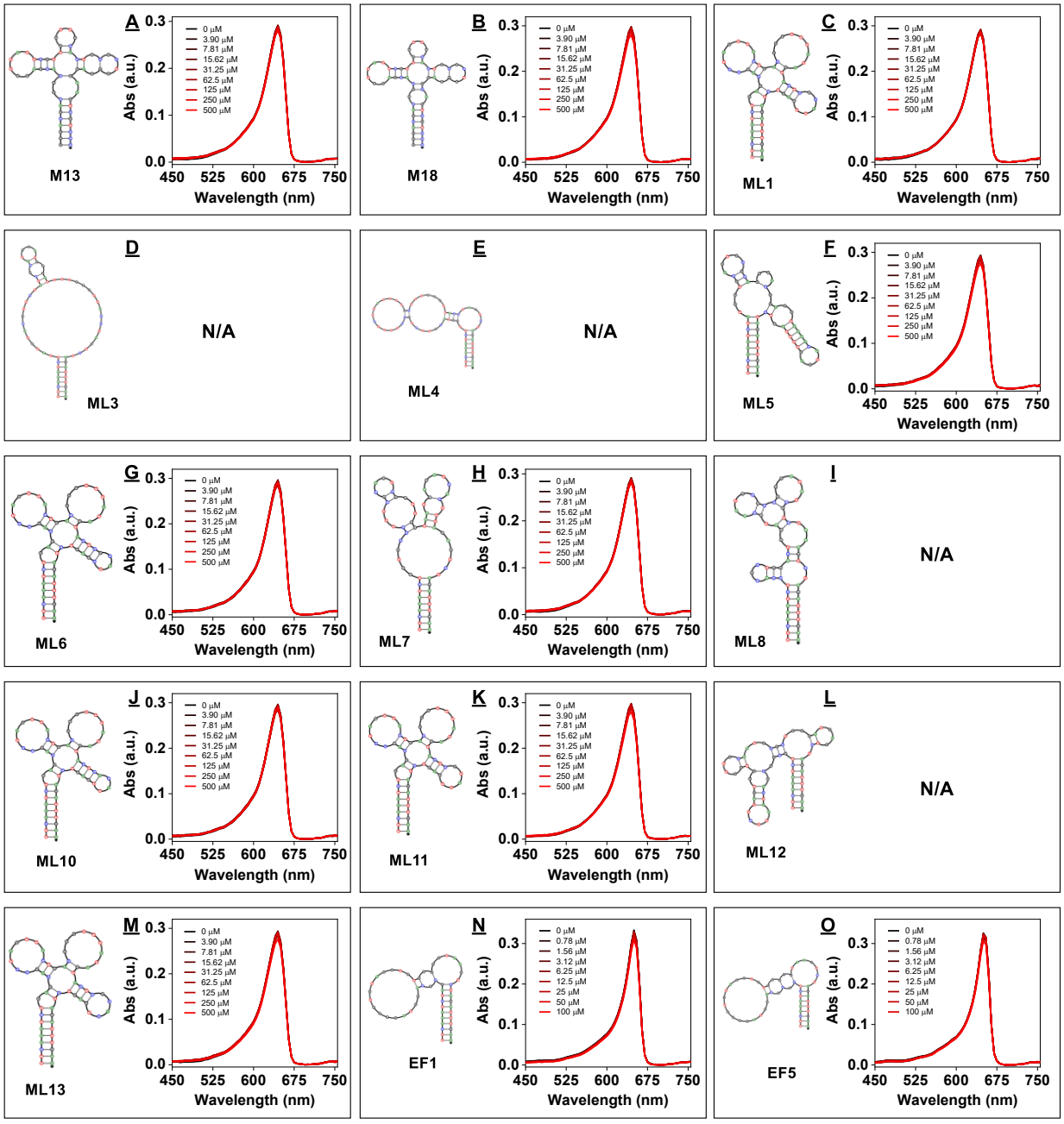

Figure S48 (continued). Absorbance spectra of 2.5 μM MTC in the presence of different targets at various concentrations. (**A-M**) (+)-methamphetamine and (**N-O**) AB-FUBINACA. N/A indicated that no target control experiments were performed for that aptamer since no target-induced dye-displacement was observed. Black-to-red color gradient represents increasing concentrations of target.

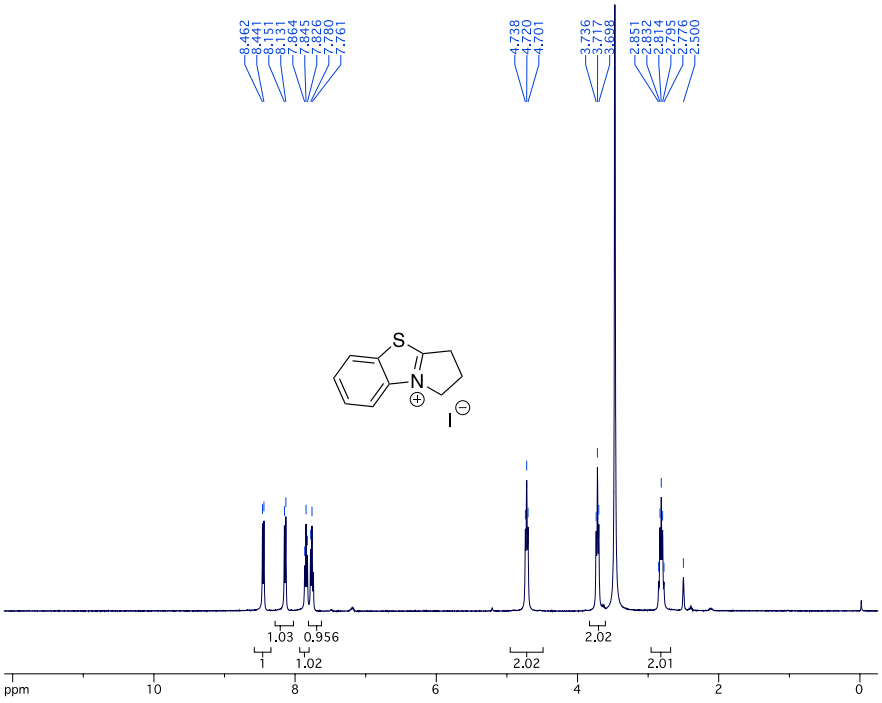

Figure S49. ^{1}H NMR spectrum of compound **1-I** (DMSO-d_6, 400 MHz, 22°C).

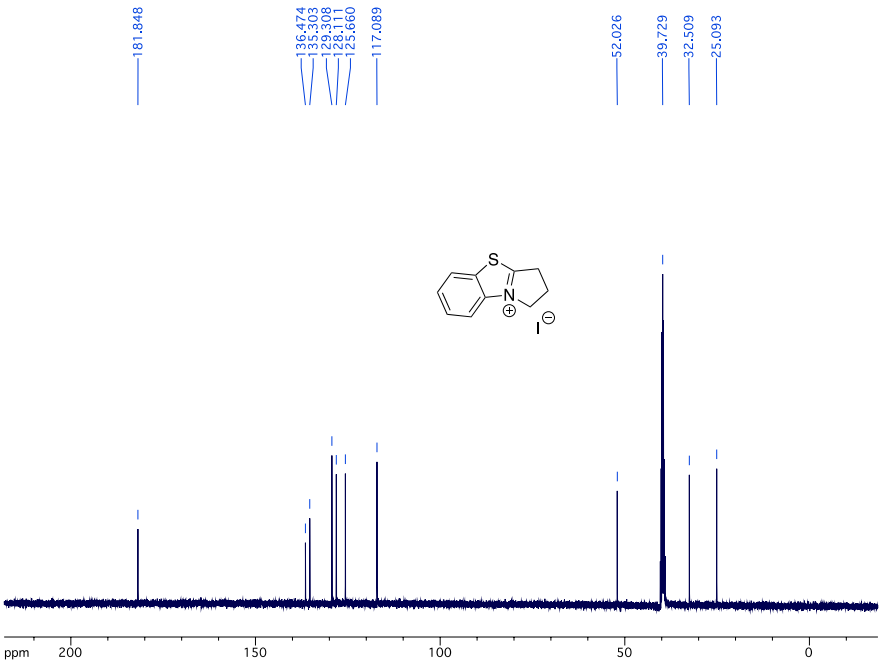

Figure S50. ^{13}C NMR spectrum of compound **1-I** (DMSO-d_6, 101 MHz, 22°C).

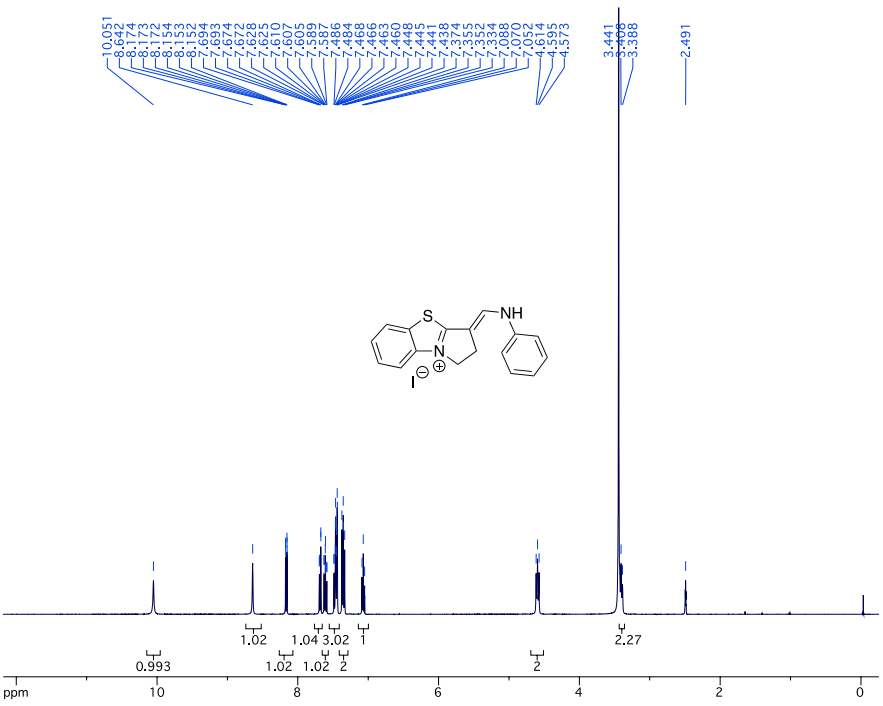

Figure S51. ^{1}H NMR spectrum of compound **2** (DMSO-d_6, 400 MHz, 22°C).

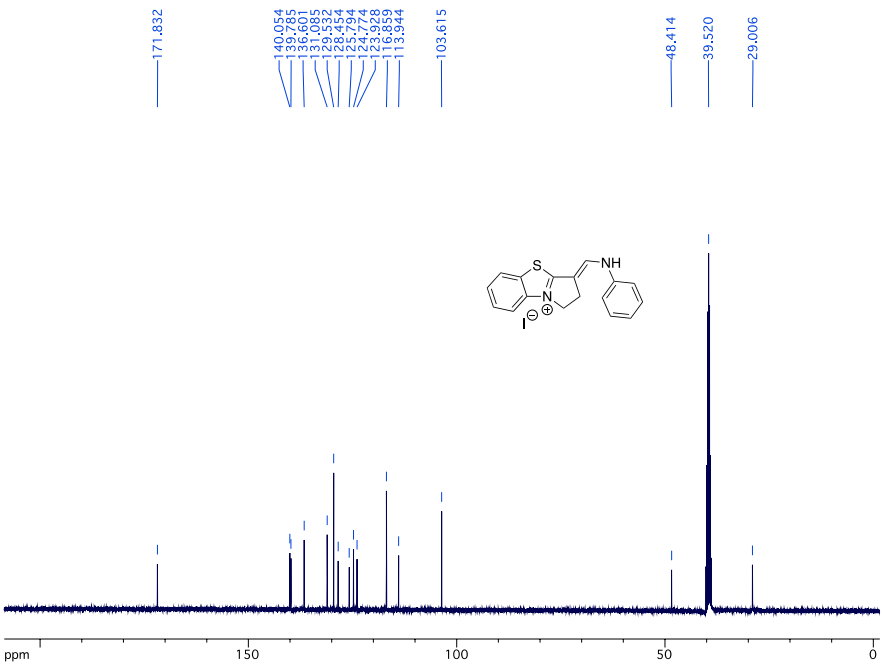

Figure S52. ^{13}C NMR spectrum of compound **2** (DMSO-d_6, 101 MHz, 22°C).

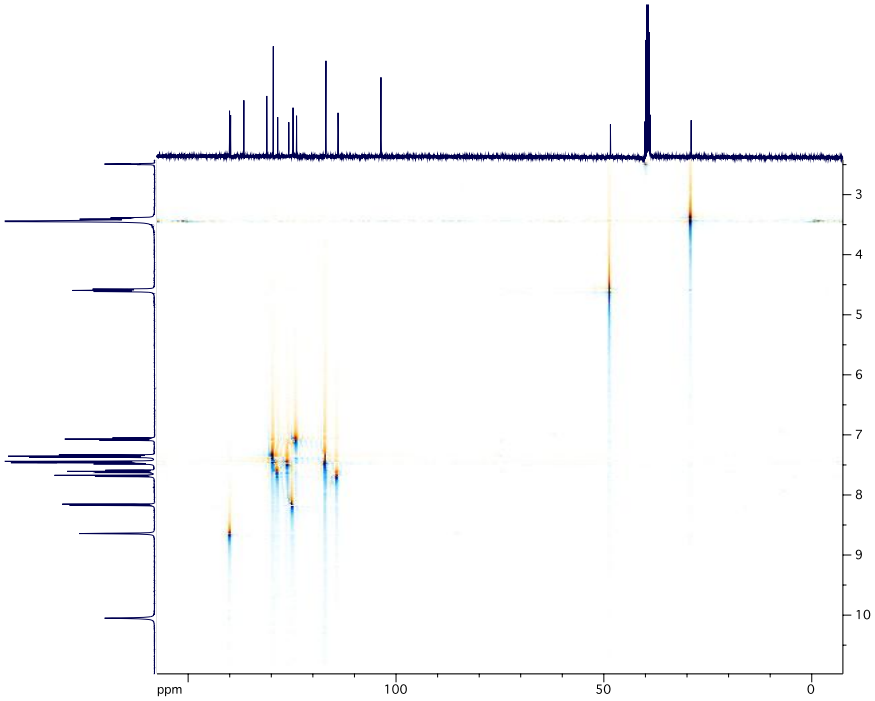

Figure S53. HSQC spectrum of compound **2** (DMSO-d_6, 22°C).

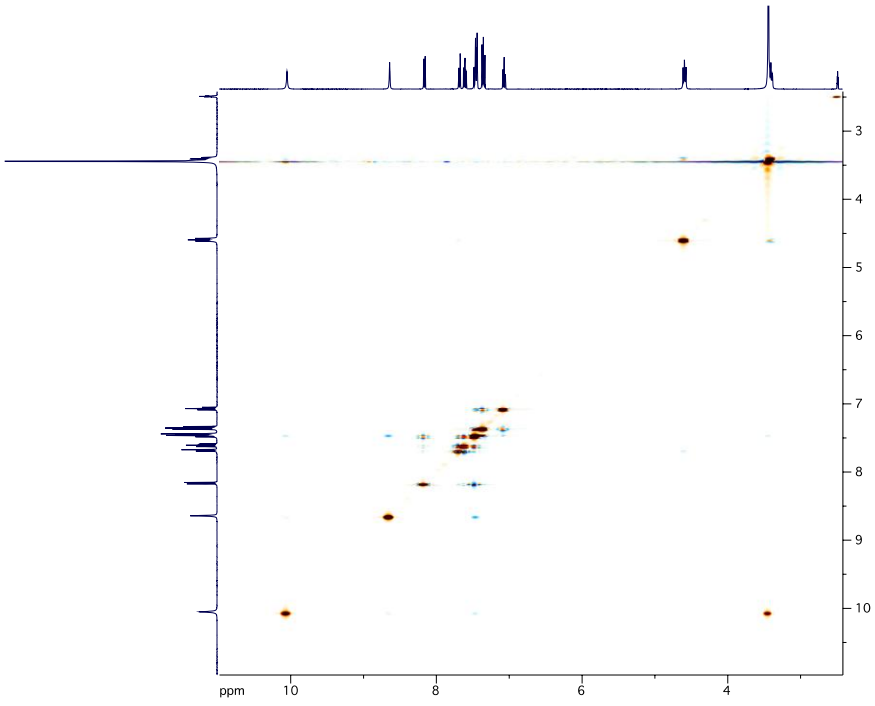

Figure S54. NOESY spectrum of compound **2** (DMSO-d_6, 22°C).

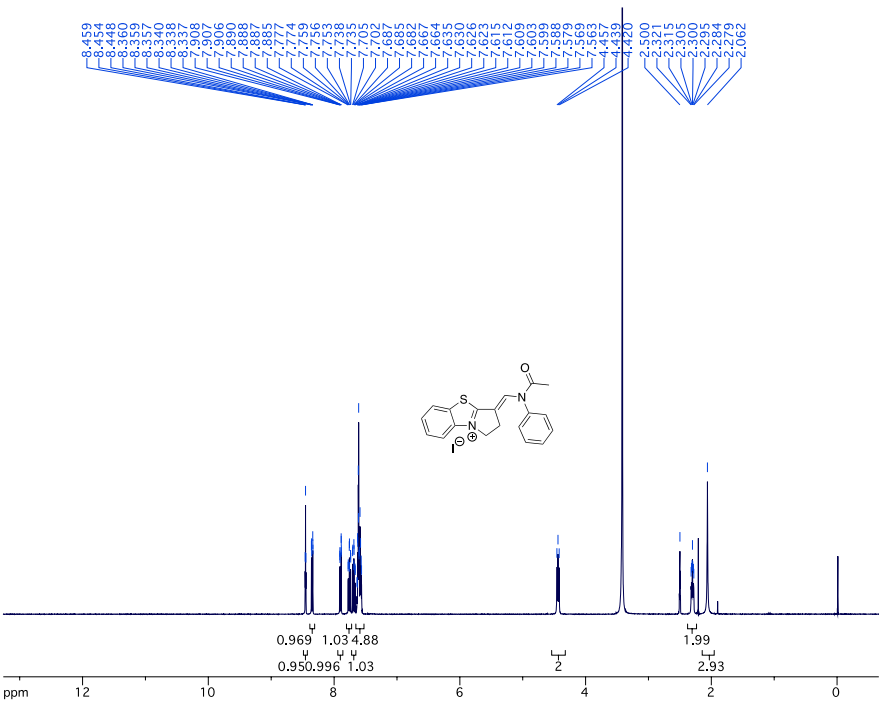

Figure S55. ^{1}H NMR spectrum of compound **3** (DMSO-d_6, 400 MHz, 22°C).

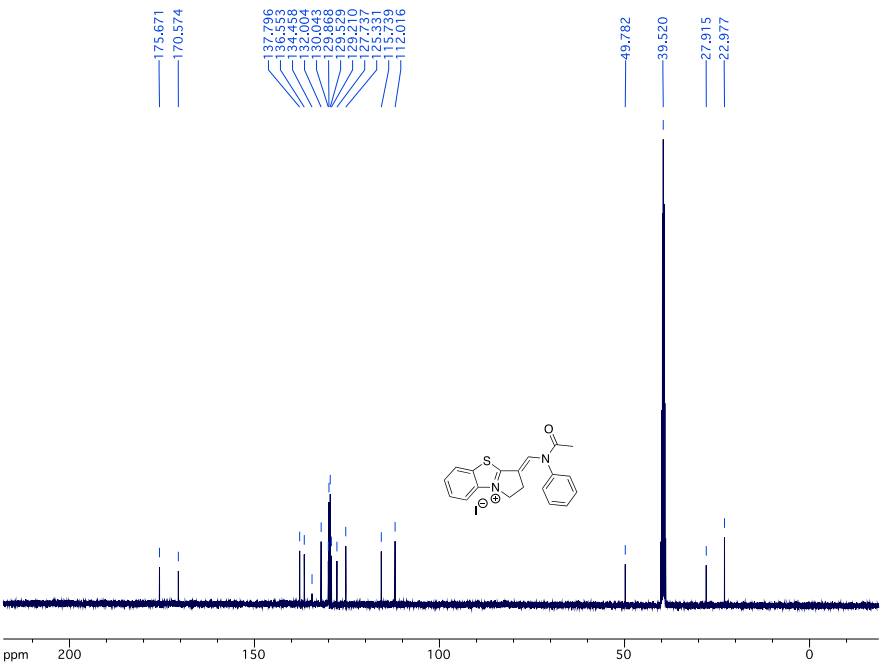

Figure S56. ^{13}C NMR spectrum of compound **3** (DMSO-d_6, 101 MHz, 22°C).

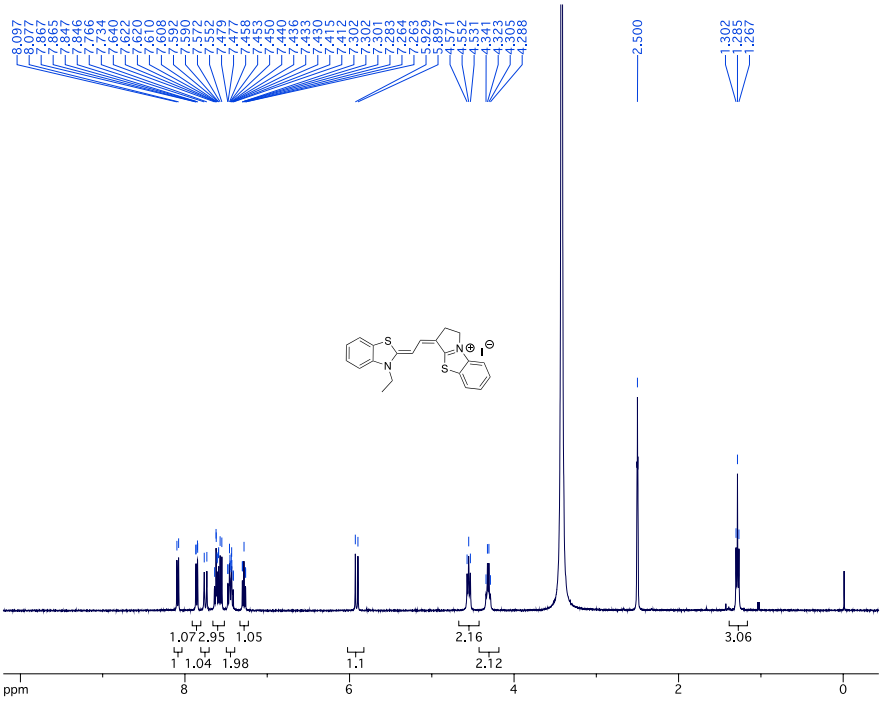

Figure S57. ^{1}H NMR spectrum of compound 5 (X-732-91B) (DMSO-d_6, 400 MHz, 22°C).

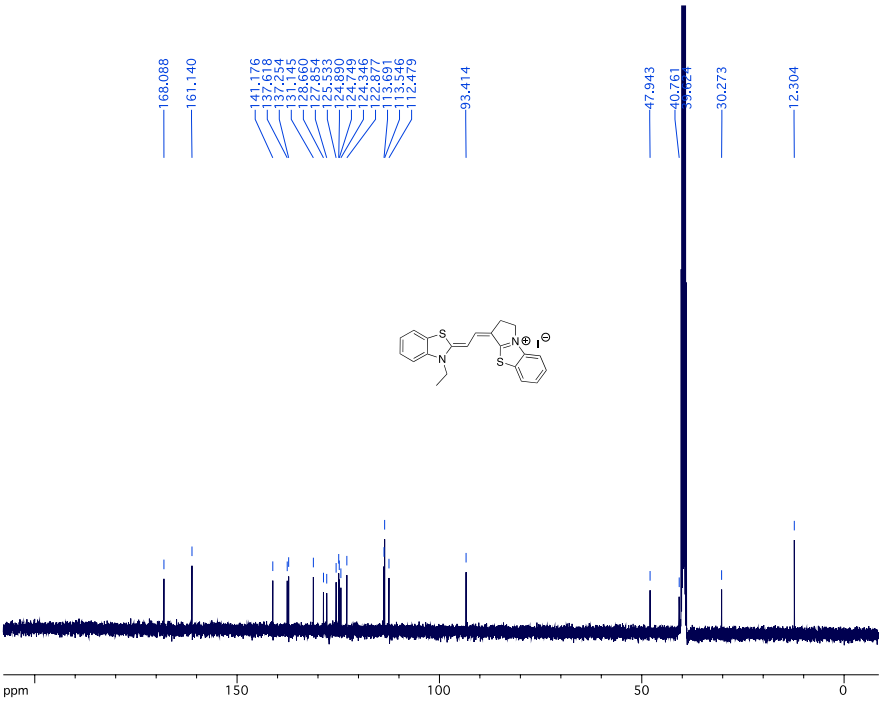

Figure S58. ^{13}C NMR spectrum of compound 5 (X-732-91B) (DMSO-d_6, 101 MHz, 22°C).

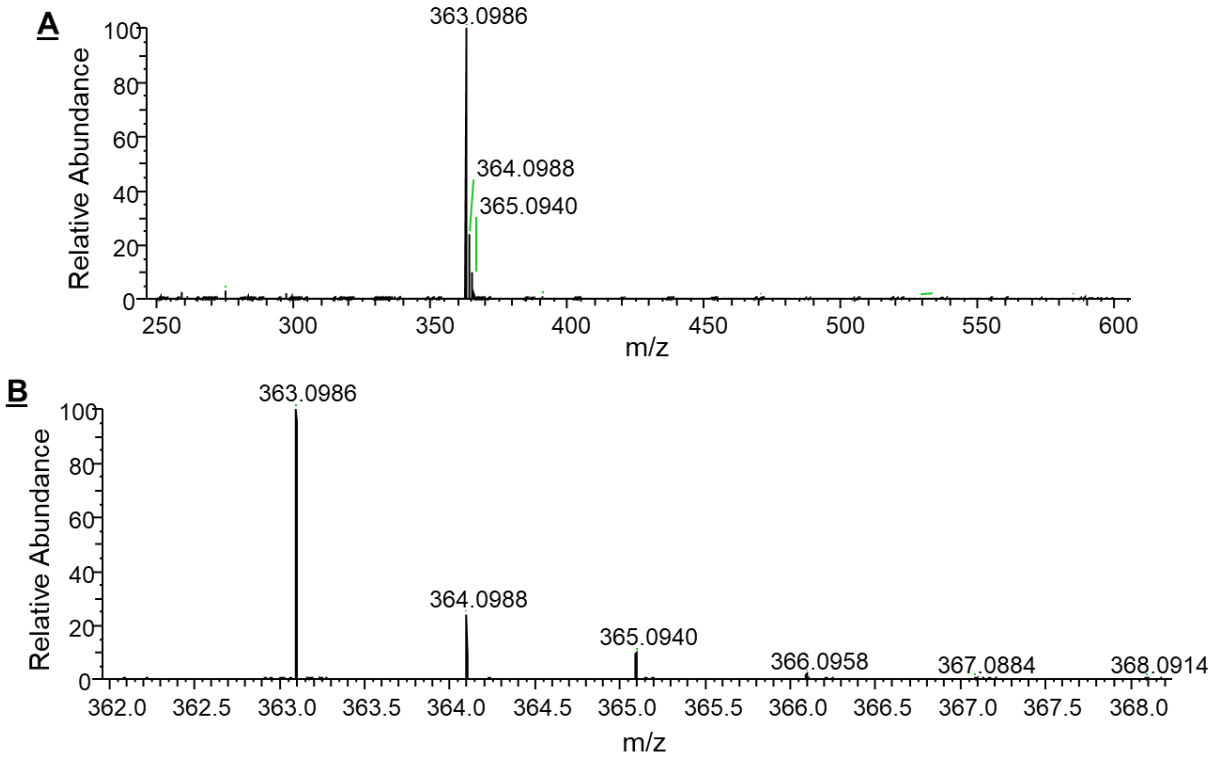

Figure S59. The mass spectrum of X-732-91B runs in positive mode using a Thermo Scientific Ultimate 3000 system coupled with an Exactive Plus Orbitrap mass spectrometer. (**A**) is the spectrum of X-732-91B and (**B**) is a magnification of the spectrum from *m/z* 362 to 368. The cation of X-732-91B dye has a *m/z* of 363.0986 with an error of 0.50 ppm compared to its theoretical *m/z* of 363.09842 to give a chemical formula of $C_{21}H_{19}N_2S_2^+$.

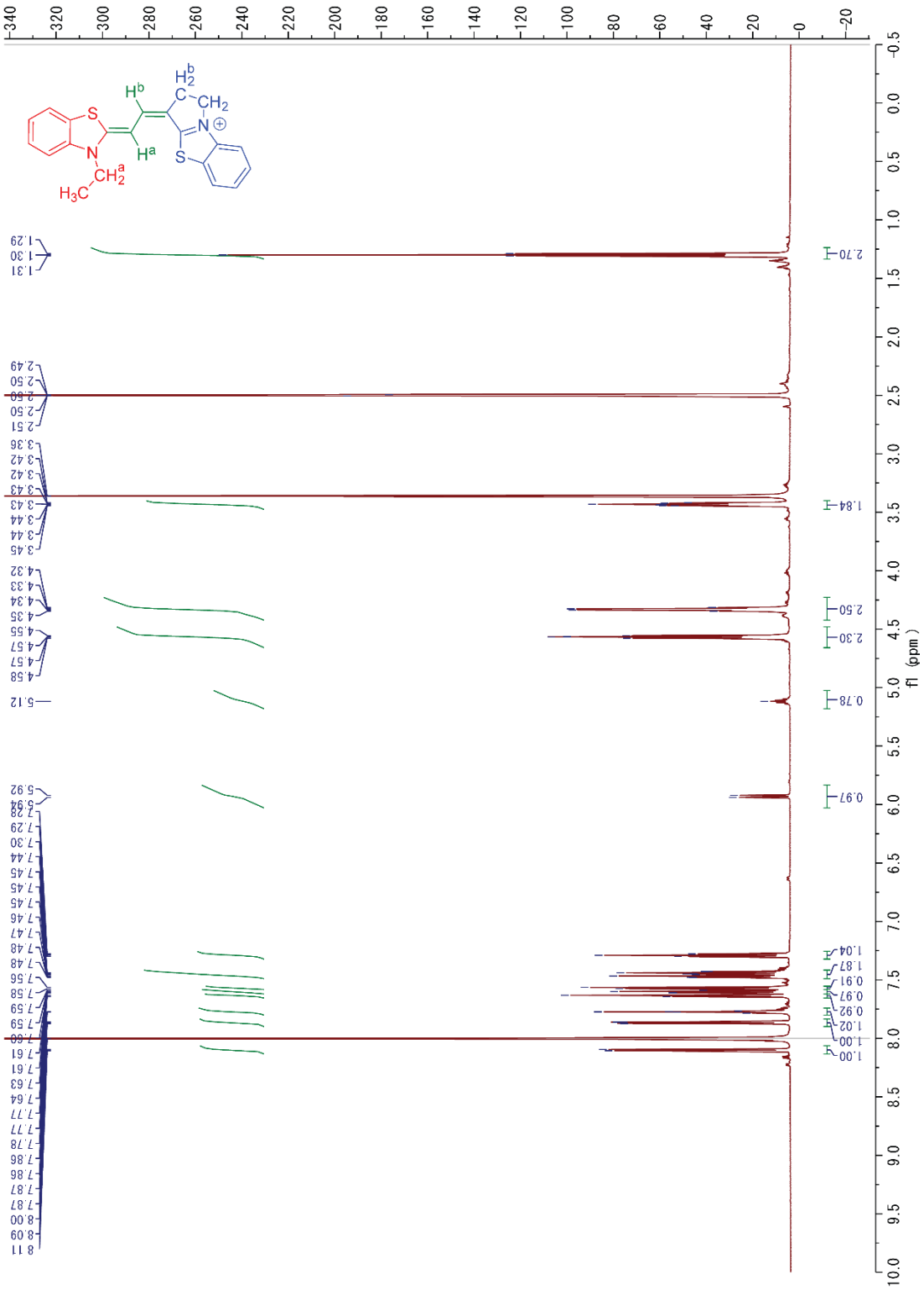

Figure S60. ^{1}H NMR spectrum of X-732-91B in 95:5 DMSO-d_6/HFIP-d_2.

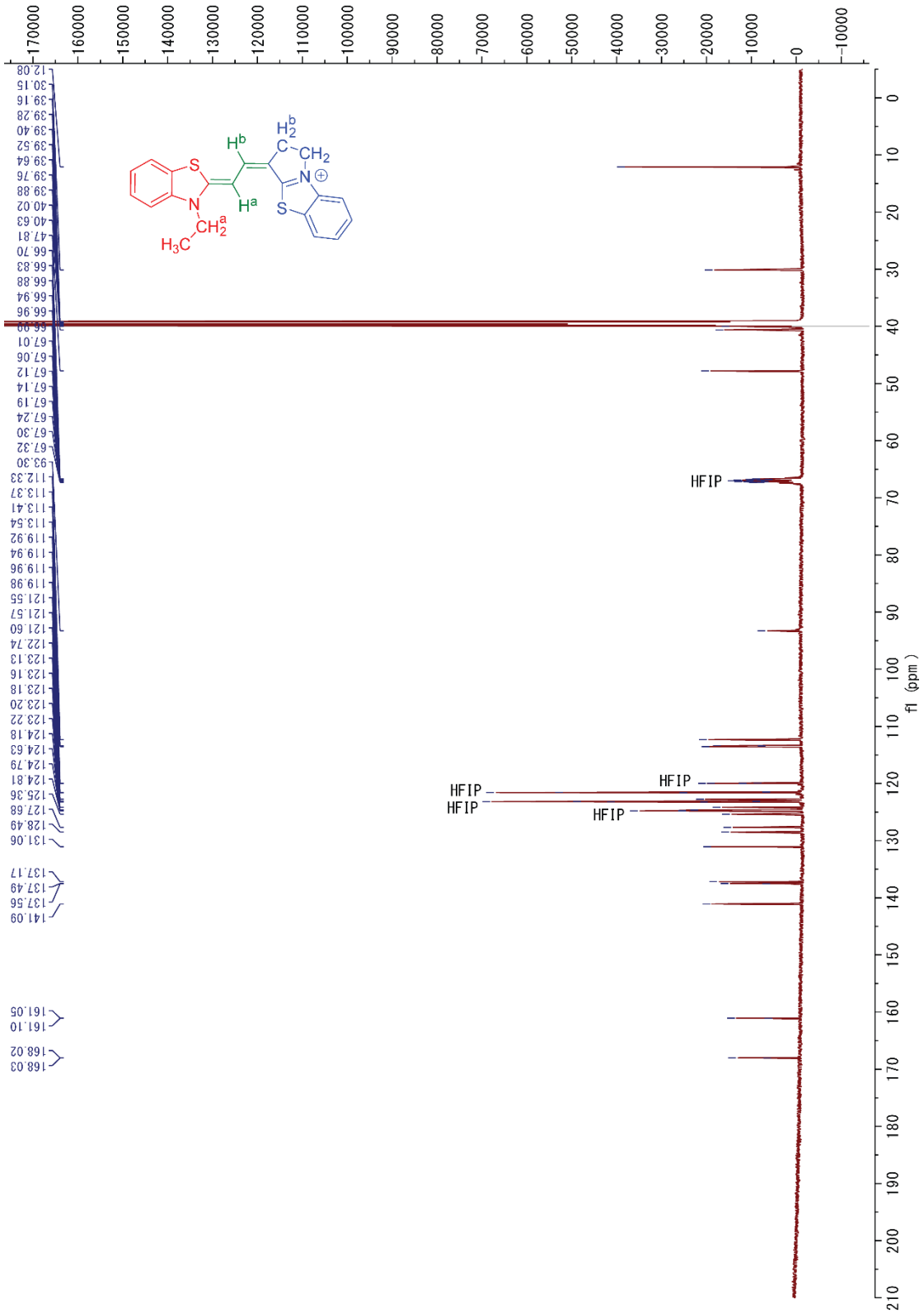

Figure S61. ^{13}C NMR spectrum of X-732-91B in 95:5 DMSO-d_6/HFIP-d_2.

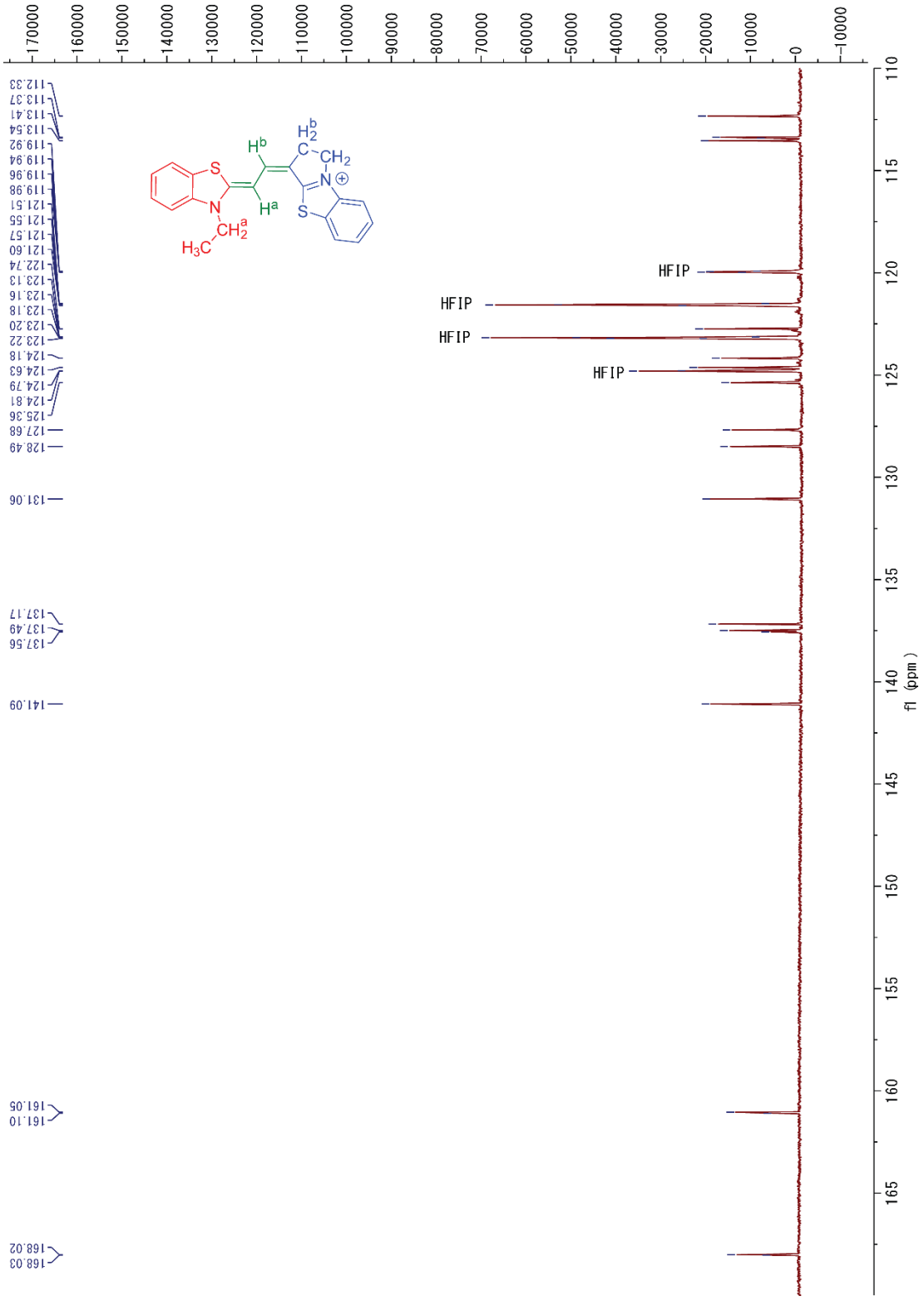

Figure S62. The 110–170-ppm region of the ^{13}C NMR spectrum of X-732-91B in 95:5 DMSO-d_6/HFIP-d_2.

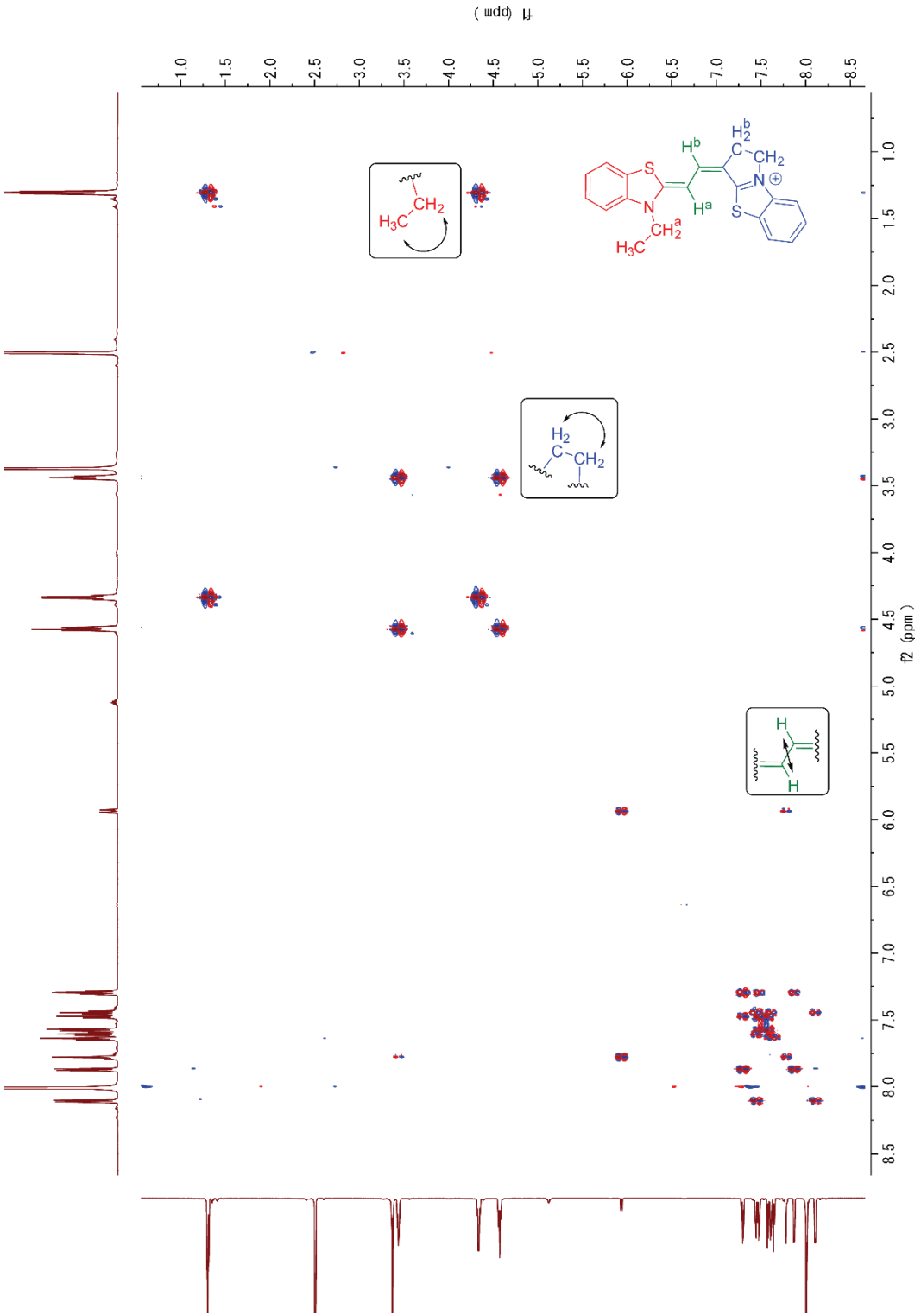

Figure S63. ^{1}H-^{1}H COSY NMR spectrum of X-732-91B in 95:5 DMSO-d_6/HFIP-d_2. Representative correlations were labeled with chemical structures.

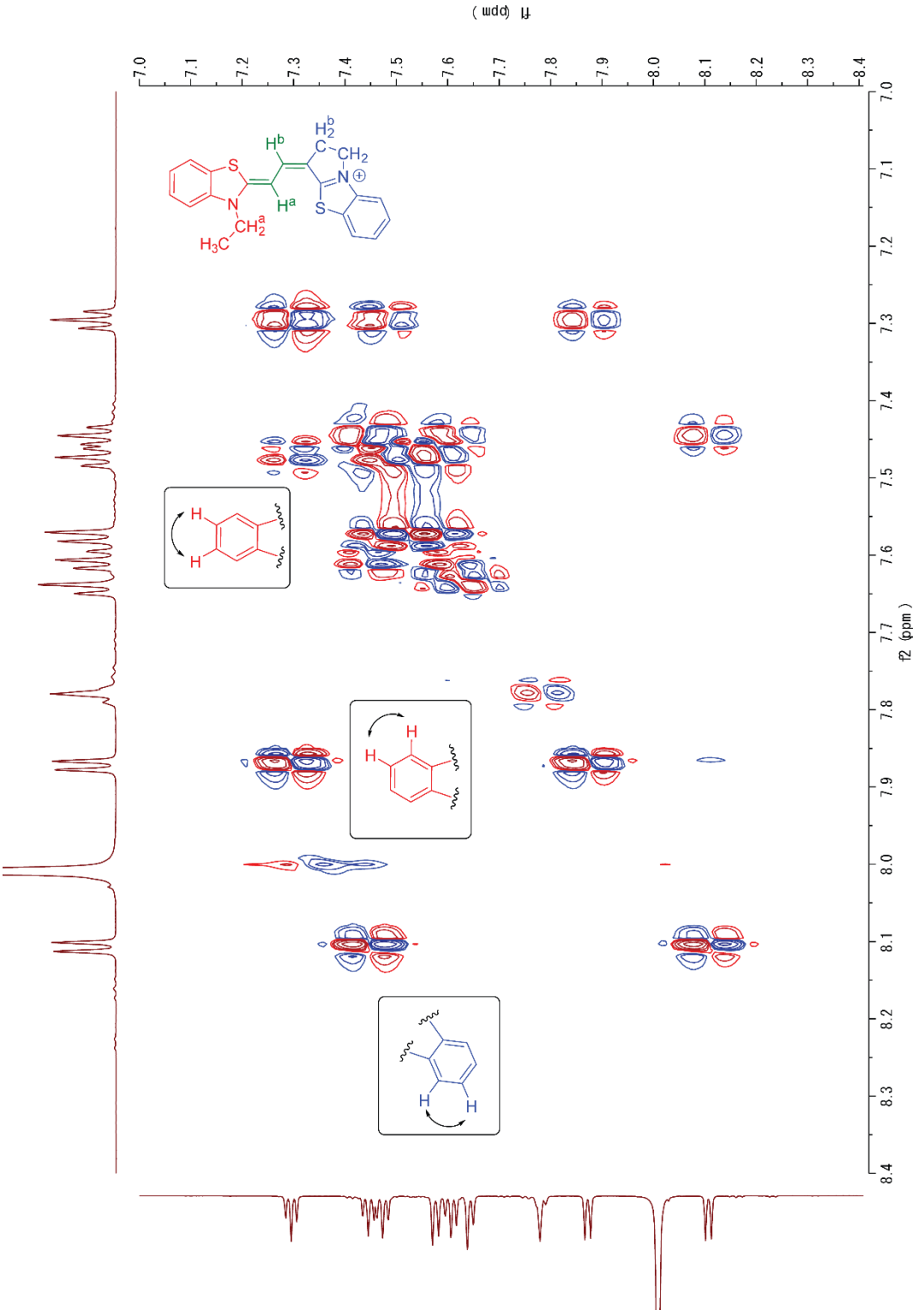

Figure S64. The aromatic region of the ^{1}H-^{1}H COSY NMR spectrum of X-732-91B in 95:5 DMSO-d_6/HFIP-d_2. Representative correlations were labeled with chemical structures.

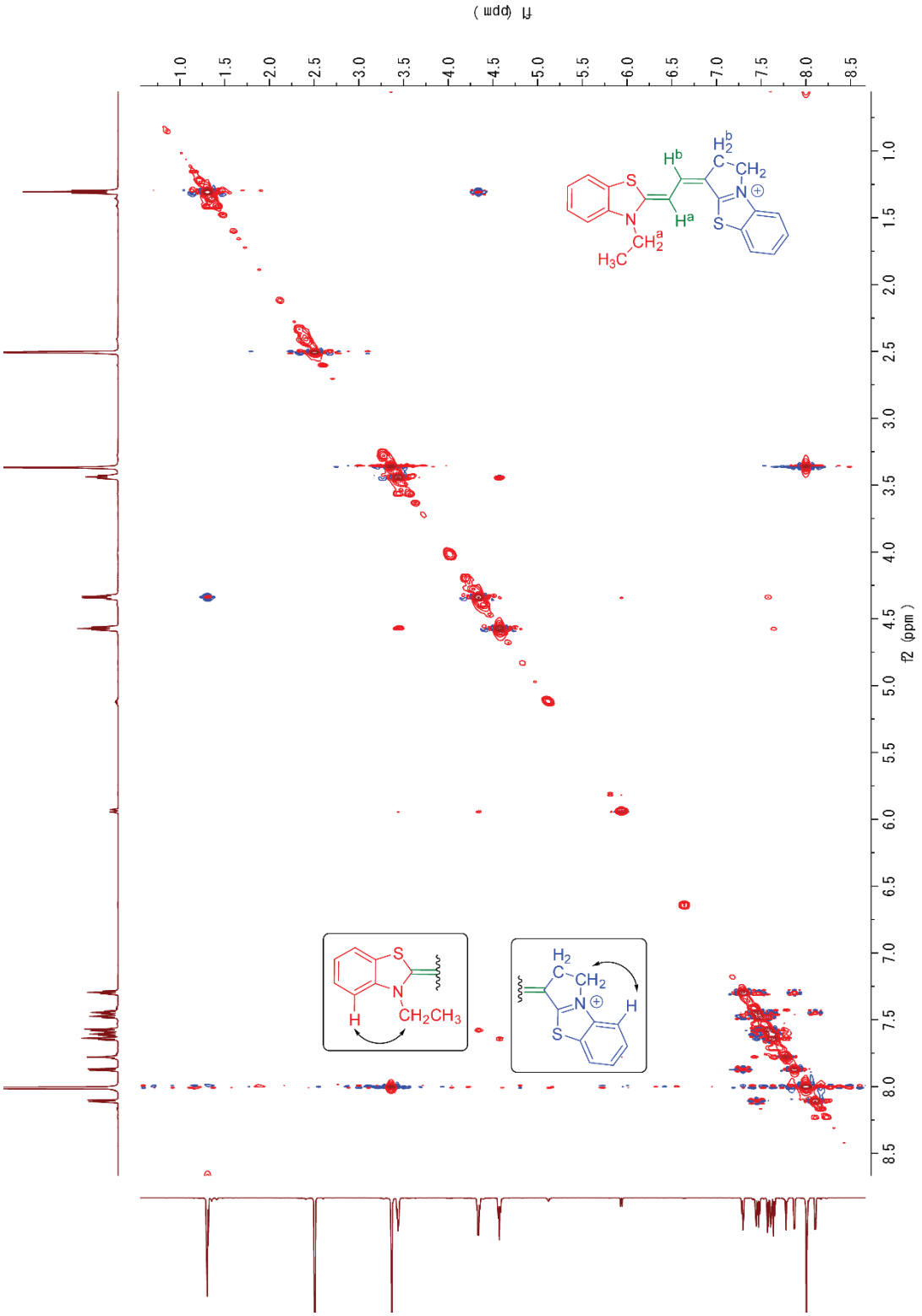

Figure S65. ^{1}H-^{1}H NOESY NMR spectrum of X-732-91B in 95:5 DMSO-d_6/HFIP-d_2. Representative correlations were labeled with chemical structures.

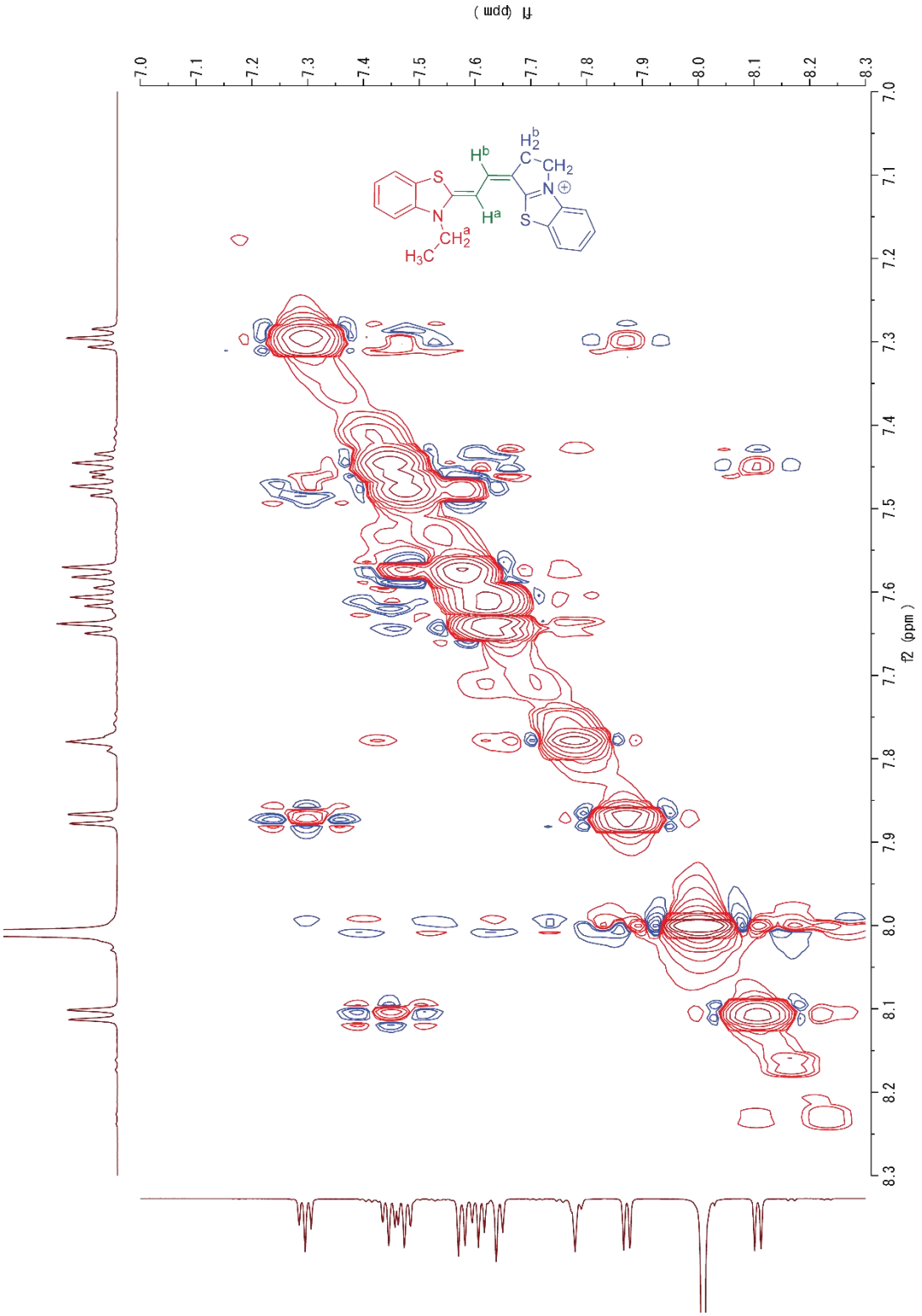

Figure S66. The aromatic region of the ^{1}H-^{1}H COSY NMR spectrum of X-732-91B in 95:5 DMSO-d_6/HFIP-d_2.

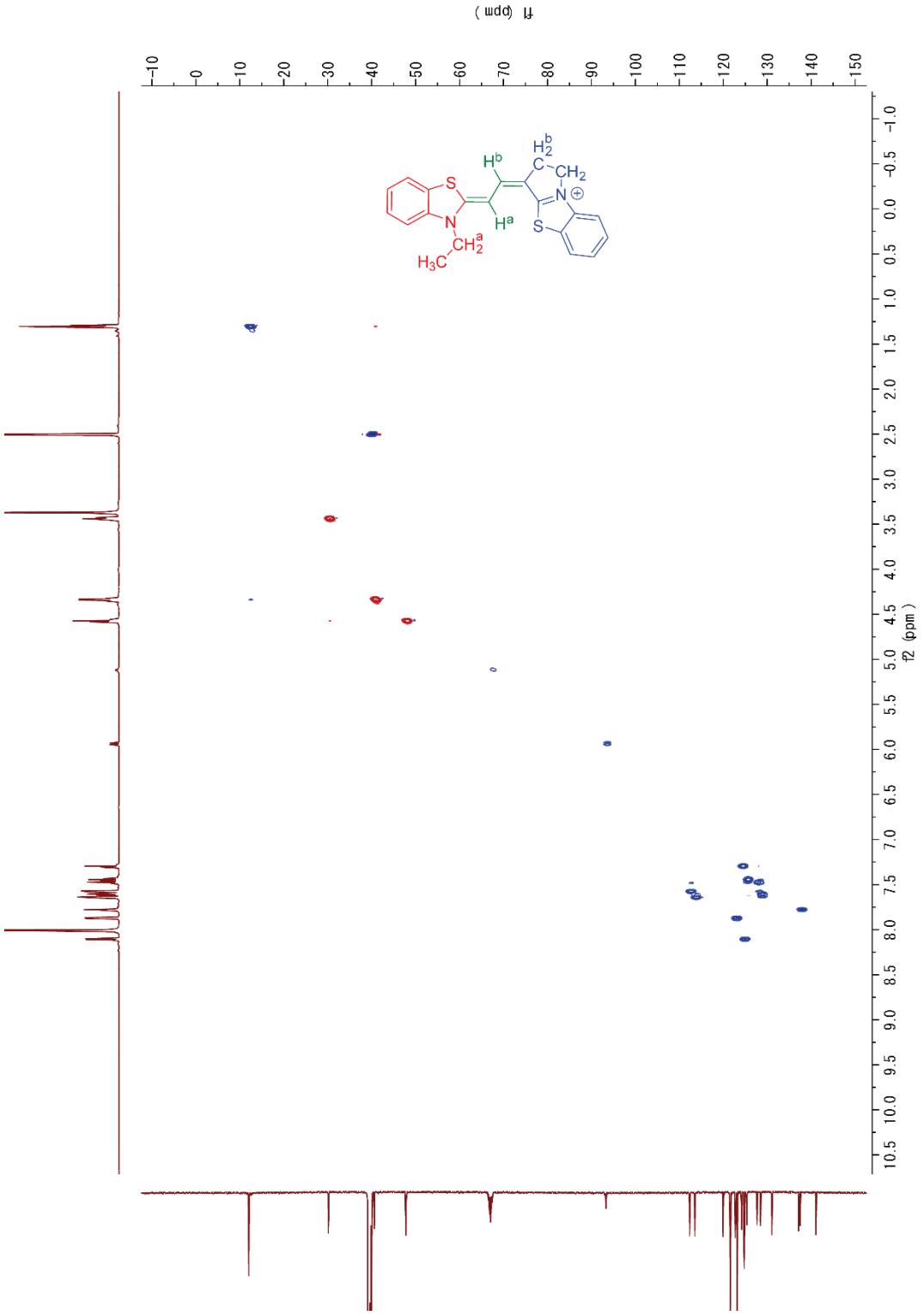

Figure S67. ^{1}H-^{13}C HSQC NMR spectrum of X-732-91B in 95:5 DMSO-d_6/HFIP-d_2.

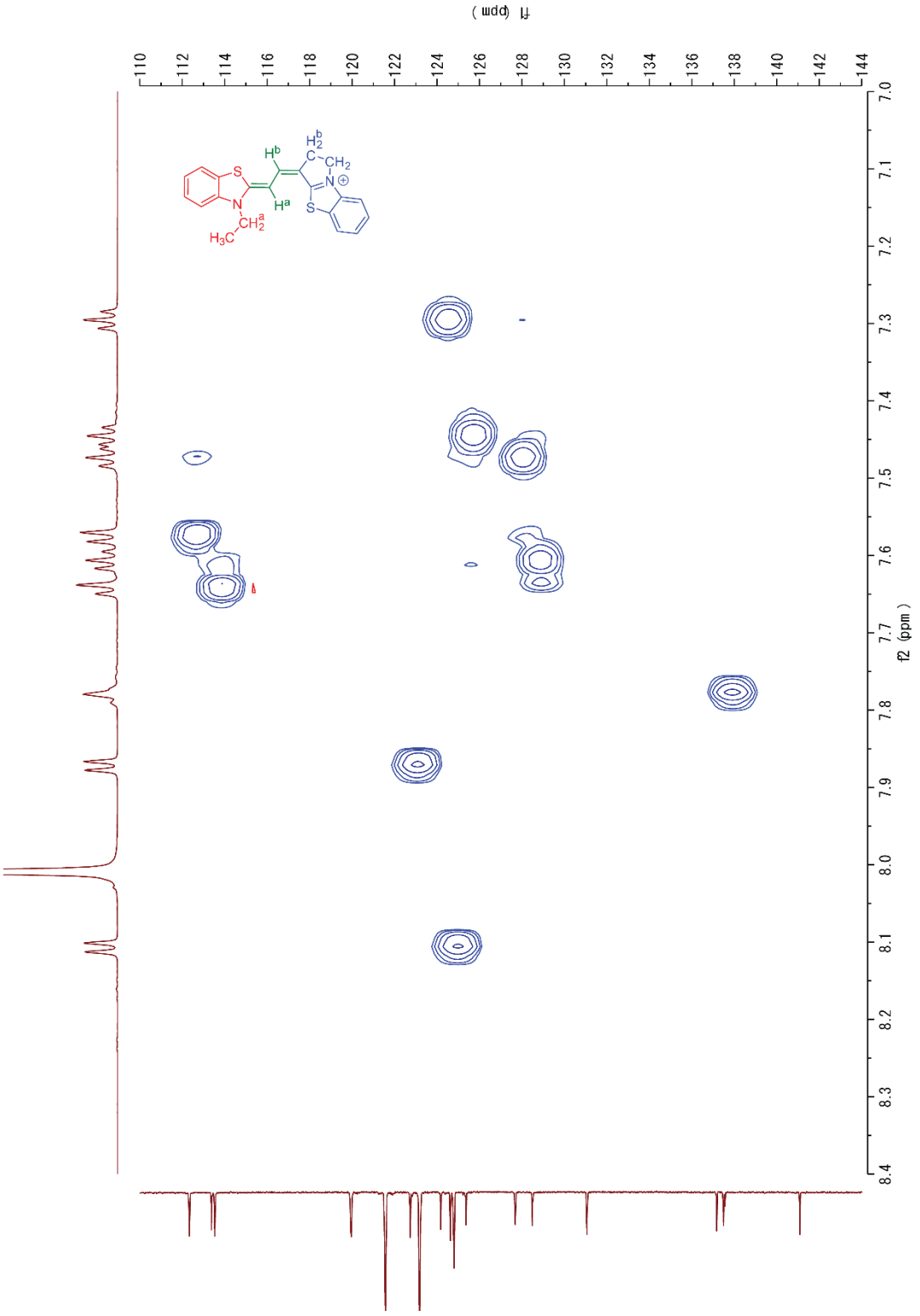

Figure S68. The aromatic region of the ^{1}H-^{13}C HSQC NMR spectrum of X-732-91B in 95:5 DMSO-d_6/HFIP-d_2.

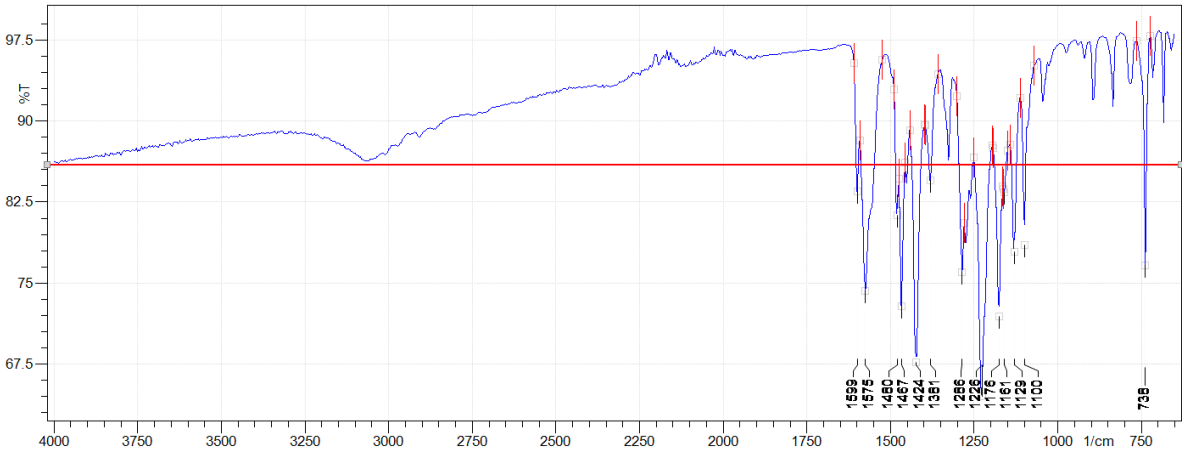

Figure S69. FT-IR spectrum of X-732-91B.

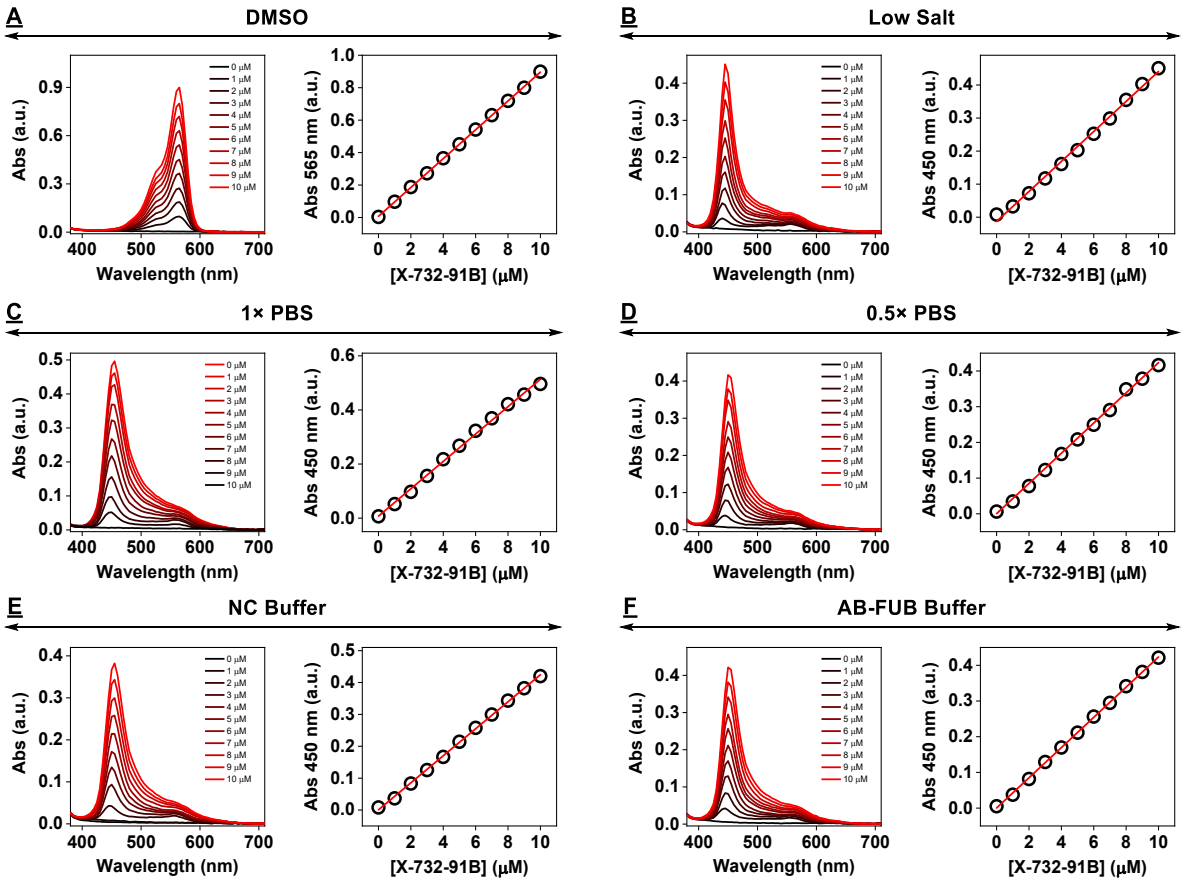

Figure S70. Optical properties of X-732-91B under different experimental conditions. Absorbance spectra and calibration curve of X-732-91B in (**A**) 100% DMSO, (**B**) low salt buffer (10 mM Tris (pH 7.4), 20 mM NaCl, 0.5 mM $MgCl_2$), (**C**) 1× PBS (1× PBS (pH 7.4), 1 mM $MgCl_2$), (**D**) 0.5× PBS (0.5× PBS (pH 7.4), 2 mM $MgCl_2$, (**E**) NC buffer (20 mM Tris (pH 7.4), 140 mM NaCl, 4 mM KCl, 2 mM $MgCl_2$) and (**F**) AB-FUB buffer (10 mM Tris (pH 7.4), 137 mM NaCl, 2.7 mM KCl, 1 mM $MgCl_2$). All buffer formulations included 1% (v/v) DMSO for (A-E) or 3% (v/v) DMSO for (F) and 0.01% (v/v) SDS.

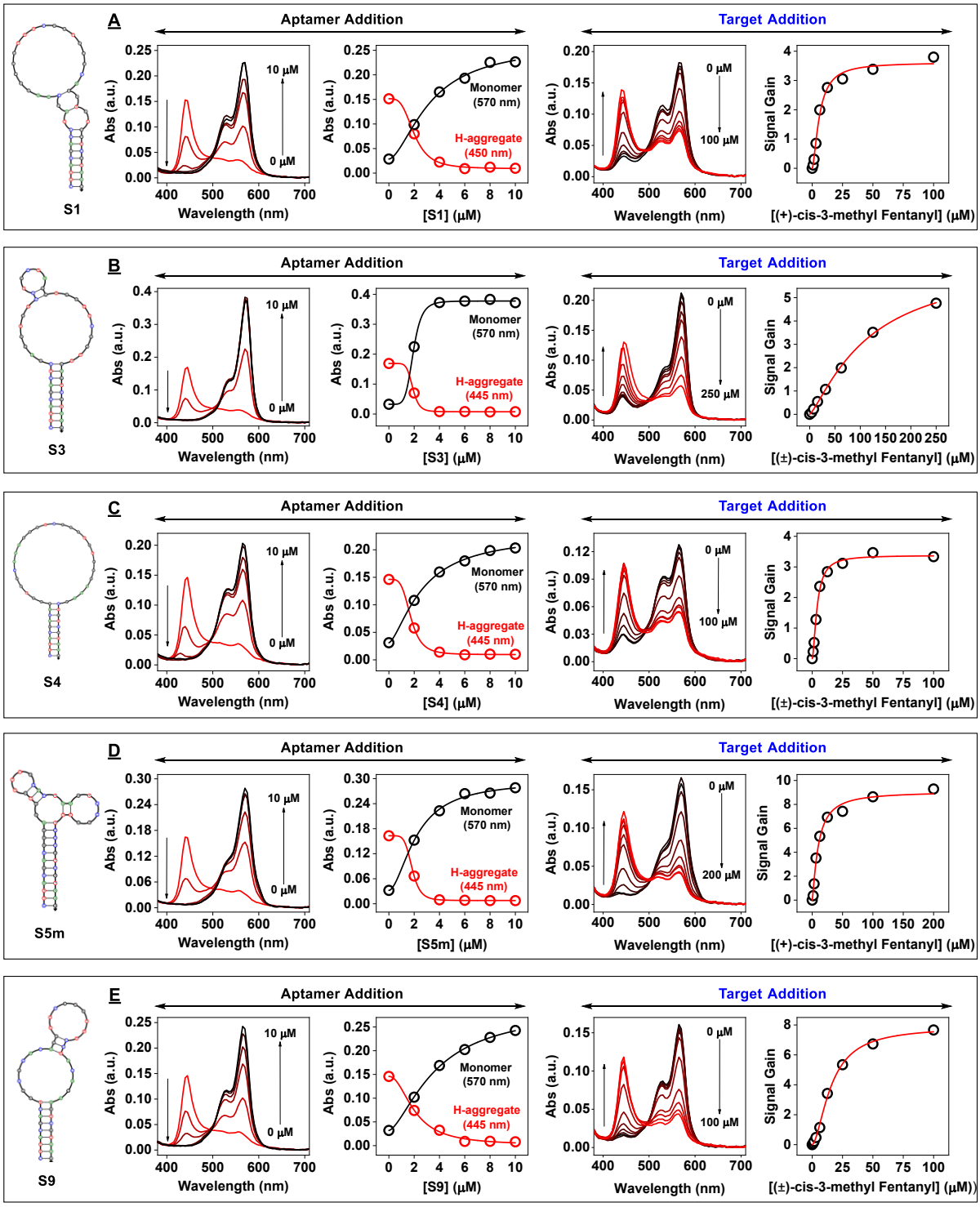

Figure S71. Target detection based on aptamer-based X-732-91B displacement assay. For each panel, from left to right are: Secondary structure of the aptamer predicted by NUPACK; 'aptamer addition', which presents the absorbance spectra of 4 μM X-732-91B with various concentrations of aptamer and a plot of X-732-91B monomer and H-aggregate peak absorbance (respectively at 570 nm and 445-450 nm) against aptamer concentration; and 'target addition', which presents the absorption spectra of solutions containing aptamer-X-732-91B complex challenged with various concentrations of target as well as plot depicting the calibration curve for target detection. (**A**) S1, (**B**) S3, (**C**) S4, (**D**) S5m and (**E**) S9.

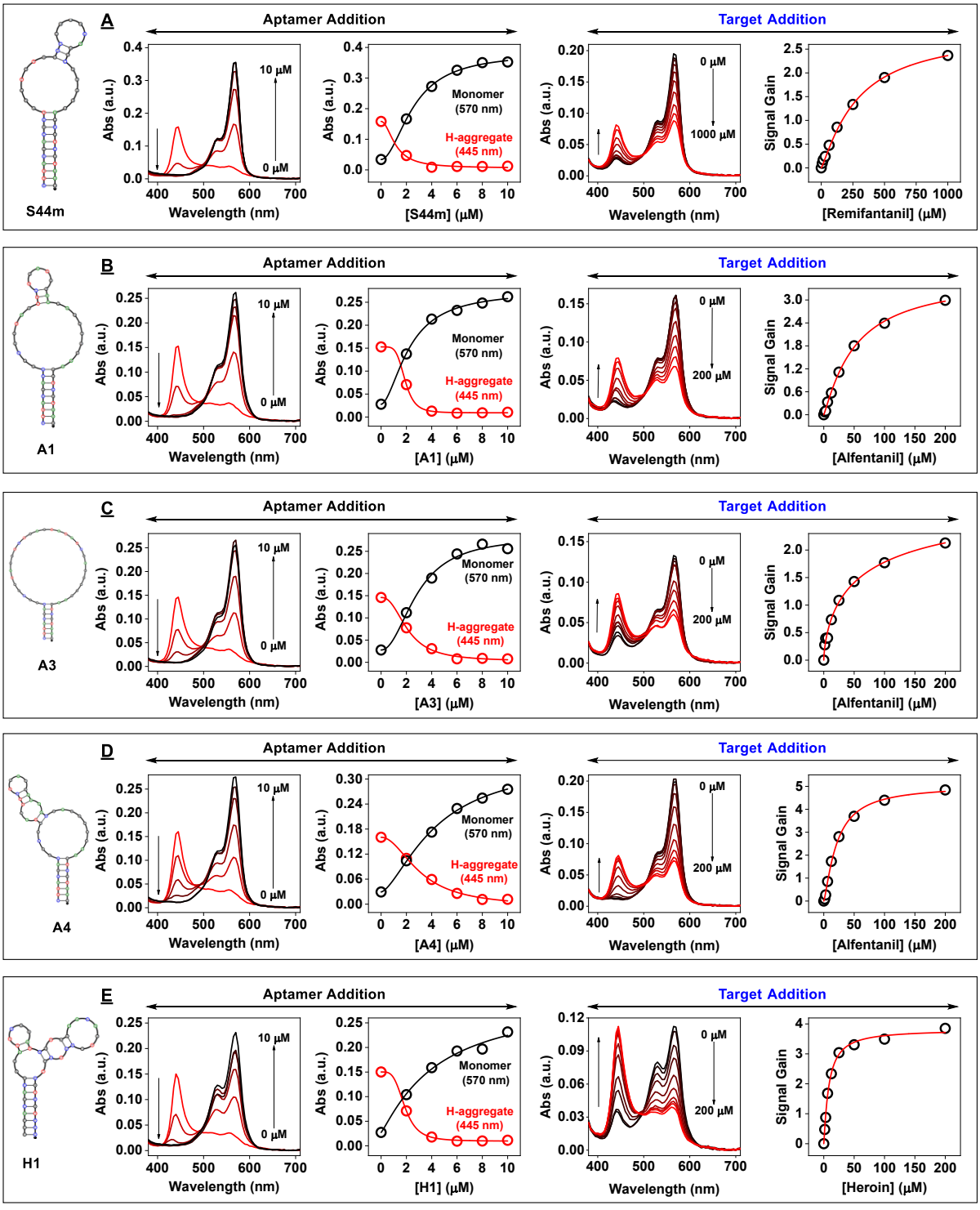

Figure S72. Target detection based on aptamer-based X-732-91B displacement assay. For each panel, from left to right are: Secondary structure of the aptamer predicted by NUPACK; 'aptamer addition', which presents the absorbance spectra of 4 μM X-732-91B with various concentrations of aptamer and a plot of X-732-91B monomer and H-aggregate peak absorbance (respectively at 570 nm and 445 nm) against aptamer concentration; and 'target addition', which presents the absorption spectra of solutions containing aptamer-X-732-91B complex challenged with various concentrations of target as well as plot depicting the calibration curve for target detection. (**A**) S44m, (**B**) A1, (**C**) A3, (**D**) A4 and (**E**) H1.

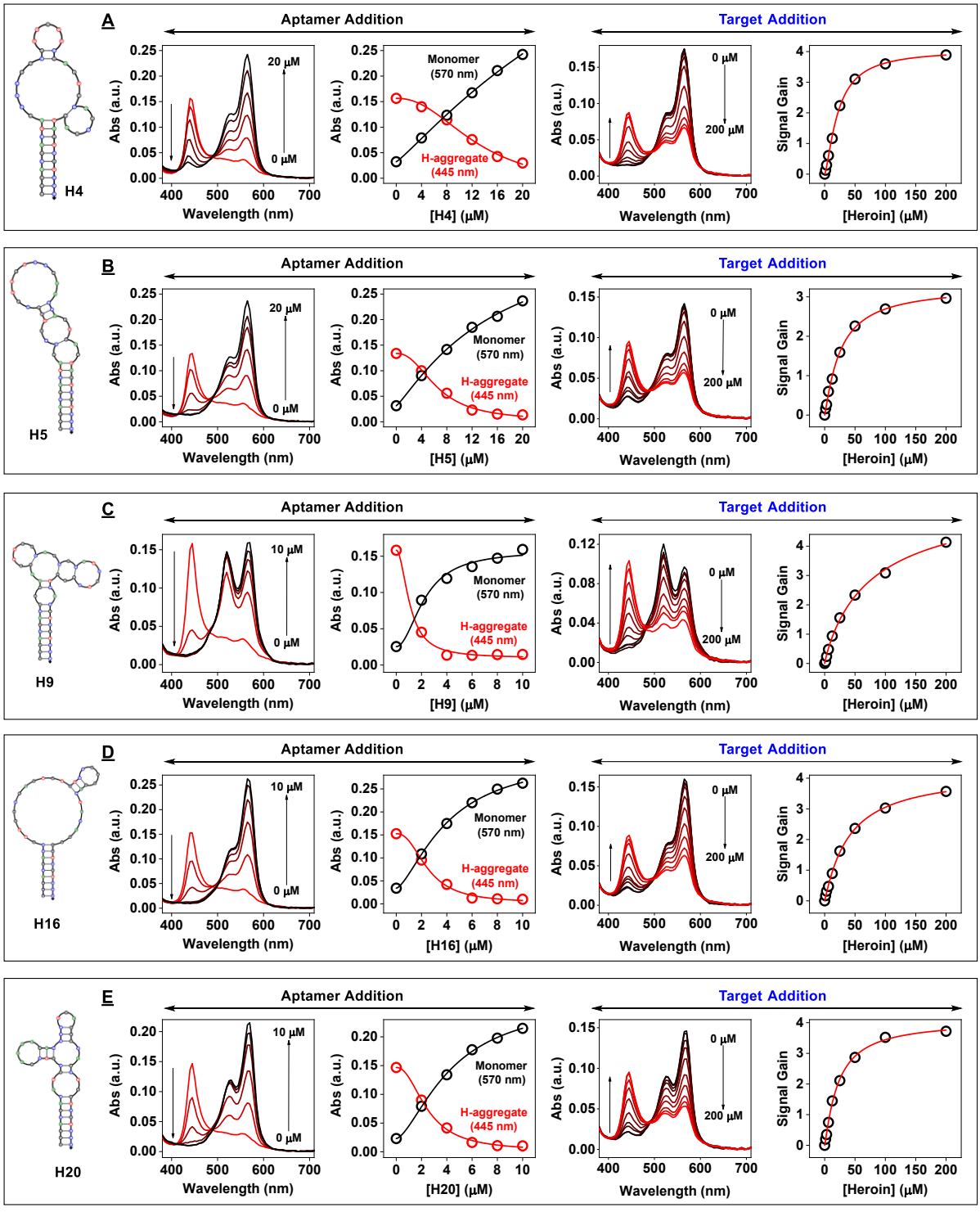

Figure S73. Target detection based on aptamer-based X-732-91B displacement assay. For each panel, from left to right are: Secondary structure of the aptamer predicted by NUPACK; 'aptamer addition', which presents the absorbance spectra of 4 μM X-732-91B with various concentrations of aptamer and a plot of X-732-91B monomer and H-aggregate peak absorbance (respectively at 570 nm and 445 nm) against aptamer concentration; and 'target addition', which presents the absorption spectra of solutions containing aptamer-X-732-91B complex challenged with various concentrations of target as well as plot depicting the calibration curve for target detection. (**A**) H4, (**B**) H5, (**C**) H9, (**D**) H16 and (**E**) H20.

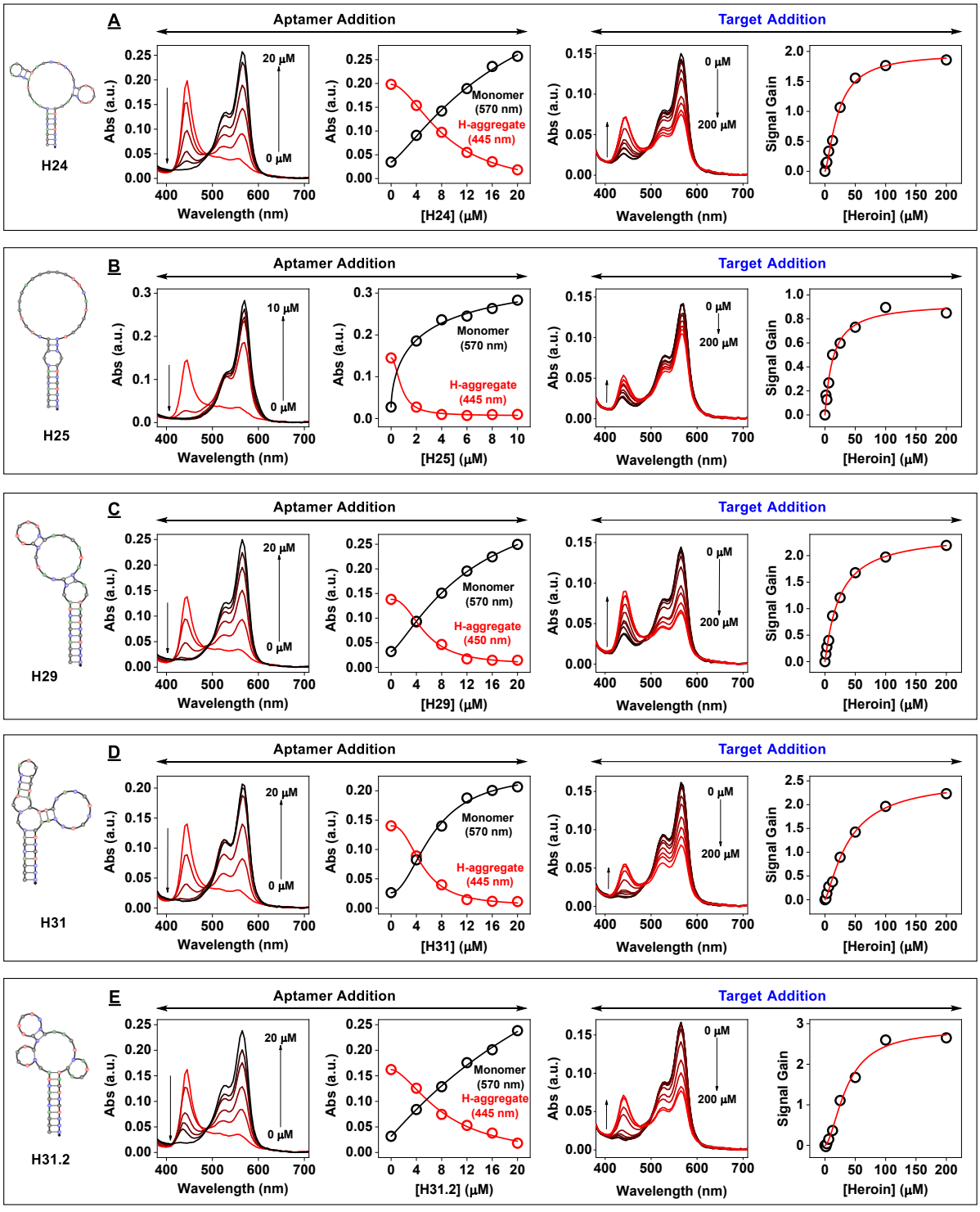

Figure S74. Target detection based on aptamer-based X-732-91B displacement assay. For each panel, from left to right are: Secondary structure of the aptamer predicted by NUPACK; 'aptamer addition', which presents the absorbance spectra of 4 μM X-732-91B with various concentrations of aptamer and a plot of X-732-91B monomer and H-aggregate peak absorbance (respectively at 570 nm and 445-450 nm) against aptamer concentration; and 'target addition', which presents the absorption spectra of solutions containing aptamer-X-732-91B complex challenged with various concentrations of target as well as plot depicting the calibration curve for target detection. (**A**) H24, (**B**) H25, (**C**) H29, (**D**) H31 and (**E**) H31.2.

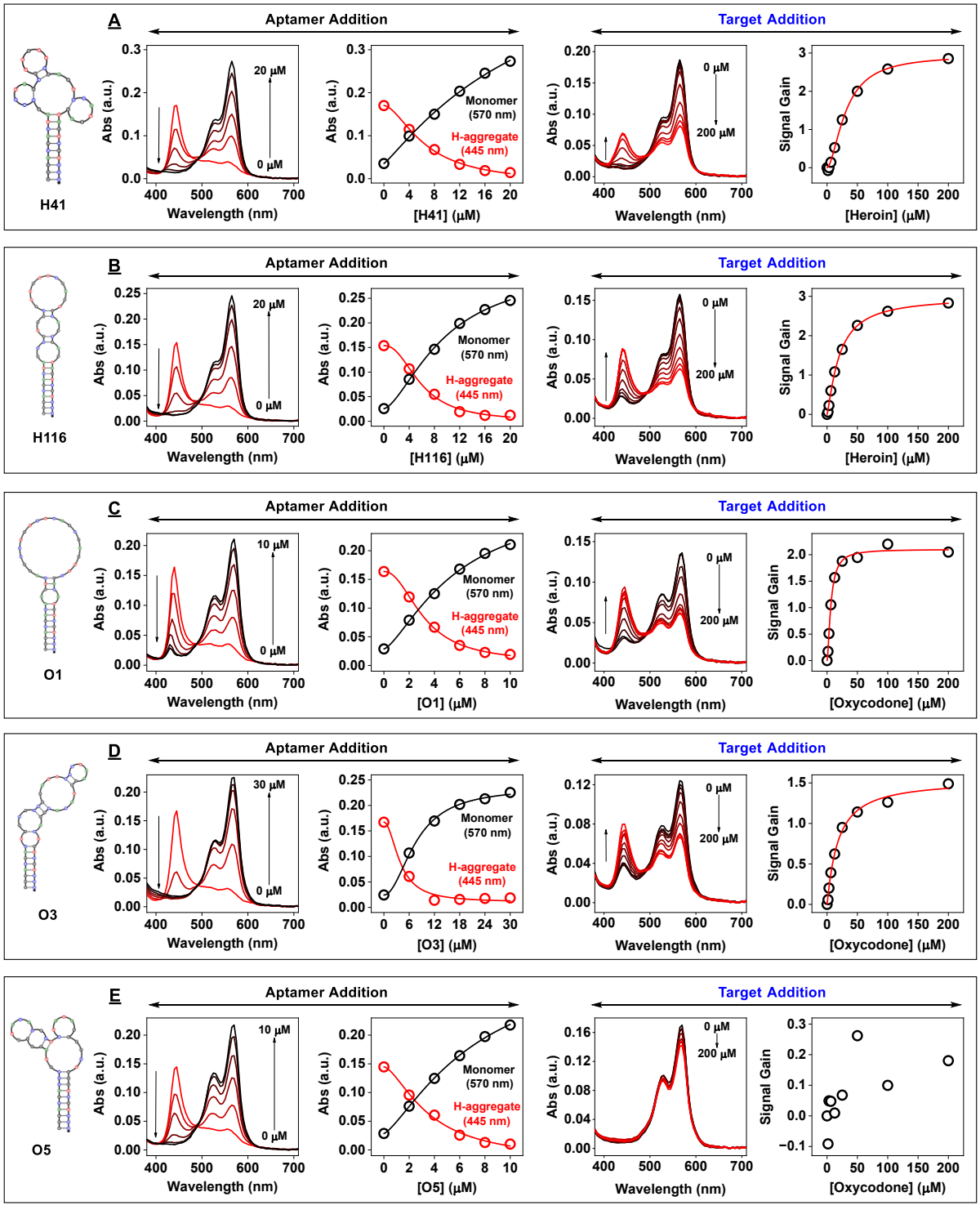

Figure S75. Target detection based on aptamer-based X-732-91B displacement assay. For each panel, from left to right are: Secondary structure of the aptamer predicted by NUPACK; 'aptamer addition', which presents the absorbance spectra of 4 μM X-732-91B with various concentrations of aptamer and a plot of X-732-91B monomer and H-aggregate peak absorbance (respectively at 570 nm and 445 nm) against aptamer concentration; and 'target addition', which presents the absorption spectra of solutions containing aptamer-X-732-91B complex challenged with various concentrations of target as well as plot depicting the calibration curve for target detection. (**A**) H41, (**B**) H116, (**C**) O1, (**D**) O3 and (**E**) O5.

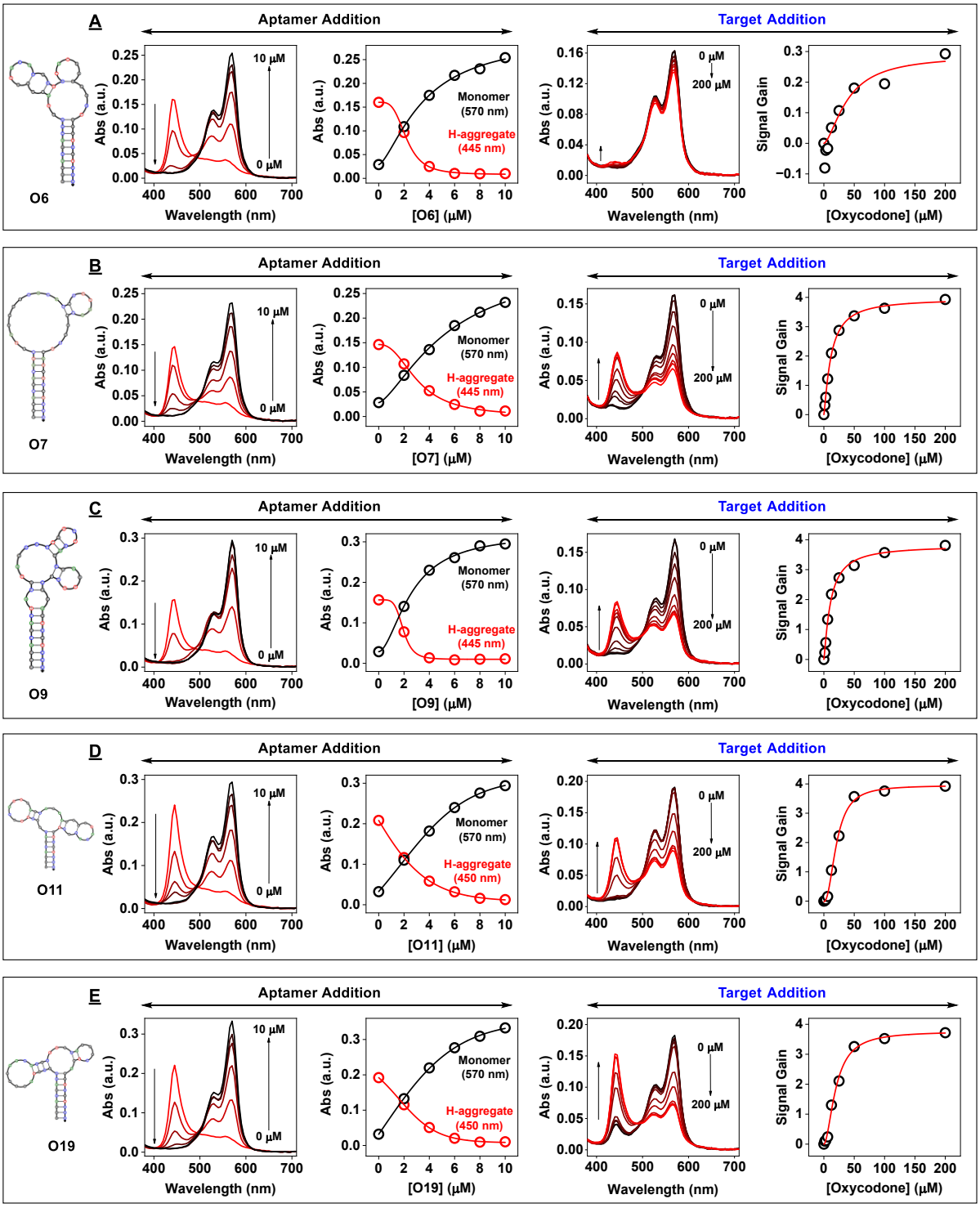

Figure S76. Target detection based on aptamer-based X-732-91B displacement assay. For each panel, from left to right are: Secondary structure of the aptamer predicted by NUPACK; 'aptamer addition', which presents the absorbance spectra of 4 μM X-732-91B with various concentrations of aptamer and a plot of X-732-91B monomer and H-aggregate peak absorbance (respectively at 570 nm and 445-450 nm) against aptamer concentration; and 'target addition', which presents the absorption spectra of solutions containing aptamer-X-732-91B complex challenged with various concentrations of target as well as plot depicting the calibration curve for target detection. (**A**) O6, (**B**) O7, (**C**) O9, (**D**) O11 and (**E**) O19.

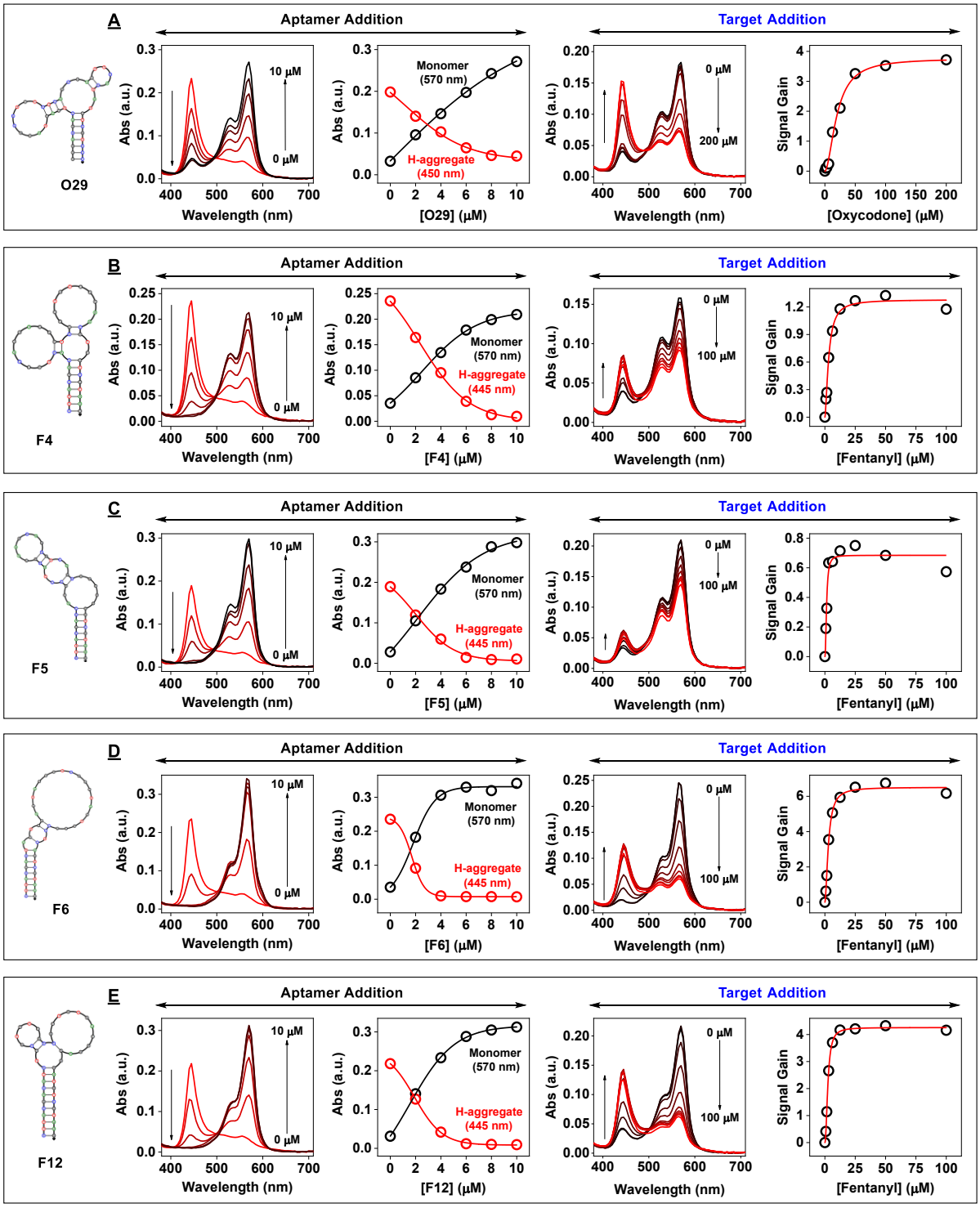

Figure S77. Target detection based on aptamer-based X-732-91B displacement assay. For each panel, from left to right are: Secondary structure of the aptamer predicted by NUPACK; 'aptamer addition', which presents the absorbance spectra of 4 µM X-732-91B with various concentrations of aptamer and a plot of X-732-91B monomer and H-aggregate peak absorbance (respectively at 570 nm and 445-450 nm) against aptamer concentration; and 'target addition', which presents the absorption spectra of solutions containing aptamer-X-732-91B complex challenged with various concentrations of target as well as plot depicting the calibration curve for target detection. (**A**) O29, (**B**) F4, (**C**) F5, (**D**) F6 and (**E**) F12.

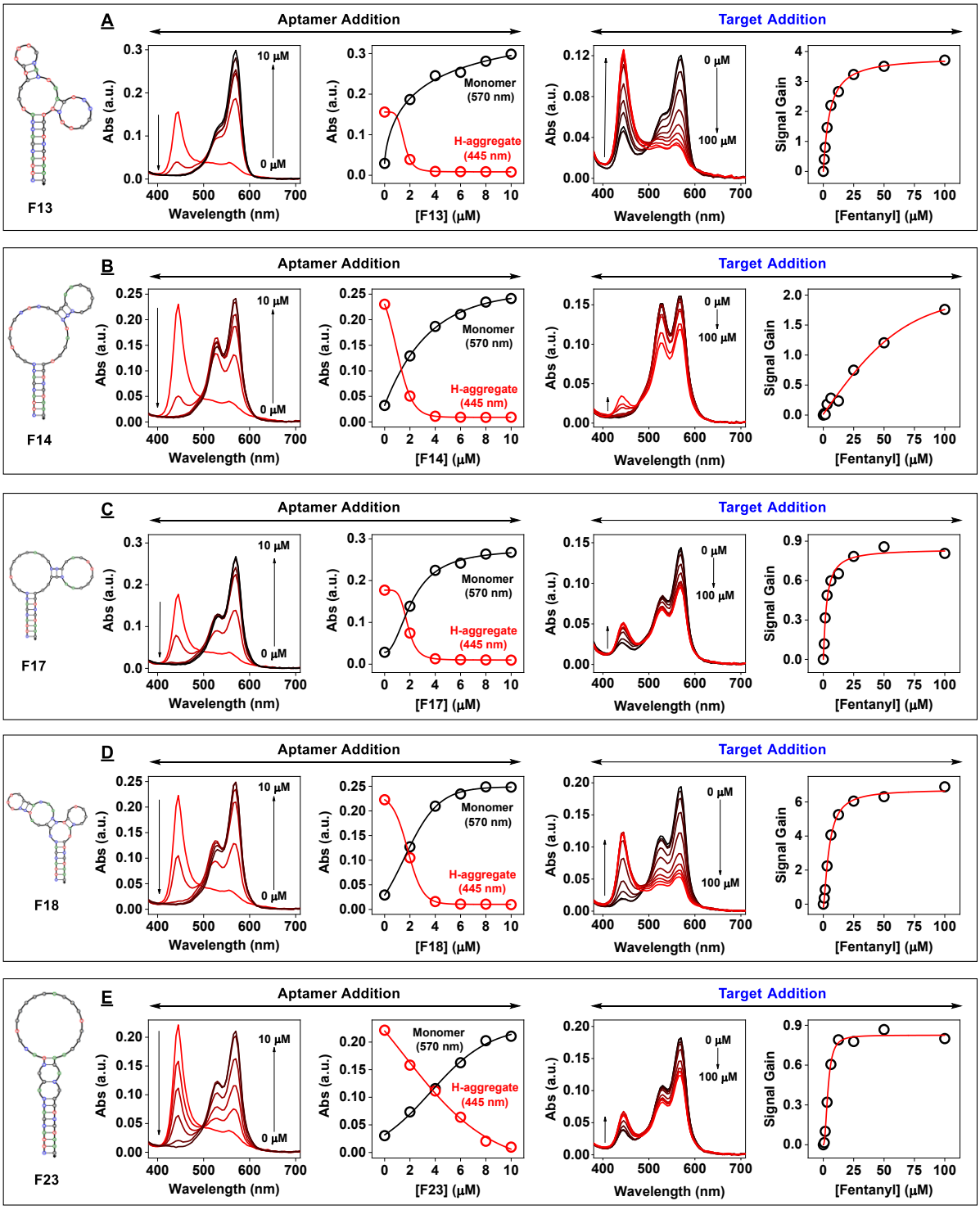

Figure S78. Target detection based on aptamer-based X-732-91B displacement assay. For each panel, from left to right are: Secondary structure of the aptamer predicted by NUPACK; 'aptamer addition', which presents the absorbance spectra of 4 µM X-732-91B with various concentrations of aptamer and a plot of X-732-91B monomer and H-aggregate peak absorbance (respectively at 570 nm and 445 nm) against aptamer concentration; and 'target addition', which presents the absorption spectra of solutions containing aptamer-X-732-91B complex challenged with various concentrations of target as well as plot depicting the calibration curve for target detection. (**A**) F13, (**B**) F14, (**C**) F17, (**D**) F18 and (**E**) F23.

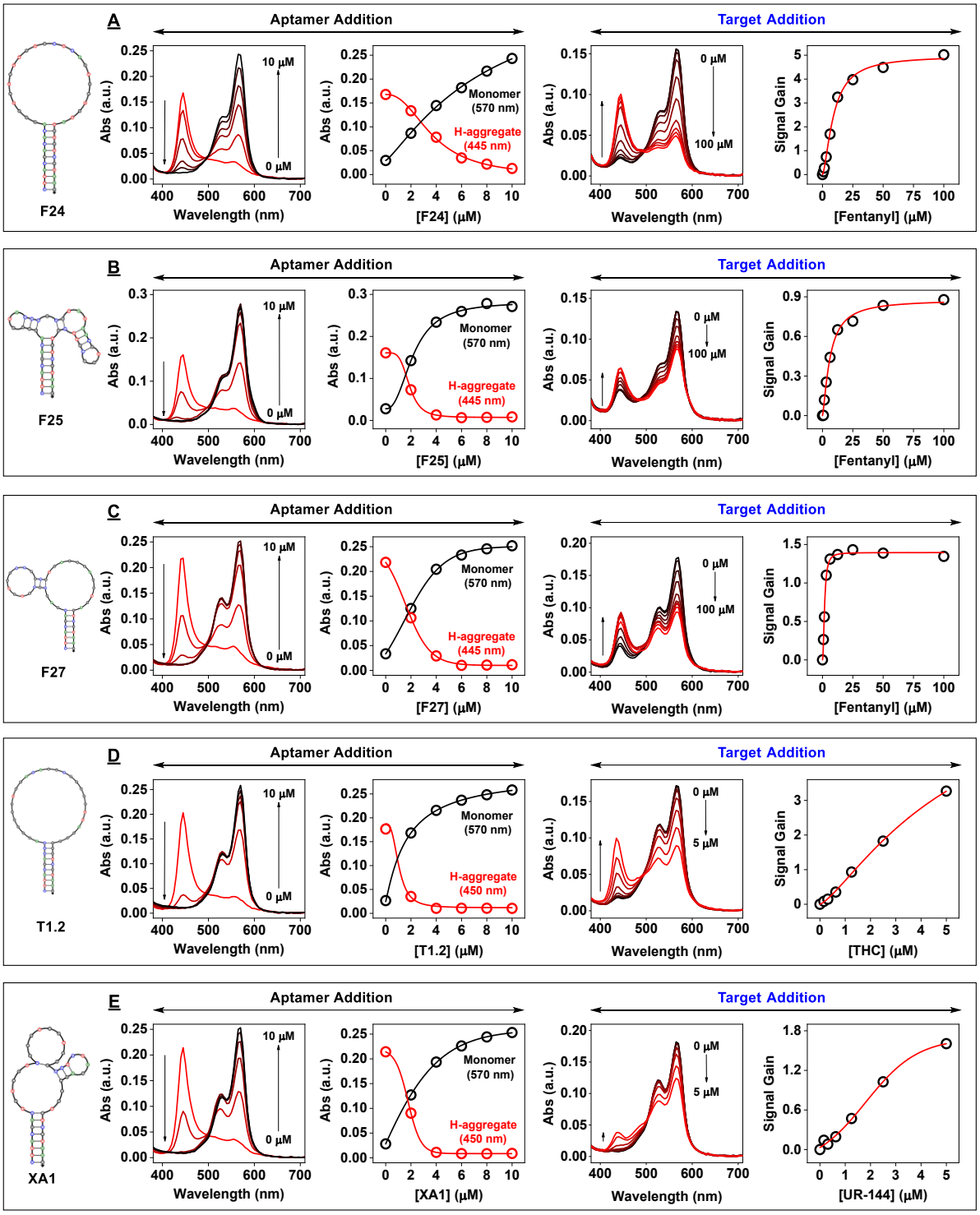

Figure S79. Target detection based on aptamer-based X-732-91B displacement assay. For each panel, from left to right are: Secondary structure of the aptamer predicted by NUPACK; 'aptamer addition', which presents the absorbance spectra of 4 µM X-732-91B with various concentrations of aptamer and a plot of X-732-91B monomer and H-aggregate peak absorbance (respectively at 570 nm and 445-450 nm) against aptamer concentration; and 'target addition', which presents the absorption spectra of solutions containing aptamer-X-732-91B complex challenged with various concentrations of target as well as plot depicting the calibration curve for target detection. (**A**) F24, (**B**) F25, (**C**) F27, (**D**) T1.2 and (**E**) XA1.

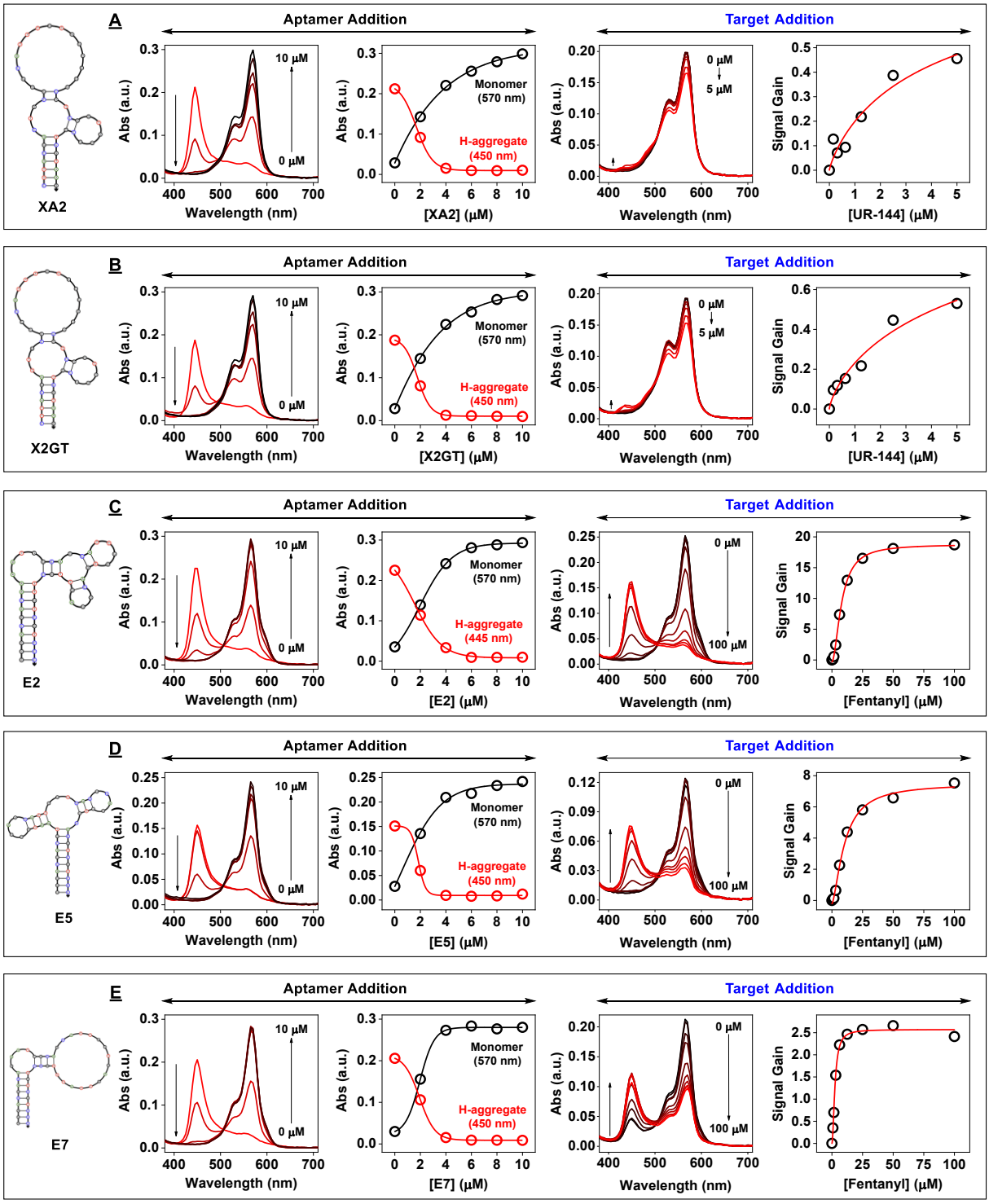

Figure S80. Target detection based on aptamer-based X-732-91B displacement assay. For each panel, from left to right are: Secondary structure of the aptamer predicted by NUPACK; 'aptamer addition', which presents the absorbance spectra of 4 µM X-732-91B with various concentrations of aptamer and a plot of X-732-91B monomer and H-aggregate peak absorbance (respectively at 570 nm and 445-450 nm) against aptamer concentration; and 'target addition', which presents the absorption spectra of solutions containing aptamer-X-732-91B complex challenged with various concentrations of target as well as plot depicting the calibration curve for target detection. (**A**) XA2, (**B**) X2GT, (**C**) E2, (**D**) E5 and (**E**) E7.

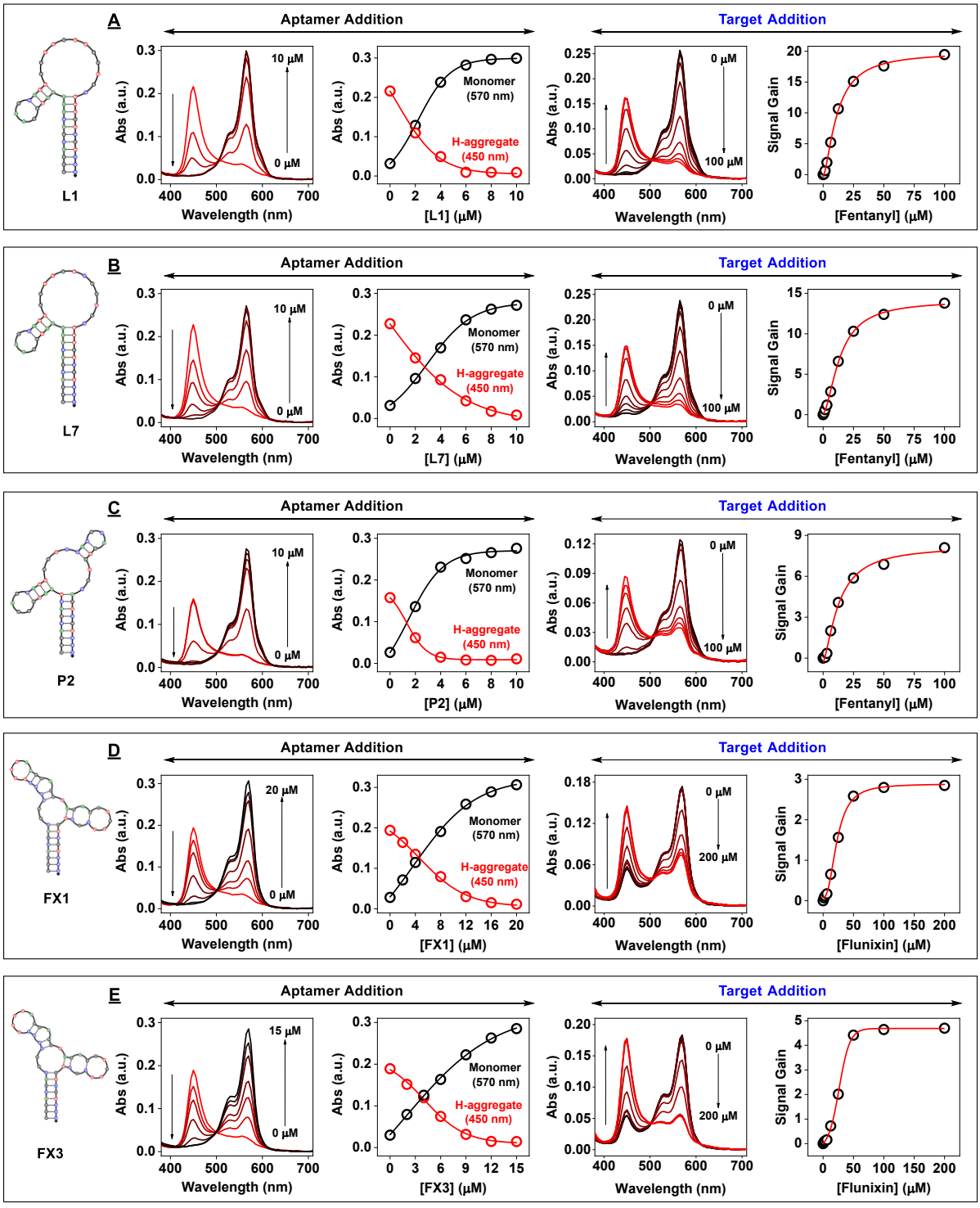

Figure S81. Target detection based on aptamer-based X-732-91B displacement assay. For each panel, from left to right are: Secondary structure of the aptamer predicted by NUPACK; 'aptamer addition', which presents the absorbance spectra of 4 μM X-732-91B with various concentrations of aptamer and a plot of X-732-91B monomer and H-aggregate peak absorbance (respectively at 570 nm and 450 nm) against aptamer concentration; and 'target addition', which presents the absorption spectra of solutions containing aptamer-X-732-91B complex challenged with various concentrations of target as well as plot depicting the calibration curve for target detection. (**A**) L1, (**B**) L7, (**C**) P2, (**D**) FX1 and (**E**) FX3.

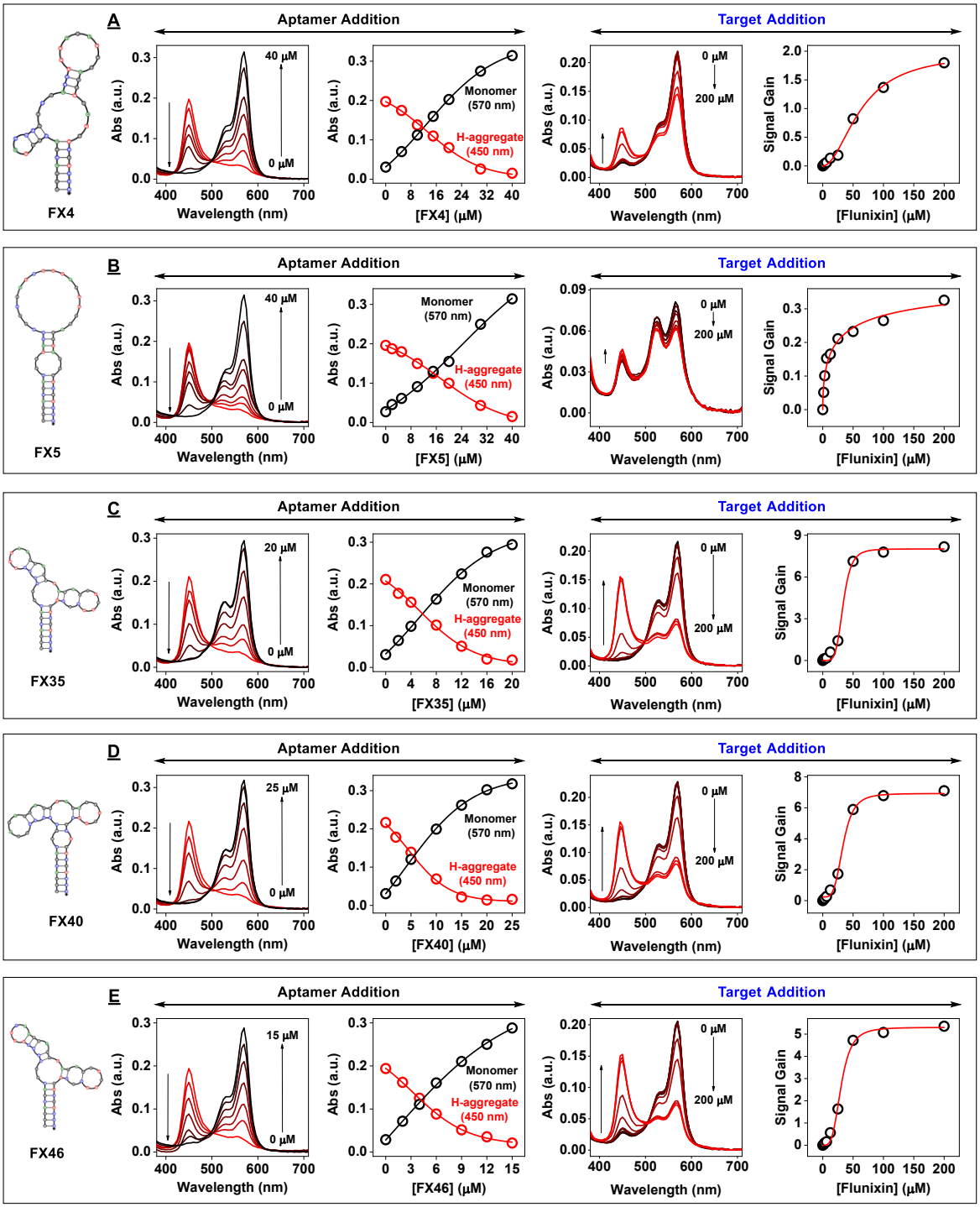

Figure S82. Target detection based on aptamer-based X-732-91B displacement assay. For each panel, from left to right are: Secondary structure of the aptamer predicted by NUPACK; 'aptamer addition', which presents the absorbance spectra of 4 µM X-732-91B with various concentrations of aptamer and a plot of X-732-91B monomer and H-aggregate peak absorbance (respectively at 570 nm and 450 nm) against aptamer concentration; and 'target addition', which presents the absorption spectra of solutions containing aptamer-X-732-91B complex challenged with various concentrations of target as well as plot depicting the calibration curve for target detection. (**A**) FX4, (**B**) FX5, (**C**) FX35, (**D**) FX40 and (**E**) FX46.

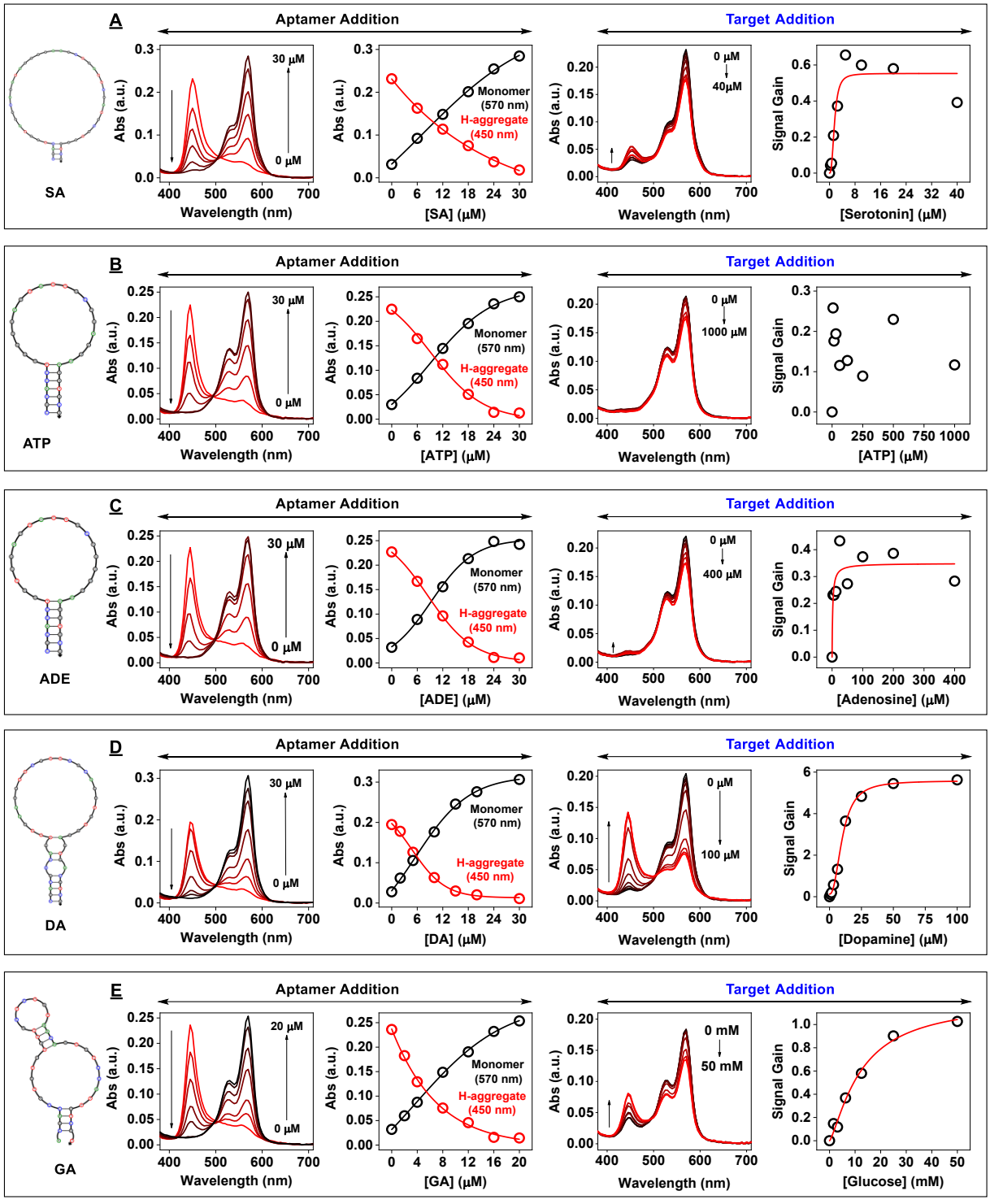

Figure S83. Target detection based on aptamer-based X-732-91B displacement assay. For each panel, from left to right are: Secondary structure of the aptamer predicted by NUPACK; 'aptamer addition', which presents the absorbance spectra of 4 μM X-732-91B with various concentrations of aptamer and a plot of X-732-91B monomer and H-aggregate peak absorbance (respectively at 570 nm and 450 nm) against aptamer concentration; and 'target addition', which presents the absorption spectra of solutions containing aptamer-X-732-91B complex challenged with various concentrations of target as well as plot depicting the calibration curve for target detection. (**A**) SA, (**B**) ATP, (**C**) ADE, (**D**) DA and (**E**) GA.

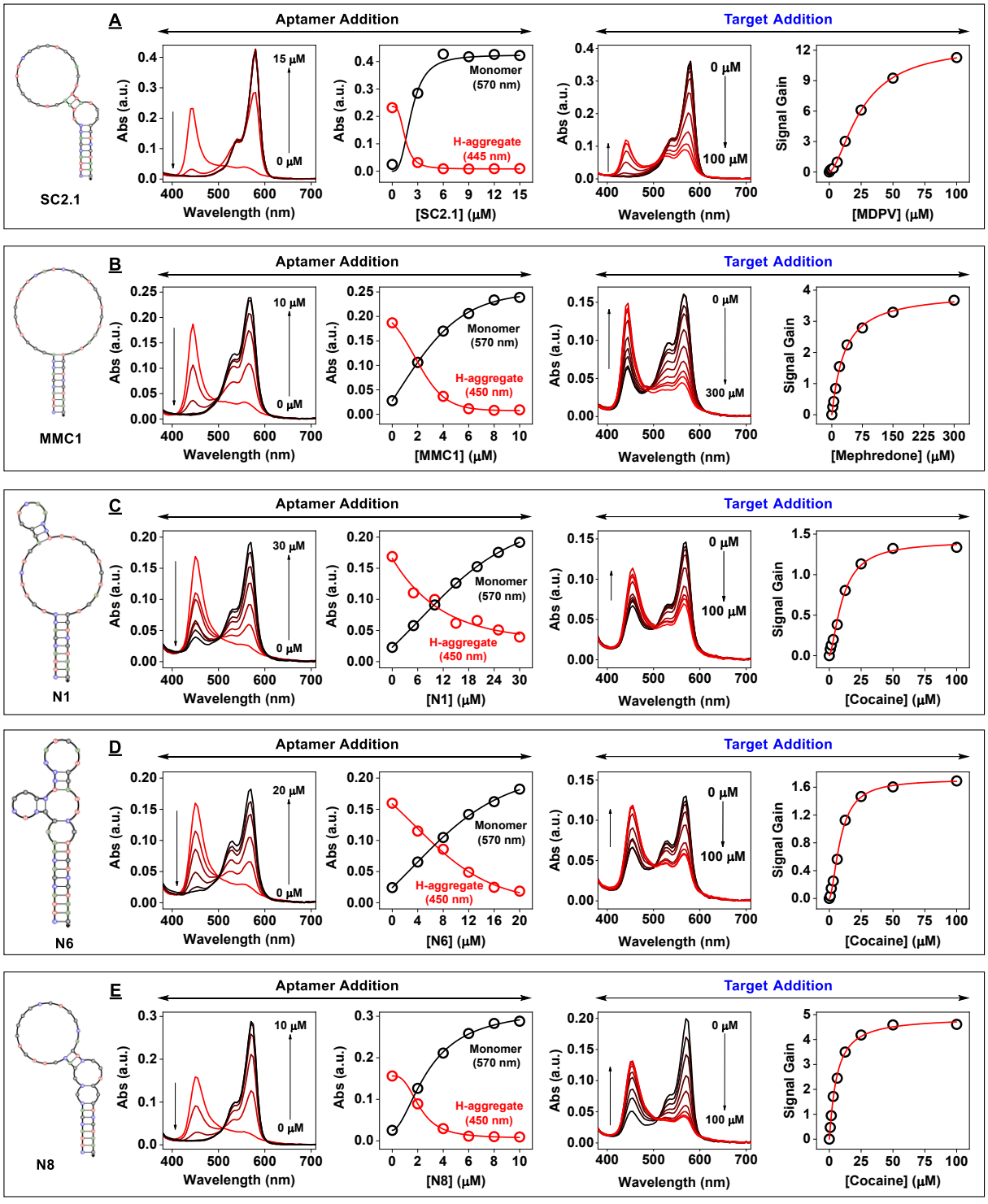

Figure S84. Target detection based on aptamer-based X-732-91B displacement assay. For each panel, from left to right are: Secondary structure of the aptamer predicted by NUPACK; 'aptamer addition', which presents the absorbance spectra of 4 µM X-732-91B with various concentrations of aptamer and a plot of X-732-91B monomer and H-aggregate peak absorbance (respectively at 570 nm and 445-450 nm) against aptamer concentration; and 'target addition', which presents the absorption spectra of solutions containing aptamer-X-732-91B complex challenged with various concentrations of target as well as plot depicting the calibration curve for target detection. (**A**) SC2.1, (**B**) MMC1, (**C**) N1, (**D**) N6 and (**E**) N8.

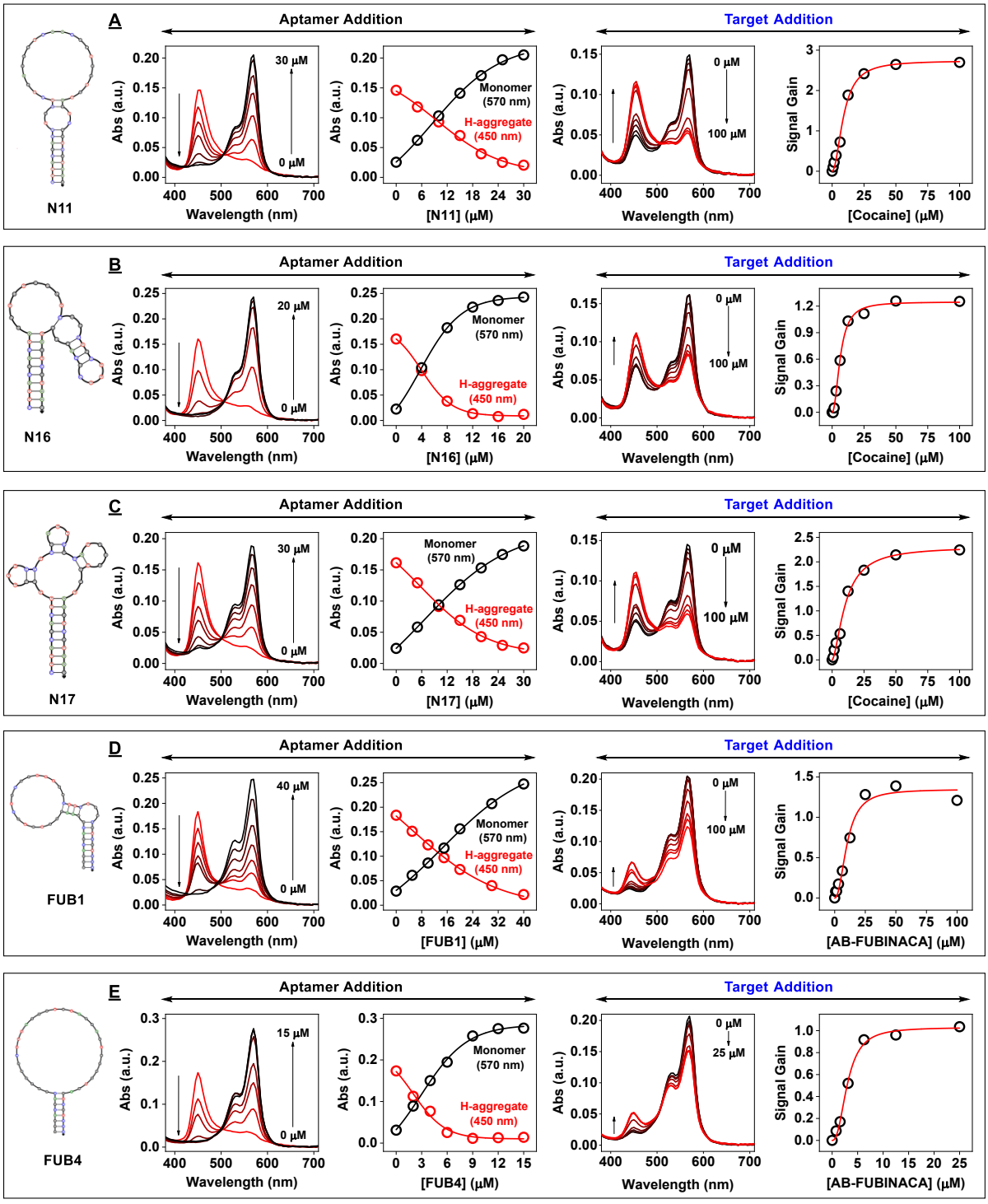

Figure S85. Target detection based on aptamer-based X-732-91B displacement assay. For each panel, from left to right are: Secondary structure of the aptamer predicted by NUPACK; 'aptamer addition', which presents the absorbance spectra of 4 µM X-732-91B with various concentrations of aptamer and a plot of X-732-91B monomer and H-aggregate peak absorbance (respectively at 570 nm and 450 nm) against aptamer concentration; and 'target addition', which presents the absorption spectra of solutions containing aptamer-X-732-91B complex challenged with various concentrations of target as well as plot depicting the calibration curve for target detection. (**A**) N11, (**B**) N16, (**C**) N17, (**D**) FUB1 and (**E**) FUB4.

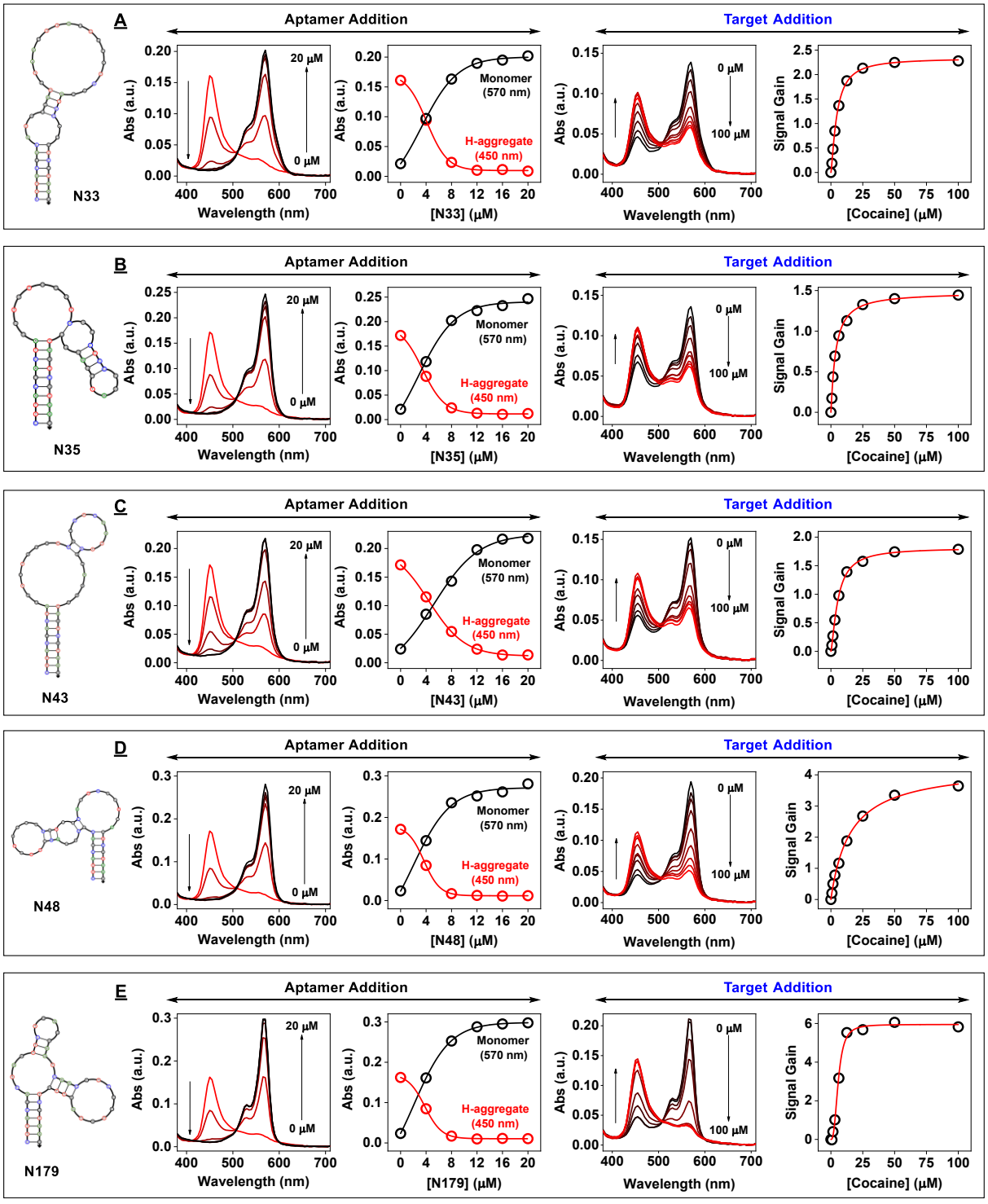

Figure S86. Target detection based on aptamer-based X-732-91B displacement assay. For each panel, from left to right are: Secondary structure of the aptamer predicted by NUPACK; 'aptamer addition', which presents the absorbance spectra of 4 μM X-732-91B with various concentrations of aptamer and a plot of X-732-91B monomer and H-aggregate peak absorbance (respectively at 570 nm and 450 nm) against aptamer concentration; and 'target addition', which presents the absorption spectra of solutions containing aptamer-X-732-91B complex challenged with various concentrations of target as well as plot depicting the calibration curve for target detection. (**A**) N33, (**B**) N35, (**C**) N43, (**D**) N48 and (**E**) N179.

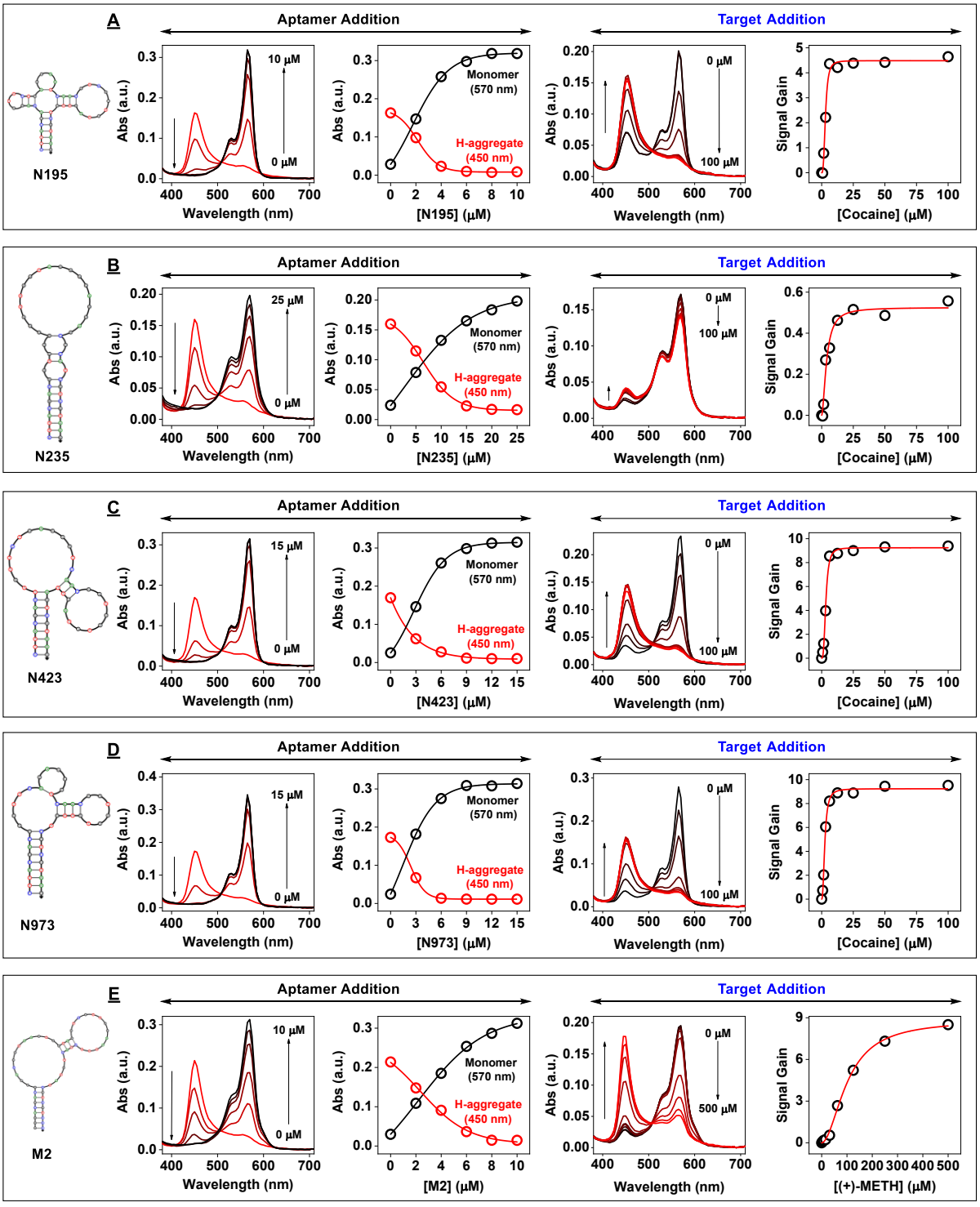

Figure S87. Target detection based on aptamer-based X-732-91B displacement assay. For each panel, from left to right are: Secondary structure of the aptamer predicted by NUPACK; 'aptamer addition', which presents the absorbance spectra of 4 μM X-732-91B with various concentrations of aptamer and a plot of X-732-91B monomer and H-aggregate peak absorbance (respectively at 570 nm and 450 nm) against aptamer concentration; and 'target addition', which presents the absorption spectra of solutions containing aptamer-X-732-91B complex challenged with various concentrations of target as well as plot depicting the calibration curve for target detection. (**A**) N195, (**B**) N235, (**C**) N423, (**D**) N973 and (**E**) M2.

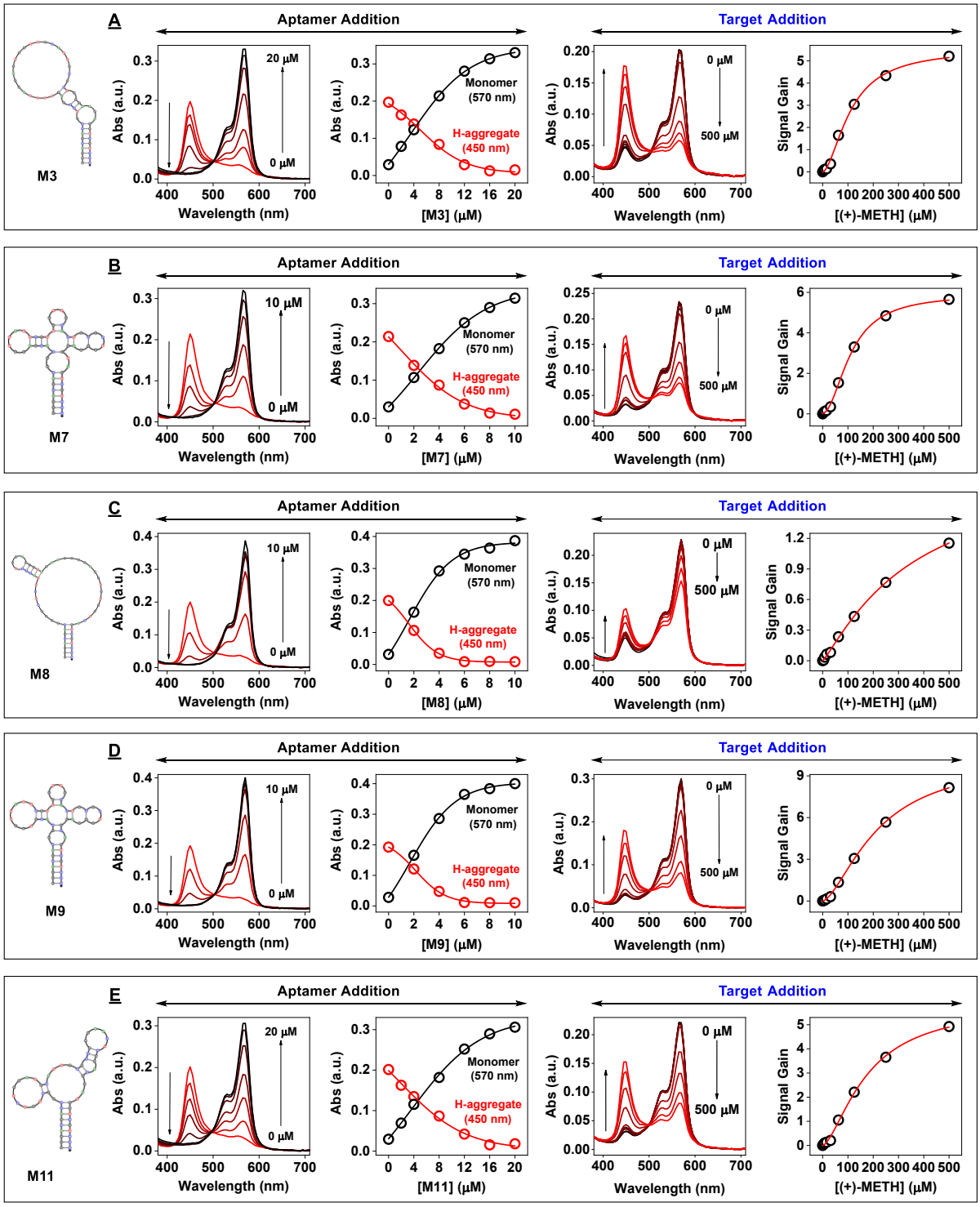

Figure S88. Target detection based on aptamer-based X-732-91B displacement assay. For each panel, from left to right are: Secondary structure of the aptamer predicted by NUPACK; 'aptamer addition', which presents the absorbance spectra of 4 µM X-732-91B with various concentrations of aptamer and a plot of X-732-91B monomer and H-aggregate peak absorbance (respectively at 570 nm and 450 nm) against aptamer concentration; and 'target addition', which presents the absorption spectra of solutions containing aptamer-X-732-91B complex challenged with various concentrations of target as well as plot depicting the calibration curve for target detection. (**A**) M3, (**B**) M7, (**C**) M8, (**D**) M9 and (**E**) M11.

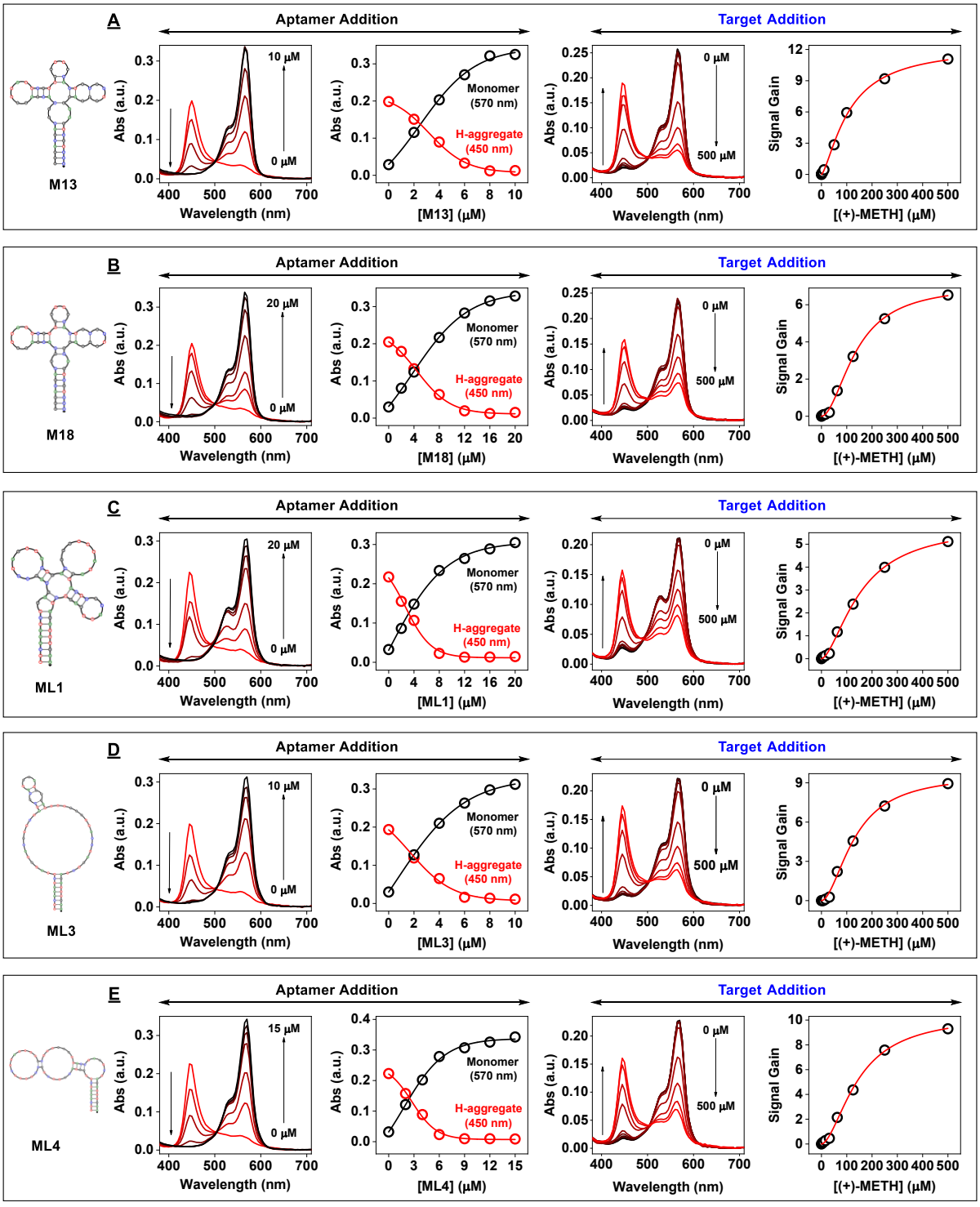

Figure S89. Target detection based on aptamer-based X-732-91B displacement assay. For each panel, from left to right are: Secondary structure of the aptamer predicted by NUPACK; 'aptamer addition', which presents the absorbance spectra of 4 µM X-732-91B with various concentrations of aptamer and a plot of X-732-91B monomer and H-aggregate peak absorbance (respectively at 570 nm and 450 nm) against aptamer concentration; and 'target addition', which presents the absorption spectra of solutions containing aptamer-X-732-91B complex challenged with various concentrations of target as well as plot depicting the calibration curve for target detection. (**A**) M13, (**B**) M18, (**C**) ML1, (**D**) ML3 and (**E**) ML4.

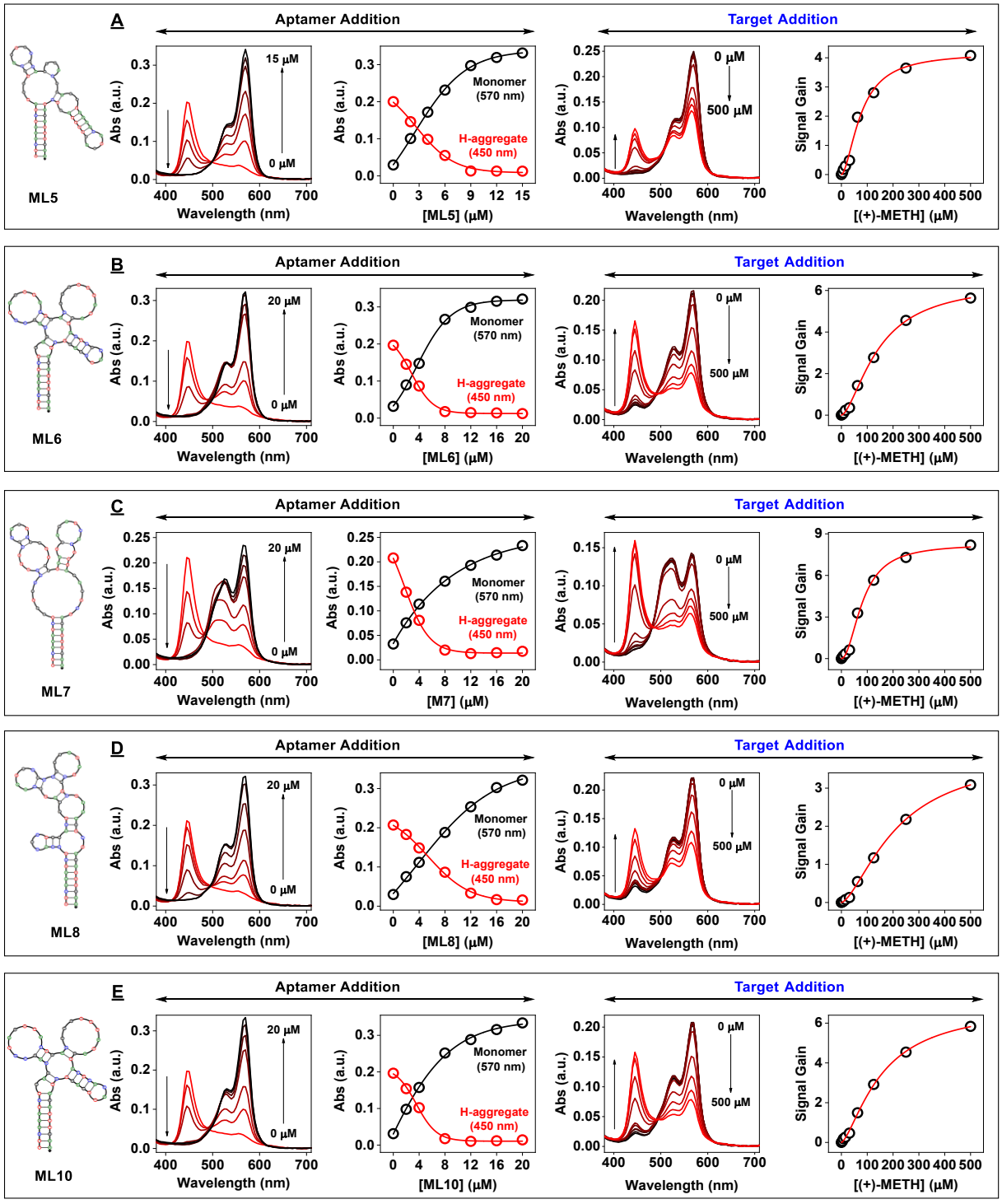

Figure S90. Target detection based on aptamer-based X-732-91B displacement assay. For each panel, from left to right are: Secondary structure of the aptamer predicted by NUPACK; 'aptamer addition', which presents the absorbance spectra of 4 μM X-732-91B with various concentrations of aptamer and a plot of X-732-91B monomer and H-aggregate peak absorbance (respectively at 570 nm and 450 nm) against aptamer concentration; and 'target addition', which presents the absorption spectra of solutions containing aptamer-X-732-91B complex challenged with various concentrations of target as well as plot depicting the calibration curve for target detection. (**A**) ML5, (**B**) ML6, (**C**) ML7, (**D**) ML8 and (**E**) ML10.

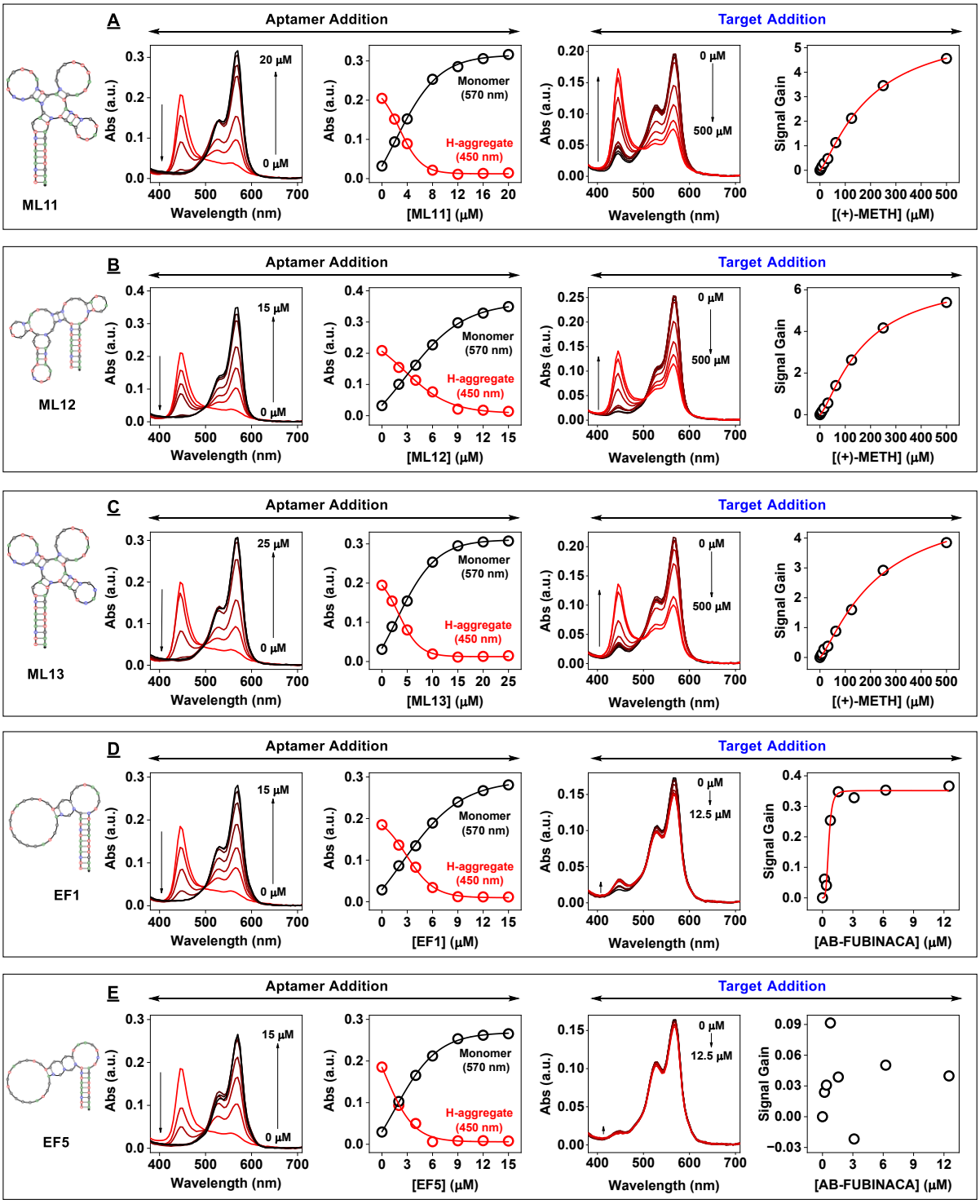

Figure S91. Target detection based on aptamer-based X-732-91B displacement assay. For each panel, from left to right are: Secondary structure of the aptamer predicted by NUPACK; 'aptamer addition', which presents the absorbance spectra of 4 µM X-732-91B with various concentrations of aptamer and a plot of X-732-91B monomer and H-aggregate peak absorbance (respectively at 570 nm and 450 nm) against aptamer concentration; and 'target addition', which presents the absorption spectra of solutions containing aptamer-X-732-91B complex challenged with various concentrations of target as well as plot depicting the calibration curve for target detection. (**A**) ML11, (**B**) ML12, (**C**) ML13, (**D**) EF1 and (**E**) EF5.

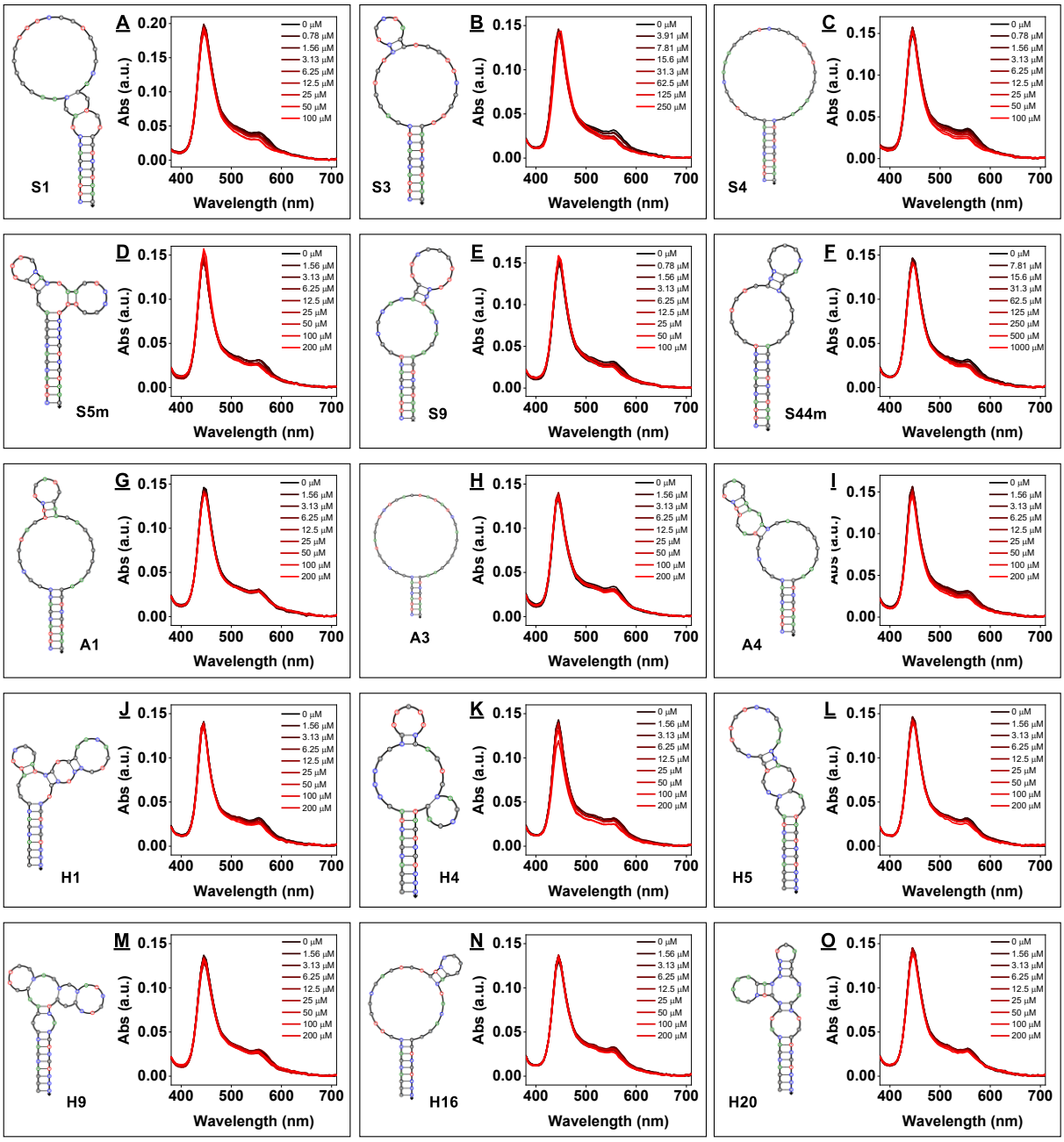

Figure S92. Absorbance spectra of 4 μM X-732-91B in the presence of different targets at various concentrations. (**A-E**) (±)-cis-3-methyl-fentanyl, (**F**) remifentanil, (**G-I**) alfentanil and (**J-O**) heroin. N/A indicated that no target control experiments were performed for that aptamer since no target-induced dye-displacement was observed. Black-to-red color gradient represents increasing concentrations of target.

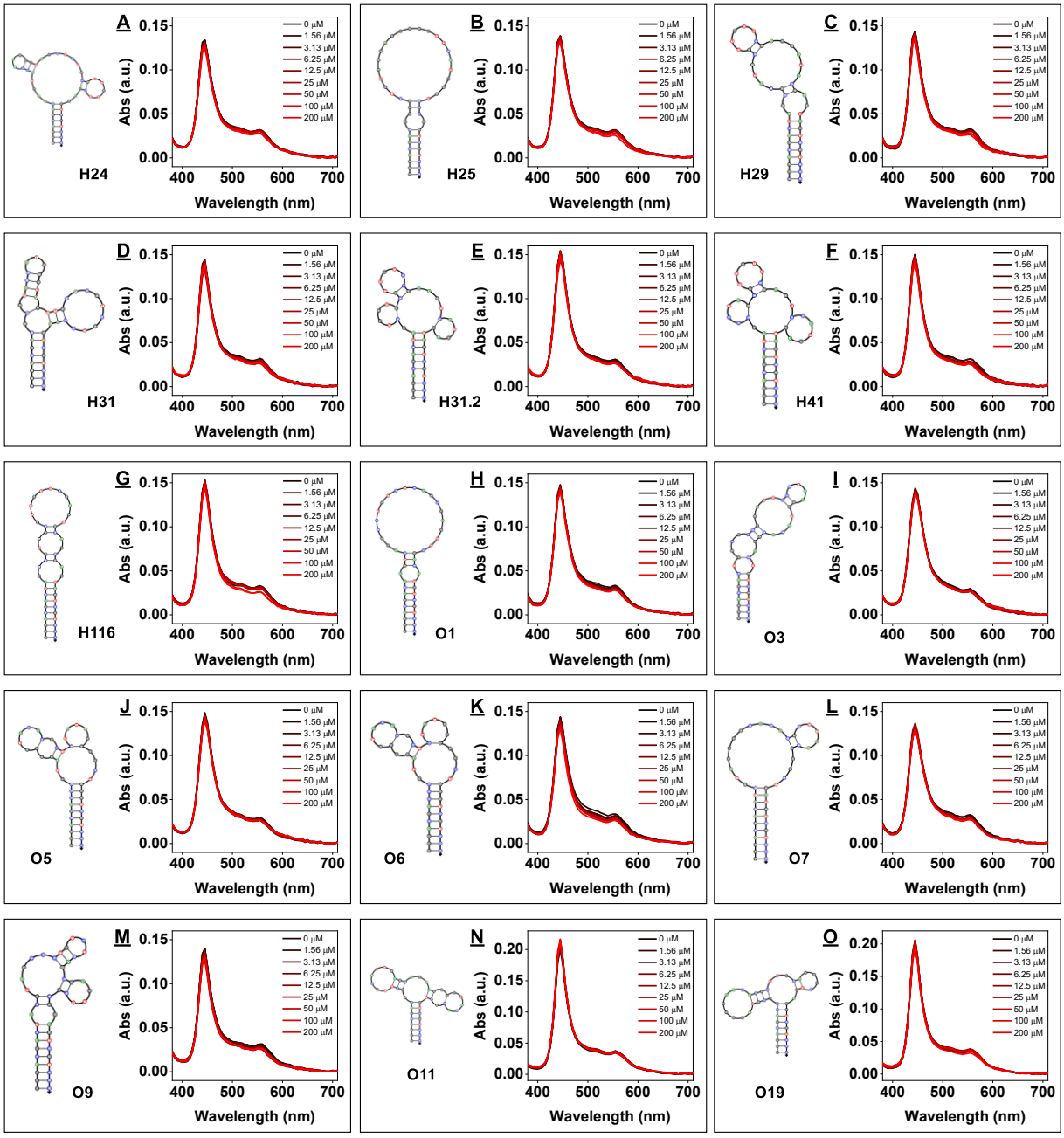

Figure S92 (continued). Absorbance spectra of 4 μM X-732-91B in the presence of different targets at various concentrations. (**A-G**) heroin and (**H-O**) oxycodone. N/A indicated that no target control experiments were performed for that aptamer since no target-induced dye-displacement was observed. Black-to-red color gradient represents increasing concentrations of target.

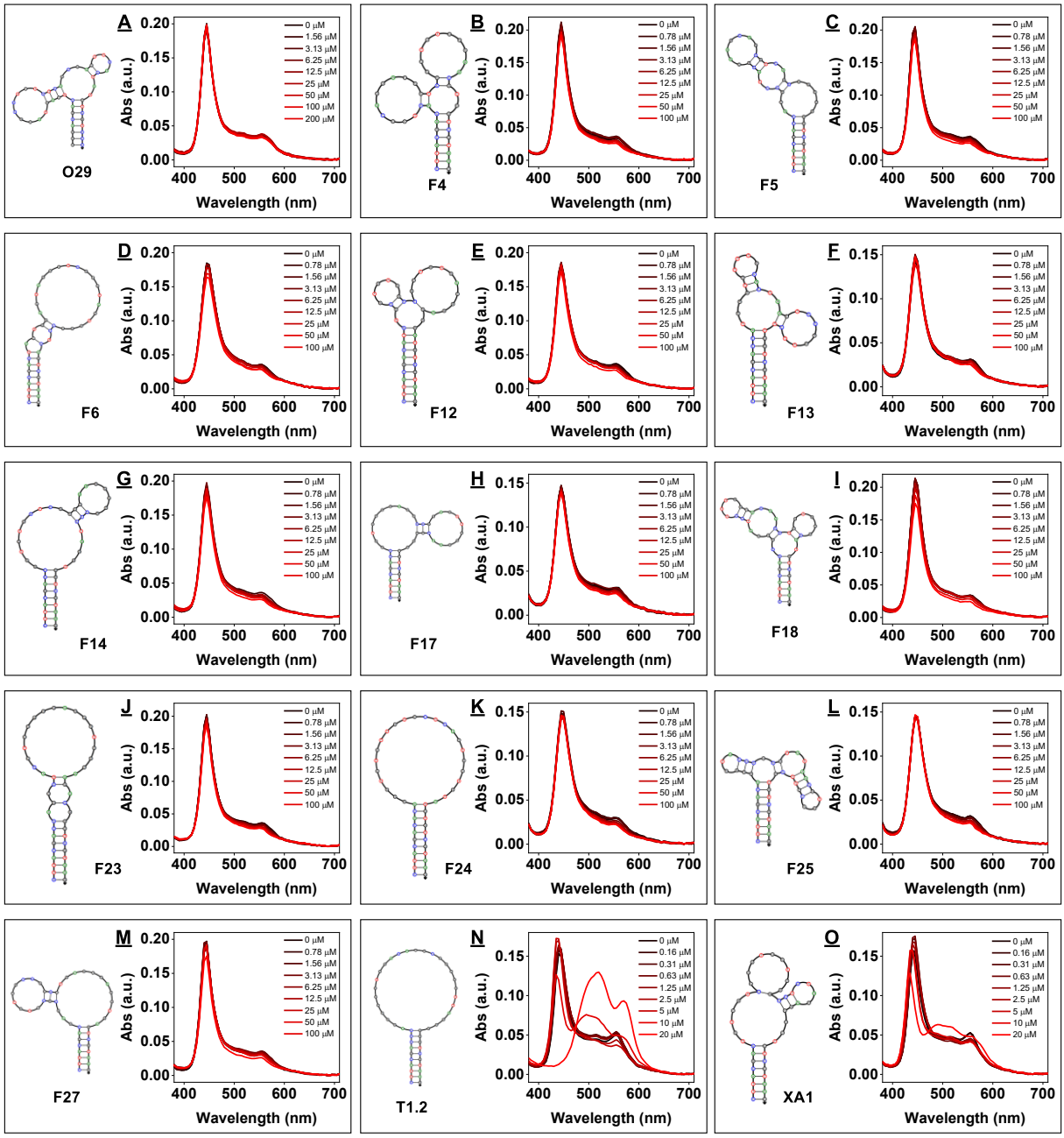

Figure S92 (continued). Absorbance spectra of 4 μM X-732-91B in the presence of different targets at various concentrations. (**A**) oxycodone, (**B-M**) fentanyl, (**N**) THC and (**O**) UR-144. Black-to-red color gradient represents increasing concentrations of target.

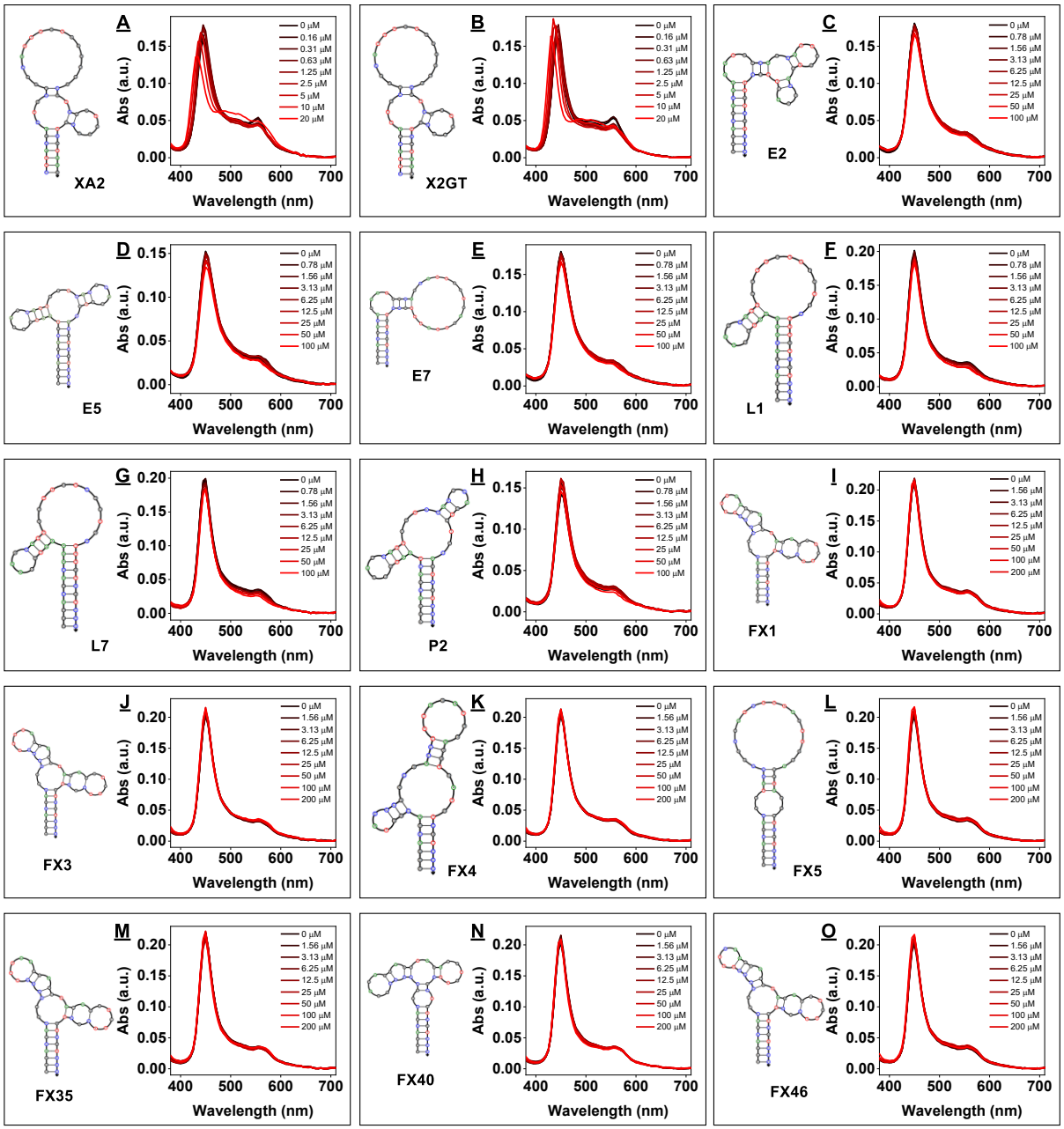

Figure S92 (continued). Absorbance spectra of 4 μM X-732-91B in the presence of different targets at various concentrations. (**A-B**) UR-144, (**C-H**) fentanyl, (**I-O**) flunixin. N/A indicated that no target control experiments were performed for that aptamer since no target-induced dye-displacement was observed. Black-to-red color gradient represents increasing concentrations of target.

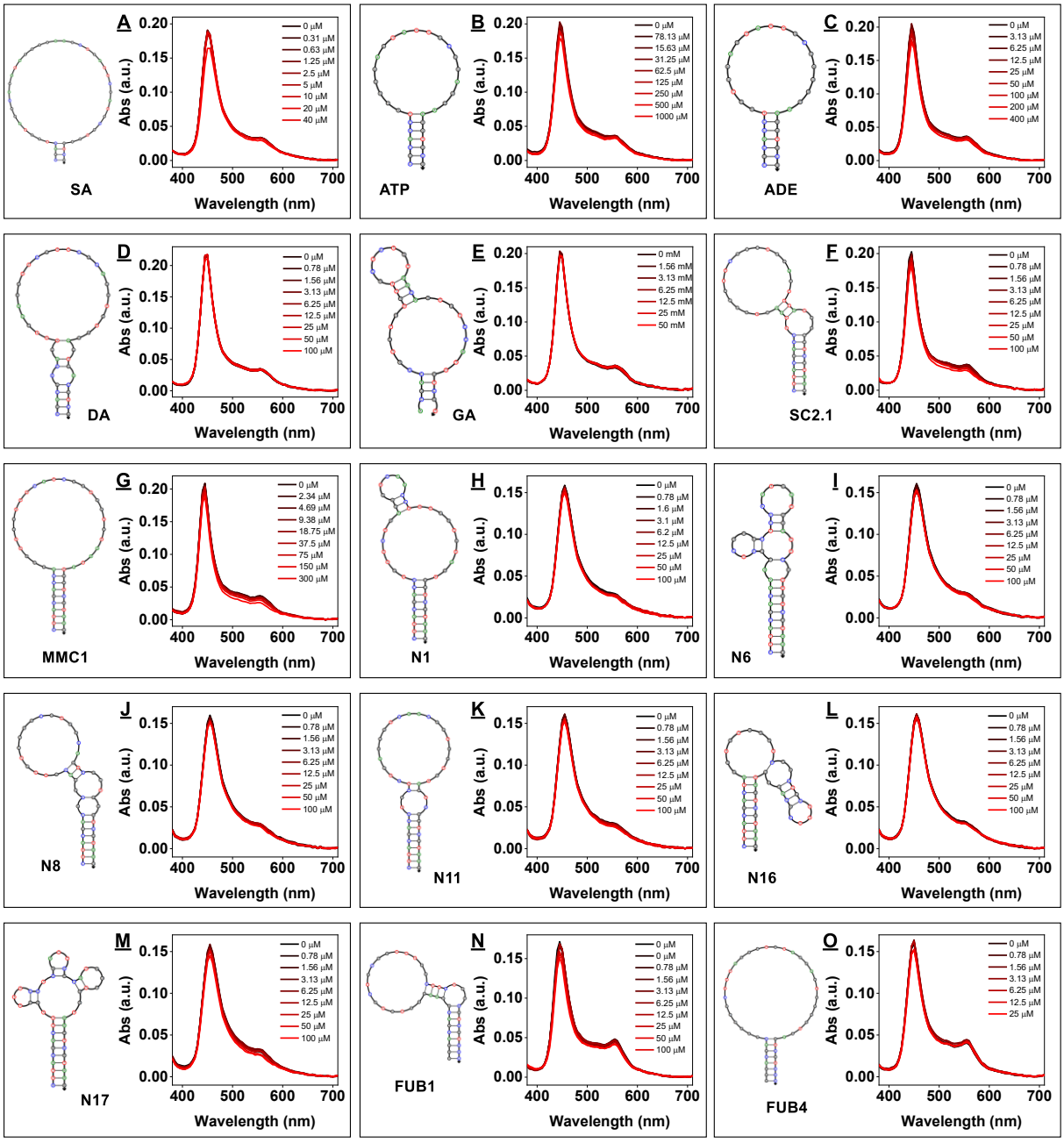

Figure S92 (continued). Absorbance spectra of 4 μM X-732-91B in the presence of different targets at various concentrations. (**A**) serotonin, (**B**) ATP, (**C**) adenosine, (**D**) dopamine, (**E**) glucose, (**F**) MDPV, (**G**) mephedrone, (**H-M**) cocaine and (**N-O**) AB-FUBINACA. N/A indicated that no target control experiments were performed for that aptamer since no target-induced dye-displacement was observed. Black-to-red color gradient represents increasing concentrations of target.

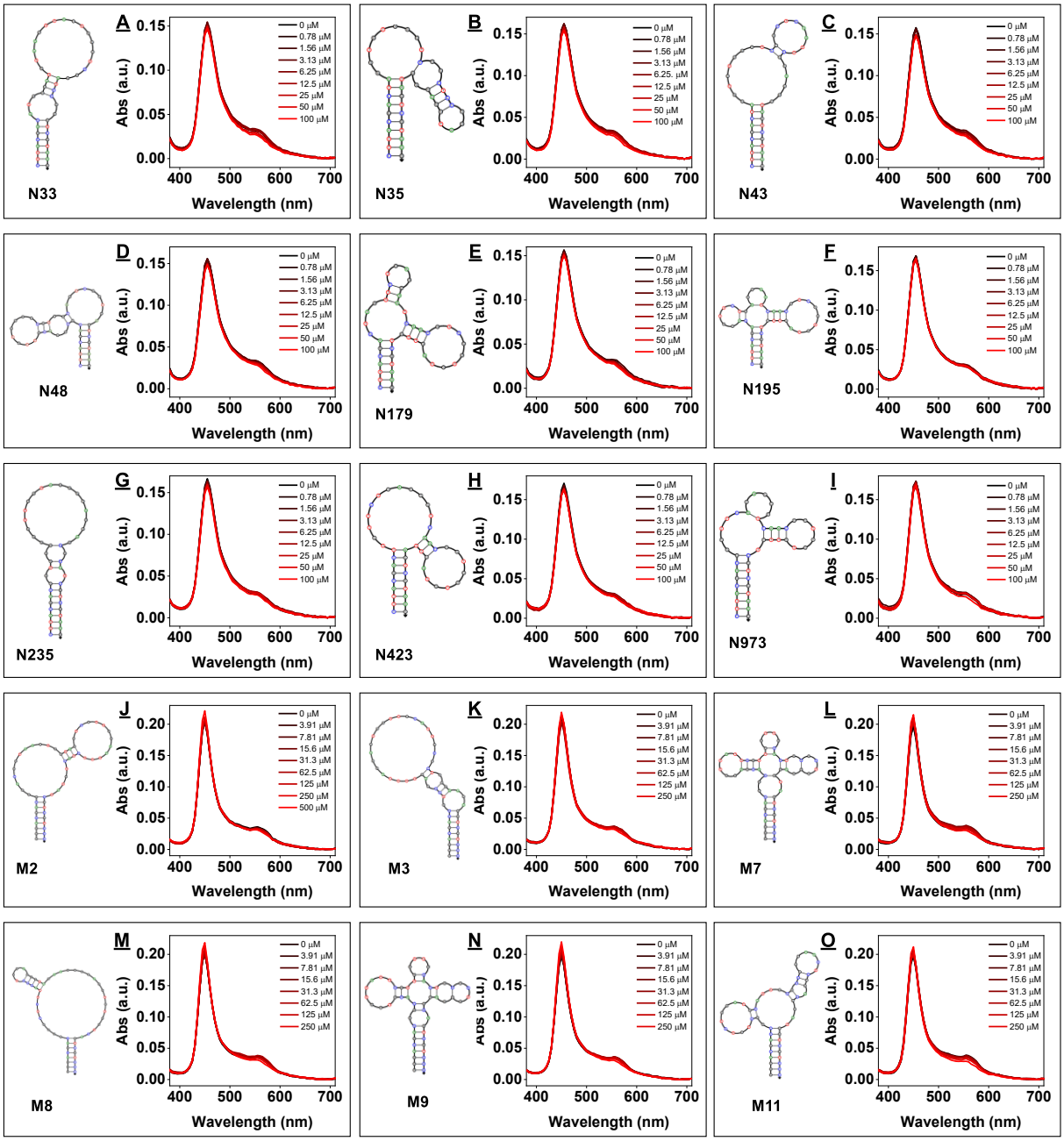

Figure S92 (continued). Absorbance spectra of 4 μM X-732-91B in the presence of different targets at various concentrations. (**A-I**) cocaine and (**J-O**) (+)-methamphetamine. N/A indicated that no target control experiments were performed for that aptamer since no target-induced dye-displacement was observed. Black-to-red color gradient represents increasing concentrations of target.

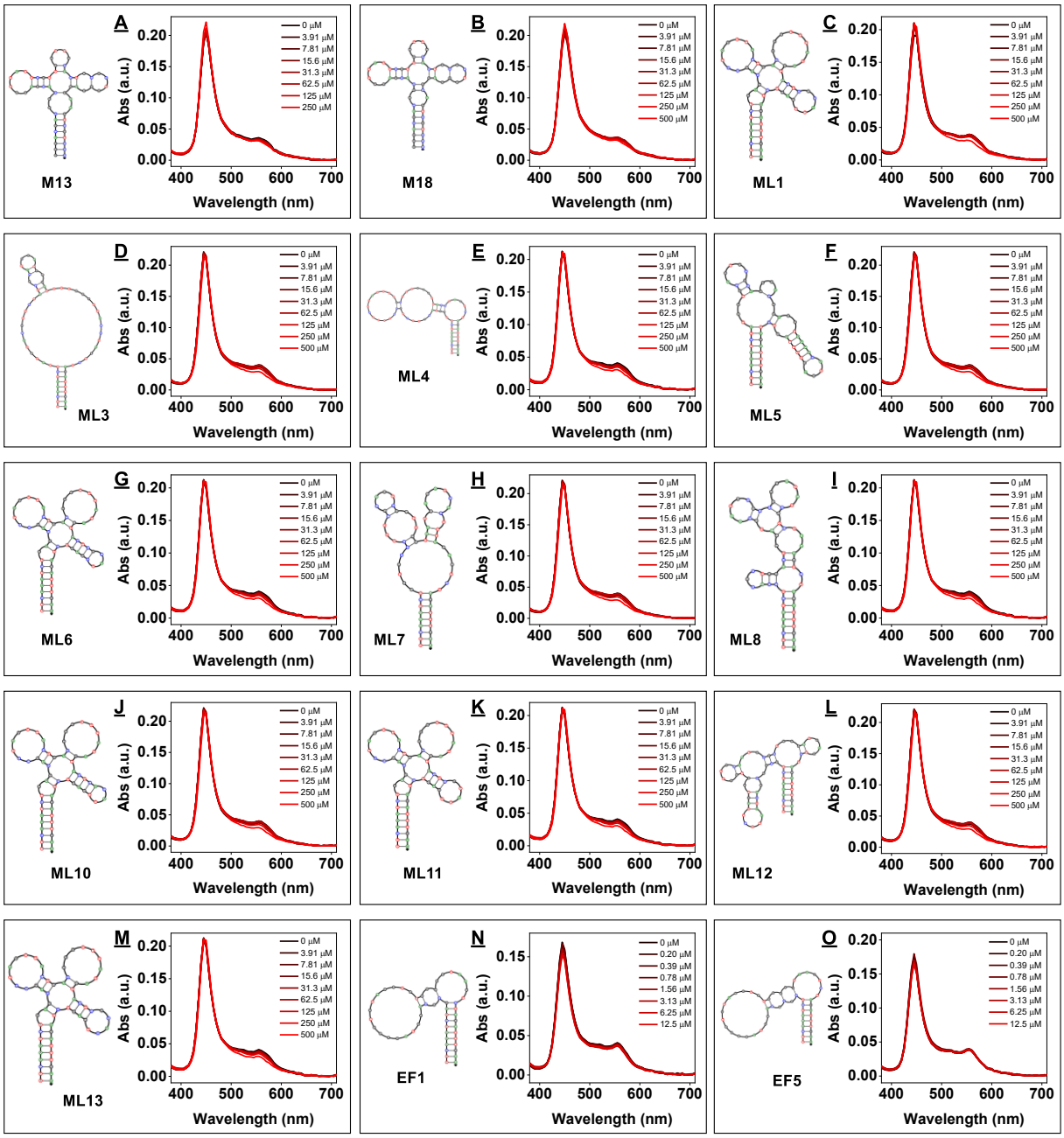

Figure S92 (continued). Absorbance spectra of 4 μM X-732-91B in the presence of different targets at various concentrations. (**A-M**) (+)-methamphetamine and (**N-O**) AB-FUBINACA. N/A indicated that no target control experiments were performed for that aptamer since no target-induced dye-displacement was observed. Black-to-red color gradient represents increasing concentrations of target.

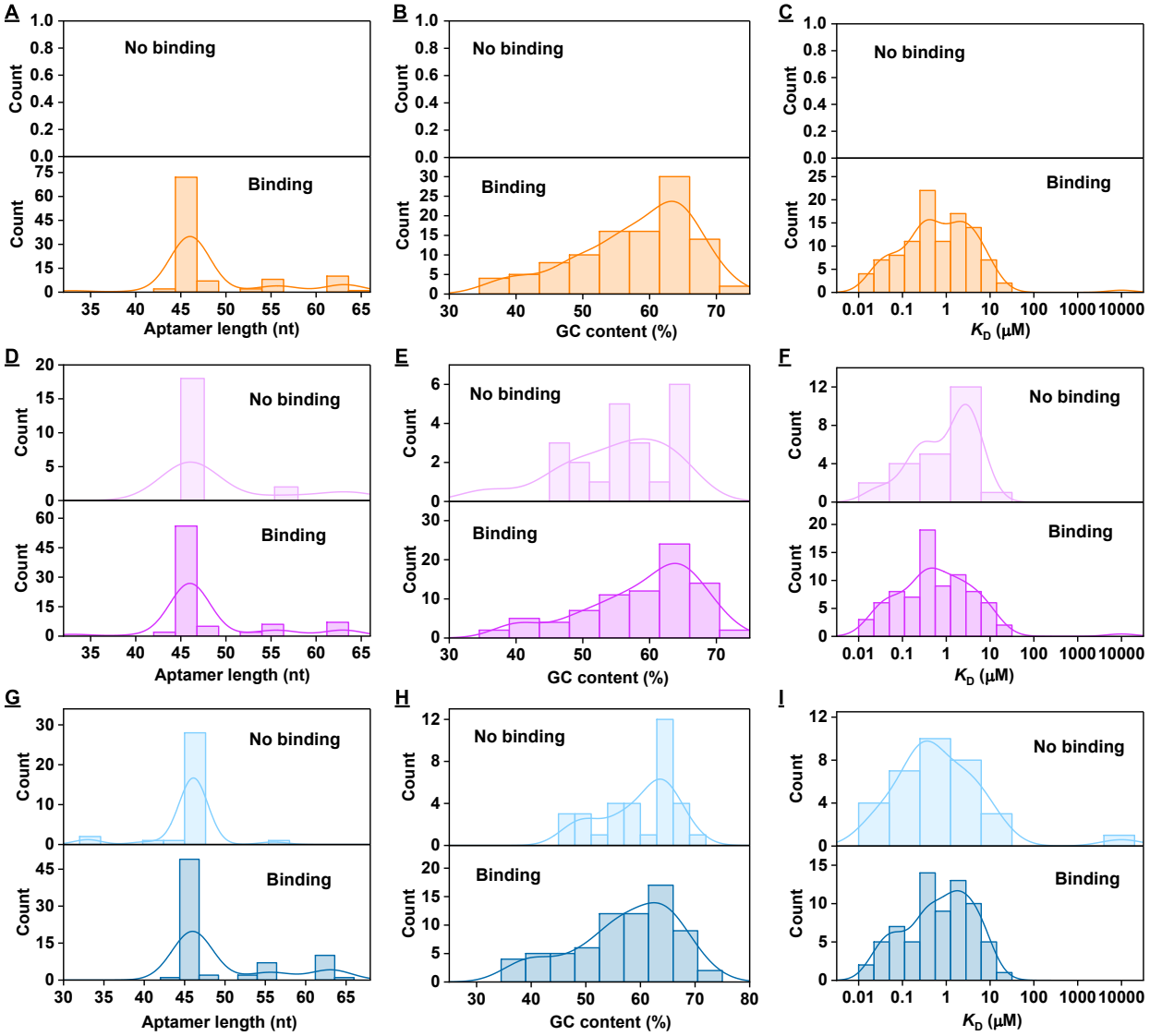

Figure S93. Identifying determinants of aptamer binding to (**A–C**) X-732-91B, (**D–F**) MTC, and (**G–I**) Cy7. Histograms show the number of aptamers that can and cannot bind X-732-91B based on (**A, D, G**) aptamer length, (**B, E, H**) percentage GC content, and (**C, F, I**) target-binding affinity.

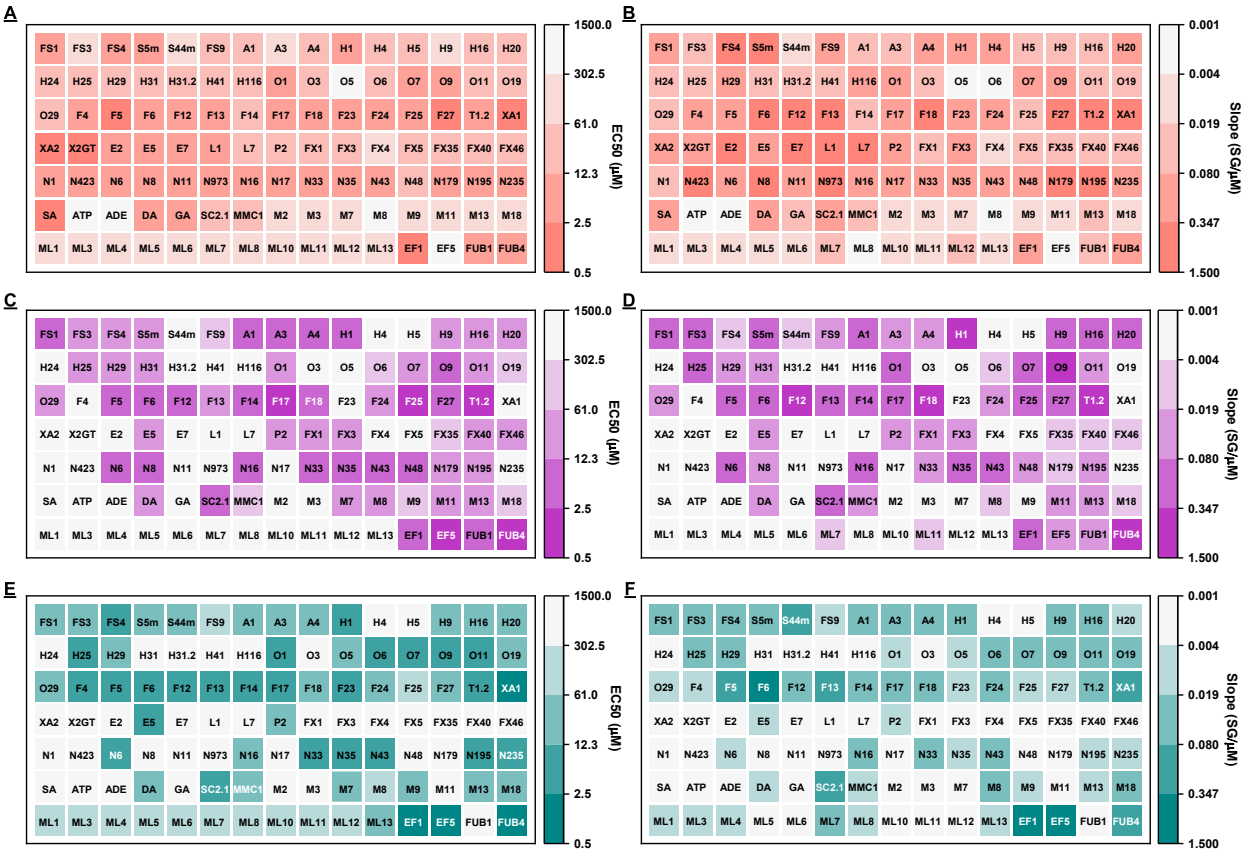

Figure S94. Analyzing the sensitivity of dye-displacement assays using different performance metrics for (**A, B**) X-732-91B, (**C, D**) MTC, and (**E, F**) Cy7. Heat maps depicting (**A, C, E**) EC_{50} values and (**B, D, F**) slope at low target concentrations for each aptamer.

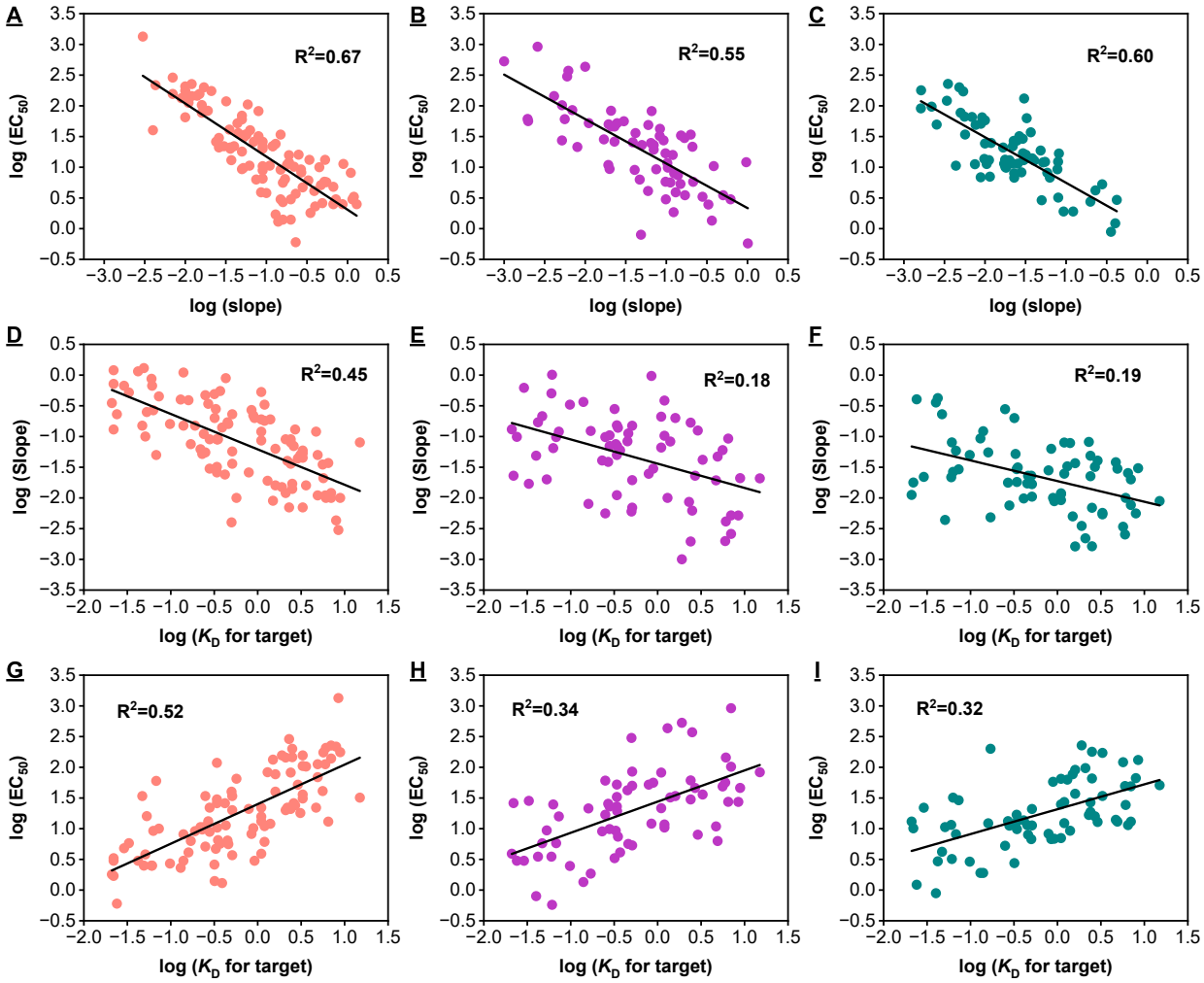

Figure S95. Correlation between different sensitivity parameters for dye-displacement assays and target-binding affinity. (**A**–**C**) Log-log plots depicting the correlation between calibration curve slope and assay EC_{50} for displacement assays based on (**A**) X-732-91B, (**B**) MTC, and (**C**) Cy7. (**D**–**F**) Log-log plots depicting the correlation between target-binding affinity (K_D) and assay calibration curve slope for displacement assays based on (**D**) X-732-91B, (**E**) MTC, and (**F**) Cy7. (**G**–**I**) Log-log plots depicting the correlation between K_D and assay EC_{50} for displacement assays based on (**G**) X-732-91B, (**H**) MTC, and (**I**) Cy7.

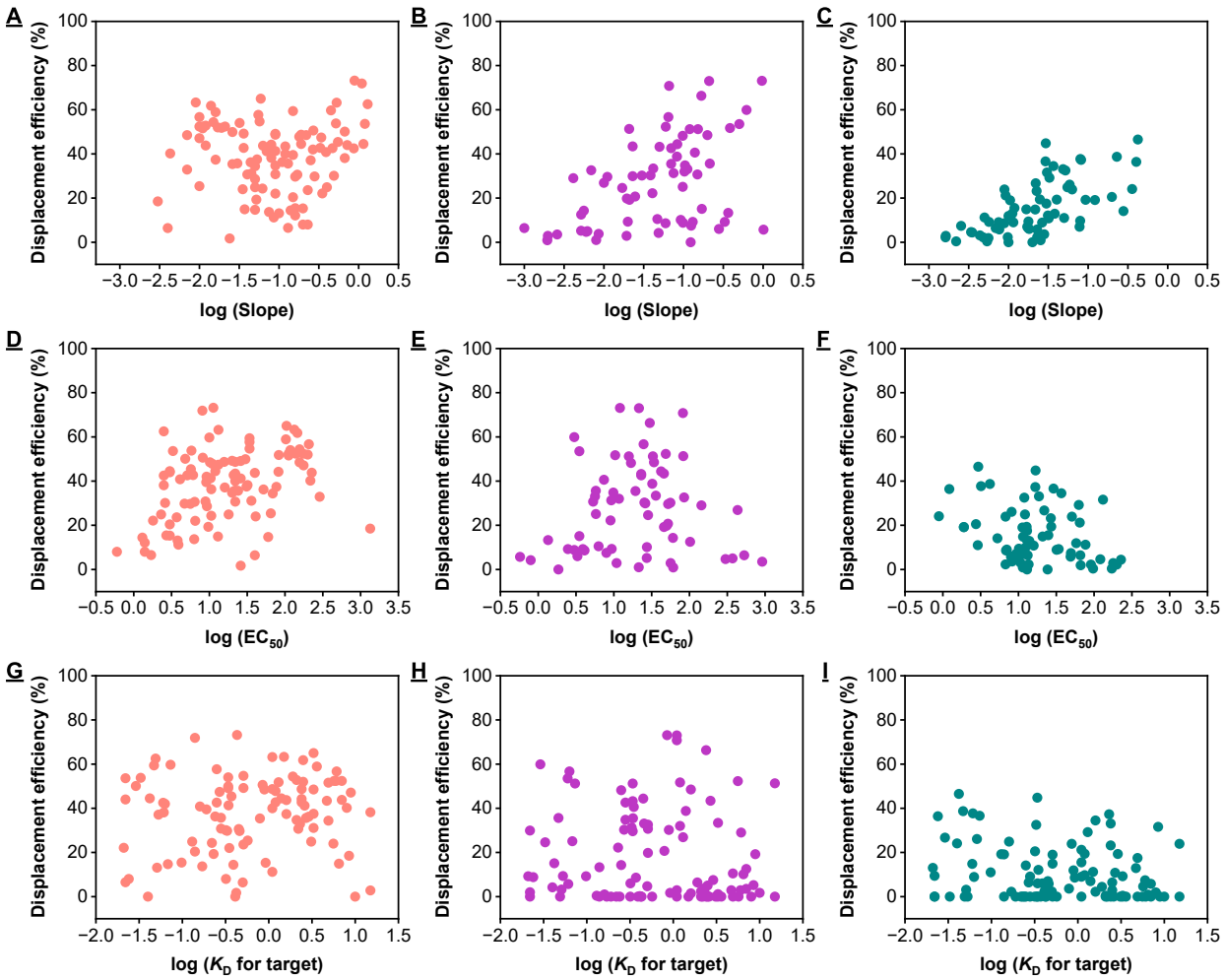

Figure S96. Correlation of different sensitivity parameters for dye-displacement assays or target-binding affinity with dye-displacement efficiency. (**A**–**C**) Log-log plots depicting the correlation between assay calibration curve slope and dye-displacement efficiency for displacement assays based on (**A**) X-732-91B, (**B**) MTC, and (**C**) Cy7. (**D**–**F**) Log-log plots depicting the correlation between assay EC_{50} and dye-displacement efficiency for displacement assays based on (**D**) X-732-91B, (**E**) MTC, and (**F**) Cy7. **(G**–**I**) Log-log plots depicting the correlation between target-binding affinity and dye-displacement efficiency for assays based on (**G**) X-732-91B, (**H**) MTC, and (**I**) Cy7.